Spring 5-15-2019

Local Environmental Controls on Sulfur Isotope Ratios in Marine Sedimentary Iron Sulfide Minerals

Roger Nicholas Bryant
Washington University in St. Louis

WASHINGTON UNIVERSITY IN ST. LOUIS

Department of Earth & Planetary Sciences

Dissertation Examination Committee:
David A. Fike, Chair
Alexander S. Bradley
Jeffrey G. Catalano
Itay Halevy
Jill D. Pasteris

Local Environmental Controls on Sulfur Isotope Ratios in Marine Sedimentary Iron Sulfide Minerals

by

Roger Nicholas Bryant

A dissertation presented to
The Graduate School
of Washington University in
partial fulfillment of the
requirements for the degree
of Doctor of Philosophy

May 2019
St. Louis, Missouri

Table of Contents

List of Figures

List of Tables

Acknowledgments

This dissertation was truly a team effort. There are dozens of people who have supported me over the last 5 years and enabled me to get to this point. Firstly, I must acknowledge the amazing support of Lee Poe. You made a real sacrifice moving to St. Louis to help me follow my dreams – I couldn't have done any of this without you and I'm so grateful. To my family (Kate, Dave, Steph, Maya, Pepsi and Peter) – you have been behind me from the start and somehow kept me sane through our fortnightly Skype sessions, even when iron sulfides took over my brain. It has been nice to be reminded on a daily basis that there's more to life than science.

To my advisor, David, I will always be grateful to you for teaching me sulfur and handing me the responsibility of taking one of your ideas forward – I hope I have done justice to your remarkable vision, and produced at least a few (nice) surprises along the way. Thank you for always challenging me, and giving me the confidence to pursue a career in academia. I look forward to many exciting projects with you in the future. To Jill, thank you for taking me under your wing and teaching me about the joys of Raman spectroscopy, co-authoring my first publication, and drumming home the message that without the context of mineralogy, inorganic geochemistry can only be so useful! To Alex, thank you for teaching me about some of the exciting applications of organic geochemistry, always keeping me on my toes in chalk talks, and encouraging me to utilize statistics (correctly) in my research. To Jeff, I'm grateful for your enthusiasm for pyrite, your unrivalled expertise in aqueous-mineral interactions, and the friendly encouragement you have provided throughout my graduate school experience. To Itay, I truly appreciate you allowing me to spend some time with you in Israel, talking to me with unbounded patience and humility, and providing me with extra motivation to develop an analytical method to help calibrate your incredible diagenetic model.

I thank all the members of the Fike, Bradley, Catalano and Konecky Labs from 2014-2019 for their gallant participation in iron sulfide-related chalk talks, paper discussions and meetings that greatly improved this dissertation. In particular, I could not have survived this process without the support and friendship of my long-suffering office mates, Scott and Joss. It has been so incredible to have you as a sounding board for some of my crazier ideas and life dilemmas, and I hope I have returned the favor on occasion. To you and the other 'first years', Melody, Michael, Xiaochen, and Kelsey – it has been an honor to go through this process with you, and I'm pretty sure we're the best cohort Wash U have had. I honestly can't imagine what this process would have been like without you guys. I hope our paths continue to cross and you find happiness in life. To current and past members of the Fike and Bradley Labs, Steph, Jen, Clive, Mel, Cole, Maya, Morgan, Wil, Derek, Harry, Ming, Seth, Catherine, Zoe – your support in the lab and friendship won't be forgotten. Jen, thanks for feeding me amazing food once a week for the past 5 years, even after I made the pesky decision to go vegan.

Finally, thank you to the McDonnell Center for the Space Sciences and the Department for Earth & Planetary Sciences at Wash U for the funding and support.

All in all, I could not have made it to this point without the support of all the people listed above, and too many more to list. Thank you and I'll see you soon.

Roger Nicholas Bryant

Washington University in St. Louis

May 2019

ABSTRACT OF THE DISSERTATION

Local environmental controls on sulfur isotope ratios in marine sedimentary iron sulfide minerals

by

Roger Nicholas Bryant

Doctor of Philosophy in Earth & Planetary Sciences

Washington University in St. Louis, 2019

Professor David A. Fike, Chair

The controls on the bulk sulfur isotopic composition of marine sedimentary iron sulfides (often referred to simply as pyrite; $\delta^{34}S_{pyr}$) are poorly understood. Nevertheless, many have employed $\delta^{34}S_{pyr}$ in efforts to reconstruct the past operation of the biogeochemical sulfur cycle, from the planetary scale down to individual microbial metabolisms. This practice has been thrown into doubt by a growing body of evidence that suggests $\delta^{34}S_{pyr}$ is strongly controlled by local environmental conditions. This dissertation describes efforts to determine the mechanisms responsible for the link between local environmental conditions and $\delta^{34}S_{pyr}$. In order to do this, we developed novel laboratory procedures and analytical techniques to facilitate the measurement of grain-specific $\delta^{34}S$ values.

Firstly, by determining the major controls on the Raman spectrum for pyrite, we demonstrate that laser Raman microprobe analysis is an effective tool for distinguishing between pyrite and other minerals (e.g., marcasite) on a grain-specific basis. This tool is used extensively throughout this dissertation, prior to any grain-specific geochemical analyses.

Secondly, we present procedures for physical isolation, mounting and grain-specific sulfur isotopic analysis of marine sedimentary iron sulfides. The sulfur isotope analysis procedure utilizes secondary ion mass spectrometry (SIMS) to generate images of sulfur ion ($^{32}S^-$

and $^{34}S^{-}$) abundance in mineral grains. These procedures are tested on isotopically homogeneous hydrothermal iron sulfides and some examples of modern and Cretaceous-aged sedimentary iron sulfides. We find that the overall procedure produces distributions of accurate and precise grain-specific $\delta^{34}S$ values that record the range of sulfur isotopic compositions of the fluid(s) from which the iron sulfide grains precipitated. This information can be used to infer local environmental conditions associated with iron sulfide mineral formation.

Thirdly, we apply the SIMS procedure to Pleistocene-aged pyrite grains sourced from the Gulf of Lion, in order to understand the driver(s) of large magnitude (75‰) stratigraphic oscillations in $\delta^{34}S_{pyr}$ over 100-kyr glacial-interglacial cycles. We find that the $\delta^{34}S_{pyr}$ changes at this site were the result of increased sedimentation rate during glacial intervals, which restricted diffusive communication between water column and sediment pore waters and led to higher $\delta^{34}S_{pyr}$ values. In contrast, the activity of sulfate reducing microbes showed no discernible response to the changing environmental conditions.

Finally, we apply the SIMS procedure to Cretaceous-aged iron sulfides from Demerara Rise, in order to understand the driver(s) of a secular decrease in $\delta^{34}S_{pyr}$ values toward the onset of the Cenomanian-Turonian Ocean Anoxic Event (OAE-2). We find that the relative abundances of different iron sulfide minerals and textures change over this interval, but that the isotopic compositions of these different minerals/textures are nearly invariant. More ^{34}S-depleted sulfide was incorporated into iron sulfide minerals during OAE-2, likely because of an increase in the rate of iron sulfide formation relative to the rate of sulfate reduction.

Overall, these findings suggest that depositional conditions can control $\delta^{34}S_{pyr}$ by modulating the flux of sulfate into sediment pore waters, although the relative kinetics of iron sulfide formation and sulfate reduction can also have a major influence.

Chapter 1: Introduction

1.1 Why study sulfur?

In the context of the current warming trend at Earth's surface (Mann et al., 1999), its causes, and its consequences, we as a society have never been more aware of the importance of present and past compositions of our planet's atmosphere. Aside from the greenhouse gases believed to be associated with the warming trend, there exists a longer-held anthropocentric fascination with oxygen. The timing and magnitude of the oxygenation of Earth's atmosphere and ocean are topics of particularly great interest in the natural sciences, due to the potential cause-and-effect relationship between oxygen and the diversification of life (Lyons et al., 2014). However, the direct record of past atmospheric partial pressures of all gases, including oxygen (p_{O2}), extends only as far back as Earth's oldest ice (~2.7 Ma) (Brook and Buizert, 2018; Kehrl et al., 2018), whose frozen bubbles trap minute quantities of ancient air. To reconstruct p_{O2} further back in time, we are forced to utilize geologic archives (i.e., proxies) bearing information that relates only indirectly to p_{O2}. In order to find a suitable proxy, it is first important to recognize that as an oxidant, the abundance of oxygen affects and is affected by the oxidation state of the ocean-atmosphere system. This is also true for other oxidants, such as sulfate (SO_4^{2-}), nitrate (NO_3^-) and iron (Fe^{3+}). Of these species, sulfate is by far the most abundant in the modern ocean (28 mM) and is readily incorporated into an array of minerals (e.g., gypsum, anhydrite, barite, and carbonates) that are believed to be thermodynamically stable under a broad range of conditions, and together are temporally continuous through Earth history (Fike et al., 2015). Thus, the burial of sulfate-bearing minerals in marine sediments forms a robust archive from which proxies for the oxidation state of the ocean-atmosphere system can be derived.

To complicate matters, sulfur does not only leave the ocean in its most oxidized form – microbial reduction of sulfate to sulfide in marine sediments, and the reaction of some of

this sulfide with dissolved iron or iron-bearing minerals, means that a similarly large flux of buried sulfur is chemically reduced, most commonly in the form of pyrite (FeS_2) (Fike et al., 2015). Broadly, the concentration of sulfate and the relative amount of buried sulfur that joins the reduced (pyrite) versus the oxidized (sulfate) sulfur pool reflect the oxidation state of the ocean. In addition, because pyrite burial leaves oxidized products in the ocean, it is also likely a large indirect source of oxygen to the atmosphere (Canfield, 2005). To date, the best estimates of past ratios of the relative burial flux of sulfides (f_{pyr}) have utilized the offset between time-averaged records of the sulfur isotopic composition ($\delta^{34}S$[1]) of pyrite and sulfate in sedimentary rocks (Δ_{pyr}) (Berner, 2006; Canfield and Farquhar, 2009). This approach uses the standard steady-state description of isotopic mass balance in the sulfur cycle

$$f_{pyr} = \frac{\delta^{34}S_{SO4} - \delta^{34}S_{in}}{\Delta_{pyr}} \quad (1.1)$$

where $\delta^{34}S_{in}$ is the average isotopic composition of sulfur entering the ocean. From Eq. 1.1, it is clear that this approach to modeling the sulfur cycle is heavily reliant on Δ_{pyr} and somewhat on assumed constancy in $\delta^{34}S_{in}$, and yet despite huge fluctuations of Δ_{pyr} on geologically short timescales (Canfield and Farquhar, 2009; Figure 1.1) and a secular expansion in the range of Δ_{pyr} values over Earth history (Canfield and Farquhar, 2009; Figure 1.1), this parameter in models is regularly set to be constant (e.g., at ~40‰ for the Phanerozoic; Berner, 2006). This is perhaps because when time-binned Δ_{pyr} values are used, this leads to unrealistic f_{pyr} values of >1 for certain intervals of Earth history (Canfield, 2004; Canfield and Farquhar, 2009). Clearly, the steady-state, 'global' view of the sulfur cycle in Eq. 1.1 is overly simplistic. However, a viable area for improvement exists – the reevaluation of the controls on $\delta^{34}S_{pyr}$ (and thus, Δ_{pyr}) values. Some have suggested that local environmental factors are responsible for much of the scatter in the Δ_{pyr} record (Fike et al., 2015; Pasquier et

[1] $\delta^{34}S_{sample} = \left(\frac{R_{sample}}{R_{VCDT}} - 1\right) \times 1000$, where $R = {}^{34}S/{}^{32}S$

al., 2017; Figure 1.1). The primary aim of this dissertation is to test this claim, and if it is confirmed, to decipher the crucial mechanisms responsible.

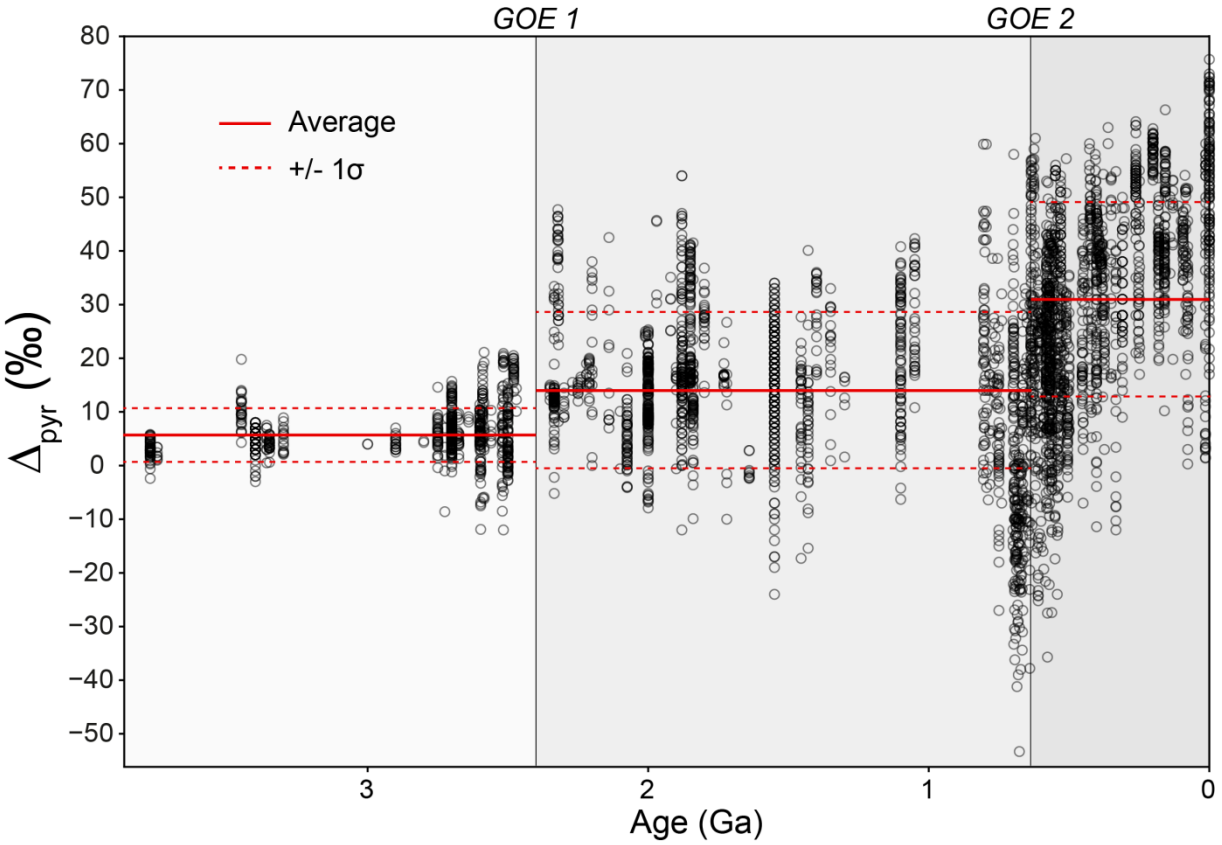

Figure 1.1. Compilation of Δ_{pyr} through Earth history, calculated using compiled $\delta^{34}S_{pyr}$ and time-binned $\delta^{34}S_{SO4}$ data from Canfield and Farquhar (2009). 'GOE 1' and 'GOE 2' refer to the Paleo- and Neo-proterozoic 'Great Oxygenation Events' (Lyons et al., 2014) – each of which coincide with increases in the average value and standard deviation of Δ_{pyr}, marked by the solid and dashed red lines, respectively.

1.2 The case for local environmental controls on Δ_{pyr}

The initial search for local controls on Δ_{pyr} focused on laboratory studies of the microbial fractionation of sulfur isotopes during sulfate reduction (ε_{mic}). Although sulfate concentration is recognized to be a major control on ε_{mic} (higher concentrations result in higher ε_{mic}; Habicht et al., 2002), sulfate concentrations in the modern ocean are high and relatively homogeneous, meaning that they are unlikely to limit ε_{mic} in most environments (Bradley et al., 2016). Of potential greater relevance to the scattered Phanerozoic Δ_{pyr} record (Figure 1.1.) are the numerous studies demonstrating a link between microbial sulfate reduction rate and

ε_{mic} (Chambers et al., 1975; Goldhaber and Kaplan, 1982; Harrison and Thode, 1958; Kaplan and Rittenberg, 1964; Leavitt et al., 2013; Sim et al., 2011b, 2011a). As lower cell-specific rates of sulfate reduction (csSRR), primarily a function of electron donor availability, result in larger ε_{mic} (Leavitt et al., 2013), changing csSRR was hypothesized to control Δ_{pyr} values through the Phanerozoic (Leavitt et al., 2013). More recently, it has emerged that energy limitation in marine sediments results in sulfate reducers metabolizing at very low rates (Hoehler and Jørgensen, 2013; Jørgensen and Marshall, 2015; Lau et al., 2016), which could serve to maximize environmental ε_{mic} (Wenk et al., 2017). In addition, the viability of Δ_{pyr} as a proxy for ε_{mic} in the rock record is far from certain, for reasons discussed later.

The first convincing evidence in support of the claim that local environmental factors can control Δ_{pyr} was the observation that, at a site in the Gulf of Papua (Papua New Guinea), sediment cores taken in deeper water (~50 m) exhibited higher and less stratigraphically variable Δ_{pyr} values than cores taken in shallower waters (down to ~8 m) (Fike et al., 2015; Gao et al., 2013). This pattern was tentatively inferred to reflect the different depositional conditions across these different water depths, including more rapid sedimentation and greater exposure to sediment reworking by storms at shallower water depths (Fike et al., 2015). Despite this empirical observation of a correlation between depositional environment and Δ_{pyr}, a mechanistic understanding of the controls on Δ_{pyr} was still lacking.

A major advance on this work was the discovery of large magnitude (~75‰) stratigraphic fluctuations in Δ_{pyr} in Pleistocene-aged sediments in the Gulf of Lion, NW Mediterranean (Pasquier et al., 2017). Intriguingly, these fluctuations appeared to coincide with glacial-interglacial transitions (i.e., 100 kyr periodicity), meaning that they occurred far too quickly to be caused by changing $\delta^{34}S_{SO4}$ due to the long residence time of marine sulfate (~13 Myr; Berner, 2001). In addition, the authors made the empirical observation that Δ_{pyr} values were higher and less variable in interglacials when sedimentation rates were lowest,

and lower and more variable in glacial when sedimentation rates were highest. Thus, a direct relationship between sedimentation rate and Δ_{pyr} was proposed (Pasquier et al., 2017). Two potential mechanisms were offered for this empirical relationship: (1; microbial) increased csSRR at higher sedimentation rates, leading to lower ε_{mic} and Δ_{pyr}, or (2; physical) decreased system "openness" (i.e., diffusive connectivity between water column and pore waters) at higher sedimentation rates, leading to enhanced distillation of pore water sulfate during microbial sulfate reduction, and the eventual preservation of lower Δ_{pyr} values. Although the former mechanism was favored in the literature (Leavitt et al., 2013), there was also precedent for invoking the latter mechanism, namely the strong negative correlation between apparent ^{34}S-enrichment factors (from the Rayleigh equation) and a parameter for system "openness" at an array of marine drilling sites (Claypool, 2004). However, it was not previously possible to determine whether mechanism (1) or (2) was actually responsible for the observed sedimentation rate-Δ_{pyr} relationship (Pasquier et al., 2017). This dissertation describes efforts to rectify this problem, and pinpoint other local factors that may affect Δ_{pyr} in other environmental scenarios not represented in the Gulf of Lion core, in the modern, and throughout Earth history.

1.3 Rationale for grain-specific S-isotope measurements

In order to allow microbial and physical influences on Δ_{pyr} to be disentangled, two things are required: a proxy for ε_{mic}, and a proxy for system "openness". Unless every pyrite grain in a marine sediment sample experienced the same growth history, it is predicted that making multiple grain-specific measurements of $\delta^{34}S_{pyr}$ could provide reasonable estimates of the ε_{mic} and system "openness" present when the sediment was deposited. The offset between coeval $\delta^{34}S_{SO4}$ and the lowest grain-specific $\delta^{34}S_{pyr}$ value in a sample would provide a minimum estimate of ε_{mic}, and assuming that abundant reactive iron was available to capture sulfide as

it was produced by microbial sulfate reduction, the range of grain-specific $\delta^{34}S_{pyr}$ values in a sample would be negatively proportional to system "openness".

1.4 Chapter-by-chapter outline for this dissertation

Before any grain-specific isotopic measurements can be made, it is necessary to identify the mineralogy of sedimentary iron sulfides in the environmental sample. Laser Raman microprobe analysis provides a perfect tool to distinguish between individual micro-sized grains of different iron sulfide minerals (particularly pyrite and marcasite), so long as analytical conditions are chosen carefully. Chapter 2 of this dissertation, published in *Applied Spectroscopy* (Bryant et al., 2018) describes efforts to investigate the major controls on the characteristics of the Raman spectrum of pyrite, with the intention of providing a blueprint for Raman analysis of iron sulfides as a non-destructive, essential precursor to grain-specific isotopic analyses. In short, we identified a laser heating effect on the positions of pyrite's Raman bands, and a crystallographic orientation effect on the relative intensities of pyrite's Raman bands. The latter is not a problem when it comes to identifying pyrite, but the former could preclude identification if bands become too down-shifted, or if enough heat accumulates to break down the analyte. We therefore recommend that only low laser powers ($\leq$ 1 mW) are used for Raman analysis of pyrite, whatever other analytical conditions are used.

The third chapter of this dissertation, published in *Rapid Communications in Mass Spectrometry* (Bryant et al., 2019), describes the methods developed to extract iron sulfides from environmental samples, mount them, and then analyze their individual sulfur isotope compositions. The novel method employed for grain-specific sulfur isotope analyses, secondary ion mass spectrometry (SIMS) scanning ion imaging, allows both inter- and intra-grain $\delta^{34}S$ measurements to be made, thus improving on existing grain-specific methods such

as laser ablation multi-collector inductively-coupled plasma mass spectrometry (LA-MC-ICP-MS) or SIMS/NanoSIMS spot analyses with Faraday cup and/or electron multiplier detectors. In sum, we find that the $\delta^{34}S$ values of diverse environmental populations of ≥1 μm-sized pyrites and marcasites can be measured accurately and precisely using this method. In addition, three-dimensional intra-grain $\delta^{34}S$ variability in sedimentary iron sulfides can be accessed when processing $^{32}S^-$ and $^{34}S^-$ ion images. Therefore, the method is suitable for disentangling microbial and physical influences on Δ_{pyr}, in addition to any contributions from less common sulfide minerals such as marcasite. These capabilities are harnessed in the next chapters of this dissertation.

In chapter 4, we use the methods detailed in chapters 2-3 to determine the microbial and physical influences on Δ_{pyr} values in the Gulf of Lion core for which the sedimentation rate-Δ_{pyr} relationship was previously observed (Pasquier et al., 2017). We find that grain-specific $\delta^{34}S_{pyr}$ minima for all samples are close to −50‰, and therefore ε_{mic} and csSRR (i.e., microbial activity) are nearly invariant over glacial-interglacial transitions at the site. In contrast, the range of grain-specific $\delta^{34}S_{pyr}$ values is on average far larger during glacial intervals, when sedimentation rates were highest and bulk Δ_{pyr} values were lowest. We are therefore able to conclude that the large magnitude fluctuations in bulk Δ_{pyr} values were caused by changes in system openness, likely driven by independently constrained changes in sedimentation rate, and that ε_{mic} didn't change substantially throughout.

In chapter 5, we use the methods detailed in chapters 2-3 to determine the cause of a marked increase in Δ_{pyr} values leading up to and spanning the Cenomanian-Turonian Ocean Anoxic Event (OAE-2; Raven et al., 2019). Interestingly, we find that the population of iron sulfides in these samples is made up of multiple distinct iron sulfide textures and minerals (each with their own diagnostic $\delta^{34}S$ values), the relative proportions of which change at the onset of OAE-2. This shift in abundance of different textures is coincident with the increase

in Δ_{pyr} values. We find no evidence for a change in system openness, or ε_{mic}. We therefore conclude that the increase in Δ_{pyr} values likely relates to an increase in the kinetics of (diagenetic) iron sulfide formation relative to microbial sulfate reduction, such that more of the earliest, most ^{34}S-depleted sulfide is captured in iron sulfides.

In sum, through demonstrating a method for making grain-specific $\delta^{34}S$ measurements, and a framework for interpreting the novel data, the content of this dissertation is a major step toward understanding the bulk Δ_{pyr} record through Earth history. It is extremely likely that the large degree of scatter in Δ_{pyr} values in the Proterozoic and Phanerozoic relate to changes in sedimentary parameters such as sedimentation rate, porosity, organic carbon loading, and bottom water O_2 content. These changes control Δ_{pyr} values through a combination of physical (system openness), microbial (ε_{mic}) and kinetic (e.g., iron reactivity) factors. The ability to distinguish between these factors using SIMS scanning ion imaging is entirely novel and ensures that the Δ_{pyr} record is no longer inscrutable.

Chapter 2: Characterizing microcrystalline iron sulfide minerals using laser Raman microprobe analysis

Roger N. Bryant[1], Jill D. Pasteris[1,2] and David A. Fike[1,2]

[1]Department of Earth & Planetary Sciences & [2]Institute for Materials Science and Engineering, Washington University in St. Louis, St. Louis, MO, USA

A version of this chapter is published as:

Bryant, R.N., Pasteris, J.D., Fike, D.A., 2018. Variability in the Raman Spectrum of Unpolished Growth and Fracture Surfaces of Pyrite Due to Laser Heating and Crystal Orientation. *Appl. Spectrosc.* 72, 37–47. doi:10.1177/0003702817736516

Abstract

Two probable causes of variability in the Raman spectrum of unpolished pyrite are well recognized, in principle, but not always in practice, namely 1) downshifting of band positions due to laser heating and 2) variations in the ratios of band intensities due to crystallographic orientation of the sample with respect to the laser's dominant polarization plane. The aims of this paper are to determine whether these variations can be used to acquire additional information about pyrites. Here, using laser Raman microprobe analysis of natural, unpolished pyrite samples, we investigate the magnitude of downshifting of band positions associated with laser heating of different sizes of pyrite grains. We demonstrate that the magnitude of this effect can be large (up to ~10 cm^{-1}), negatively proportional to grain size, of greater magnitude than the effect typically attributable to natural inter-sample differences in trace-element (TE) solid solution, and of similar magnitude among bands. Through Raman analysis of naturally occurring faces on pyrite samples at various angles of rotation, we also demonstrate that the three most common faces on pyrite can be distinguished by the ratio of the intensities of the dominant bands. We conclude that for unpolished samples, laser Raman microprobe analysis is most effective as a means of identifying pyrite, and the presence of solid solution therein, when laser power is low enough to avoid substantial heating. Once pyrite has been identified, higher laser powers can be used to produce spectra whose ratios of band intensities indicate the face or crystallographic plane being irradiated.

2.1 Introduction

Mineral identification and further characterization (e.g., size, degree of crystallinity, morphology, and neighboring phases) often provide essential environmental context for interpreting geochemical data. Laser Raman microprobe analysis – in contrast to powder X-ray diffraction (XRD), petrography, and electron microprobe analysis – allows individual grains of 1 μm or less (depending on instrumental configuration) to be assigned an accurate

mineral identification. The spectral bands produced by Raman analysis of a mineral are defined by vibrational frequencies indicative of the bonding and symmetry of the mineral structure. The positions of the bands for a mineral can be distinguished from those of other minerals, including polymorphs (e.g., marcasite and pyrite, see Figure 2.1) (White, 2009).

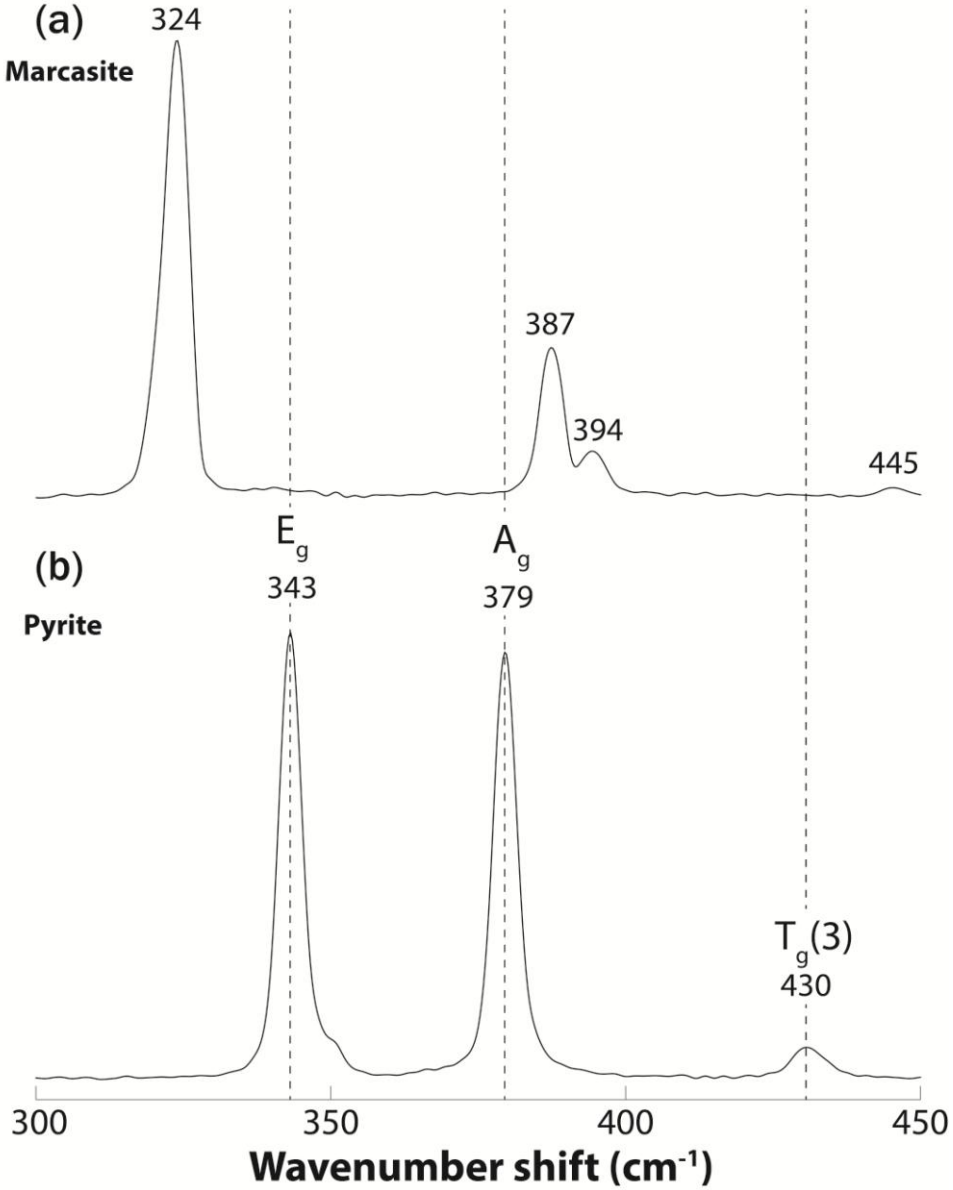

Figure 2.1. Raman spectra of: (a) a 0.3 cm-diameter marcasite sample (Ward's Natural Science) from Vintířov, Bohemia, Czech Republic, and (b) a 1 cm-diameter pyrite sample from Navajún, La Rioja, Spain. All bands are labeled with their positions (calculated as the band midpoint at half maximum intensity). Both spectra were produced using a laser power of 3 mW, an optical objective of 80x and numerical aperture (N.A.) of 0.75, and averaging over 20 spectra each with a collection time of 5 seconds. The spectral resolution for these spectra is 2.5 cm^{-1}.

Pyrite is a common accessory phase in many igneous and metamorphic rocks, is often abundant in ore deposits, and also occurs in many sedimentary rocks. Despite pyrite's abundance and importance, however, its band positions and band intensity ratios in previously published Raman spectra are markedly variable (Borjigin et al., 2014; Cavalazzi et al., 2012; Danise et al., 2012; Kleppe and Jephcoat, 2004; Mao et al., 2014; Mernagh and Trudu, 1993; Vogt et al., 1983; Wei et al., 2014; White, 2009; Xu et al., 2014). Whether this variability represents analytical artifacts, inconsistent spectral calibration between different instruments and labs, near-surface strain, or real mineral-chemical differences has yet to be addressed. Additionally, if the variability is real, its origin as the result of compositional or morphologic differences remains to be clarified. In this study, we conduct experiments to evaluate the presence and nature of variability in the Raman spectra of pyrite samples analyzed under controlled conditions. We also explore whether variation in band positions and band intensity ratios can be diagnostic for the presence of chemical impurities and for the morphology of the pyrite crystal.

2.1.1 Variability in the Raman spectrum of pyrite

Crystalline pyrite belongs to the cubic/isometric crystal system, crystal class $2/m\bar{3}$, with unit cell factor group symmetry of T_h. The Raman-active modes are traditionally referred to by their group symmetry properties E_g, A_g, and T_g (Vogt et al., 1983). We will use that nomenclature here (Figure 2.1). Figure 2.1(b) shows a typical Raman spectrum of a hand sample of pyrite, with crystals on the order of ~1 cm. The three bands from left to right correspond to the characteristic Raman-active modes for pyrite: the S_2 dumb-bell libration (E_g); the S–S in-phase, symmetric stretch (A_g); and the coupled libration and stretch ($T_g(3)$) modes (Kleppe and Jephcoat, 2004; Sourisseau et al., 1991; Vogt et al., 1983). Table 2.1 is a compilation of Raman spectral data on pyrite from the literature. Two ways in which the

published spectra vary are: (a) the positions (recorded in wavenumbers) of the bands, and (b) the intensity ratios of the bands with respect to each other.

Table 2.1. Compilation of positions (vibrational frequencies), and ratios of intensities of the bands in published Raman spectra for pyrite.

Study	Morphology/ Texture	E_g mode (cm^{-1})	A_g mode (cm^{-1})	$T_g(3)$ mode (cm^{-1})	A_g intensity/ E_g intensity
(White, 2009)	Euhedral, macroscopic	343	379	430	1.02 to 1.38
		344	378	N/A[a]	~1.2
(Vogt et al., 1983)	Euhedral, macroscopic	343	379	430	~3.5
(Mernagh and Trudu, 1993)	Euhedral, macroscopic	342	377	428	~1.5
(Kleppe and Jephcoat, 2004)	Microcrystal	344	379	430	~2.2
(Danise et al., 2012)	Framboidal, **polished**	342	379	432	~1.25
(Cavalazzi et al., 2012)	Framboidal, **polished**	343	379	430	~1.25
(Borjigin et al., 2014)	Framboidal, **polished**	343	379	432	~1.6
		343	379	430	~1.4
(Xu et al., 2014)	Microsphere, nanocrystals	338	374	424	~1
(Wei et al., 2014)	Nanochain	335	371	421	~1.6
(Mao et al., 2014)	Nanocrystal, euhedral	338	371	N/A[a]	~2.2
		342	377	N/A[a]	~2.1
RRUFF[b] R050070	Euhedral, cubic, macroscopic, **polished**	343[c]	379.2[c]	430[c]	0.90

RRUFF[b] R050190	Euhedral, macroscopic, **polished**	343.4[c]	379.9[c]	433.6[c]	3.04
RRUFF[b] R070692	Euhedral, 'fine-grained,' macroscopic	340.8[c]	374[c]	425[c]	1.94
Range of values		335 to 344 $\Delta = 9$ cm^{-1}	371 to 379.9 $\Delta = 8.9$ cm^{-1}	421 to 433.6 $\Delta = 12.6$ cm^{-1}	0.90 to 3.5

[a] 'N/A' means 'not reported'. 'Macroscopic' indicates a grain size of > 100 μm.

[b] The RRUFF Project is an online database (rruff.info) for Raman spectral data (Downs, 2006; Lafuente et al., 2016). Files of spectral intensity vs. frequency shifts are publicly available and were assessed quantitatively.

[c] When not explicitly listed in published papers, band positions and intensity ratios were determined by the present authors by inspection of enlarged print-outs of the spectra.

Figure 2.2 shows the substantial variability in the position of each major band previously published in the literature. A displacement in the position of one band is typically accompanied by sympathetic displacements in the other two bands. The band position of the A_g and $T_g(3)$ modes of pyrite are positively correlated with the band position of the E_g mode of pyrite, with R^2 values of 0.85 and 0.80, respectively.

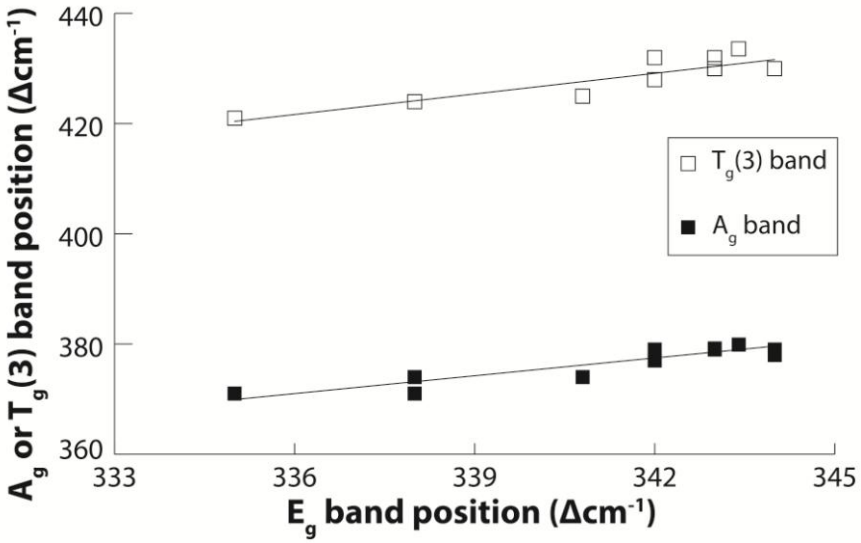

Figure 2.2. The positions of the three dominant bands for pyrite (~343, ~379 and ~430 Δcm^{-1}), as reported in the literature (Table 2.1). The positions of the three bands co-vary, with slopes of ~1.

2.1.2 Potential causes of variability in band positions

Differential calibration: If the Raman instruments in different laboratories are calibrated differently, this could result in apparent offsets in band positions for pyrite samples analyzed in separate labs (Nasdala et al., 2012). Typically, a Si wafer is used as a standard to determine the amount of offset of the measured position from the standard's accepted position due to inaccurate calibration. As all pyrite's bands occur close to that of Si (band at ~520.5 Δcm^{-1}), any amount of offset due to incorrect calibration should be the same for all bands. While calibration error alone may therefore be able to produce the covariance of band positions (with a slope of ~1) seen in Figure 2.2, calibration error alone is unlikely to explain the full range of variation in band positions in Table 2.1 and Figure 2.2.

Analytical artifacts: Laser heating has been shown to result in downshifting of bands for many materials (Bassil et al., 2006; Calizo et al., 2007; Chio et al., 2003; Ci et al., 2003; Everall et al., 1991; Hart et al., 1970; Huang et al., 1998; Li et al., 2000; Nasdala et al., 2004; Raravikar et al., 2002; Tan et al., 1999; Tsu and Hernandez, 1982; Viera et al., 2001; Zouboulis and Grimsditch, 1991), especially those that are opaque. Pyrite is opaque and has a prominent optical absorption band in the wavelength region of ~300-1200 nm (Bhandari et al., 2015), which encompasses the wavelength of lasers typically used for Raman analysis (e.g., 532 nm, this study), so this effect is expected to be relevant to pyrite. As pyrite's bands occur close together, this effect should be of similar magnitude for each band (Tsu and Hernandez, 1982), potentially facilitating the covariance of band positions (with a slope of ~1) in Figure 2.2.

Incident laser light does not penetrate far into opaque materials such as pyrite, so any near-surface strain will also affect band positions. This effect is not likely to be relevant for growth faces and fracture surfaces (Libowitzky, 1994), but can cause bands to be upshifted

by up to 12 cm^{-1} if samples are prepared mechanically (Nasdala et al., 2012), i.e., by polishing (Libowitzky, 1994; Nasdala et al., 2012; Pačevski et al., 2008).

Phonon confinement: In various nanometer-scale (<25 nm diameter) materials, band positions have been shown to vary with analyte size due to a phonon (lattice vibration) confinement effect (Dash et al., 2002; Nemanich et al., 1981; Osswald et al., 2009; Prabhu and Khadar, 2008; Rajalakshmi et al., 2003, 2000; Rajalakshmi and Arora, 1999; Richter and Wang, 1981; Rolo et al., 1998; Vasilevskiy et al., 2001; Viera et al., 2001; Wang et al., 2000; Yu et al., 1998; Zhu et al., 2005). This effect is expected to be relevant for nanometer-scale pyrite, and could result in band downshifts of >10 cm^{-1} if grains are <5 nm in diameter (Wang et al., 2000).

Trace element chemistry: The presence of trace elements (TEs) in substitutional solid solution can, due to their differences in atomic mass from that of Fe, shift the positions of the Raman bands for pyrite. For example, Pačevski et al. (2008) found that natural pyrite with ~8 wt. % Cu (inferred to be in solid solution) yielded Raman spectra with E_g, A_g and $T_g(3)$ bands downshifted by ~11 cm^{-1}, ~2 cm^{-1} and ~13 cm^{-1}, suggesting that band position variation in pyrite due to solid solution is not inherently likely to be uniform for all bands. Additionally, of all TE contents reported, for most natural pyrites only Ni, Co, Se and As are likely to be present predominantly within the unit cell, while others (Cu, Zn, Pb, Bi, Sb, Tl, Mo, Ag, Cd, Mn, Hg, and Te) can occur both within the unit cell and in micro-inclusions within matrix material or other sulfide minerals (Large et al., 2014).

2.1.3 Potential causes of variability in band intensity ratios

It well known that band intensity and area ratios depend on crystal orientation with respect to the polarization plane of the incident laser beam (Nasdala et al., 2004), as has been demonstrated for other minerals (e.g., phlogopite) (Loh, 1973; Tlili et al., 1989). Accordingly, analyses of faces representing different crystallographic planes through the

pyrite unit cell (i.e., {100} vs. {111} vs. {210}) (Sunagawa, 1957) or rotation of a single face on a horizontal stage should result in appreciable changes in band intensity and area ratios.

In summary, for a suite of unpolished, larger than nano-sized pyrite crystals analyzed under the same instrumental and calibration conditions, one might expect differences both in: (a) band positions, due to compositional variations and differential laser heating, and (b) the relative intensities of bands, due to crystal orientation with respect to the plane of polarization of the laser.

2.2 Methods & Materials

In order to test the above hypotheses, three series of experiments were conducted using a fiber-optically coupled Raman microprobe (HoloLab Series 5000, Raman Microprobe, Kaiser Optical Systems, Inc.). The spectral region of 100-4000 Δcm^{-1} was recorded using an excitation wavelength of 532 nm from a frequency-doubled Nd:YAG laser. Further details on the Raman system's calibration are found in the Supplement (Raman Instrumental and Methods Specifications). The effect of the inherently strong polarization of the laser combined with some depolarization from other optical elements in the beam path produced a transmission ratio in the x:y directions of 25:2. We used GRAMS/32 AI™ v. 6.00 spectroscopy software (Galactic, Waltham, MA) to fit bands (using combined Gaussian-Lorentzian band-shape), and thereby calculate band position, intensity, and area values. The spectral resolution for all spectra herein is 2.5 cm^{-1}. For all experiments on pyrite, a 50x objective (N.A. = 0.55) was used and analyzed faces were oriented perpendicular to the laser beam. Daily instrumental precision for band positions (± 0.1 cm^{-1}) was determined by analysis of a Si wafer (100) at maximum laser power, using the 80x objective, at the start and end of each analysis session.

Firstly, to test the effect of laser-induced heating on the band positions as a function of crystal size, we collected spectra (20 spectra of 1-second duration, averaged; these settings were sufficient to produce high ratios of signal-to-noise (S/N)) for three unpolished pyrite samples (Supplement, Figure S2.1) measuring ~1 cm, ~100 μm, and ~1 μm in diameter. To change the (unmeasured) temperature at the surface of the crystal, the power density on the sample surface was changed by adjusting the laser power to the sample surface (measured, as in Supplement, Figure S2.2). The laser power was evaluated between spectral collections without moving the sample by collecting a Raman spectrum from a polished silicon wafer mounted adjacent to the sample. The silicon wafer had been calibrated by recording its count rate as a function of the laser power measured by a laser power meter (Metrologic Instruments, Inc.). The silicon was always measured in the same orientation, using an 80x ultra-long-working distance Olympus objective (N.A. = 0.75). The average error of the laser power based on the measured count rate was 0.1 mW.

Secondly, to evaluate the range in band positions among typical geological samples, we analyzed unpolished faces on five pyrite samples from worldwide localities (Supplement, Figure S2.3) on which we obtained chemical analyses (see below). To avoid excessive sample heating, a laser power of 1 mW at the sample surface was used. For these experiments, 32 spectra of 4-second duration were collected and averaged, as the previously used 20 spectra of 1-second duration did not result in sufficiently high S/N for every sample. The instrumental reproducibility for the positions of the E_g, A_g, and $T_g(3)$ bands (1σ = 0.02, 0.03 and 0.1 Δcm^{-1}) was determined by collecting 10 spectra on the same spot on a single sample, moving away from the spot and defocusing between each spectral collection. For two grams of the same samples, the abundances of Ni, Co, Se, As, Cu, Zn, Pb, Bi, Tl, Mo, and Te were measured by Activation Laboratories (ON, Canada) using ICP-MS.

Finally, to test the effect of crystal orientation on the intensity and area ratios of bands, centimeter-scale samples (Supplement, Figure S2.4) featuring {100}, {111}, and {210} faces (Sunagawa, 1957), were mounted on a rotating stage and rotated clockwise, with 20 spectra of 1-second duration collected and averaged at 10-degree increments. This experiment was repeated using two different laser powers: 5 mW, and the highest achievable, 14.4 mW. Although the reproducibility of the intensity and area ratios of the A_g and E_g bands was measured to be ± 0.01 (1σ) at 1 mW, 5 mW and 14.4 mW, the 5 and 14.4 mW laser powers offered improved S/N, and peaks were fit with higher confidence ($R^2 > 0.997$). Due to the high laser powers used in this test, sample heating likely modified the resultant data, though any modifications were modulated by the use of large (~1 cm) pyrite crystals. Data from all reproducibility tests are listed in the supplement (Supplement, Table S2.1).

2.3 Results

2.3.1 Effects of sample heating on spectra

As laser power was increased, all bands were downshifted (Figure 2.3; Supplement, Figure S2.5) and, in general, broadened (Supplement, Figure S2.6). The downshifting of bands with respect to laser power was approximately linear in most cases (Figure 2.3). The magnitude of this effect and the lowest-wavenumber positions attained by each band were also negatively correlated with the grain size of the analyte (Figure 2.3; Table 2.2). The total downshifting was greatest for the A_g band, followed by the $T_g(3)$ band, and then the E_g band (Figure 2.3; Table 2.2).

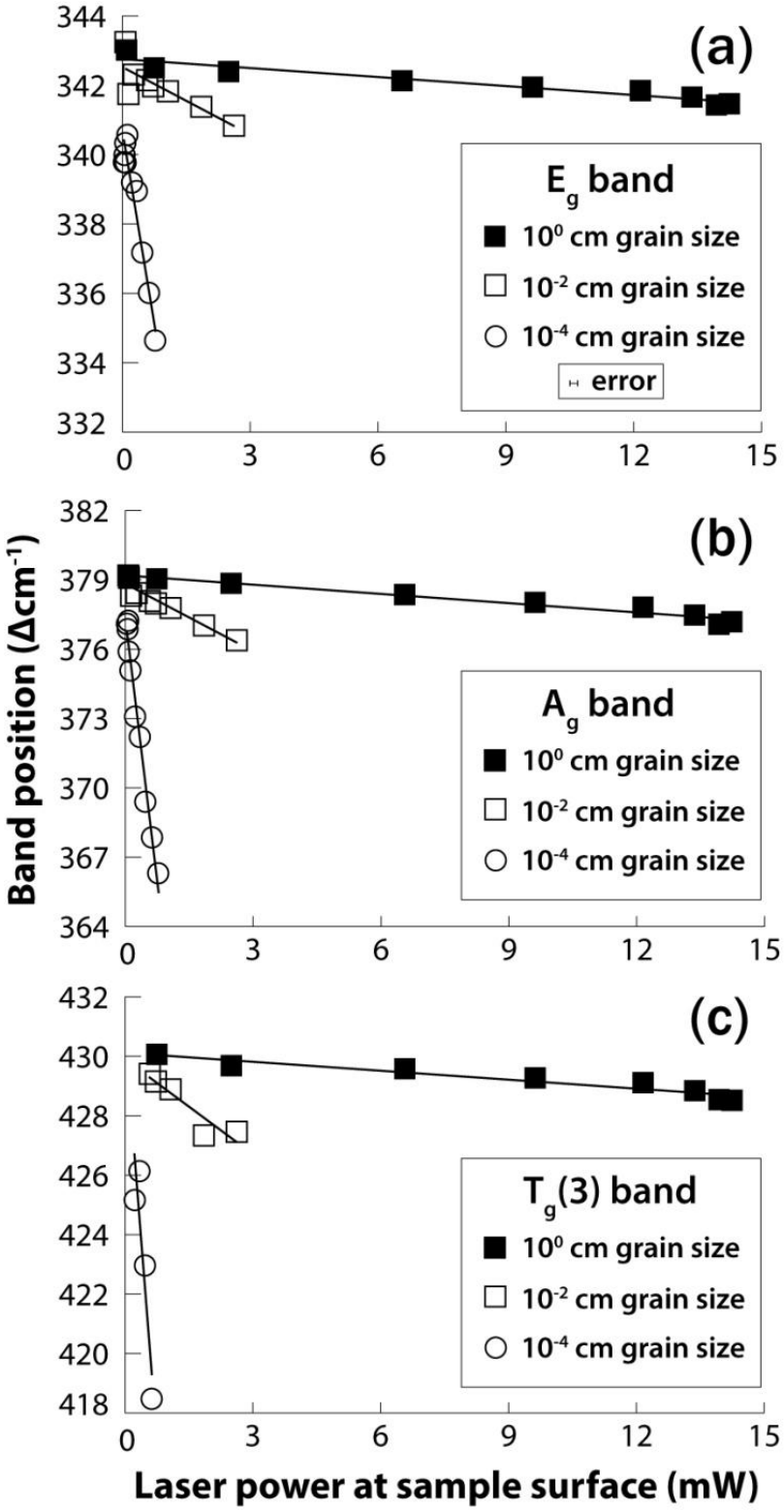

Figure 2.3. Changes in the position of the (a) E_g, (b) A_g, and (c) $T_g(3)$ bands, with an increase in laser power at the sample surface. The average laser power measurement error was ± 0.1 mW. Instrumental reproducibility (1σ) for band positions varied with laser power and between bands (Supplement, Table S2.1) but was always smaller than the symbols used here, so is not shown.

Table 2.2. The lowest-wavenumber positions attained by each Raman band in the laser heating experiment, using the 50x objective, for analytes with different grain sizes.

	Lowest-wavenumber band position (cm^{-1})		
Grain diameter (cm)	E_g	A_g	$T_g(3)$
1	341.4 (Δ=0.6)	377.1 (Δ=1.9)	428.5 (Δ^a=1.5)
0.01	340.8 (Δ=1.2)	376.4 (Δ=2.6)	427.3 (Δ=2.7)
0.001	334.6 (Δ=7.4)	366.3 (Δ=12.7)	418.5 (Δ=11.5)

[a]Here, 'Δ' refers to the downshift of each band from the "ideal" position, taken as 342, 379, and 430 Δcm^{-1}, for the E, A_g and $T_g(3)$ bands, respectively (White, 2009).

The lowest-wavenumber positions (in Table 2.2) were constrained by: (a) the maximum attainable laser power at the sample's surface for the analytical setup (14.4 mW), and (b) the maximum laser power reached without apparent volatilization of the sample (~2.6 ± 0.1 mW for the 0.01 cm-diameter fragment; ~0.8 ± 0.1 mW for the 1 μm-diameter framboidal microcrystal; no volatilization was apparent for the 1 cm-diameter crystal), which was indicated both by lack of visible alteration of the sample and absence of newly created Raman bands (e.g., at ~217 and 282.4 Δcm^{-1}). It also should be noted on Figure 2.3 that even at the lowest laser powers employed (~0.1 mW), greater downshifts in peak position occurred in the smaller, compared to the larger grains.

2.3.2 Spectral differences among samples

The five geologic samples measured under constant analytical conditions yielded spectra with slightly different positions for the same bands (Figure 2.4; Table 2.3). The positions of the A_g and $T_g(3)$ bands co-vary with those of the E_g band, but with different slopes (Figure 2.4 (a) and (b)) to those for bands in published spectra (Figure 2.2). Other spectral parameters such as band area and intensity ratios are explored in the Supplement (Supplement, Figure S2.7).

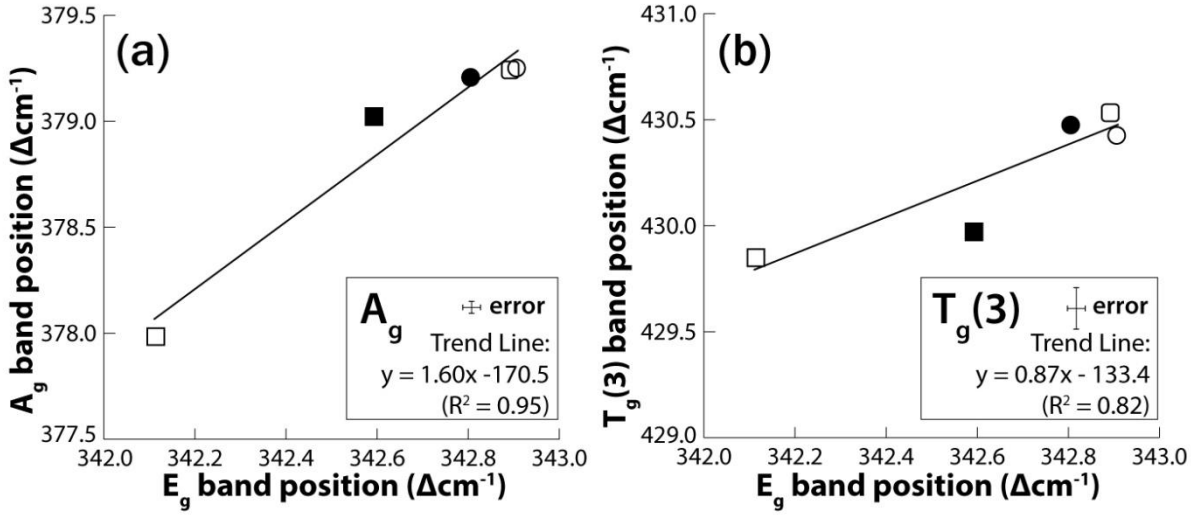

Figure 2.4. The positions of bands generated from five macroscopic pyrite samples (see Supplement, Figure S2.3) from different localities. (a) A_g plotted vs. E_g, (b) $T_g(3)$ plotted vs. E_g. The different symbols correspond to different samples in Table 2.3: open rounded square = A; filled circle = B; open circle = C; filled square = D, and open square = E. Error bars in legend correspond to 1σ instrumental reproducibility data (Supplement, Table S2.1).

Table 2.3. Summary of Raman band positions and TE abundances for the geologic samples used in this experiment. Sample names correspond to labels in Supplement, Figure S2.3.

Sample	E_g band position (Δcm^{-1})	A_g band position (Δcm^{-1})	$T_g(3)$ band position (Δcm^{-1})	Ni (wt%)	Co (wt%)	Se (wt%)	As (wt%)
A	342.9	379.2	430.5	0.0006	0.0001	< 0.0001	0.0491
B	342.8	379.2	430.5	0.0002	< 0.0001	0.0009	0.0279
C	342.9	379.3	430.4	0.1174	0.0112	< 0.0001	0.0033
D	342.6	379.0	430.0	0.0002	0.0004	0.0013	0.9875
E	342.1	378.0	429.8	0.0028	0.0091	0.0019	0.0399
Range of values	342.1 – 342.9	378.0 – 379.2	429.8 – 430.5	0.0002 – 0.1174	< 0.0001 – 0.0112	< 0.0001 – 0.0019	0.0033 – 0.9875

The samples additionally exhibit variable TE content (Table 2.3; Supplement, Table S2.2). In the context of the present study, the most important message is that the wavenumber range among these "typical" pyrite samples (Table 2.3) is only about one-tenth of that shown in Raman spectra in the pyrite literature (Table 2.1, Figure 2.2).

2.3.3 Spectral differences, due to crystallographic orientation within a sample

{100} Faces, cubic pyrite

At a laser power of 5 mW, the average intensity ratio of the A_g band relative to the intensity of the E_g band was 0.99 ± 0.05 (2σ) (Figure 2.5(a)).

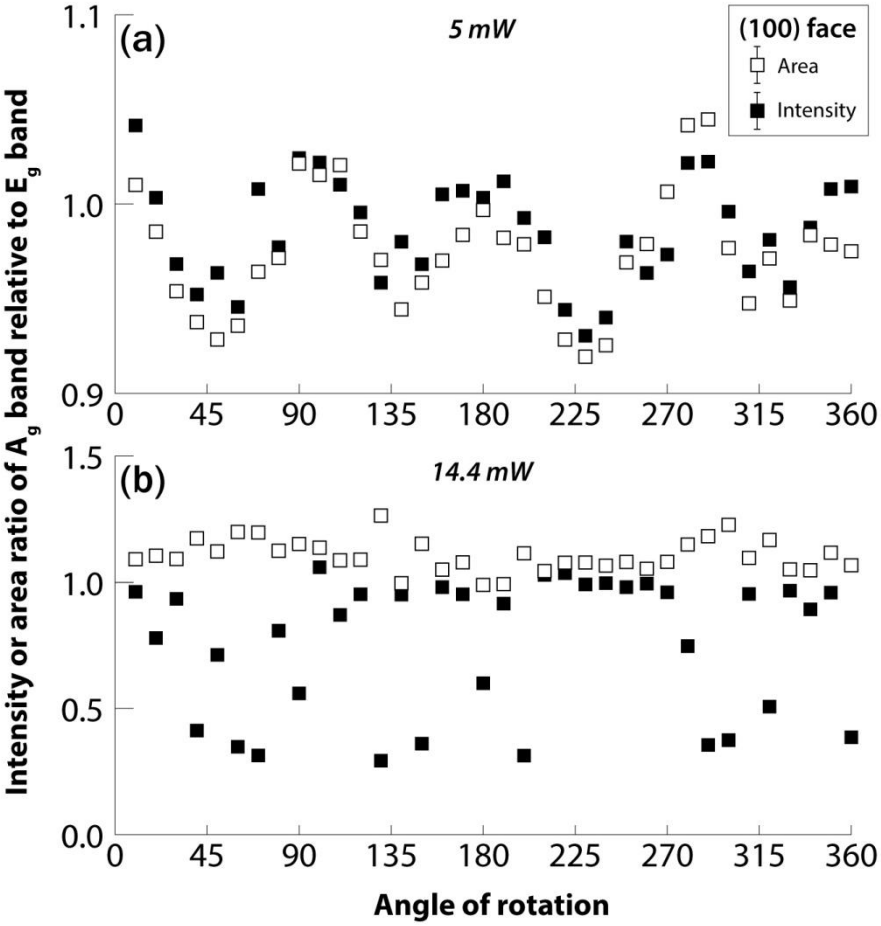

Figure 2.5. Changes in the intensity and area ratios of the A_g band relative to the E_g band, with rotation of a (100) face, at laser powers of (a) 5 mW and (b) 14.4 mW. Error bars in legend correspond to 1σ instrumental reproducibility data (Supplement, Table S2.1) for (a), but error bars for (b) are smaller than the symbols used, so are not shown.

The intensity ratio varied slightly as the sample was rotated from 0° (in which a pair of vertical faces were oriented parallel to the laser's plane of polarization) to 360°, and peaked when the face was oriented at 0° (or 360°), 90°, 180°, and 270°, with minima at 45°, 135°, 225°, and 315°. The average area ratio of the A_g band relative to the area of the E_g band was 0.97 ± 0.06 (2σ) (Figure 2.5(a)). The area ratio also peaked at 0°, 90°, 180°, and 270°,

with minima at 45°, 135°, 225°, and 315°. Note that the maxima at 90° and 270° were of slightly greater amplitude than those at 0° and 180°. Likewise, the minima at 45° and 225° were of slightly greater amplitude than those at 135° and 315°. The E_g and A_g bands' FWHM values were generally smallest when the band area ratios peaked, at 0°, 90°, 180°, and 270°(FWHM ~4.4 cm^{-1} to ~4.7 cm^{-1}, compared with typical values of ~4.8 cm^{-1} to ~5.1 cm^{-1}; Supplement, Figure S2.8). The very small (~ 0.2 cm^{-1}) variations in the band positions showed no obvious trend with sample rotation. At a laser power of 14.4 mW, the average intensity ratio of the A_g band relative to the intensity of the E_g band was 0.76 ± 0.54 (2σ) (Figure 2.5(b)). The average area ratio of the A_g band relative to the area of the E_g band was 1.1 ± 0.13 (2σ) (Figure 2.5(b)). Intensity ratio variations during rotation were much larger, but less clearly defined, at 14.4 mW compared to 5 mW. As the FWHM of the A_g band increased during rotation, the intensity ratio of the A_g and E_g bands decreased as a negative power function (Supplement, Figure S2.9), and the A_g band was downshifted (Supplement, Figure S2.10).

{111} Faces, octahedral pyrite

In the starting orientation (0°) of the crystal, one exterior edge of the (111) face was perpendicular to the laser's plane of polarization. At a laser power of 5 mW, the average intensity ratio of the A_g band relative to E_g band was 1.84 ± 0.08 (2σ) (Figure 2.6(a)). The average area ratio of the A_g band relative to the E_g band was 1.77 ± 0.06 (2σ). Although the data acquired at 5 mW in Figure 2.6(a) show small-amplitude oscillations, there is no clear relationship between angle of rotation and the ratios of band intensities or areas. There is no correlation between any band's FWHM value and: (a) its position; (b) its intensity ratio, or (c) its area ratio.

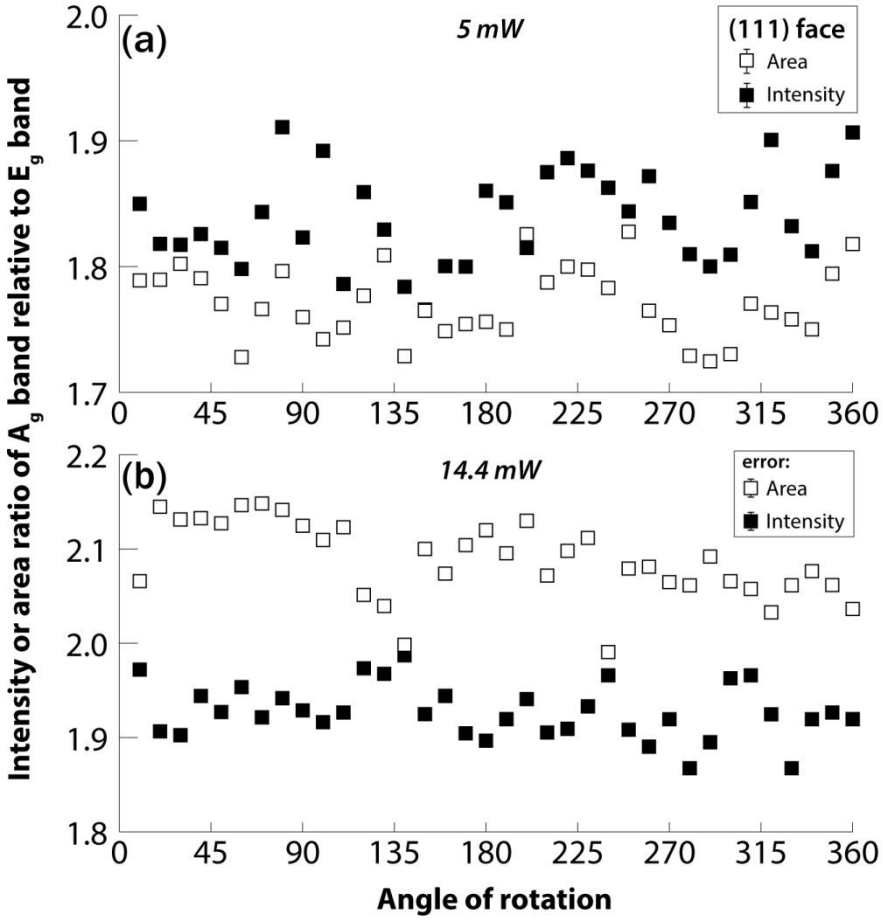

Figure 2.6. Changes in the intensity and area ratios of the A_g band relative to the E_g band, with rotation of a (111) face, at laser powers of (a) 5 mW and (b) 14.4 mW. Error bars in legends of (a) and (b) correspond to 1σ instrumental reproducibility data (Supplement, Table S2.1).

At a laser power of 14.4 mW, the average intensity ratio of the A_g band relative to the E_g band was 1.93 ± 0.06 (2σ) (Figure 2.6(b)). The average area ratio of the A_g band relative to the E_g band was 2.08 ± 0.1 (2σ). As at 5 mW, there is no correlation between any band's FWHM value and: (a) its position; (b) its intensity ratio, or (c) its area ratio.

{210} Faces, pyritohedral pyrite

In the chosen starting orientation of the crystal, the longest edge of the (210) face was oriented perpendicularly to the laser's plane of polarization. At a laser power of 5 mW, the average intensity ratio of the A_g band relative to the E_g band was 1.41 ± 0.6 (2σ) (Figure 2.7(a)). The average area ratio of the A_g band relative to the E_g band was 1.35 ± 0.54 (2σ).

The origin of the large standard deviations is a clear 180° periodicity in both datasets, with minima at ~20° and 200° and maxima at ~110° and ~290° (the exact rotational positions being a function of the "arbitrary" starting orientation). The second maximum has smaller amplitude than the first. Periodicity of a different type occurs in the FWHM (Supplement, Figure S2.11(a)) and band position (Supplement, Figure S2.12) data with rotation. For each of them, a single broad maximum occurs at ~200° and a much narrower local maximum occurs at ~290-310°.

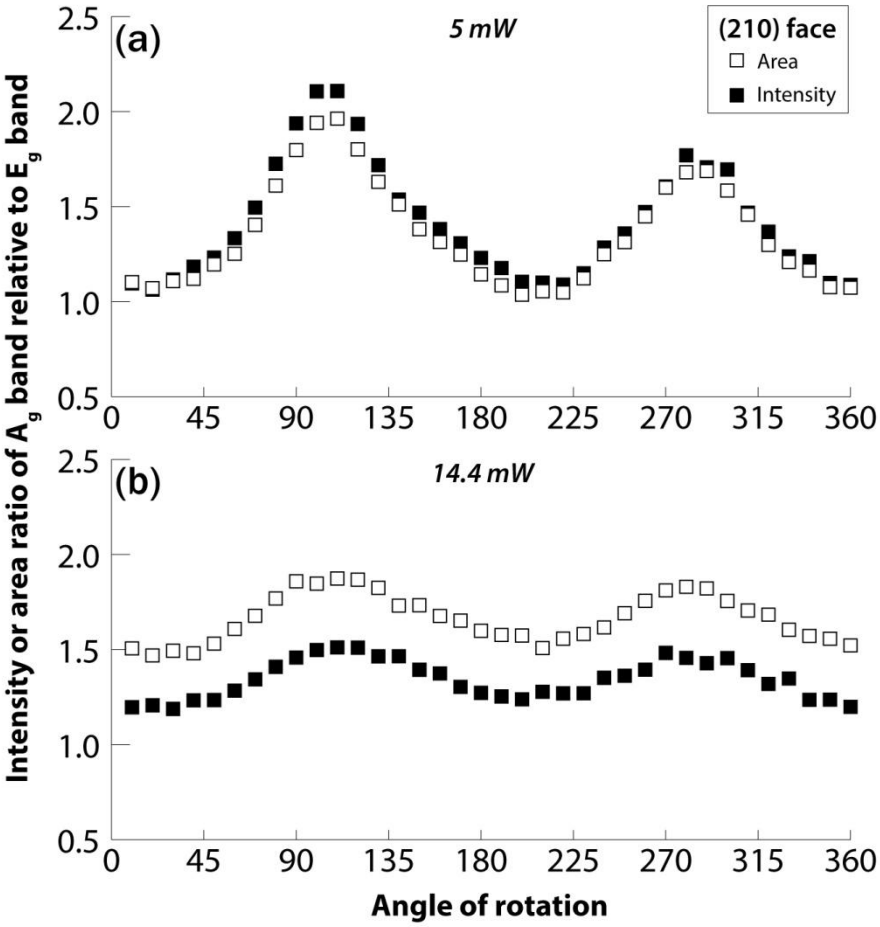

Figure 2.7. Changes in the intensity and area ratios of the A_g band relative to the E_g band, with rotation of a (210) face, at laser powers of (a) 5 mW and (b) 14.4 mW. Instrumental reproducibility (1σ) (Supplement, Table S2.1) was smaller than the symbols used here, so is not shown.

At a laser power of 14.4 mW, the average intensity ratio of the A_g band relative the E_g band was 1.34 ± 0.21 (2σ) (Figure 2.7(b)). The average area ratio of the A_g band relative to the E_g band was 1.66 ± 0.25 (2σ). Again, the origin of the large standard deviations is a 180° periodicity in both datasets, with minima at ~10-20° and ~190-210°, and maxima at ~110° and ~280-290° (Figure 2.7(b)). In contrast to the 5 mW experiment, there is no apparent periodicity in the FWHM (Supplement, Figure S2.11(b)) or band position data (Supplement, Figure S2.12). The FWHM and band position data are discussed further in the Supplement.

2.4 Discussion

Our observation that increasing laser power leads to downshifted (Figure 2.3; Supplement, Figure S2.5) and broadened (Supplement, Figure S2.6) Raman bands, particularly for small grains (Figure 2.3), strongly supports the hypothesis that there exists a temperature effect for the Raman spectrum of pyrite. The observed volatilization or oxidation of the 0.01 cm- and 1 μm-diameter samples at laser powers of 2.6 ± 0.1 mW and 0.8 ± 0.1 mW, respectively, provides further evidence that the observed changes in the Raman spectrum were in direct response to rising temperature at the sample surface. The major difference between these two observed types of heating effects is that the former represents a non-destructive, reversible displacement of atoms and the latter, the destruction of the mineral. It is also worth noting that the literature band positions farthest from the typical values are for nano-crystals (Table 2.1) – an observation of the variation in band positions with grain size, which this study explains.

When laser power and objective N.A. were held constant, Raman spectra for pyrite samples of various morphologies and provenance demonstrated a narrow range in the positions of each of the three bands (Figure 2.4; Table 2.3), about one tenth of the range we have found to be attributable to laser heating (Figure 2.3; Table 2.2). The strong positive correlations ($R^2 > 0.94$) between the relative areas and relative intensities of the bands

(Supplement, Figure S2.7) rule out differential heating as the cause of this (small) inter-sample variability because heating results in band-broadening in spectra (Supplement, Figure S2.6), thereby weakening the correlation between relative intensities and relative areas of bands. We thus suggest that the variations in band positions among these samples likely are related to physical-chemical differences among them, such as in TE content (Table 2.3; Supplement, Table S2.2). Importantly, these TE differences are associated with no more than a 0.8 ± 0.04, 1.3 ± 0.06, and 0.7 ± 0.2 cm^{-1} difference for positions of the E_g, A_g and $T_g(3)$ bands.

The observed covariance of area and intensity ratios (Figures 2.5(a), 2.6(a), 2.6(b) 2.7(a), 2.7(b)) with rotation of (100), (111) and (210) faces suggests that – rather than being subject to a differential rotation-dependent broadening of the A_g and E_g bands – both ratios are a function of the relative degrees of excitation of the A_g mode compared to the E_g mode for pyrite, which depend on the crystallographic orientation with respect to the plane of polarization of the incident laser beam. The clear oscillations of the (100) and (210) data with rotation are likely a function of the 2-fold symmetry of crystal structure of pyrite as viewed perpendicularly to the (100) and (210) faces (Figure 2.8(e), 8(g)). The lack of covariation of area and intensity ratios with rotation of the (100) face at a laser power of 14.4 mW (Figure 2.5(b)) can likely be attributed to greater thermal broadening of the A_g band relative to the E_g band at random angles of rotation (Supplemental Figures S2.8(b), S2.9, S2.10 – discussed further in Supplement). Differences in the average ratios of band areas and intensities between the crystallographic planes analyzed here, and changes in ratios of band areas and intensities with rotation of these individual crystallographic planes (summarized in Figure 2.8) are likely the result of directionally dependent differential excitation of the E_g and A_g modes.

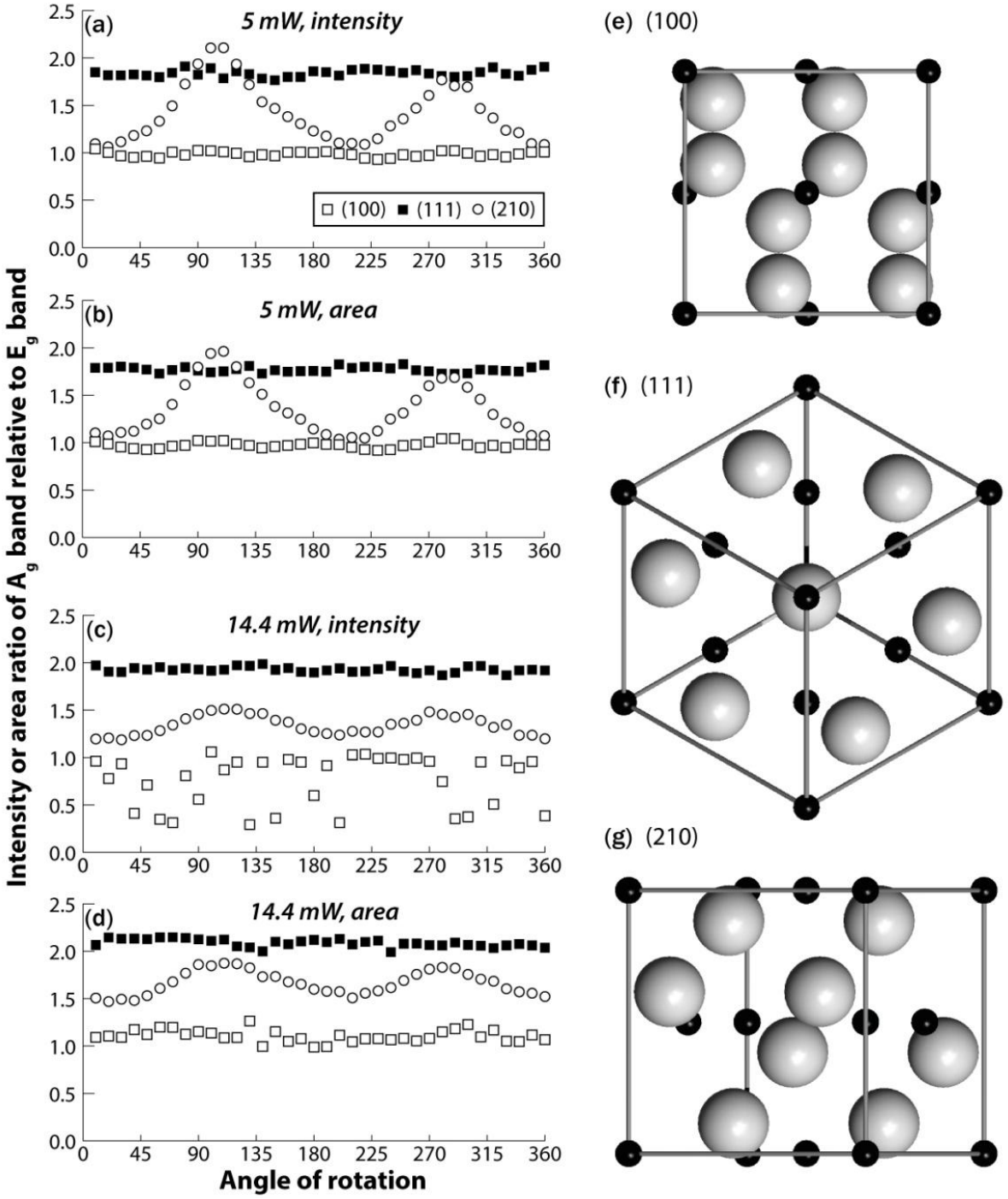

Figure 2.8. Changes in the intensity ((a) & (c)) and area ((b) & (d)) of the A_g band relative to the E_g band, with rotation of (100), (111) and (210) pyrite faces (distinguished by symbols), at laser powers of 5 mW ((a) & (b)), and 14.4 mW ((c) & (d)). Instrumental reproducibility (1σ) (Supplement, Table S2.1) was smaller than the symbols used here, so is not shown. The unit cell of pyrite (Bayliss, 1977), visualized in XtalDraw (Downs and Hall-Wallace, 2003), looking perpendicularly onto (e) the (100) face, (f) the (111) face, and (g) the (210) face. Gray spheres represent S^-, black spheres Fe^{2+}. Only one S-S dumbbell is visible, at the center of the unit cell. The remaining S atoms are bonded to S in adjacent unit cells.

For geologic applications, the most important finding is that, despite their spectral variations due to rotation, the different face types (i.e., crystallographic planes) of pyrite still can be clearly distinguished by the values of their typical band intensity ratios. Particularly at a laser power of 14.4 mW, the average ($\pm 2\sigma$) band intensity ratios and area ratios for the three crystallographically different face types do not overlap (Figure 2.8(c) and (d)). Based on this relationship, Raman microprobe analysis in which the laser beam is approximately perpendicular to the mineral face could be used to distinguish among these three face types on pyrite samples, regardless of rotation. The specific laser power needed will depend on the instrument configuration and the degree of heat dissipation for the pyrite samples under consideration. Given that certain face types represent specific pyrite morphologies (e.g., the {210} form represents the pyritohedral morphology), Raman microprobe analysis could be used to infer crystal morphology, although connection of samples to a good heat-sink may be necessary to prevent volatilization of nano-/micro-crystalline pyrites.

2.5 Conclusions & Future Work

We have determined the magnitude of several effects on the Raman spectrum of pyrite. Firstly, the heating effect identified here can cause sufficient downshift in Raman bands to encompass, and also explain, most of the band position variability in previously reported Raman spectra for pyrite. The magnitude of this effect, which is far greater than that likely to result from differential calibration, can be reduced through the use of lower laser powers, by analyzing larger grains, or by ensuring that the analyte is connected to a good heat-sink. If laser heating is demonstrably avoided, Raman band positions may be related to physical-chemical differences (e.g., TE content) among samples. However, it is worth noting that several of the literature data are from polished samples (a common state for geologic samples being studied). Further work is necessary to extend the results of the present study to polished sections, which would include evaluation of the effects of different polishing techniques.

Secondly, we confirmed the expectation that the band intensity ratios in Raman spectra for pyrite vary due to changes in unit cell orientation with respect to the laser's plane of polarization. Given that the band intensity ratios were distinguishable for the three most commonly developed face types on pyrite, laser Raman microprobe analysis could be used to infer pyrite crystal morphology in sedimentary records, even when pyrite is present in trace amounts and of very fine grain size. Future work will involve developing a method applicable to framboidal pyrites, then experimentally calibrating the relationship between various environmental conditions and pyrite crystal morphology. Because different morphologies are thought to reflect different formation conditions (e.g., degrees of supersaturation) (Murowchick and Barnes, 1987), Raman-based determination of the crystal morphology of naturally occurring pyrite could then potentially be used as a method for inferring specific environmental conditions at the location of pyrite formation.

This work should serve as a blueprint for those wishing to use laser Raman microprobe analysis to characterize pyrite and, perhaps, other unpolished opaque phases after testing as documented here. It is clear that the experimental set-up (laser wavelength and power, objective N.A.) and physical nature of the sample (grain size, morphology, and orientation) are of paramount importance in determining the position, relative intensity, and relative area of Raman bands. A Raman spectrum is thus of limited diagnostic use without accompanying information on the experimental setup and samples analyzed. To promote inter-laboratory consistency, published Raman spectral studies should also report detailed information on their instrument calibration procedure.

Acknowledgements

We thank four anonymous reviewers and the editor, whose comments greatly improved the manuscript. We especially thank Dr. John Freeman for his helpful comments on an earlier version of the manuscript. Additionally, we thank the members of the Fike and Bradley Labs at Washington University, whose enthusiastic discussions yielded several useful additions and improvements to this work. R.N.B. gratefully acknowledges support from the McDonnell Center for the Space Sciences.

Funding statement

Funding for this work was generously provided by the Packard Foundation and McDonnell Center for the Space Sciences.

Supplement

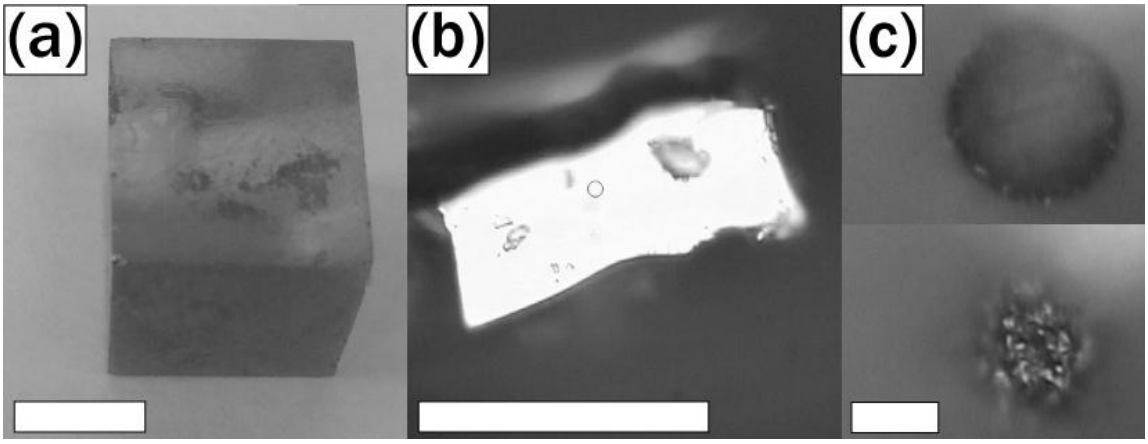

Figure S2.1. Photos/microscope images of the samples used for laser heating experiments. (a) Cubic pyrite ({100} faces) from Navajún (La Rioja, Spain), scale bar = 0.5 cm; (b) Conchoidal pyrite face (WU 85-70 – Perkinsville, VT), scale bar = 50 μm; (c) Framboidal pyrite with octahedral microcrystals (ODP Site 1123, Sample 2H4 50-60), scale bar = 10 μm – the upper of the two images is at a slightly greater depth of focus.

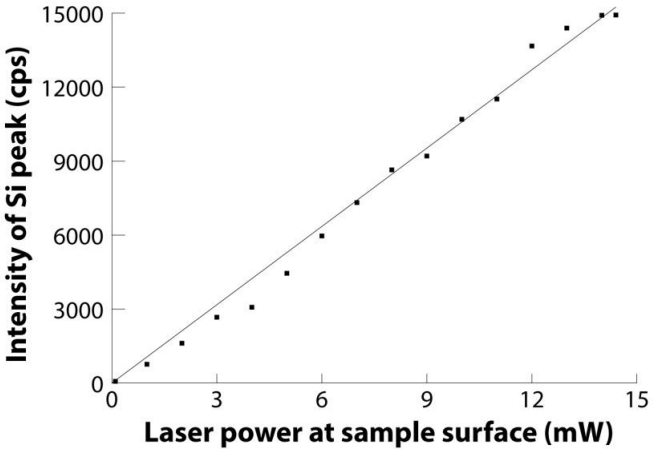

Figure S2.2. The measured absolute intensity of the ν_1 Raman band for Si {100} at laser powers between 0 and 14.4 mW. The data are fit fairly well ($R^2 = 0.99$) by a linear function. The equation of the function (y = 1058.6x) was used to back-calculate the laser power at the surface of the pyrite sample based on the Raman spectrum obtained for the adjacent Si wafer.

Raman Instrumental and Methods Specifications: Raman spectra were obtained with a Kaiser Optical Systems, Inc. (Ann Arbor, MI) 5000 series Hololab Raman microprobe with fiber-optic connection between the laser and the microscope and from the microscope to the detector. The spectral band pass is controlled by a 62.5-μm-diameter collection fiber that essentially acts as a pinhole, delivering the scattered radiation to the thermoelectrically cooled CCD array detector with 2048 channels (Andor Technology, Belfast, Northern Ireland). The collected beam is split into two spectral components upon passage through a holographic grating, with the 100-2500 Δcm^{-1} spectral region dispersed across the top of the CCD array and the 2500-4000 Δcm^{-1} spectral region across the bottom. This arrangement provides a spectral resolution of 2.5 cm^{-1} over the simultaneously collected spectral range of 100-4000 Δcm^{-1}. The absolute wavenumber assignments of the detector channels are calibrated with a Ne calibration lamp. The Raman relative wavenumber positions are calibrated against a polystyrene standard to ±0.3 cm^{-1}, whose measurement also assures the stability of the laser wavelength to ±0.03 nm. The excitation source is a 100-mW Coherent laser DPSS 532, which is a frequency-doubled Nd-YAG laser operating at 532 nm. The relative wavenumber axis is checked before and after each analytical session by analyzing a polished (100) Si wafer whose peak position is 520.5 ± 0.1 Δcm^{-1}. Every 2 hours a spectrum is collected in the total absence of light, providing a spectral file that is subtracted from each sample spectrum to remove the effects of dark noise. The intensity values of the spectra are calibrated against the white-light spectrum of a tungsten lamp, in turn calibrated against a secondary NIST standard.

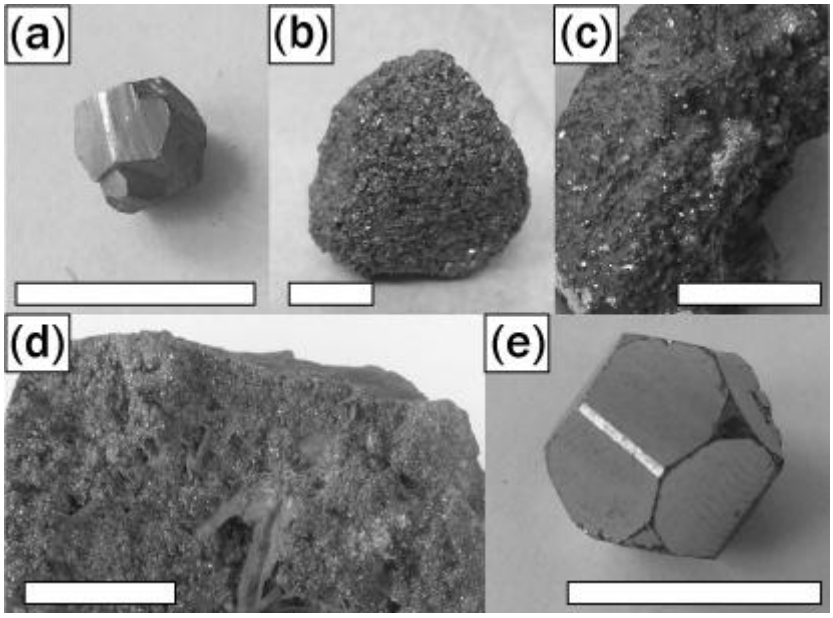

Figure S2.3. Photos of the samples used for the experiments conducted with constant analytical conditions. (a) Pyritohedral pyrite (WU 85-22 – unknown provenance); (b) Cubic pyrite (WU 85-76, Hanover, IL); (c) Cubic pyrite (WU 85-84, Hanover, IL); (d) Pyritohedral pyrite (WU 85-10 – unknown provenance); (e) Octo-pyritohedral pyrite, Peru. Scale bar = 1 cm.

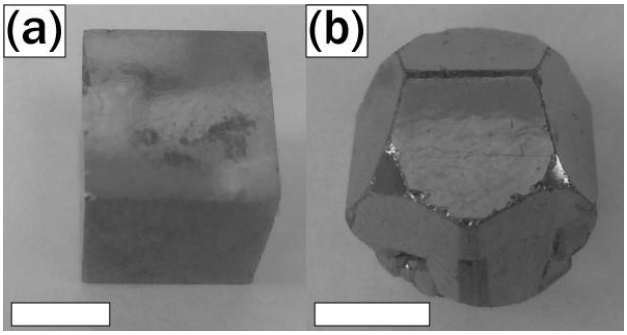

Figure S2.4. Photos of the samples used for sample rotation experiments. (a) Cubic pyrite ({100} faces) from Navajún (La Rioja, Spain); (b) Octo-pyritohedral pyrite ({111} and {210} faces) from Peru. Scale bar = 0.5 cm.

Table S2.1. Standard deviations (1σ) of various spectral characteristics of 10 repeated spectral collections (after moving stage and de-focusing objective, then returning) on Navajún pyrite grain (Supplement Figure S2.4(a)) at the laser powers relevant to this study.

Laser power (mW)	Band positions (cm^{-1})			Band intensities (a.u.)			Band FWHMs (cm^{-1})			Intensity ratio	Area ratio
	E_g	A_g	$T_g(3)$	E_g	A_g	$T_g(3)$	E_g	A_g	$T_g(3)$	A_g/E_g	A_g/E_g
1	0.02	0.03	0.10	4.50	4.01	0.63	0.05	0.05	0.28	0.01	0.01
5	0.02	0.03	0.09	14.07	12.84	1.08	0.12	0.06	0.46	0.01	0.01
14.4	0.09	0.19	0.17	27.37	20.18	0.98	0.05	0.15	0.29	0.01	0.01

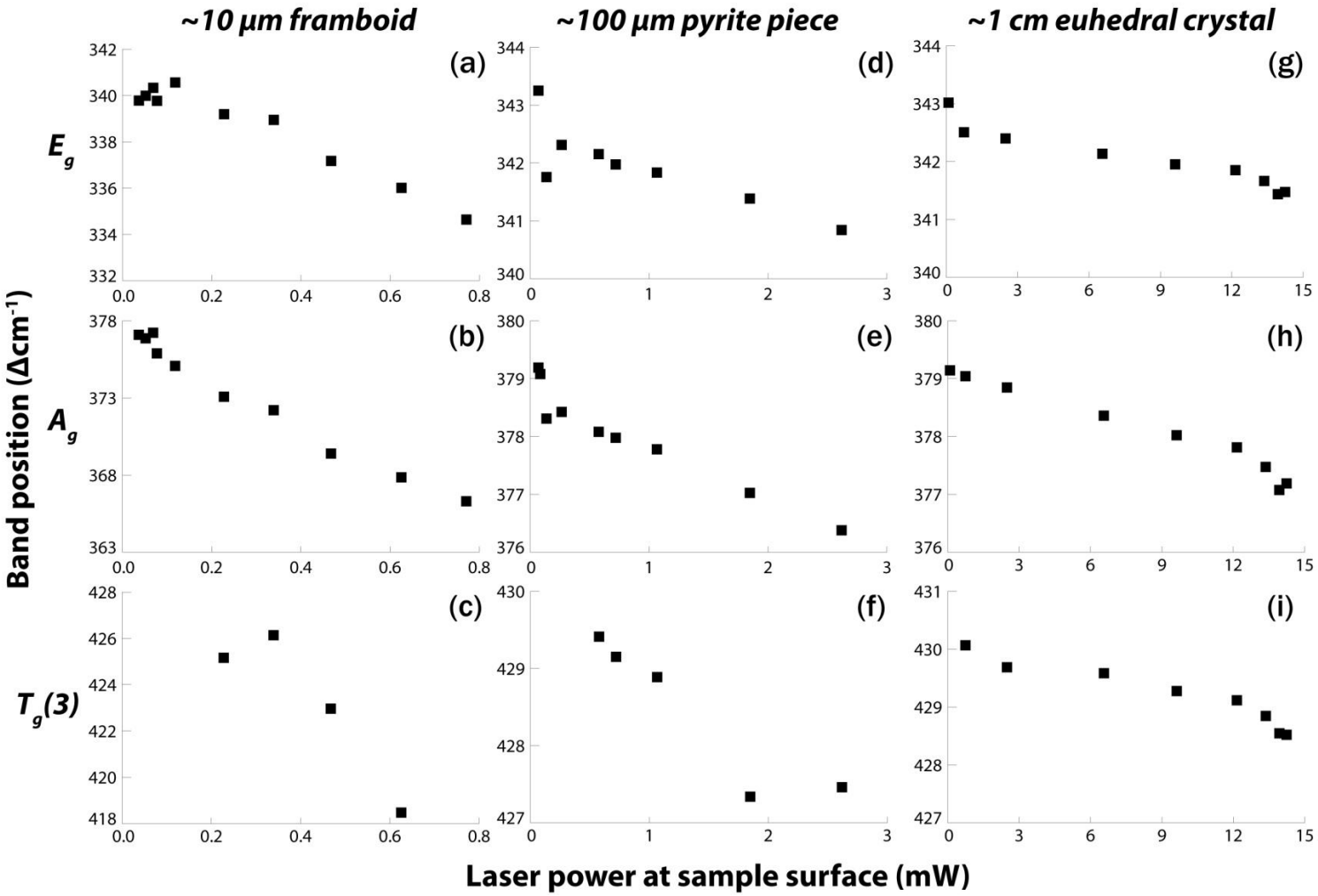

Figure S2.5. Changes in the position of the (a) E_g band, of a framboidal sample, (b) A_g band, of a framboidal sample, (c) $T_g(3)$ band, of a framboidal sample (d) E_g band, of a smaller fractured sample, (e) A_g band, of a smaller fractured sample, (f) $T_g(3)$ band, of a smaller fractured sample, (g) E_g band, of a large euhedral crystal, (h) A_g band, of a large euhedral crystal, and (i) $T_g(3)$ band, of a large euhedral crystal – with increasing laser power. Instrumental reproducibility for band positions varied with laser power and between bands (Supplement, Table S2.1) but was always smaller than the symbols used here, so is not shown.

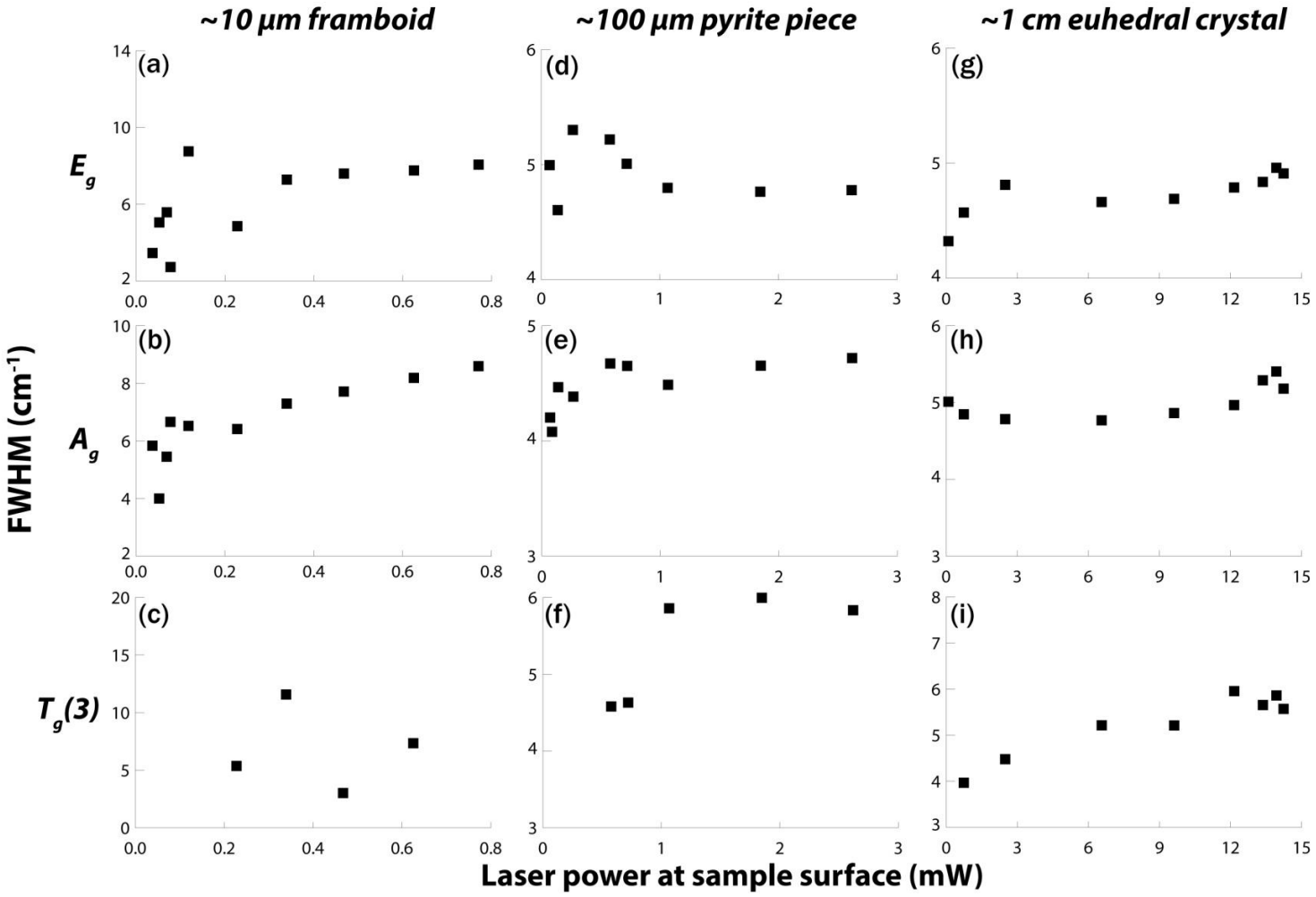

Figure S2.6. Changes in the FWHM of the (a) E_g band, of a framboidal sample, (b) A_g band, of a framboidal sample, (c) $T_g(3)$ band, of a framboidal sample (d) E_g band, of a smaller fractured sample, (e) A_g band, of a smaller fractured sample, (f) $T_g(3)$ band, of a smaller fractured sample, (g) E_g band, of a large euhedral crystal, (h) A_g band, of a large euhedral crystal, and (i) $T_g(3)$ band, of a large euhedral crystal – with increasing laser power. Instrumental reproducibility for FWHMs varied with laser power and between bands (Supplement, Table S2.1), but is not shown here for the sake of graphical simplicity.

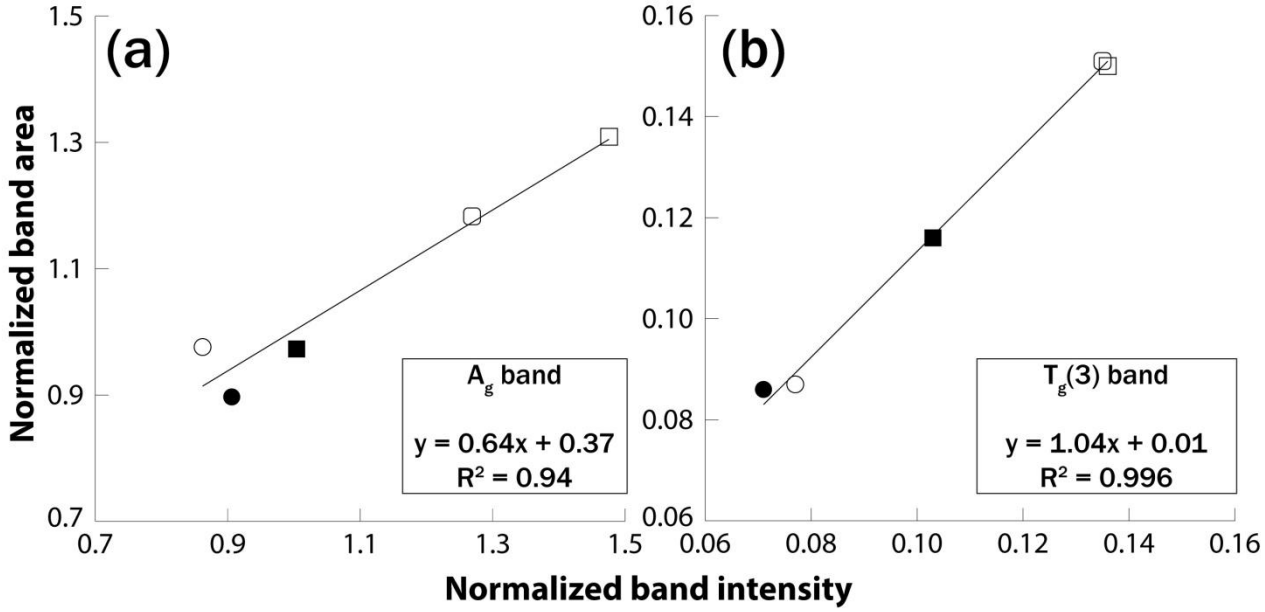

Figure S2.7. The intensities and areas of the (a) A_g, and (b) $T_g(3)$, bands generated for the experiments conducted with constant analytical conditions, normalized to those of the E_g band. A strong linear relationship suggests that differential band broadening has not occurred and implies that a ratio of band intensities is a reasonable substitute for a ratio of band areas when peak-fitting software is not available. The instrumental reproducibility (1σ) (Supplement, Table S2.1) for all data shown was ± 0.01.

Table S2.2. Summary of ICP-MS TE abundances and Raman band positions for the geologic samples in Figure S2.3. Sample names correspond to labels in Supplement, Figure S2.3.

Sample	As (wt%)	Bi (wt%)	Co (wt%)	Cu (wt%)	Mo (wt%)	Ni (wt%)	Pb (wt%)	Se (wt%)	Te (wt%)	Tl (wt%)	Zn (wt%)	E_g band position (Δcm^{-1})	A_g band position (Δcm^{-1})	$T_g(3)$ band position (Δcm^{-1})
A	0.0491	0.0008	0.0001	0.0005	0.0005	0.0006	0.0157	< 0.0001	0.0093	0.0001	0.0776	342.9	379.2	430.5
B	0.0279	0.0003	< 0.0001	0.0104	0.0013	0.0002	0.1047	0.0009	0.0001	0.0037	> 1	342.8	379.2	430.5
C	0.0033	< 0.0001	0.0112	0.0487	0.0046	0.1174	0.0214	< 0.0001	< 0.0001	0.0006	0.0854	342.9	379.3	430.4
D	0.9875	0.4093	0.0004	> 1	0.0019	0.0002	0.1329	0.0013	0.0145	0.0003	0.0386	342.6	379.0	430.0
E	0.0399	0.0002	0.0091	0.0034	0.0003	0.0028	0.0001	0.0019	0.0001	< 0.0001	< 0.0001	342.1	378.0	429.8
Range of values	0.0033 – 0.9875	< 0.0001 – 0.4093	< 0.0001 – 0.0112	0.0005 – > 1	0.0003 – 0.0046	0.0002 – 0.1174	0.0001 – 0.1329	< 0.0001 – 0.0019	< 0.0001 – 0.0145	< 0.0001 – 0.0037	< 0.0001 – > 1	342.1 – 342.9	378.0 – 379.2	429.8 – 430.5

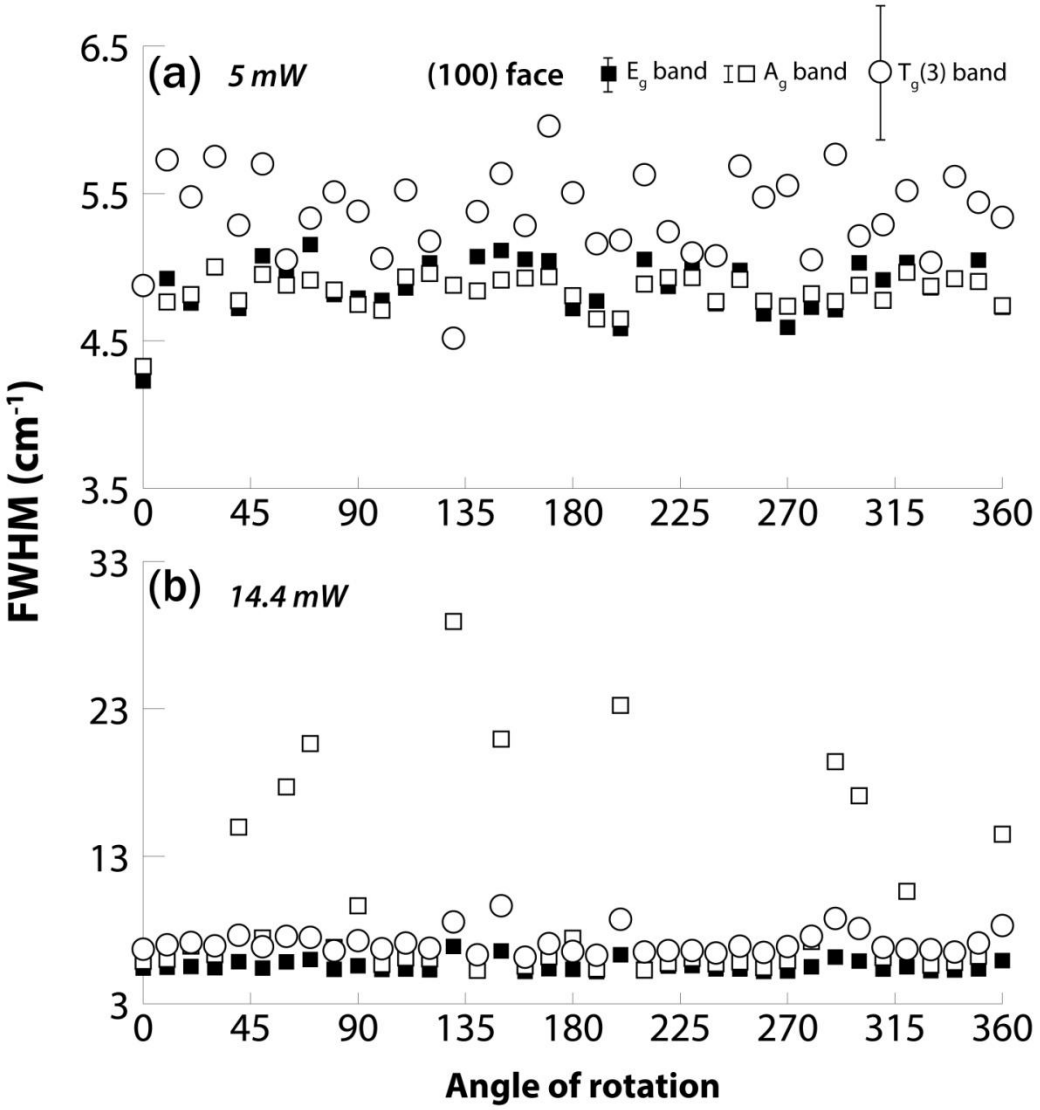

Figure S2.8. Changes in the FWHM of the A_g, E_g and $T_g(3)$ bands with horizontal rotation of a (100) face, at a laser power of (a) 5 mW, and (b) 14.4 mW. Filled squares represent E_g band values, open squares represent A_g band values and open circles represent $T_g(3)$ band values. Instrumental reproducibility (1σ) for FWHMs (Supplement, Table S2.1) differed with laser power and between bands (shown in (a)), but was smaller than the symbols used in (b), so is not shown.

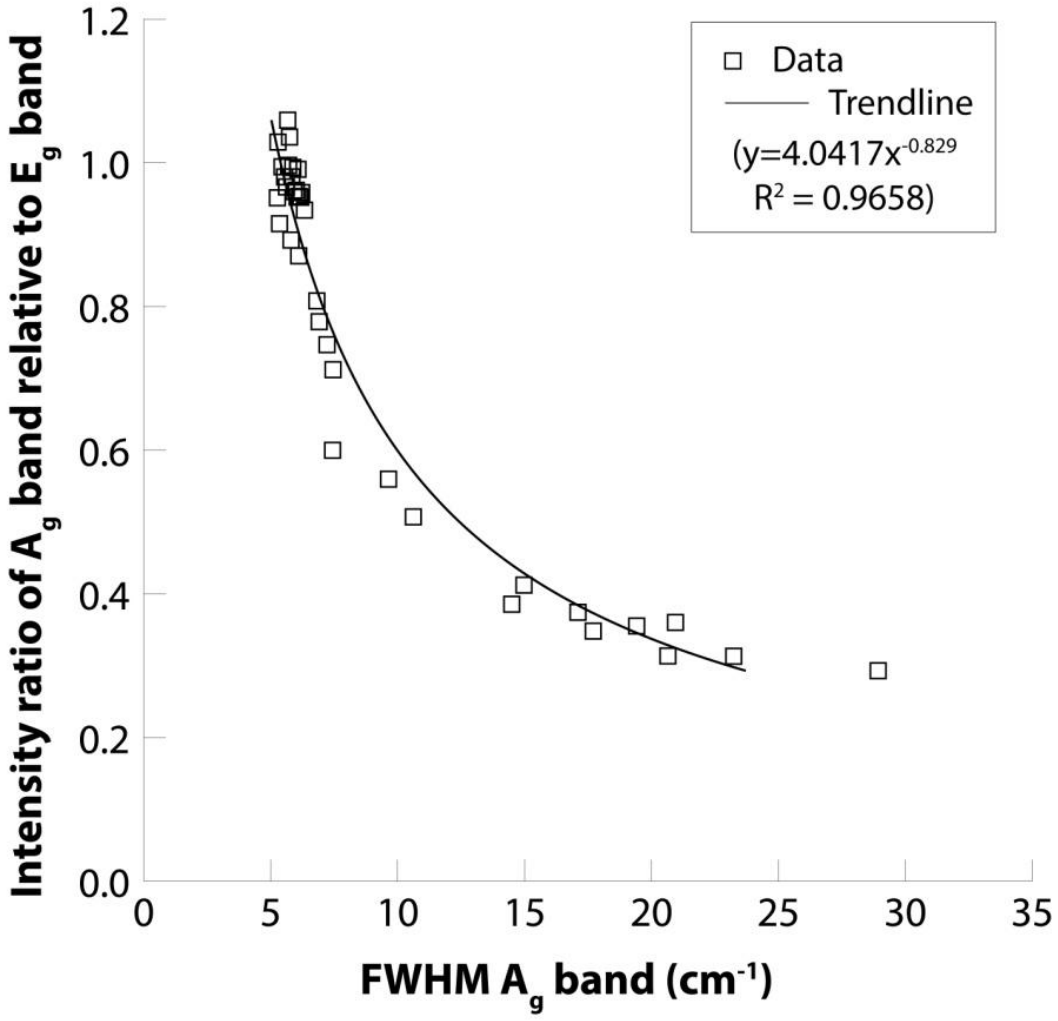

Figure S2.9. FWHM of the A_g band versus changes in the intensity of the A_g band relative to that of the E_g band, from the 14.4 mW laser power experiment on a (100) face. Instrumental reproducibility (1σ) for both axes (Supplement, Table S2.1) was smaller than the symbols used here, so is not shown.

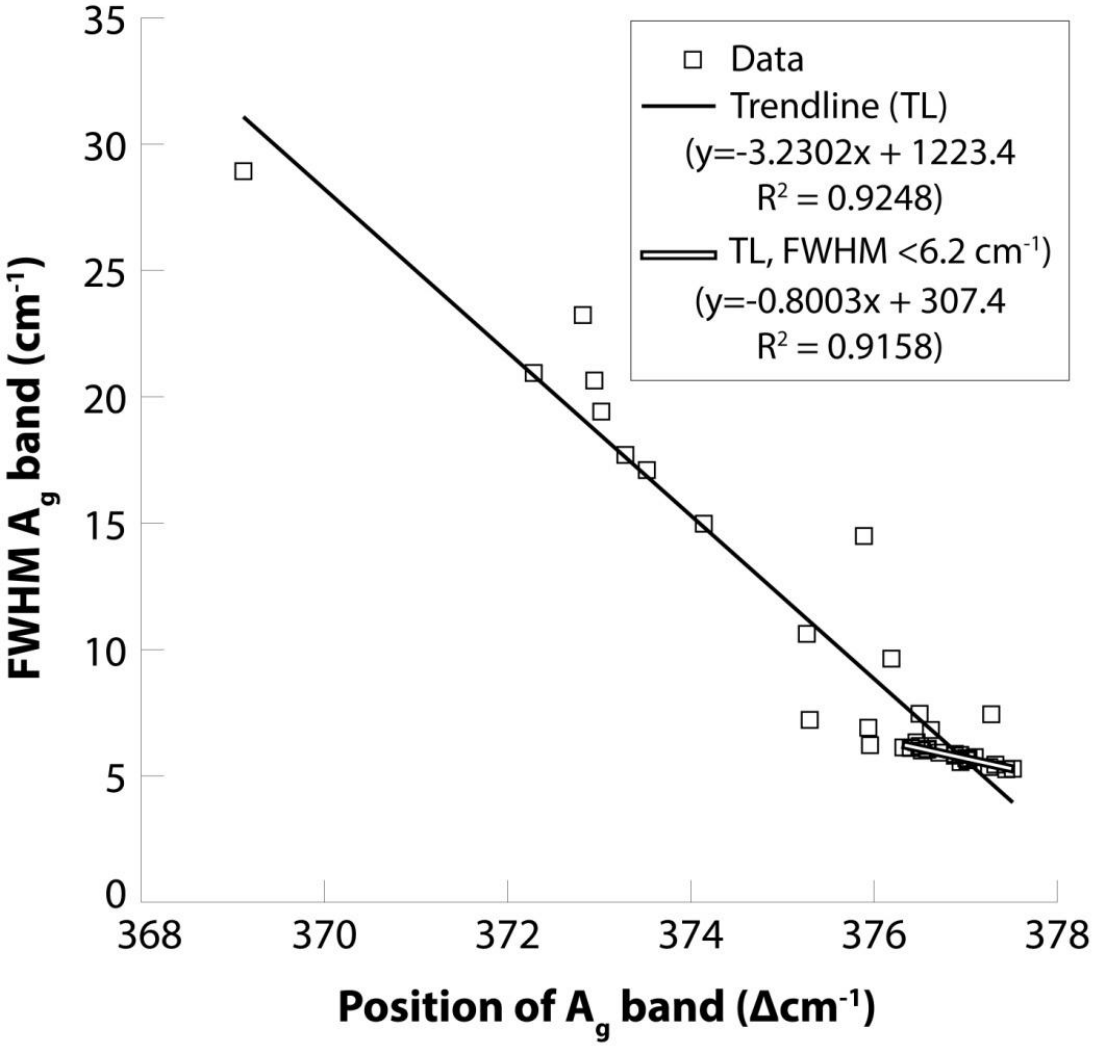

Figure S2.10. Changes in FWHM of the A_g band versus changes in the position of the A_g band, from the 14.4 mW laser power experiment on the {100} face. When only the spectra whose A_g band has a FWHM of <6.2cm^{-1} are plotted, the slope of the data trend line decreases by a factor of 4. Instrumental reproducibility (1σ) for both axes (Supplement, Table S2.1) was smaller than the symbols used here, so is not shown.

Additional discussion of Supplemental Figure S2.8, Figure S2.9, and Figure S2.10 – the origin of variability in the FWHM and band position data, with rotation:

Spectral data from the analyses at 14.4 mW laser power on the (100) face during rotation display a negative linear correlation between band position and FWHM (Supplement, Figure S2.10) of the A_g band. This correlation is to be expected, given that an increase in laser power causes both a downshift in position (Supplement, Figure S2.5) and consequent band broadening (Supplement, Figure S2.6). However, there are two very different linear slopes above and below a FWHM value of 6.2 cm^{-1}. The shallower of these slopes, below a FWHM of 6.2 cm^{-1}, is likely associated with concurrent band broadening and down-shifting, which are symptomatic of laser-induced sample heating. The steeper slope, above a FWHM of 6.2 cm^{-1}, could be due to a more extreme laser heating effect appears to be exclusive to the (100) face at high laser powers, and that depends on the angle of rotation (Figure 2.4 and Supplement, Figure S2.8).

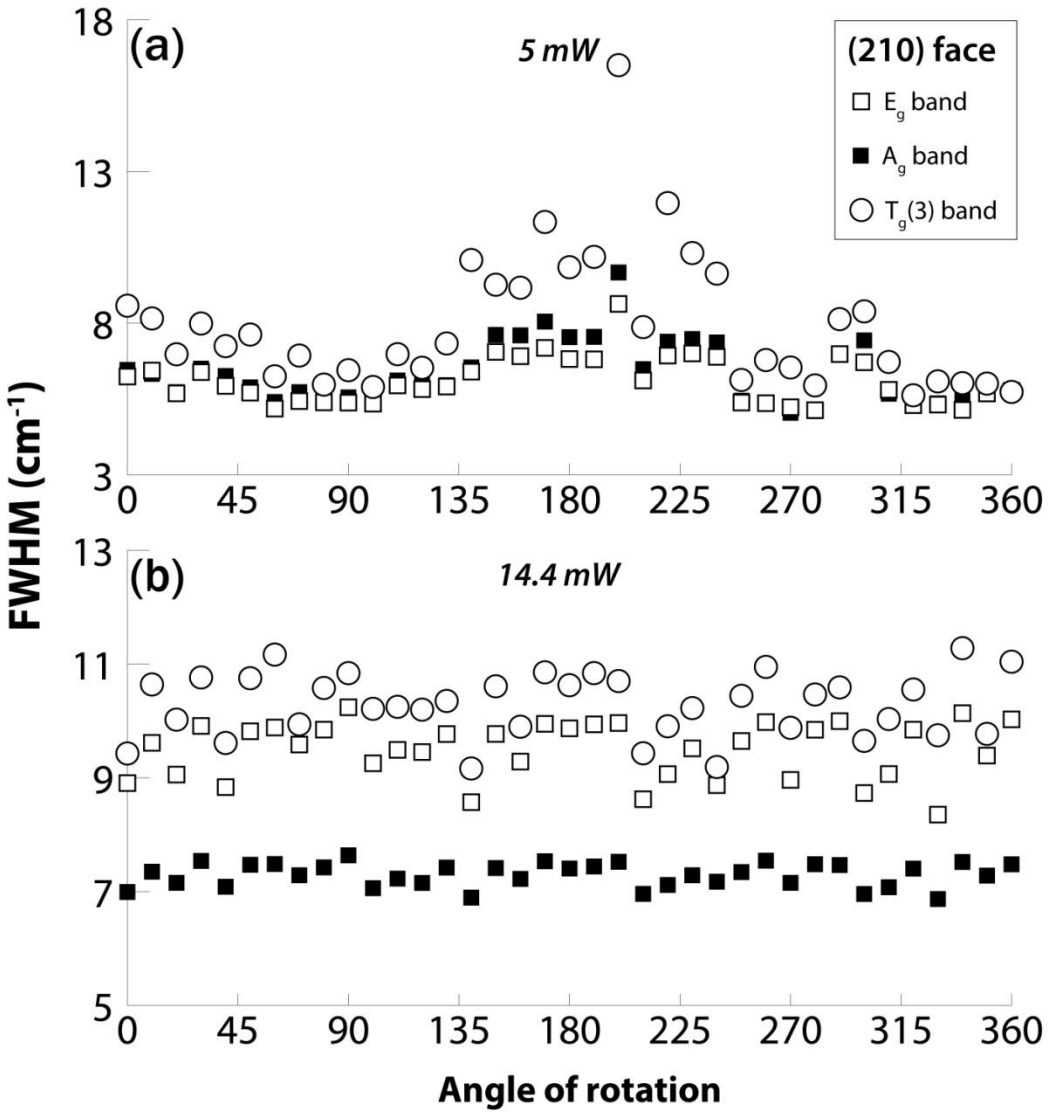

Figure S2.11. Changes in the FWHM of the A_g, E_g and $T_g(3)$ bands with rotation of a (210) face, at a laser power of (a) 5 mW, and (b) 14.4 mW. Filled squares represent E_g band values, open squares represent A_g band values and open circles represent $T_g(3)$ band values. Instrumental reproducibility (1σ) for FWHMs (Supplement, Table S2.1) differed with laser power and between bands, but was smaller than the symbols used here (and is not shown), except for $T_g(3)$ in (a), where $1\sigma = \pm 0.46$ cm^{-1} and in (b), where $1\sigma = \pm 0.29$ cm^{-1}.

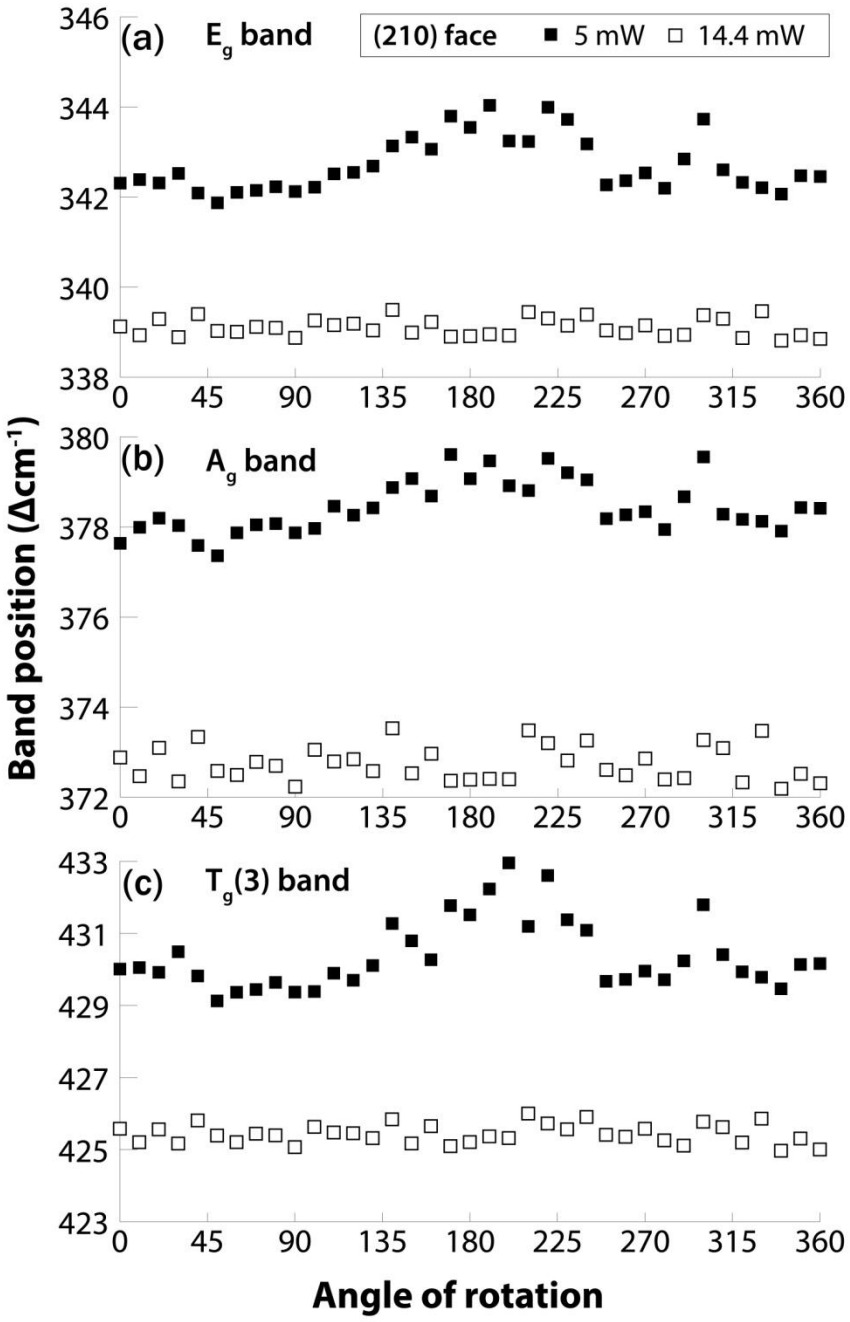

Figure S2.12. Changes in position of (a) E_g band, (b) A_g band, and (c) T_g(3) band, with rotation of a (210) face. Filled squares represent data values from experiments conducted using a laser power of 5 mW; open squares represent data values from experiments conducted using a laser power of 14.4 mW. Instrumental reproducibility (1σ) for band positions (Supplement, Table S2.1) differed with laser power and between bands, but was smaller than the symbols used here, so is not shown.

Additional discussion of Supplemental Figure S2.11 & Figure S2.12 – the origin of variability in the FWHM and band position data with rotation of the (210) face:

The second relative intensity minimum at 200 degrees coincides with a maximum in the FWHM (Supplement, Figure S2.11) and in the band position (Supplement, Figure S2.12) data acquired with 5mW laser power. Both the FWHM and band positions increase, which does not support a laser heating effect – rather, it suggests that changing the angle of the pyrite crystal lattice with respect to the polarization of the laser beam can result in changes in the inherent physical response of the material to the laser beam. In this case, the sample may be dissipating heat more effectively than at other angles of rotation, whilst displaying a lower apparent crystallographic ordering than at other angles. However, the absence of any periodicity in the FWHM (Supplement, Figure S2.11) and band position (Supplement, Figure S2.12) data from the 14.4 mW laser power experiment suggests that this particular physical response of the material may be dependent on laser power, or may simply be an experimental artifact.

Chapter 3: Extraction and sulfur isotope analysis of microcrystalline iron sulfide minerals

Roger N. Bryant[1], Clive Jones[1], Morgan R. Raven[1,2], Maya L. Gomes[3], William M. Berelson[4], Alexander S. Bradley[1], David A. Fike[1]

[1]Department of Earth & Planetary Sciences, Washington University in Saint Louis, St. Louis, MO 63130, USA.

[2]Department of Earth Science, University of California, Santa Barbara, CA 93106-9630, USA.

[3]Department of Earth & Planetary Sciences, Johns Hopkins University, Baltimore, MD 21218, USA.

[4]Department of Earth Sciences, University of Southern California, Los Angeles, CA 90089-0740, USA.

A version of this chapter is published as:

Bryant, R.N., Jones, C., Raven, M.R., Gomes, M.L., Berelson, W.M., Bradley, A.S., Fike, D.A., 2018. Sulfur isotope analysis of microcrystalline iron sulfides using SIMS imaging: Extracting local paleo-environmental information from modern and ancient sediments. *Rapid Commun. Mass Spectrom.* doi:10.1002/rcm.8375

Abstract

RATIONALE: Sulfur isotope ratio measurements of bulk sulfide from marine sediments have often been used to reconstruct environmental conditions associated with their formation. In-situ microscale spot analyses by secondary ion mass spectrometry (SIMS) and laser ablation multiple-collector inductively coupled plasma mass spectrometry (LA-MC-ICP-MS) have been utilized for the same purpose. However, these techniques are not often suitable for small (≤10 μm) grains or for detecting intra-grain variability. **METHODS**: Here, we present a method for the physical extraction (using lithium polytungstate heavy liquid), and subsequent sulfur isotope analysis (using SIMS; CAMECA IMS 7f-GEO) of microcrystalline iron sulfides. SIMS sulfur isotope ratio measurements were made via Cs^+ bombardment of raster squares with sides of 20-130 μm, using an electron multiplier (EM) detector to collect counts of $^{32}S^-$ and $^{34}S^-$ for each pixel (128x128 pixel grids) for between 20 and 960 cycles. **RESULTS**: The extraction procedure did not discernibly alter pyrite grain-size distributions. Apparent inter-grain variability in $^{34}S/^{32}S$ in 1-4 μm-sized pyrite and marcasite fragments from isotopically homogeneous hydrothermal crystals was ~ ±2‰ (1σ), comparable to the standard error of the mean for individual measurements (≤ ±2‰, 1σ). In contrast, grain-specific $^{34}S/^{32}S$ in modern and ancient sedimentary pyrites and marcasites can have inter- and intra-grain variability >60‰. Distributions of intra-sample isotopic variability are consistent with bulk $^{34}S/^{32}S$ values. **CONCLUSIONS**: SIMS analyses of isolated iron sulfide grains yielded distributions that are isotopically representative of bulk $^{34}S/^{32}S$ values. Populations of iron sulfide grains from sedimentary samples record the evolution of the S-isotopic composition of pore water sulfide in their S-isotopic compositions. These data allow past local environmental conditions to be inferred.

3.1 Introduction

Iron sulfide minerals, particularly pyrite (FeS_2), represent a substantial geologic reservoir of sulfur. Pyrite is a key constituent of many iron sulfide ore deposits (LaFlamme et al., 2016), a common accessory phase in an array of igneous and metamorphic rocks (Large et al., 2007; Newhouse, 1936), and a nearly ubiquitous mineral in marine sedimentary rocks of all ages (Berner, 1982). Sedimentary pyrites have diverse morphologies, crystal sizes, and S-isotope compositions, and these characteristics have proven to be invaluable archives for reconstructing local environmental conditions as well as global-scale changes in biogeochemistry (Berner, 2001; Canfield and Farquhar, 2009; Fike et al., 2015; Thode et al., 1961). The S-isotopic composition of pyrite is expressed here in the standard delta notation (in units of per mil, ‰) relative to the Vienna Canyon Diablo Troilite (VCDT) reference standard for sulfur (Ding et al., 1999),

$$\delta^{34}S_{sample} = \left(\frac{R_{sample}}{R_{VCDT}} - 1\right) \quad (3.1)$$

where R represents $^{34}S/^{32}S$ ratios. Pyrite $\delta^{34}S$ values are commonly obtained by bulk extraction of chromium-reducible sulfur (CRS), using Cr^{2+} to reduce and volatilize FeS_2 to H_2S gas, which can subsequently be trapped as zinc or silver sulfide (Canfield et al., 1986; Fossing and Jørgensen, 1989). Isotope ratios for the isolated CRS can be measured by combustion elemental analysis isotope ratio mass spectrometry (EA-IR-MS) (Giesemann et al., 1994; Grassineau, 2006; Grassineau et al., 2001; Grassineau and Mattey, 1998; Morrison et al., 2000; Studley et al., 2002), or by solution multiple-collector inductively coupled plasma mass spectrometry (MC-ICP-MS) (Clough et al., 2006; Craddock et al., 2008; Mason et al., 2006; Paris et al., 2013). Such approaches yield an integrated $\delta^{34}S$ value for the CRS pool and are thus blind to patterns of isotopic variability within the pyrite pool. In addition, the CRS pool can potentially also include

marcasite (FeS_2), elemental S, organic polysulfides, and other metal sulfides in addition to multiple morphologies or generations of pyrite (Canfield et al., 1986; Fike et al., 2015; Fossing and Jørgensen, 1989).

The degree of isotopic variability within the pyrite pool is hypothesized to reflect depositional conditions and may record critical information about the location(s) and condition(s) of pyrite formation (Claypool, 2004; Fike et al., 2015). For example, if pyrite in a sample is isotopically homogeneous, this would suggest that all grains formed from the same fluid. In contrast, a bimodal pyrite $\delta^{34}S$ distribution might indicate two distinct sulfide sources, e.g., from successive exposure to distinct sulfide-bearing fluids. Pyrites from a single source may also have a range of $\delta^{34}S$ values, representing their continuous formation in the presence of an evolving sulfide reservoir (Fischer et al., 2014; Marin-Carbonne et al., 2018). In diffusively limited environments like marine sediments, pore water sulfate can be drawn down by microbial sulfate reduction (MSR). Sulfate reducers have a strong preference for the lighter isotopes of S in sulfate (Johnston et al., 2007; Leavitt et al., 2013), which leads to increasingly ^{34}S-enriched sulfate and sulfide with depth in the sediment (Jorgensen, 1979). As a result, later-formed pyrite crystals or the outer layers of large pyrite crystals may be more ^{34}S-enriched than pyrite that formed earlier (Fischer et al., 2014). These distinct scenarios (unimodal distribution, bimodal distribution, or evolved source) would not be distinguishable using bulk $\delta^{34}S$ values. Therefore, there is great potential for a grain-specific method for pyrite S-isotope measurements to enhance our understanding of pyrite $\delta^{34}S$ records, providing a new dimension of information to inform our interpretations of this powerful archive.

Progress has been made using spot analyses by SIMS (Cui et al., 2018; Drake et al., 2018, 2013; Fischer et al., 2014; Gomes et al., 2018; Greenwood et al., 2000; Kamber and

Whitehouse, 2007; Kozdon et al., 2010; LaFlamme et al., 2016; Meyer et al., 2017; Papineau et al., 2005; Riciputi et al., 1998; Whitehouse et al., 2005), or LA-MC-ICP-MS (Craddock et al., 2008; Fu et al., 2017; Zhu et al., 2017), to make spatially resolved $\delta^{34}S$ measurements. Some have already attributed detectable intra-sample pyrite $\delta^{34}S$ variability to temporal changes in the S-isotopic composition of the fluids from which the pyrites precipitated (Gomes et al., 2018; Marin-Carbonne et al., 2018). The method described here, scanning ion imaging by SIMS, is designed to address several of the limitations of currently available methods for micro-scale analysis of $\delta^{34}S$ in sedimentary pyrite. First, by rastering over grains, scanning ion imaging can generate a continuous record of isotope variations (Drake et al., 2018), one that can be interrogated at variable spatial resolution after data collection. Previously, most SIMS studies of pyrites relied on analyses of fairly large (≥10 μm-diameter) spots within grains (Cui et al., 2018; Drake et al., 2018, 2013; Fischer et al., 2014; Gomes et al., 2018; Greenwood et al., 2000; Kamber and Whitehouse, 2007; Kozdon et al., 2010; LaFlamme et al., 2016; Meyer et al., 2017; Papineau et al., 2005; Riciputi et al., 1998; Whitehouse et al., 2005). This precludes analyses of many sedimentary pyrites (i.e., those with diameters <10 μm). Moreover, while spot analyses can be sufficient to determine the presence of inter-grain isotopic variability on larger grains, they are not able to discern intra-grain variability (Drake et al., 2013; Greenwood et al., 2000; Kamber and Whitehouse, 2007; Kozdon et al., 2010; Papineau et al., 2005; Riciputi et al., 1998; Whitehouse et al., 2005), except for the case of unusually large (diameters > ~100 μm) pyrites (Fischer et al., 2014).

Additionally, by reducing the primary beam current, we achieve the spatial resolution necessary to measure inter- and intra-grain $\delta^{34}S$ variability in microcrystalline pyrites. In comparison, spot analyses are not ideal for many micro-sized pyrites or necessarily even for

larger pyrites that are composed of many small parts (e.g., framboids). Relatively high primary beam currents (e.g., ≥ 1 nA) inherently limit the three-dimensional resolution of isotopic measurements (Gomes et al., 2018; Meyer et al., 2017). As scanning ion imaging requires the use of very low primary beam currents (e.g., ≤ 20 pA) to prevent the saturation of the electron multiplier detector (Drake et al., 2018), the associated low sputter rates and small diameter of the focused primary beam (≤1 μm) result in excellent three-dimensional resolution (Drake et al., 2018).

Finally, we introduce a physical extraction procedure to enable pyrite to be concentrated for optimized SIMS analyses for samples where pyrite is a trace phase. As pyrite is not a high abundance phase in most sedimentary rocks, and grains are often broadly disseminated (Rickard, 2012), this limits the number of grains likely to be present at the polished surface of a 1-inch round thin section. Additionally, when grains are close to the edge of the sample holder, this adversely affects precision (Valley and Kita, 2009). Therefore, the physical extraction of pyrites from sedimentary samples is in many cases a necessary precondition for efficient SIMS analysis on a sufficient number of grains to characterize the population. Most early physical extraction procedures for pyrite used magnetic separation, although because pyrite is only paramagnetic, these approaches are inefficient (Flinter, 1959). Alternative separation procedures utilize heavy liquids (Ivor Roberts, 1982; Proske et al., 2015; Raiswell and Plant, 1980; Vallentyne, 1963; Volkov and Fomina, 1974), as these represent an opportunity to separate dense phases like pyrite (5.01 g/cm^3) from less dense, but common insoluble minerals like quartz (2.65 g/cm^3) and clays (2-2.7 g/cm^3). For this study, lithium polytungstate (LST; working density of 2.85 g/cm^3) is preferred due to its low toxicity and high recyclability.

In the following, we present the details of our SIMS scanning ion imaging-based sulfur isotope analysis procedure. We first test the validity of the method on micron-scale fragments of cm-scale isotopically homogeneous hydrothermal pyrite and marcasite crystals. By comparing SIMS results to bulk $^{34}S/^{32}S$ ratio data obtained via EA-IR-MS, we quantify overall analytical biases associated with the method and determine its general limitations in order to provide a robust platform for future grain-specific SIMS analyses of modern and ancient microcrystalline iron sulfides. By generating continuous $^{34}S^-$ and $^{32}S^-$ ion maps for inter/intra-grain variability and probing variation in hydrothermal crystals, we increase our confidence that the observed variation in sedimentary samples is environmentally meaningful and not an analytical artefact. Lastly, we apply the method to a set of extensively studied sediment samples that are thought to represent distinct styles and histories of pyritization, demonstrating its applicability and value to investigations of modern and ancient marine sediments.

3.2 Materials & Methods

3.2.1 Samples

For use in density separation procedure tests, and as a S-isotopic standard for SIMS experiments, we obtained a single large (~2cm-diameter) euhedral pyrite crystal from Ward's Science (Rochester, NY), sourced from the San Jose de Huanzala Mine, Peru. The pyrite at this locality is of hydrothermal origin, and has been shown in previous studies to be stoichiometric FeS_2 (Imai et al., 1985). For use as an additional S-isotopic standard for SIMS experiments, we obtained a single large (~1cm-diameter) euhedral marcasite crystal from Ward's Science, sourced from the Jiří open-pit lignite mine in the Czech Republic. For use in further SIMS S-isotope experiments, we selected a modern sediment sample from Santa Barbara Basin (Berelson et al., 2018), and

two mid-Cretaceous, Cenomanian-Turonian Ocean Anoxia Event (OAE 2) shale samples from the Cismon section in Italy (Gomes et al., 2016), and the Demerara Rise (Raven et al., 2019).

3.2.2 Extraction of microcrystalline pyrite from geologic samples

A ~0.5g fragment of the hydrothermal pyrite crystal was ground to a fine powder by mortar and pestle, and homogenized. The resulting grain size distribution of the powdered crystal ('pre'; Table S3.1) was characterized using a combination of optical microscopy and image processing in ImageJ (Schneider et al., 2012). This involved suspending ~0.001 g of powder in ethanol and dispersing the sample on a glass microscope slide, then capturing 20 focused images of unique parts of the slide through a 40× optical objective. These images were overlain by 20×20 μm grids, and a random number generator was used to select 5 grid squares to analyze per image. In ImageJ, images of grid squares were scale-calibrated, converted to grayscale, and a bandpass filter (filtering large structures down to 10 pixels) and threshold were applied to highlight grains. Overlapping/touching grains, or grains with a circularity of <0.9 were removed, to approximate the near-sphericity of natural pyrite grains. Grain areas were calculated for the remaining particles using the 'Analyze Particles' function in ImageJ, and grain sizes were estimated by assuming that each grain was perfectly circular in cross-section.

A separation procedure was then carried out on subsamples of the powdered crystal. Three 0.01 g aliquots of powder were added to 45 mL of LST in three 50 mL centrifuge tubes. These tubes were mixed for a minute using a vortex mixer at the highest speed, then placed in an ultrasonic bath (35 kHz) for 15 minutes. Tubes were then spun in a centrifuge for 38 minutes at 3000 rpm, as these conditions were estimated (see equation 3.2) to allow ≥0.5 μm diameter spherical pyrite fragments to settle in LST. Particle settling time (t_s) was estimated using Stokes' Law (Lentfer et al., 2003; Loveday, 1973):

$$t_s = \frac{9\mu h}{2(\rho_p - \rho_l)R_p^2 a} \qquad (3.2)$$

where μ is the dynamic viscosity of the fluid (0.011 Pa·s for LST), h is the height of the liquid in the centrifuge tube (10 cm in our setup), ρ_p and ρ_l are the mass densities of the particles and the fluid (5.01 and 2.85 g/cm^3 for pyrite and LST), R_p^2 is the radius of the settling particle squared, and a is the centrifugal acceleration (in m/s^2), given by:

$$a = \omega^2 r \qquad (3.3)$$

where r is the centrifuge radius (18 cm in our setup), and ω is angular velocity (in radians/s), given by:

$$\omega = 2\pi f \qquad (3.4)$$

where f is the rotational frequency (50/s in our setup). It should be noted that the settling time calculated using equation 3.2 is likely an underestimate due to hindering effects such as particle-particle and particle-container interactions. After centrifugation, settled fragments were removed from the tubes using a plastic micro-pipette, placed in new 50 mL centrifuge tubes, rinsed and spun down (5 minutes at 2000 rpm) five times in deionized water. This process was repeated three times sequentially (Table S3.1, 'a-c') for each 0.01 g portion of powder. In order to more closely approximate insoluble residues from marine sediments, the extraction procedure was also repeated for a 1:99 mixture of pyrite and ~300 μm-sized quartz grains (0.01 g pyrite, 0.99 g quartz), and a 1:99 mixture of pyrite and ~50 μm-sized quartz grains. Each extract was dried and weighed, and grain size distributions were calculated for the first sequential extracts for the pure pyrite ('post'), pyrite with large quartz grains ('postQz'), and pyrite with small quartz grains ('postSmQz').

A shatter box was employed to powder the Cretaceous-age shale samples, for no longer than one minute. There was no obvious sign of sulfide mineral fragmentation after this procedure. For the Santa Barbara Basin sediment sample, one gram of dried sediment was powdered gently in a mortar and pestle. For the Cretaceous shales and modern Santa Barbara Basin sediment, carbonate minerals were removed by three sequential 10-minute treatments with 6M hydrochloric acid, before the insoluble residue was rinsed five times with deionized water and dried in an oven at 60°C for 24 hours. The insoluble residues were then powdered by mortar and pestle prior to performing a single density separation as described above on 0.25 g aliquots of each.

3.2.3 Mounting of samples

Dried iron sulfide samples were carefully transferred onto the surface of the base of a 1-inch round acrylic mould that had been coated with a release agent, isooctane. After adding iron sulfide samples and powdered hydrothermal pyrite and marcasite for use as internal S-isotopic standards (kept separate using a Parafilm M grid), the upper half of the mould was then attached and filled with epoxy (2:1:13.63 ratio mixture of 1-(2-aminoethyl) piperazine; 1,-8-diamino-p-menthane; and Araldite 506 epoxy resin). After degassing in a vacuum oven for 10 minutes, and removing any remaining bubbles with a 21G needle, the epoxy was cured for 72 h at 60°C in an oven. The epoxy was then removed from the mould and sequentially polished with a 6 μm polishing pad, 3 μm diamond paste, and 1 μm diamond paste, in order to expose the standards and sample, and minimize surface topography and roughness. After using Raman microprobe analysis (1 mW laser power and 50x objective) (Bryant et al., 2018) and optical microscopy (50x objective, plane-polarized light) to confirm the presence and mineralogy of analyte at the surface

of the polished epoxy pucks, the pucks were coated with ~50 nm thick Au to ensure conductivity for SIMS analysis.

3.2.4 Sample imaging

For iron sulfide extracts from the Cismon and Demerara shale samples, ~20 µg aliquots were mounted on carbon tape, coated with 5 nm Au by physical vapor deposition using a Kurt J. Lesker PVD 75 (Jefferson Hills, PA, USA), before representative mineral textures were imaged by Scanning Electron Microscopy (SEM) using a JEOL JSM-7100 LVF Field Emission SEM (Tokyo, Japan).

3.2.5 Bulk sulfur isotope analyses

To determine $\delta^{34}S$ values for the hydrothermal pyrite and marcasite crystals, and to assess their degrees of isotopic homogeneity, three fragments of each crystal were randomly selected, and powdered in an agate mortar. Small (~125 µg) aliquots of powdered FeS_2 were loaded into tin capsules with 1-2 mg V_2O_5, combusted in a Costech ECS 4010 Elemental Analyzer (Valencia, CA, USA); $^{34}S/^{32}S$ ratios were then measured in a Thermo Scientific Delta V Plus isotope ratio mass spectrometer (Waltham, MA, USA), and corrected to VCDT by bracketing analyses of in-house VCDT-calibrated ZnS, BaS and $BaSO_4$ standards. For the fragments of pyrite and marcasite, the average $\delta^{34}S$ values measured by EA-IR-MS were –1.0 ± 0.1‰ (1σ, n=3) and 4.6 ± 0.2‰ (1σ, n=3), respectively. The same analytical procedure was used to generate 'bulk' $\delta^{34}S$ data for the pyrite physically extracted from the Cismon section sample.

3.2.6 SIMS sulfur isotope analyses

After pre-sputtering by Cs^+ bombardment for 300 seconds with a 1 nA beam current at the desired raster size, sulfur isotopic ratio experiments were performed in "scanning ion imaging

mode" by Cs^+ bombardment (beam diameter of <1 μm, current of ~10 pA) of raster squares of 20-130 μm, using an electron multiplier (EM) detector on a CAMECA IMS 7f-GEO (Fitchburg, WI, USA) at Washington University in St. Louis to collect counts of $^{32}S^-$ and $^{34}S^-$ for each pixel (grids of 128x128 or 256x256 pixels) for between 20 and 960 planes (1 minute per plane).

The size of each exposed grain analyzed was measured using calibrated optical microscope images before analyses. The SIMS stage was x-y calibrated to a stitched optical microscope image of the epoxy puck using digital video camera footage of the gold-coated sample surface in the analysis chamber. Raw isotope ratios for each grain were calculated by taking the mean $^{34}S^-/^{32}S^-$ ion count ratio of a central area of the grain over the multiple analysis planes. Various corrections were applied to data, including a dead-time correction, an interpolation of $^{34}S^-$ counts to align in time with those on $^{32}S^-$, and a quasi-simultaneous arrival (QSA) effect correction.(Jones et al., 2017) The magnitude of the QSA undercounting correction is proportional to instrument transmission, i.e., the number of secondary ions reaching the detector per incident primary ion. However, it is not possible to determine primary currents <50 pA very accurately on the 7f-GEO instrument. Therefore, the ratio of the QSA coefficient (β) to the primary ion flux (*J*) was used to facilitate the correction (Jones et al., 2017). β/*J* values were determined for each session, via data obtained from the internal standard grains, using the relationship:

$$R_{\mathrm{exp}} = R_{\mathrm{cor}} + (\beta/J) \times {}^{34}\mathrm{S}_{\mathrm{exp}} \qquad (3.5)$$

where R_{exp} and $^{34}S_{exp}$ are dead time corrected $^{34}S/^{32}S$ ratio and ^{34}S count rate, respectively, and R_{cor} is the QSA corrected $^{34}S/^{32}S$ ratio. The instrumental mass fractionation was then corrected for by calculating the mineral-specific fractionation factor ($^{34}\alpha$) based on the mean raw (from SIMS) and expected (from EA-IR-MS) $\delta^{34}S$ value of the population of internal hydrothermal

pyrite or marcasite fragments and dividing the average $^{34}S^{-}/^{32}S^{-}$ ratio of each environmental iron sulfide grain by the appropriate $^{34}\alpha$.

3.3 Results

3.3.1 Extraction procedure

The grain size distribution of the powdered hydrothermal pyrite crystal ('pre') suggested that 92.5% of grains were >0.5 μm, the smallest size expected to settle in our setup, so this was set as the expected maximum level of recovery. Recovery of initial pyrite (summarized in Table S3.1) was highest for 'post' (58±12%, 1σ) and for 'postSmQz' (57%), but lower for 'postQz' (23±4%, 1σ). Initial extractions ('a') recovered most pyrite, and subsequent extractions ('b' and 'c') were generally not effective in recovering the remaining pyrite. At grain sizes larger than 1.1 μm (close to the lower limit of what can be precisely measured on the 7f-GEO; Figure 3.1), grain size distributions of pre, post, postSmQz and postQz ('1a') were all similar, within the power of our technique to resolve differences (Figure 3.1, inset). Therefore, the extraction procedure does not impose a grain-size bias for grains ≥1.1 μm.

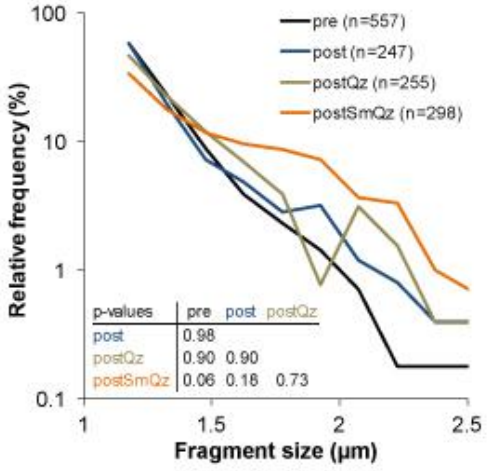

Figure 3.1. Pyrite fragment size distributions with a bin size of 0.15 μm before and after three different extraction tests with LST heavy liquid. The inset table shows chi square test p-values between these distributions.

Recovery of pyrite for the Santa Barbara Basin sediment sample was estimated to be 41.3% by comparing extract mass to previously measured total S abundance (Berelson et al., 2018). Extract purity for the Cismon section FeS_2 was estimated using EA to be 61% and by comparing extract mass to CRS abundance, FeS_2 recovery was estimated to be 54.5%, which again closely matches measured recovery for our synthetic sediment samples. In addition, the physically extracted iron sulfides had a bulk $\delta^{34}S$ value of −42.5 ± 0.2‰, whereas the bulk untreated sample had a $\delta^{34}S$ value of −42.1 ± 0.2‰ (Gomes et al., 2016). The agreement between the isotopic compositions of the chemically and physically extracted iron sulfides indicates that the physical extraction procedure did not impart any isotopic bias on the population of iron sulfides in the sample.

3.3.2 SIMS sulfur isotope experiments

Hydrothermal pyrite

Sub-angular, randomly oriented 1-3 µm diameter fragments of the hydrothermal pyrite (Figure 3.2A) were analyzed in a 50 um raster over 375 cycles (30 seconds integration time per ion, per cycle; Figure 3.2B; see Jones et al. (2018) for justification). The fragment-to-fragment reproducibility (n=14, 1σ) was ±1.9‰ (Figure 3.1C; Figure S3.1A), and using the EA-IRMS bulk $\delta^{34}S$ value of –1.0 ± 0.2‰, $^{34}\alpha_{pyrite}$ was calculated to be 0.9964 (Table S3.2). The standard error associated with individual fragments was ±0.9 to ±3.3‰ (1σ; Figure 3.2C), with an average of ±2.1‰ (Figure S3.1A), and was better for larger fragments due to better counting statistics (Figure S3.2). Lateral intra-fragment reproducibility in the largest fragment (Figure S3.3A) was ±2.8‰ (n=8, 1σ; Figure S3.3B, C), with an average standard error of ±3.0‰ (1σ; Figure S3.3C).

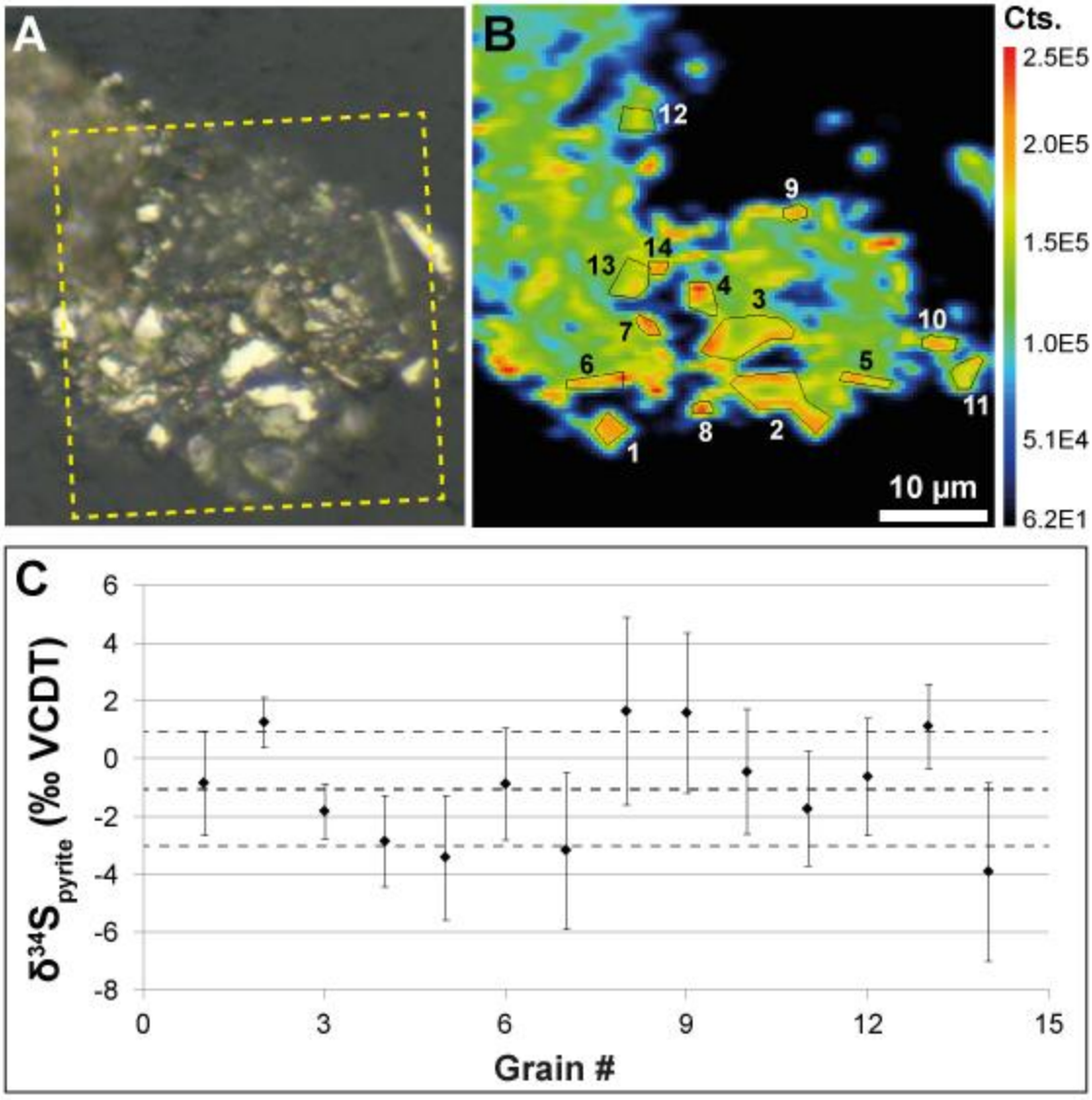

Figure 3.2. (A) Optical microscope image of hydrothermal pyrite fragments embedded in epoxy, viewed using 50x objective, (B) $^{32}S^-$ ion image of 50x50 micron region highlighted in A, integrated over 375 cycles, and (C) corrected isotopic composition of ≥1 µm diameter fragments (grains numbered in B), where error bars are standard error over 375 cycles (1σ), and dashed lines indicate 1σ around the mean.

Hydrothermal marcasite

Sub-angular, randomly oriented 1-5 µm diameter fragments of the hydrothermal marcasite crystal (Figure 3.3A) were analyzed in a 50 um raster over 375 cycles (30 seconds integration time per ion, per cycle; Figure 3.3B). The fragment-to-fragment reproducibility (n=25, 1σ) was ±2.3‰ (Figure 3.3C; Figure S3.1B), and using the EA-IRMS bulk $\delta^{34}S$ value of +4.6 ± 0.2‰,

$^{34}\alpha_{marcasite}$ was calculated to be 1.0014 (Table S3.2). The standard error associated with individual fragments was between ±1.1 to ±5.2‰ (1σ; Figure 3.3C), with an average of ±2.6‰ (Figure S3.1B), and was better for larger fragments due to improved counting statistics (Figure S3.2). Lateral intra-fragment variability in the largest fragment (Figure S3.4A) was ±1.9‰ (n=6, 1σ; Figure S3.4B, C), with an average standard error of ±3.6‰ (1σ; Figure S3.4C).

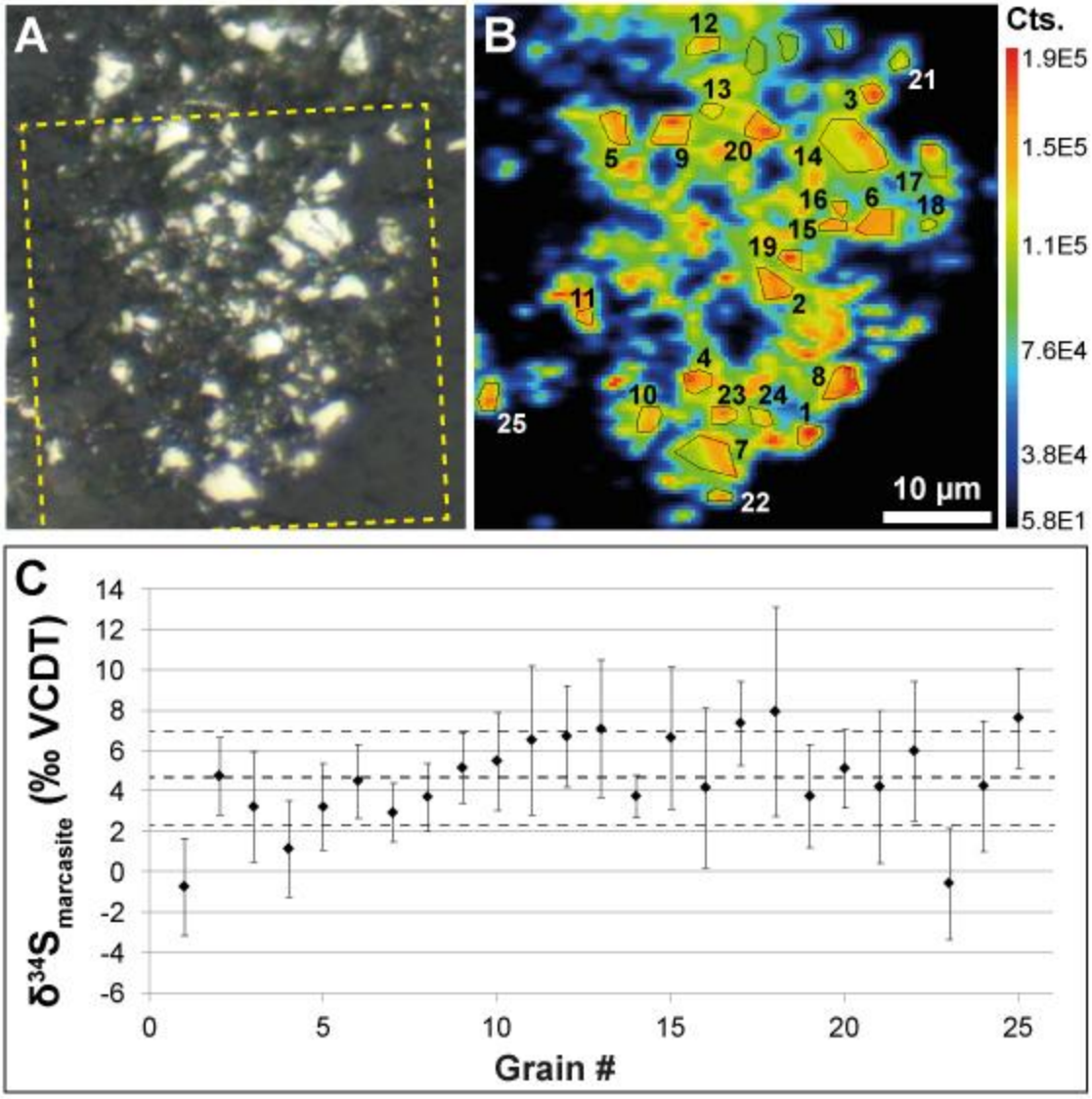

Figure 3.3. (A) Optical microscope image of hydrothermal marcasite fragments embedded in epoxy, viewed using 50x objective, (B) $^{32}S^-$ ion image of 50x50 micron region highlighted in A, accumulated over 375 cycles, and (C) corrected isotopic composition of ≥1 µm diameter fragments in A and B, where error bars are standard error over 375 cycles (1σ), and dashed lines indicate 1σ around the mean.

Modern sedimentary pyrites (Santa Barbara Basin)

Optical microscope images (Figure 3.4A) suggest that the majority of pyrites in this modern sediment sample are 1-80 μm-diameter irregular aggregates of intergrown euhedral-to-anhedral microcrystals.

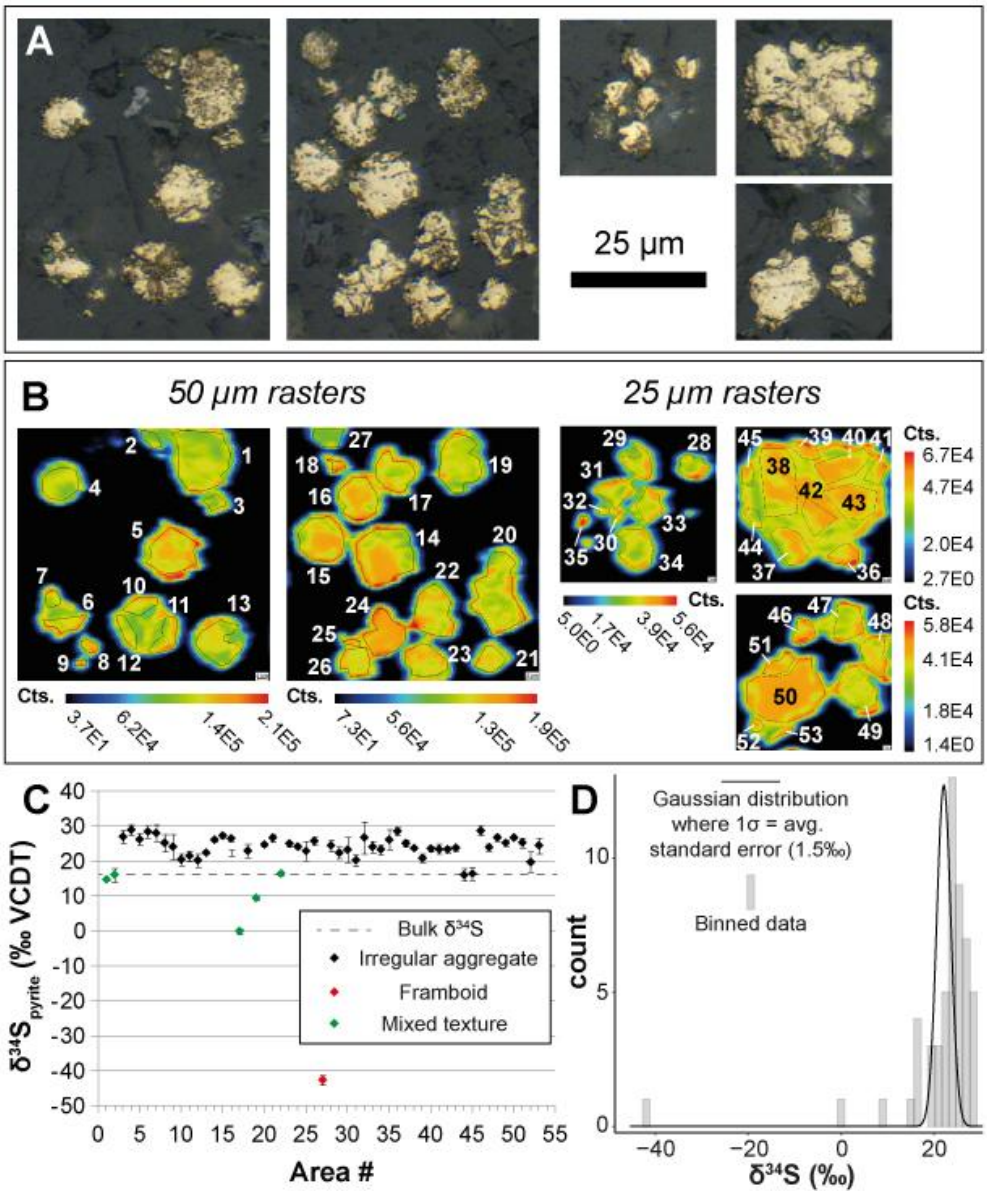

Figure 3.4. (A) Optical microscope images of pyrites from Santa Barbara Basin, taken though 50x objective, (B) $^{32}S^-$ ion images of pyrites shown in A, accumulated over 375 cycles for 50 μm rasters and 120 cycles for 25 μm rasters, (C) corrected $\delta^{34}S_{pyrite}$ values of areas highlighted in B, where error bars are standard error over cycles (1σ), and (D) Corrected SIMS data histogram for areas in A; centered on the average $\delta^{34}S_{pyrite}$ value is a Gaussian distribution whose width is consistent with the average standard error associated with individual measurements in C.

A minority of pyrites are framboidal (i.e., 5-10 µm-diameter pseudo-spheroidal aggregates of equant, equidimensional, non-intergrown microcrystals), while some grains display a mixture of the framboidal and irregular textures (Figure 3.4A). The one pristine framboid measured by SIMS (Grain 27; Figure 3.4B-C) had a $\delta^{34}S_{pyrite}$ value of −42.7 ± 1.5‰ (1σ; Figure 3.4C), the irregular aggregates (Figure 3.4B) had an average $\delta^{34}S_{pyrite}$ value of +24.2 ± 2.9‰ (1σ, n=47; Figure 3.4C), and five grains displaying mixed textures (Grains 1–2, 17, 19, and 22; Figure 3.4B) had $\delta^{34}S_{pyrite}$ values between +0.1 ± 0.8‰ (1σ) and +16.4 ± 0.7‰ (1σ; Figure 3.4C; Table S3.2). Within the mixed textured grains, the framboidal areas were usually depleted in ^{34}S with respect to the irregular areas (Figure S3.5). Within the solely irregular aggregates, variability in $\delta^{34}S$ was minimal (±3.5‰, 1σ, n=11; Area 14 in Figure 3.4; Figure S3.6) and comparable to the average standard error associated with measurements (±2.6‰, 1σ; Figure S3.6D). Where present, the apparent variability had no consistent directionality (Figure S3.6). The average standard error associated with individual fragments was ±1.5‰ (1σ; Figures 3.4C, D). The sample average $\delta^{34}S_{pyrite}$ value was +21.7 ± 10.3‰ (1σ; n=53; Figure 3.4D). The $\delta^{34}S_{pyrite}$ variability in this sample (Figures 3.4C, D) overlaps the bulk $\delta^{34}S_{CRS}$ value for the sample of +16.1‰ (Berelson et al., 2018), and is not normally distributed (Figure 3.4D).

Ancient sedimentary pyrites and marcasites (Cismon and Demerara Rise)

Optical microscope images of mounted extract from Cismon (Figure S3.7) display the presence of both euhedral marcasite and framboidal pyrite, as supported by laser Raman microprobe spot analyses and SEM (Figure S3.8). Pyrite and marcasite grains from Cismon measured by SIMS had average $\delta^{34}S$ values of −41.9 ± 5.2‰ (1σ; n=113) and −48.5 ± 5.1‰ (1σ; n=161; Figure 3.5), and cemented pyrite aggregates had an average $\delta^{34}S$ value of −42.2 ± 0.6‰ (1σ; n=2), as compared with the bulk $\delta^{34}S$ composition of −42.1‰ (Gomes et al., 2016).

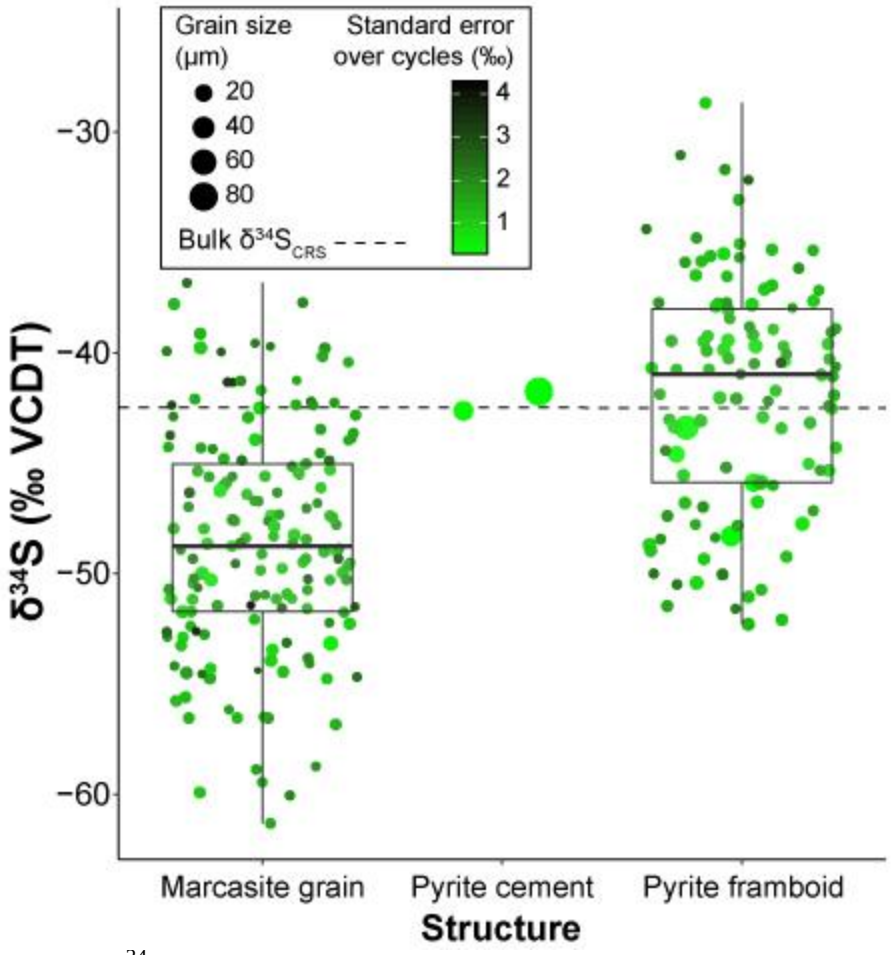

Figure 3.5. Corrected $\delta^{34}S$ data for iron sulfide grains from Cismon section sample, arranged into box plots by mineralogy.

There was little intra-grain $\delta^{34}S$ variation in marcasite grains (average 1σ = ±2.9‰, compared to an average intra-grain standard error of ±3.5‰, 1σ; Figure S3.9A-D), and very little intra-grain $\delta^{34}S$ variation in pyrite grains (average 1σ = ±3.7‰, compared to an average intra-grain standard error of ±2.9‰, 1σ; Figure S3.9E-H).

As with the Cismon section sample, optical microscope images of mounted extract from Demerara (Figure S3.10) display the presence of both euhedral marcasite (in this case mostly in irregular aggregates) and framboidal pyrite, as supported by laser Raman microprobe spot analyses and SEM (Figure S3.8). Pyrite and marcasite grains measured by SIMS had average

$\delta^{34}S$ values of −24.9 ± 11.2‰ (1σ; n=45) and −26.1 ± 6.1‰ (1σ; n=19; Figure 3.6), as compared with a bulk $\delta^{34}S$ composition of −24.4 ± 0.2‰ (Raven et al., 2019).

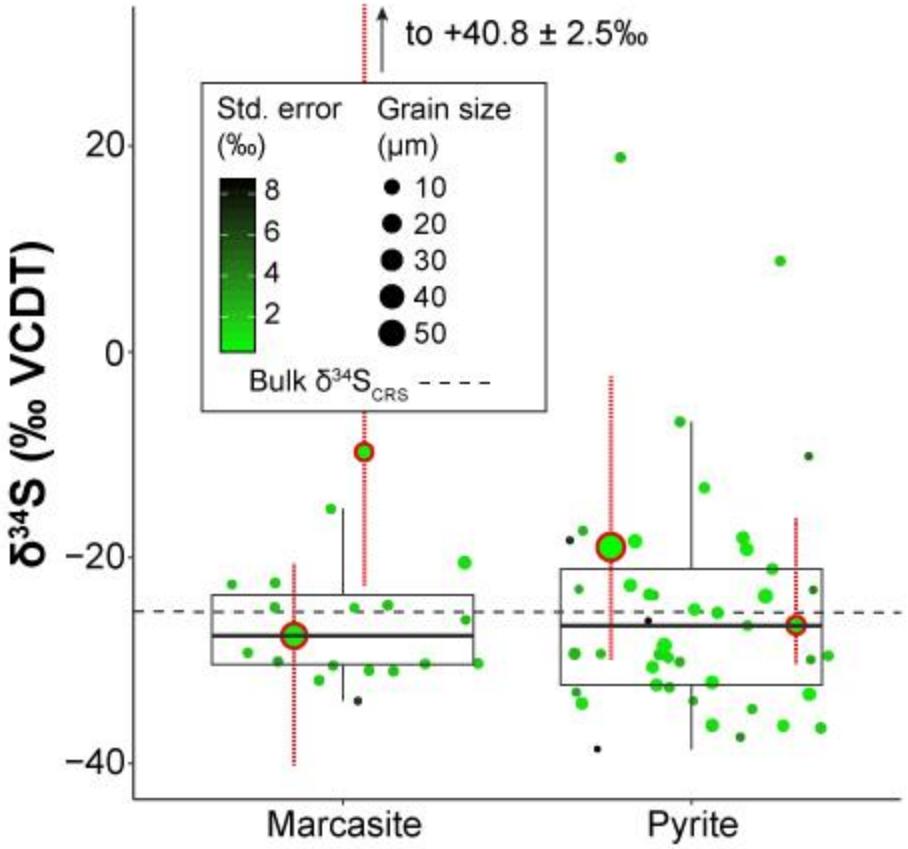

Figure 3.6. Corrected $\delta^{34}S$ data for iron sulfides from the Demerara sample, arranged into box plots by mineralogy. Points highlighted in red are aggregates whose internal range in $\delta^{34}S$ was measured (see Figure S3.11), as indicated by the red dashed lines.

In contrast to those from the Cismon section sample, pyrites from the Demerara sample sometimes featured larger, more easily-resolved intra-grain variation in $\delta^{34}S$ (average 1σ = ±6.0‰, compared to an average intra-grain standard error of ±1.6‰, 1σ; Figures 3.6, S3.11A-D). This was even more obviously the case for the marcasites (average 1σ = ±13.3‰, compared to an average intra-grain standard error of ±2.1‰, 1σ; Figures 3.6, S3.11E-H). Generally, the largest relative enrichments in ^{34}S were found near the edges of pyrite framboids (Figure S3.11A-B), and in the extremities of irregular aggregates of both minerals (Figure S3.11C-H).

3.4 Discussion

3.4.1 Evaluating the method

Despite incomplete recovery (reasons for which are discussed in the Supplement), the similarity between artificial pyrite grain size distributions before and after being treated with the extraction procedure (Figure 3.1) suggests that this protocol does not bias pyrite grain size distributions, even when grains are at the lower end of sizes that can be measured using a 7f-GEO SIMS instrument (~1 μm) or when they are mixed with large proportions of quartz grains. This is important because where grain size variability exists in populations of iron sulfide grains in sedimentary samples, such variability may be coupled to isotopic variability (Gomes et al., 2018); thus, a size bias in extraction protocol could produce an isotopic bias in the measured results relative to the parent sample.

Analysis of fragments of hydrothermal pyrite and marcasite crystals, used as S-isotopic standards for our other SIMS experiments, resulted in little inter- (Figures S3.1-3.2) or intra-fragment (Figures S3.3-3.4) variability in $\delta^{34}S$ (i.e., the standard deviation of measurements between or within fragments was always smaller than the average standard error associated with those inter- or intra-grain measurements). Therefore, the method is suitable for the detection of the potentially large variations in $\delta^{34}S$ that may exist within or between sedimentary iron sulfide grains (Drake et al., 2018, 2013; Fischer et al., 2014; Gomes et al., 2018; Marin-Carbonne et al., 2018).

The average SIMS $\delta^{34}S$ values for iron sulfides from samples from the Cismon section (–45.8 ± 6.1‰, 1σ; n=274; Figure 3.5) and the Demerara Rise (–25.3 ± 11.2‰, 1σ; n=45; Figure 3.6) are close to the previously reported bulk $\delta^{34}S_{CRS}$ values (–42.1‰, and –24.4‰, respectively) (Gomes et al., 2016; Raven et al., 2019). The Santa Barbara Basin pyrites' average $\delta^{34}S$ value

(+21.7 ± 10.3‰, 1σ; n=53; Figure 3.4) is 5.6‰ higher than the bulk $\delta^{34}S_{CRS}$ value (+16.1‰) (Berelson et al., 2018), but the large range of grain-specific values (–42.7‰ to +28.9‰) overlaps with the bulk value, and corresponds to a textural dichotomy between isotopically light framboids and isotopically heavy irregular aggregates. Accordingly, the discrepancy between bulk and average grain-specific $\delta^{34}S$ values is likely the result of insufficiently representative sampling of the two textural components for SIMS analysis. The extraction and analytical procedures introduced in this study are not likely to give rise to any isotopic biases, though areas analysed by SIMS may not always be entirely representative of the bulk iron sulfides in a sample. In the future, this could be rectified by ensuring that SIMS analyses of each texture are in proportion to their relative abundances.

Importantly, the method documents $\delta^{34}S$ variability within a sample, which is critical for interpreting bulk 'CRS' $\delta^{34}S$ values. Inter-grain (Figures 3.4-3.7), intra-grain (Figures S3.5-3.6, S3.9, S3.11), and inter-mineralogy (Figures 3.5-3.6) variability all contribute to a single bulk $\delta^{34}S$ value from CRS extraction (which integrates both pyrite and marcasite, as well as potentially other reduced S phases). Each type of variability should be considered and investigated when making environmental interpretations based on $\delta^{34}S$ data.

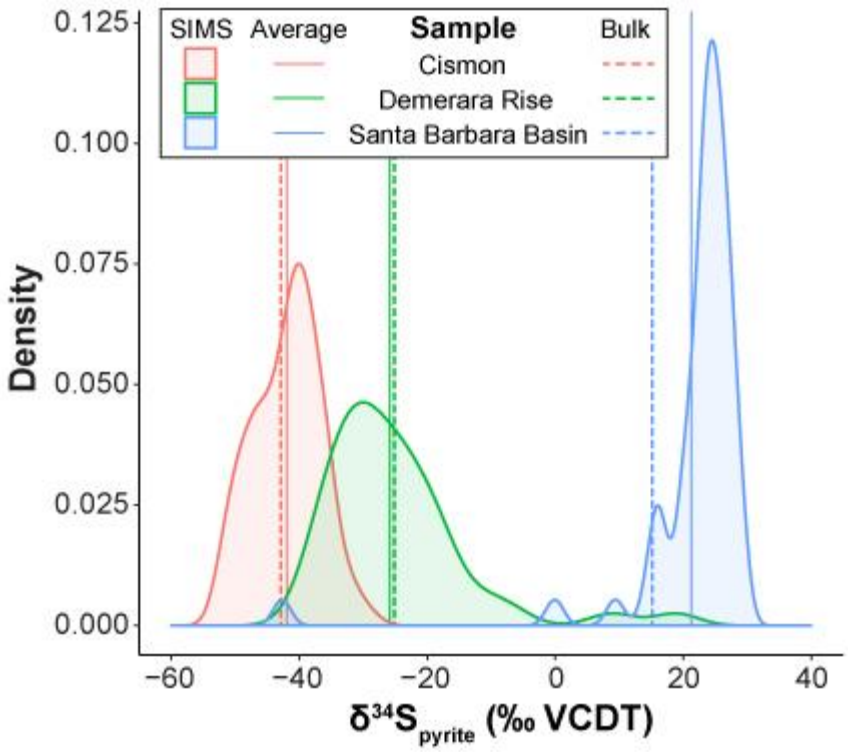

Figure 3.7. Density plots of all SIMS $\delta^{34}S_{pyrite}$ data for the samples from the Cismon section, Demerara Rise and Santa Barbara Basin. Dashed lines are the bulk $\delta^{34}S_{CRS}$ for each sample. Bulk data are from: Gomes et al. (2016), Raven et al. (2019) and Berelson et al. (2018).

3.4.2 Interpreting sedimentary $\delta^{34}S$ data

The three samples studied here are distinct in terms of their bulk $\delta^{34}S$ values and internal $\delta^{34}S$ variability (Figure 3.7). Thus, they can be used to map out the environmental phase space that can be explored using this SIMS ion imaging method. The first step to this process is to consider that iron sulfide minerals formed in marine sediments record the $\delta^{34}S$ composition of reduced sulfur-bearing aqueous phases (e.g., hydrogen sulfide or polysulfides) in the fluid from which they nucleate or grow (Fike et al., 2015; Rickard, 2012). In most cases, this fluid is likely to be pore water in marine sediments, but pyrites can also precipitate from sulfide-rich water columns (Suits and Wilkin, 1998). Secondly, iron sulfide mineral growth requires a source of iron. Different sources (i.e., mineral or aqueous) are differentially reactive to aqueous reduced sulfur species (Meyers, 2007), and therefore the extent to which iron sulfide minerals record spatio-

temporal changes in the $\delta^{34}S$ composition of aqueous sulfur is highly dependent on the abundance, mineralogy, and speciation of available iron (Fike et al., 2015).

The sample from Santa Barbara Basin comprises silt-clay sized material from one of the "gray layers" that have been hypothesized to represent extremely rapid deposition associated with major flood events (Fleischer, 1972; Li et al., 2011; Thornton, 1986). Rapid deposition results in pore water sulfate being consumed faster than it is supplied (Claypool, 2004). We predict a broad range of pyrite $\delta^{34}S$ values corresponding to progressive pyrite precipitation in such a scenario. Berelson et al. (2018) found that iron disulfides from the sample are highly ^{34}S-enriched in bulk, and are predominantly irregular aggregates of pyrite. In this study, we found that the irregular aggregates noted by Berelson et al. (2018) are even more highly-enriched in ^{34}S than the bulk sample (Figure 3.4), and feature very little intra-grain $\delta^{34}S$ variability (Figure S3.6). Conversely, framboidal pyrites are depleted in ^{34}S, and feature irregular overgrowths that are usually relatively enriched in ^{34}S (Figure S3.5). This clearly implies a spatial or temporal separation in the growth of these two textures. The ^{34}S-depleted framboids likely formed in a relatively open, sulfate-replete system, such as pore waters close to the sediment-water interface, or in the water column (e.g., in sinking particles harboring anoxic microenvironments; Bianchi et al. (2018)). In contrast, the ^{34}S-enriched irregular aggregates likely formed in a system in which rapid MSR led to ^{34}S-enriched aqueous sulfate and sulfide (Aller et al., 2004; Claypool, 2004). MSR must have greatly outpaced pyrite formation, leading to the build up of an aqueous reduced sulfur pool in pore fluids with a similar S-isotopic composition to the initial sulfate reservoir. The majority of pyrite in the sample precipitated from this aqueous reduced sulfur pool. The high rate of MSR relative to the rate of pyrite formation was very likely a result of the slow kinetics of iron reduction (Meyers, 2007).

Sediments from the Cismon section are thought to represent nearly the opposite end-member case to Santa Barbara Basin, with very low bulk CRS $\delta^{34}S$ values (avg. –42.7‰) (Gomes et al., 2016; Raven et al., 2019). These values have been interpreted to represent pyrite formation in a system that was open to the diffusive supply of sulfate (Bellanca et al., 1996; Gambacorta et al., 2016), so a narrow intra-sample range of $\delta^{34}S$ values is expected. Accordingly, we find that the sample lacks both inter-grain (Figures 3.5, 3.7) and intra-grain (Figure S3.9) $\delta^{34}S$ variability. Individual pyrite grain $\delta^{34}S$ values (−41.9 ± 5.2‰, 1σ; n=113) and marcasite grain $\delta^{34}S$ values (−48.5 ± 5.1‰, 1σ; n=161; Figure 3.5) cluster close to the bulk CRS $\delta^{34}S$ value, suggesting that the S-isotopic composition of aqueous reduced sulfur species in the fluid from which the iron sulfides formed was not highly variable. This is consistent with a scenario in which all iron sulfides (pyrite framboids, pyrite cements and marcasite euhedra) formed either in the water column or in sediments where the rate of sulfate diffusion from the water column exceeded the rate of sulfate consumption by MSR.

Finally, sediments from the Demerara Rise are thought to represent an intermediate case between the Cismon section and Santa Barbara Basin, with a corresponding bulk CRS $\delta^{34}S$ value of –24.4‰ for our sample. This black shale sample (422.8 m depth, ODP Leg 207, Hole 1258a) was deposited under a euxinic water column, so sulfate consumption by MSR very likely outpaced the diffusive replenishment of sulfate (Raven et al., 2019). Therefore, a larger intra-sample range of $\delta^{34}S$ values relative to the Cismon section sample is expected. Accordingly, the sample from Demerara Rise features a large amount of $\delta^{34}S$ variability – both inter- (Figures 3.6, 3.7) and intra-grain (Figure S3.11), in pyrites and marcasites. The mean $\delta^{34}S$ values of marcasite and pyrite grains (Figure 3.6) are very similar. However, unlike in the Cismon section sample, both pyrite framboids (Figure S3.11A), and pyrite (Figure S3.11C) and marcasite clusters

(Figure S3.11E, G), have large internal ranges in $\delta^{34}S$, of ~10‰ to 65‰, with more ^{34}S-enriched material on the outer layer of framboids or in discrete zones in the extremities of clusters. This pattern is evidence for the formation of these grains over a time interval with evolving pore fluid $\delta^{34}S$. As in the case of the Santa Barbara Basin sample, these results suggest that MSR led to ^{34}S-enrichment of aqueous sulfate and sulfide with time in the sediment (Aller et al., 2004; Claypool, 2004). We also see a 'tail' of relatively ^{34}S-enriched pyrites in the $\delta^{34}S$ distribution (Figure 3.7), which suggests that there must have been sufficiently abundant and reactive iron available to sustain iron sulfide mineral growth as pore waters became progressively ^{34}S-enriched (Fike et al., 2015; Meyers, 2007).

Marcasite is thought to be a relatively rare mineral in sedimentary rocks, most notably occurring in black shales (Schieber, 2011, 2007). The environmental implications of its presence are still poorly understood. Experimental work suggests that a very low pH is required for its formation (Murowchick and Barnes, 1987). Given that pyrite oxidation can give rise to acidic conditions (Soetaert et al., 2007), this has led to the suggestion that the partial oxidation of pre-existing pyrite led to the formation of marcasite in black shales (Schieber, 2011, 2007). However, given that black shales are thought to represent low pO_2 conditions in water column, it is unclear how early diagenetic pyrite oxidation could have occurred in these sediments. In addition, the general isotopic similarity between the highly abundant marcasite in the Demerara and Cismon samples used in this study, and the coexisting pyrite (Figures 3.5-3.6), suggests that the two minerals share a formation history. Therefore, marcasite formation was probably not a result of low pH conditions created by pyrite oxidation. Another way to generate more acidic pore waters than are typical for marine sediments is oxic organic matter respiration (Soetaert et al., 2007). This process could have been exacerbated by the high organic loading at both sites

(Raven et al., 2019). Future work using SIMS will provide further constraints on the relative abundance of marcasite and the genetic relationship(s) between pyrite and marcasite in black shales.

In conclusion, the methods detailed here provide a basis for the physical extraction and accurate and precise sulfur isotopic measurement of microcrystalline iron sulfide grains within a range of sediments and sedimentary strata. The minimal size-biasing during the extraction procedure suggests that the iron sulfide extracts obtained should be isotopically representative of the bulk sample, as confirmed by our samples. The low apparent inter-grain variability between isotopically identical pyrite (and marcasite) micro-fragments implies that the sulfur isotope composition of diverse environmental populations of ≥1 μm-sized pyrites and marcasites can be measured accurately and precisely by SIMS ion imaging. Micrometer-scale intra-grain variability in $\delta^{34}S$ can also be measured. Ultimately, it is possible to use this approach to unpack local environmental (geochemical and depositional), metabolic, and diagenetic signals recorded in iron sulfide grains in both unlithified sediments and rocks. With this in mind, the method could be applied to the both the modern and ancient bulk sedimentary records of $\delta^{34}S$ to test previous wide-ranging interpretations of apparent excursions in bulk data (Gill et al., 2011; Parnell et al., 2010; Pasquier et al., 2017).

Acknowledgements

The authors thank Crystal LaFlamme and one anonymous reviewer, whose insightful comments greatly improved this manuscript. We also thank Itay Halevy, and the members of the Fike and Bradley Labs at Washington University, whose enthusiastic discussions yielded improvements to this work. RNB acknowledges support from the McDonnell Center for the Space Sciences at Washington University in St. Louis. We also acknowledge funding to DAF from DOE/BER (#DE-SC0014613) and from the donors of the American Chemical Society Petroleum Research Fund (#57548-ND2) for partial support of this research.

Supplement

Table S3.1. Recovery of pyrite during sequential centrifugal heavy liquid extractions.

Extraction	Recovery (%)	Recovery totals (%)	Average (%)
post 1a	52.85	52.85	58 ± 12
post 2a	47.07	48.36	
post 2b	1.29		
post 3a	68.05	71.73	
post 3b	3.19		
post 3c	0.48		
postQz 1a	27.16	27.16	23 ± 4
postQz 2a	19.24	19.38	
postQz 2b	0.14		
postQz 3a	22.10	22.20	
postQz 3b	0.10		
postQz 3c	0.00		
postSmQz 1a	57.03	57.03	57

Discussion of reasons for incomplete recovery of pyrite via extraction procedure

The discrepancy between predicted and actual recovery could be because many grains smaller than >0.5 μm were not counted by our grain size distribution method (Figure 3.1) due to the limitations imposed by the optical objective magnification. In addition, the settling time in equation 2 is probably an underestimate due to 'hindering effects'. This may explain why pyrite fragments mixed with quartz grains were less effectively recovered. Despite these potential shortcomings, recovery levels associated with the method are within a factor of two of predictions.

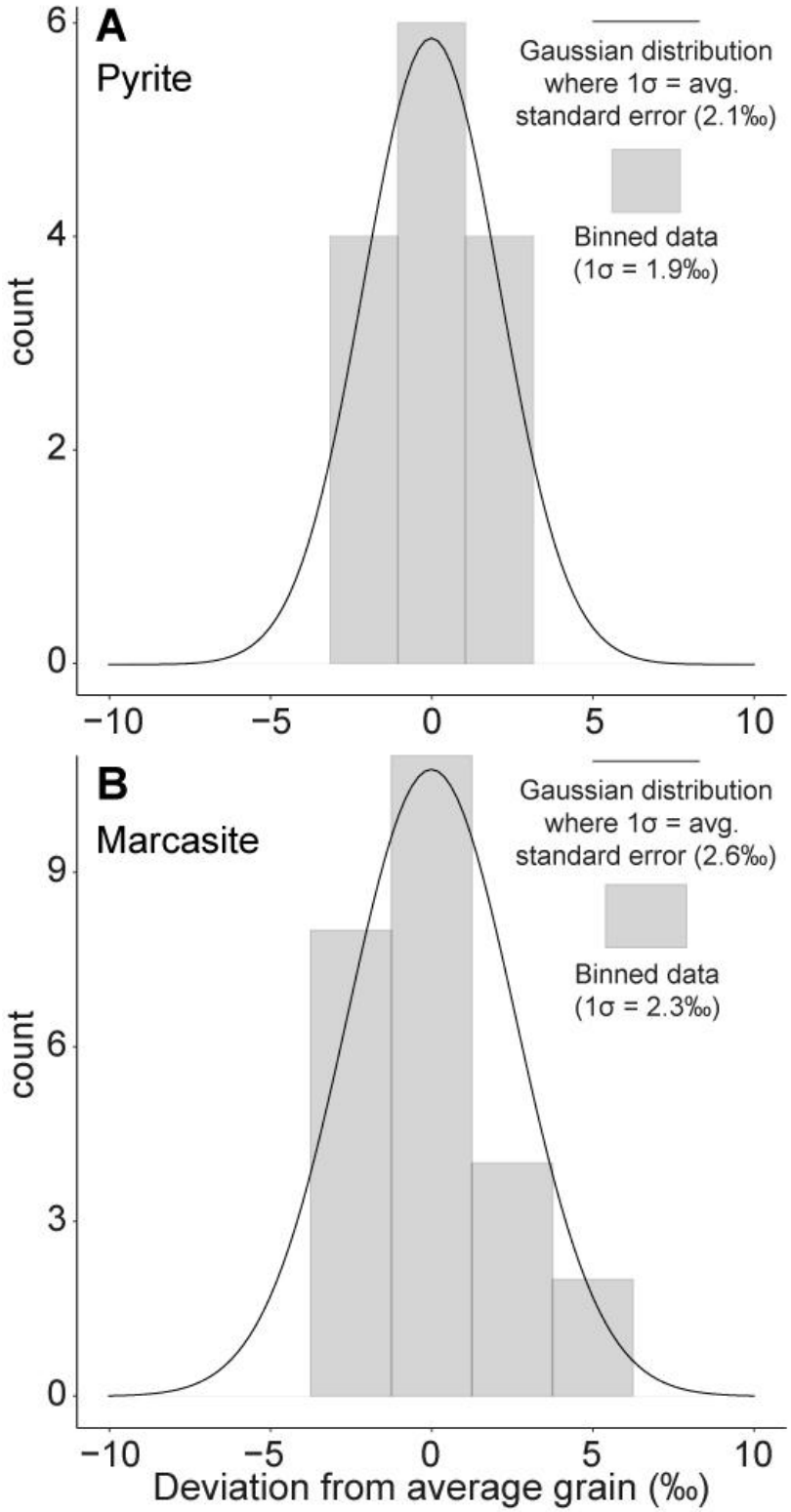

Figure S3.1. (A) Corrected SIMS data histograms for fragments of igneous pyrite, and (B) marcasite; data are normalized to $^{34}S/^{32}S$ ratio of the average grain. Overlain on histograms are Gaussian distributions whose widths are consistent with the average standard error associated with individual measurements.

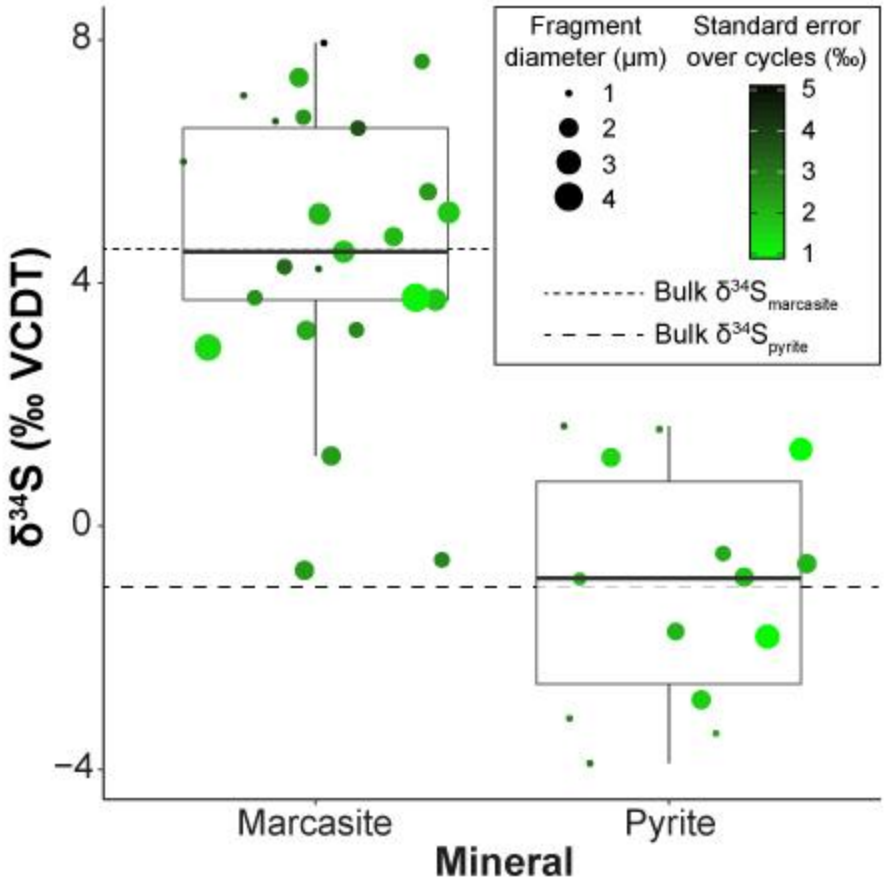

Figure S3.2. Corrected SIMS data for fragments of igneous marcasite and pyrite, displayed as box plots, with data points jittered for clarity.

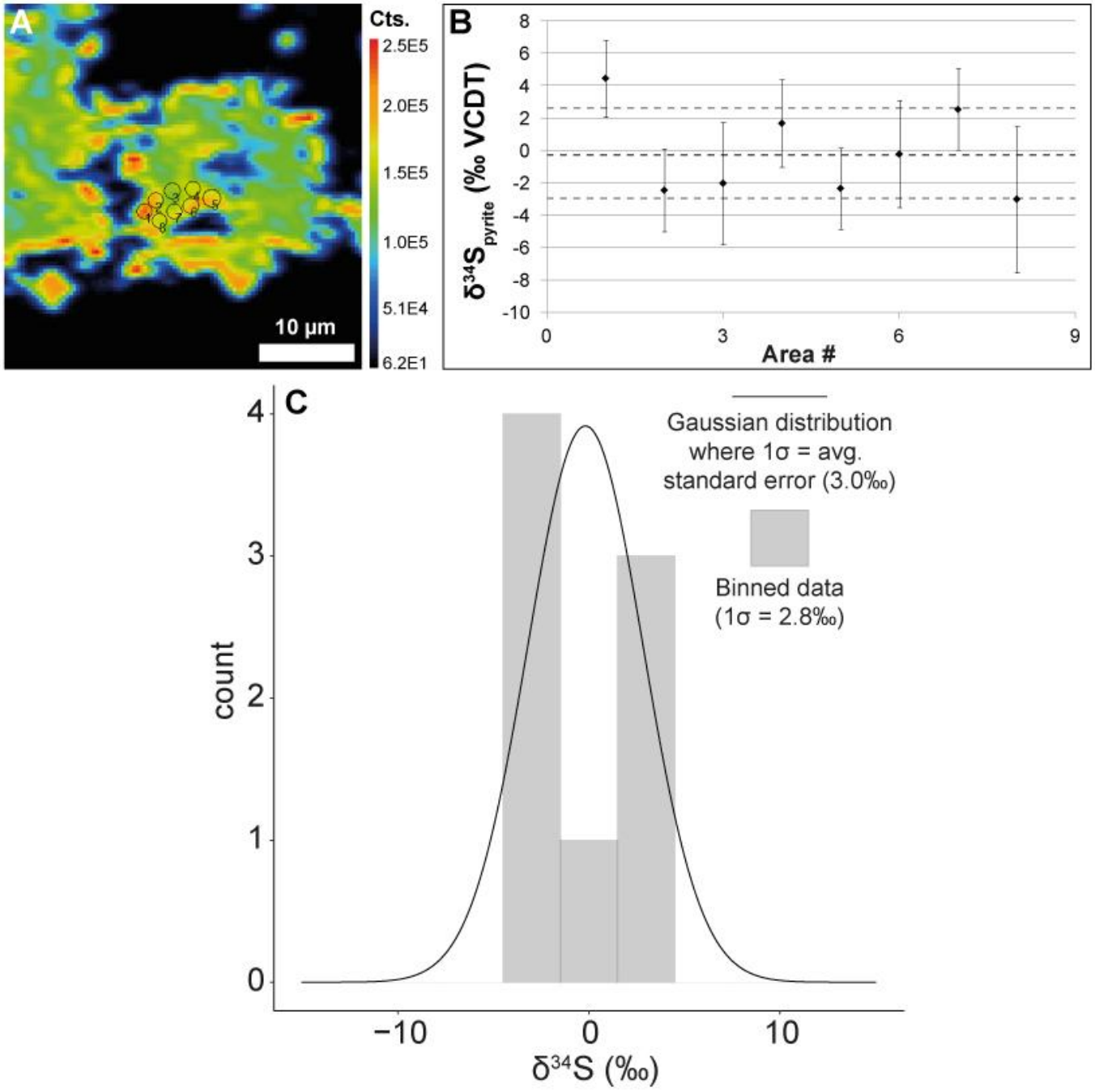

Figure S3.3. (A) $^{32}S^-$ ion image of igneous pyrite fragments, accumulated over 375 cycles; (B) $\delta^{34}S$ composition of areas (highlighted in A) of a single fragment, where error bars are standard error over cycles (1σ), and dashed lines indicate 1σ around the mean; (C) Corrected SIMS data histogram for areas in A; overlain is a Gaussian distribution whose width is consistent with the average standard error associated with individual measurements in B.

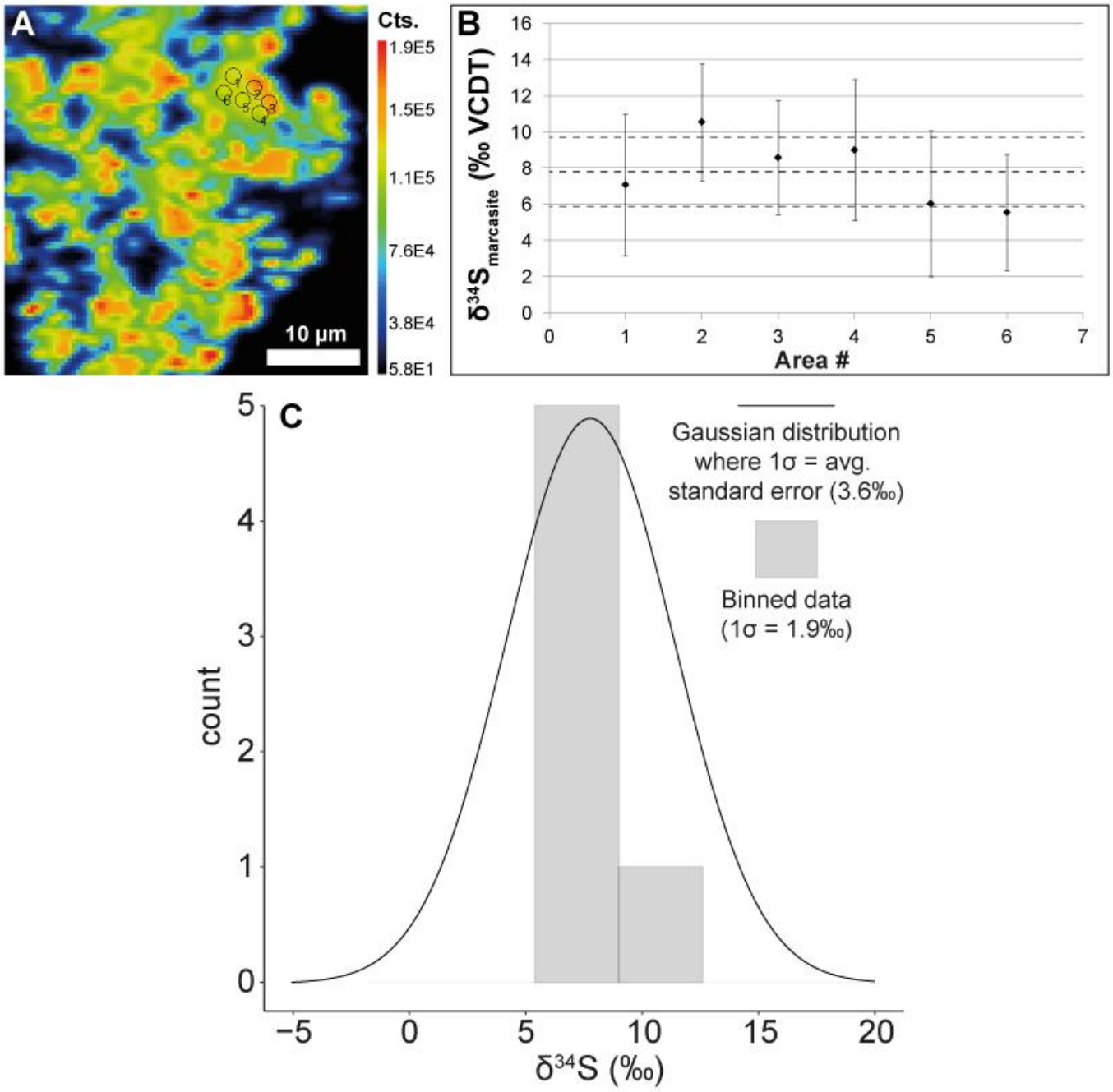

Figure S3.4. (A) $^{32}S^-$ ion image of igneous marcasite fragments accumulated over 375 cycles; (B) $\delta^{34}S$ composition of areas (highlighted in A) of a single fragment, where error bars are standard error over cycles (1σ), and dashed lines indicate 1σ around the mean; (C) Corrected SIMS data histogram for areas in A; overlain is a Gaussian distribution whose width is consistent with the average standard error associated with individual measurements in B.

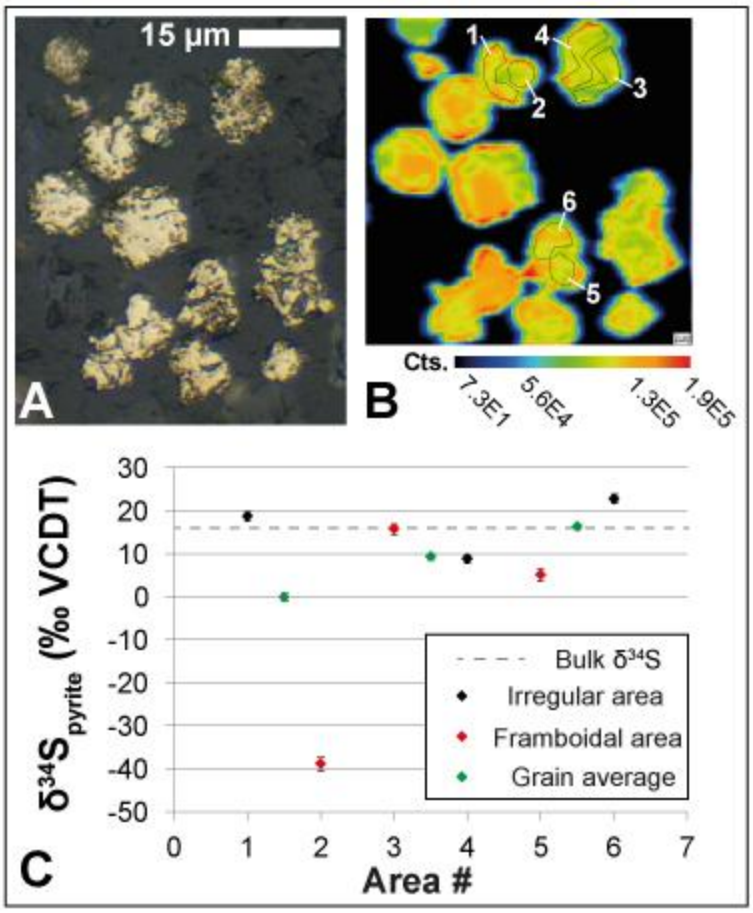

Figure S3.5. (A) Optical microscope image of pyrites from Santa Barbara Basin, taken though 50x objective, (B) $^{32}S^-$ ion images of pyrites shown in A, accumulated over 375 cycles, and (C) corrected isotopic composition of pyrites 17, 19, and 22 from Figure 3.4, and areas of those pyrites highlighted in B, where error bars are standard error over cycles (1σ).

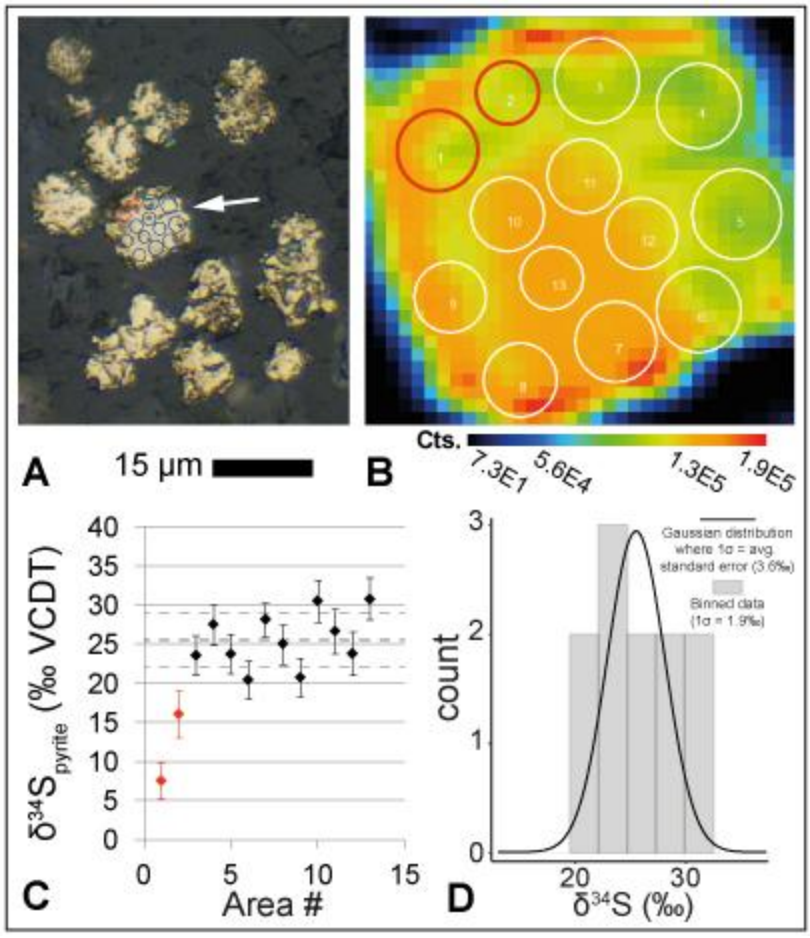

Figure S3.6. (A) Optical microscope image of pyrites from Santa Barbara Basin, taken though 50x objective, (B) $^{32}S^-$ ion image of irregular aggregate marked by arrow in A, accumulated over 375 cycles, (C) corrected isotopic composition of areas highlighted in B, where error bars are standard error over cycles (1σ), and dashed lines indicate 1σ around the mean, and (D) Corrected SIMS data histogram for areas in B; centered on the average $\delta^{34}S_{pyrite}$ value is a Gaussian distribution whose width is consistent with the average standard error associated with individual measurements in C. NB. The mean and standard deviation plotted in C and the data in D exclude areas 1 and 2 due to the areas' position on the rough upper left edge of the grain (see red circles in A and B), which produced anomalous data.

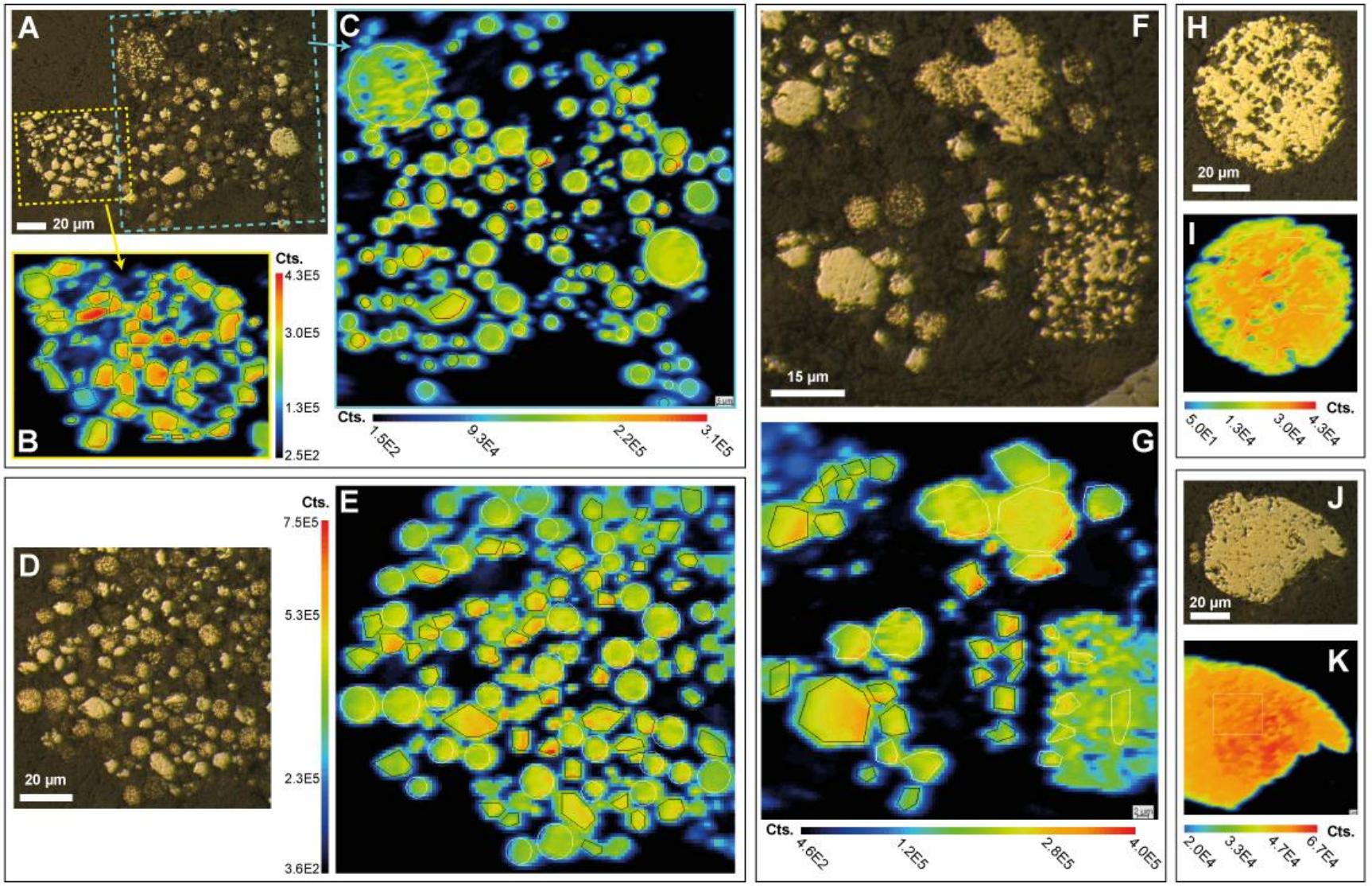

Figure S3.7. (A) Optical microscope image of framboidal pyrites and euhedral marcasites from Cismon sample; (B) SIMS $^{32}S^-$ accumulated map of yellow region in A; (C) $^{32}S^-$ map of blue region in A; (D) Optical microscope image of framboidal pyrites and euhedral marcasites; (E) $^{32}S^-$ map corresponding to D; (F) Optical microscope image of framboidal pyrites and euhedral marcasites; (G) $^{32}S^-$ map corresponding to F; (H) Optical microscope image of large, partially-infilled pyrite framboid; (I) $^{32}S^-$ map corresponding to H; (J) Optical microscope image of cemented pyrite aggregate; (K) $^{32}S^-$ map corresponding to J. NB. In all $^{32}S^-$ maps, pyrite ROIs are selected in white and marcasite ROIs are selected in black.

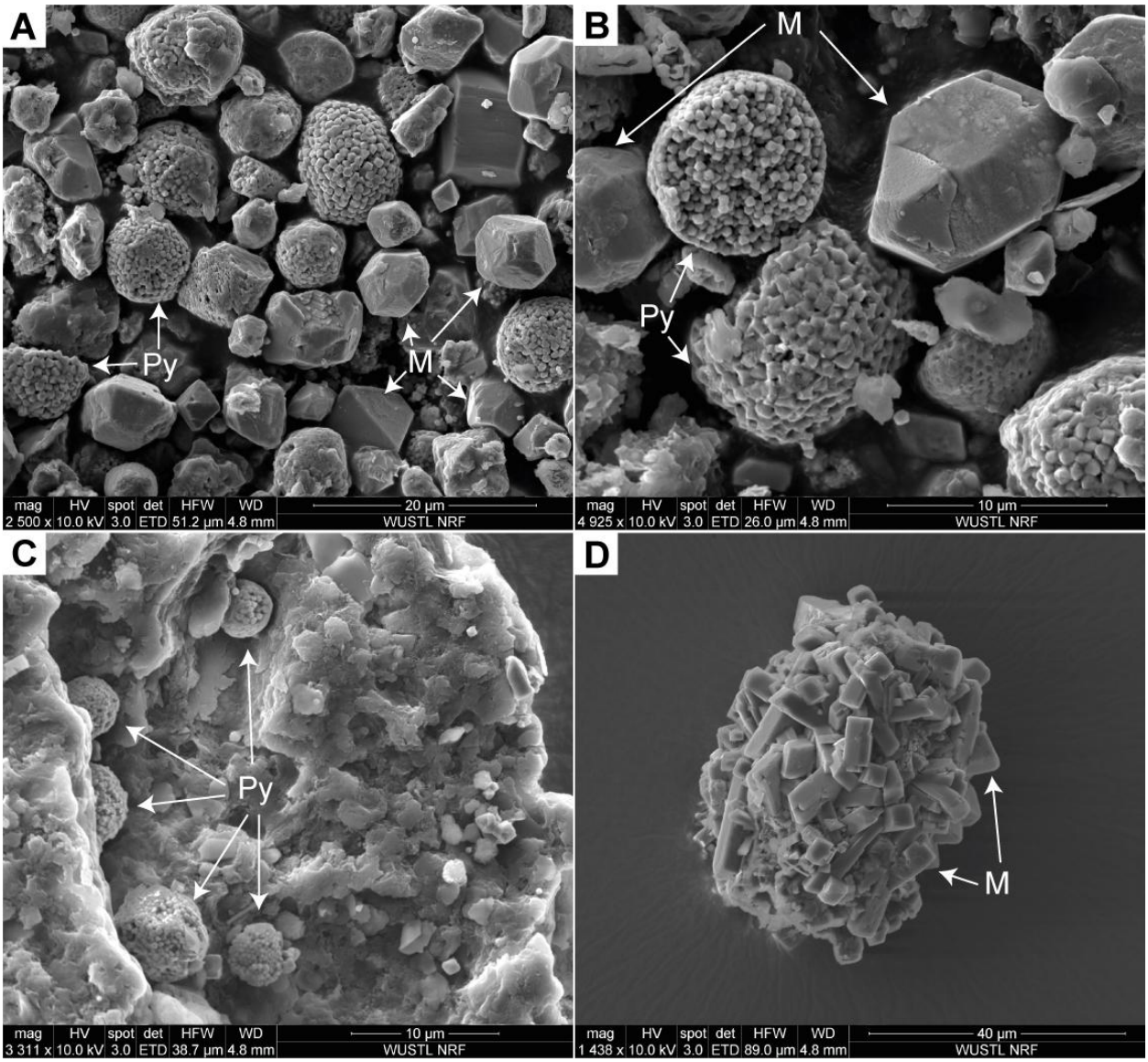

Figure S3.8. SEM images of pyrites and marcasites from Cismon (A, B) and Demerara (C, D). Examples of pyrites are indicated by 'Py'; Examples of marcasites are indicated by 'M'.

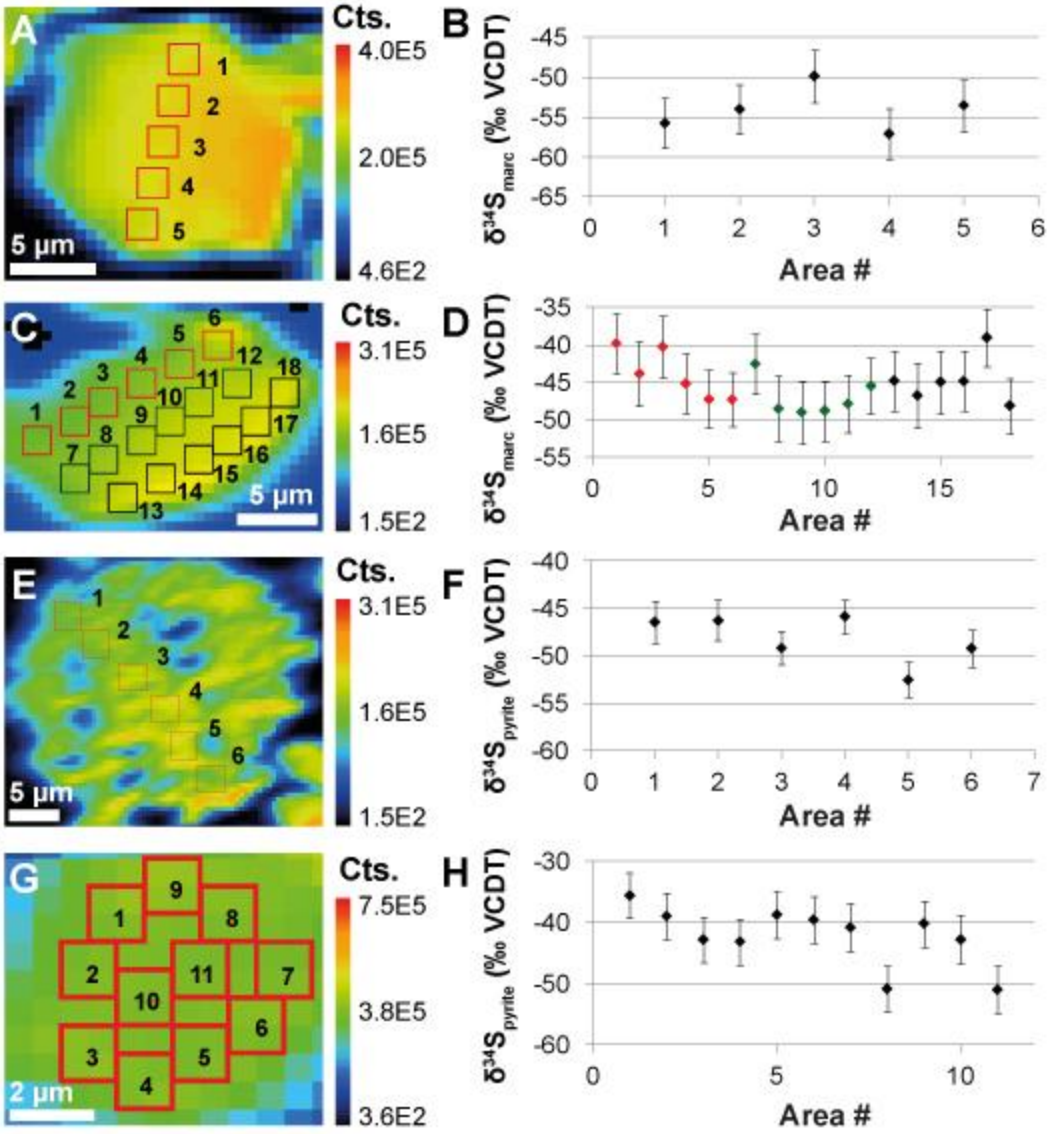

Figure S3.9. $^{32}S^-$ ion images of marcasite (A, C) and pyrite (E, G) grains from Cismon, accumulated over 480, 700, 700, and 960 cycles, respectively; $\delta^{34}S$ composition of areas highlighted in A, C, E, and G (B, D, F, and H), where error bars are standard error over cycles (1σ). Grains in A, C, E and G are representative of those in Figure S3.8a-b, and are also seen in Figure S3.6c, e, and g.

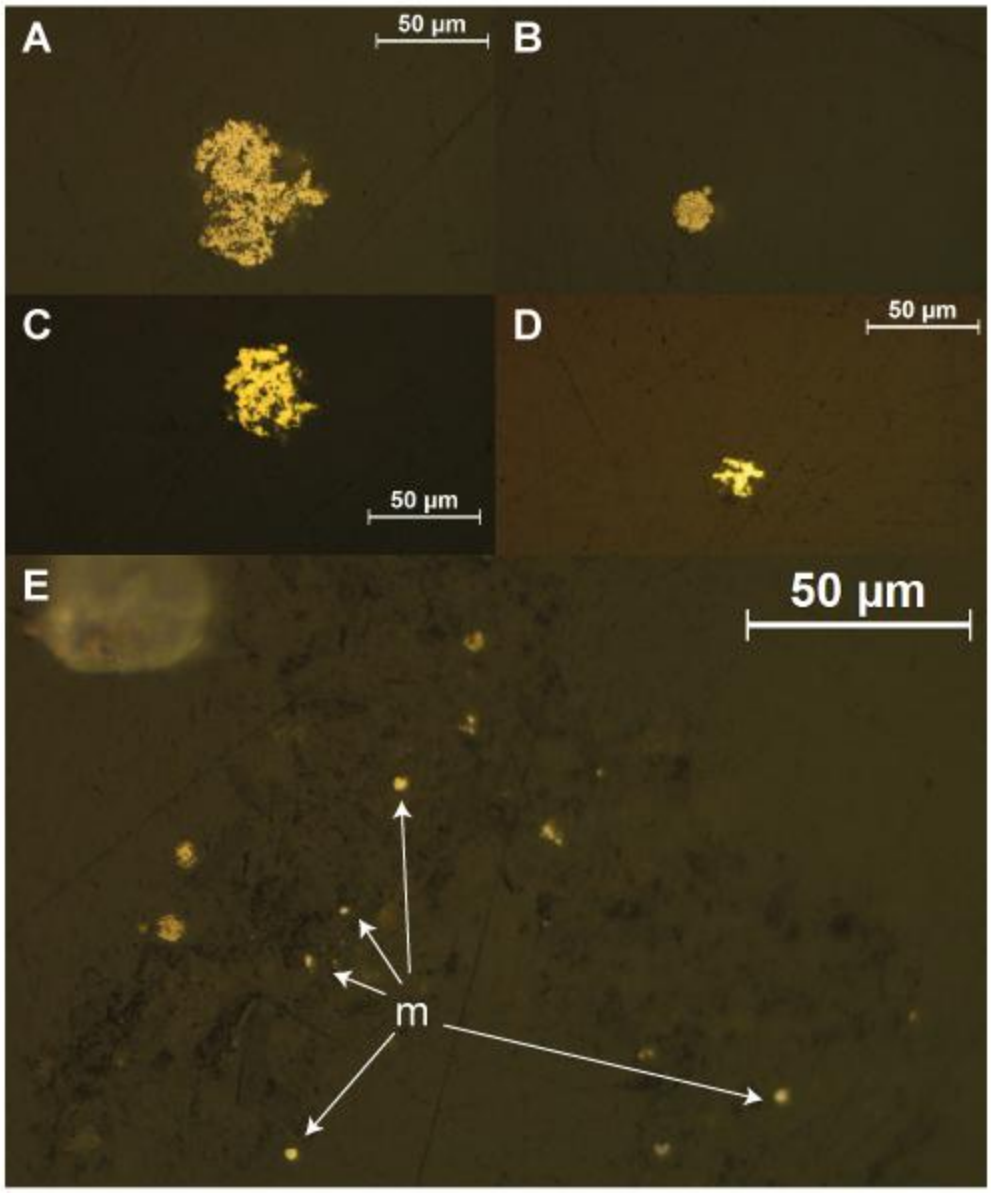

Figure S3.10. Optical microscope images of Demerara iron sulfide grains using the 50x objective; (A) and (B) are large, individual pyrite grains, (C) is a polycrystalline agglomerate of marcasite, (D) is a single large irregularly-shaped, anhedral marcasite grain, and (E) is an organic matter-bound aggregate bearing sparse pyrite framboids and tiny marcasite crystals (marked by 'm'). The majority of iron sulfide grains in the sample were similar to those in (E).

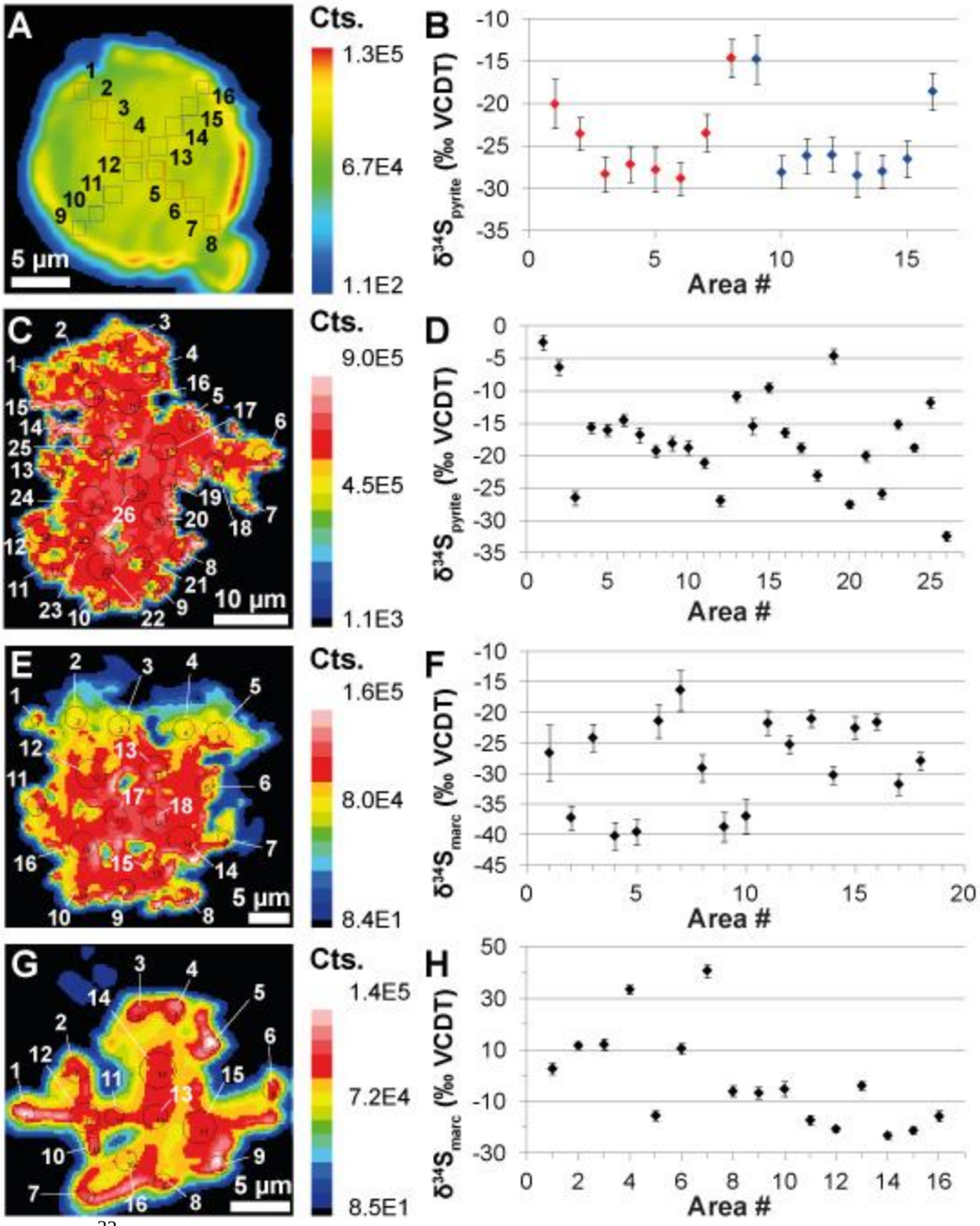

Figure S3.11. $^{32}S^-$ ion images of pyrite (A, C) and marcasite (E, G) grains from Demerara, accumulated over 90 cycles; $\delta^{34}S$ composition of areas highlighted in A, C, E, and G (B, D, F, and H), where error bars are standard error over cycles (1σ). Grains in A, C, E and G correspond to those in Figure S3.7b, a, c, and d.

Table S3.2. All SIMS data relevant to this manuscript.

Sample	Grain size (μm)	c ^{34}S/s/px	c ^{32}S/s/px	Raster size (μm)	Cycles	IMF ($^{34}\alpha$)	$\delta^{34}S_{pyrite}$ values (‰ VCDT)	Std error (‰)
Wards Marcasite 1	2.0	9.98E+03	2.26E+05	50	375	1.001387	-0.7	2.4
Wards Marcasite 2	2.0	1.03E+04	2.32E+05	50	375	1.001387	4.8	1.9
Wards Marcasite 3	1.5	1.05E+04	2.37E+05	50	375	1.001387	3.2	2.7
Wards Marcasite 4	2.0	9.94E+03	2.25E+05	50	375	1.001387	1.2	2.4
Wards Marcasite 5	2.0	9.73E+03	2.19E+05	50	375	1.001387	3.2	2.2
Wards Marcasite 6	2.5	1.03E+04	2.31E+05	50	375	1.001387	4.5	1.8
Wards Marcasite 7	3.5	8.80E+03	1.98E+05	50	375	1.001387	2.9	1.5
Wards Marcasite 8	2.5	1.09E+04	2.47E+05	50	375	1.001387	3.7	1.7
Wards Marcasite 9	2.5	9.61E+03	2.16E+05	50	375	1.001387	5.2	1.7
Wards Marcasite 10	1.8	9.11E+03	2.05E+05	50	375	1.001387	5.5	2.4
Wards Marcasite 11	1.5	9.49E+03	2.13E+05	50	375	1.001387	6.5	3.7
Wards Marcasite 12	1.5	8.74E+03	1.96E+05	50	375	1.001387	6.7	2.5
Wards Marcasite 13	1.0	8.27E+03	1.86E+05	50	375	1.001387	7.1	3.4
Wards Marcasite 14	4.0	8.74E+03	1.97E+05	50	375	1.001387	3.8	1.1
Wards Marcasite 15	1.0	9.85E+03	2.21E+05	50	375	1.001387	6.7	3.5
Wards Marcasite 16	1.0	9.33E+03	2.10E+05	50	375	1.001387	4.2	3.9
Wards Marcasite 17	2.0	8.14E+03	1.83E+05	50	375	1.001387	7.4	2.1
Wards Marcasite 18	1.0	7.63E+03	1.71E+05	50	375	1.001387	7.9	5.2
Wards Marcasite 19	1.5	9.75E+03	2.20E+05	50	375	1.001387	3.8	2.5
Wards Marcasite 20	2.5	1.03E+04	2.31E+05	50	375	1.001387	5.1	2.0
Wards Marcasite 21	1.0	7.61E+03	1.71E+05	50	375	1.001387	4.2	3.8
Wards Marcasite 22	1.0	9.36E+03	2.10E+05	50	375	1.001387	6.0	3.5
Wards Marcasite 23	1.5	9.48E+03	2.15E+05	50	375	1.001387	-0.6	2.7
Wards Marcasite 24	1.5	8.46E+03	1.91E+05	50	375	1.001387	4.3	3.2
Wards Marcasite 25	1.5	9.47E+03	2.12E+05	50	375	1.001387	7.6	2.5
Wards Pyrite 1	2.0	1.28E+04	2.91E+05	50	375	0.996604	-0.8	1.8
Wards Pyrite 2	2.8	1.17E+04	2.66E+05	50	375	0.996604	1.3	0.9
Wards Pyrite 3	3.0	1.10E+04	2.51E+05	50	375	0.996604	-1.8	1.0
Wards Pyrite 4	2.0	1.17E+04	2.66E+05	50	375	0.996604	-2.9	1.6
Wards Pyrite 5	1.0	1.14E+04	2.59E+05	50	375	0.996604	-3.4	2.2
Wards Pyrite 6	1.3	1.18E+04	2.69E+05	50	375	0.996604	-0.9	1.9
Wards Pyrite 7	1.0	1.32E+04	3.00E+05	50	375	0.996604	-3.2	2.7
Wards Pyrite 8	1.0	1.36E+04	3.09E+05	50	375	0.996604	1.6	3.3

Wards Pyrite 9	1.0	1.16E+04	2.63E+05	50	375	0.996604	1.6	2.8
Wards Pyrite 10	1.5	1.12E+04	2.55E+05	50	375	0.996604	-0.4	2.2
Wards Pyrite 11	1.8	1.05E+04	2.38E+05	50	375	0.996604	-1.7	2.0
Wards Pyrite 12	2.0	9.13E+03	2.08E+05	50	375	0.996604	-0.6	2.0
Wards Pyrite 13	2.0	1.01E+04	2.28E+05	50	375	0.996604	1.1	1.5
Wards Pyrite 14	1.0	1.24E+04	2.82E+05	50	375	0.996604	-3.9	3.1
Wards Pyrite 15	18.0	9.04E+03	2.05E+05	25	60	0.9984	-1.0	1.1
Santa Barbara Pyrite 28	2.3	7.82E+03	1.73E+05	25	120	0.999007	24.4	1.7
Santa Barbara Pyrite 29	2.4	7.90E+03	1.75E+05	25	120	0.999007	22.3	1.6
Santa Barbara Pyrite 30	1.0	8.00E+03	1.77E+05	25	120	0.999007	23.2	3.6
Santa Barbara Pyrite 31	2.6	7.81E+03	1.74E+05	25	120	0.999007	20.2	1.7
Santa Barbara Pyrite 32	1.0	7.81E+03	1.72E+05	25	120	0.999007	26.7	4.6
Santa Barbara Pyrite 33	2.5	7.92E+03	1.75E+05	25	120	0.999007	24.0	1.7
Santa Barbara Pyrite 34	3.3	7.64E+03	1.69E+05	25	120	0.999007	23.3	1.4
Santa Barbara Pyrite 35	1.0	9.59E+03	2.12E+05	25	120	0.999007	26.0	3.0
Santa Barbara Pyrite 46	2.1	9.64E+03	2.12E+05	25	120	1.000092	28.6	1.4
Santa Barbara Pyrite 47	3.0	8.24E+03	1.82E+05	25	120	1.000092	23.9	1.0
Santa Barbara Pyrite 48	2.9	8.83E+03	1.95E+05	25	120	1.000092	26.7	1.1
Santa Barbara Pyrite 49	3.5	8.12E+03	1.79E+05	25	120	1.000092	25.1	0.9
Santa Barbara Pyrite 50	5.8	9.56E+03	2.11E+05	25	120	1.000092	26.6	0.5
Santa Barbara Pyrite 51	2.0	9.20E+03	2.03E+05	25	120	1.000092	25.2	1.4
Santa Barbara Pyrite 52	1.1	8.67E+03	1.93E+05	25	120	1.000092	19.6	2.9
Santa Barbara Pyrite 53	1.3	8.78E+03	1.94E+05	25	120	1.000092	24.4	2.2
Santa Barbara Pyrite 36	2.3	1.10E+04	2.42E+05	25	120	1.00118	28.5	1.2
Santa Barbara Pyrite 37	3.1	9.98E+03	2.20E+05	25	120	1.00118	25.0	0.9
Santa Barbara Pyrite 38	4.7	1.03E+04	2.27E+05	25	120	1.00118	23.6	0.6
Santa Barbara Pyrite 39	1.8	1.07E+04	2.38E+05	25	120	1.00118	20.7	1.3
Santa Barbara Pyrite 40	3.3	1.05E+04	2.33E+05	25	120	1.00118	23.5	0.8
Santa Barbara Pyrite 41	1.9	1.00E+04	2.21E+05	25	120	1.00118	23.3	1.4
Santa Barbara Pyrite 42	2.7	1.06E+04	2.35E+05	25	120	1.00118	23.3	1.0
Santa Barbara Pyrite 43	3.7	1.06E+04	2.33E+05	25	120	1.00118	23.7	0.7
Santa Barbara Pyrite 44	1.5	8.79E+03	1.96E+05	25	120	1.00118	16.0	1.8
Santa Barbara Pyrite 45	1.5	9.78E+03	2.18E+05	25	120	1.00118	16.3	1.8
Wards Pyrite 15b	18.0	6.13E+03	1.39E+05	25	60	1.002226	-1.0	1.2
Wards Pyrite 16	45.0	1.15E+04	2.61E+05	50	60	0.998865	-1.0	0.4
Santa Barbara Pyrite 14	6.4	8.82E+03	1.95E+05	50	375	0.998838	26.0	0.5

Santa Barbara Pyrite 15	5.0	9.03E+03	1.99E+05	50	375	0.998838	27.2	0.7
Santa Barbara Pyrite 16	4.5	9.11E+03	2.01E+05	50	375	0.998838	26.4	0.8
Santa Barbara Pyrite 17	4.1	8.23E+03	1.87E+05	50	375	0.998838	-0.1	0.8
Santa Barbara Pyrite 18	1.5	1.01E+04	2.24E+05	50	375	0.998838	22.9	2.0
Santa Barbara Pyrite 19	5.2	7.74E+03	1.74E+05	50	375	0.998838	9.4	0.6
Santa Barbara Pyrite 20	6.4	8.17E+03	1.81E+05	50	375	0.998838	24.7	0.6
Santa Barbara Pyrite 21	2.9	8.48E+03	1.87E+05	50	375	0.998838	26.6	1.1
Santa Barbara Pyrite 22	4.9	8.60E+03	1.92E+05	50	375	0.998838	16.4	0.7
Santa Barbara Pyrite 23	4.0	8.73E+03	1.93E+05	50	375	0.998838	24.9	0.8
Santa Barbara Pyrite 24	4.4	9.94E+03	2.20E+05	50	375	0.998838	24.1	0.7
Santa Barbara Pyrite 25	1.1	9.16E+03	2.03E+05	50	375	0.998838	22.8	2.8
Santa Barbara Pyrite 26	3.3	8.81E+03	1.95E+05	50	375	0.998838	25.7	1.0
Santa Barbara Pyrite 27	2.7	5.86E+03	1.39E+05	50	375	0.998838	-42.7	1.5
Santa Barbara Pyrite 1	6.5	8.36E+03	1.87E+05	50	375	0.998695	14.7	0.5
Santa Barbara Pyrite 2	1.8	7.39E+03	1.65E+05	50	375	0.998695	16.0	2.0
Santa Barbara Pyrite 3	1.8	8.44E+03	1.86E+05	50	375	0.998695	26.9	1.9
Santa Barbara Pyrite 4	3.9	8.49E+03	1.87E+05	50	375	0.998695	28.9	1.4
Santa Barbara Pyrite 5	5.0	9.89E+03	2.19E+05	50	375	0.998695	26.2	1.7
Santa Barbara Pyrite 6	2.6	9.72E+03	2.14E+05	50	375	0.998695	28.3	1.8
Santa Barbara Pyrite 7	1.8	8.69E+03	1.92E+05	50	375	0.998695	28.0	2.4
Santa Barbara Pyrite 8	1.6	1.03E+04	2.28E+05	50	375	0.998695	25.1	2.4
Santa Barbara Pyrite 9	1.0	1.01E+04	2.24E+05	50	375	0.998695	24.0	3.7
Santa Barbara Pyrite 10	2.5	8.76E+03	1.95E+05	50	375	0.998695	20.4	1.7
Santa Barbara Pyrite 11	3.0	9.31E+03	2.07E+05	50	375	0.998695	21.4	1.5
Santa Barbara Pyrite 12	2.3	8.69E+03	1.93E+05	50	375	0.998695	20.2	2.0
Santa Barbara Pyrite 13	4.4	8.69E+03	1.93E+05	50	375	0.998695	22.3	0.9
Wards Pyrite 16b	45.0	1.14E+04	2.58E+05	50	60	0.998554	-1.0	0.5
Wards Pyrite 17	80.0	1.21E+04	2.75E+05	100	20	0.998614	-1.0	0.7
Cismon Pyrite 1	52.5	1.27E+04	3.01E+05	60	60	0.998614	-43.4	0.4
Cismon Pyrite 2	80.0	1.13E+04	2.69E+05	60	120	0.998614	-41.8	0.3
Cismon Pyrite 3	30.0	1.33E+04	3.16E+05	60	120	0.998614	-42.6	0.3
Cismon Marcasite 1	7.0	1.44E+04	3.41E+05	70	480	1.004171	-48.2	1.0
Cismon Marcasite 2	6.6	1.53E+04	3.62E+05	70	480	1.004171	-49.0	0.9
Cismon Marcasite 3	4.1	1.48E+04	3.52E+05	70	480	1.004171	-48.8	1.0
Cismon Marcasite 4	4.6	1.52E+04	3.60E+05	70	480	1.004171	-50.9	1.3
Cismon Marcasite 5	3.7	1.26E+04	2.97E+05	70	480	1.004171	-45.6	1.7

Cismon Marcasite 6	6.0	1.67E+04	3.95E+05	70	480	1.004171	-46.0	0.8
Cismon Marcasite 7	4.2	1.36E+04	3.24E+05	70	480	1.004171	-50.4	1.5
Cismon Marcasite 8	3.0	1.51E+04	3.56E+05	70	480	1.004171	-46.3	1.9
Cismon Marcasite 9	4.7	1.23E+04	2.95E+05	70	480	1.004171	-56.5	1.7
Cismon Marcasite 10	4.6	1.40E+04	3.32E+05	70	480	1.004171	-47.4	1.2
Cismon Marcasite 11	5.8	1.58E+04	3.75E+05	70	480	1.004171	-48.6	1.0
Cismon Marcasite 12	5.0	1.61E+04	3.81E+05	70	480	1.004171	-45.3	1.0
Cismon Marcasite 13	2.7	1.40E+04	3.32E+05	70	480	1.004171	-52.8	1.8
Cismon Marcasite 14	6.2	1.37E+04	3.26E+05	70	480	1.004171	-49.9	1.1
Cismon Pyrite 4	5.3	1.06E+04	2.49E+05	70	480	0.998614	-36.5	1.2
Cismon Marcasite 15	6.2	1.57E+04	3.73E+05	70	480	1.004171	-47.4	0.9
Cismon Marcasite 16	3.0	1.04E+04	2.45E+05	70	480	1.004171	-46.7	2.0
Cismon Marcasite 17	3.2	1.27E+04	3.01E+05	70	480	1.004171	-50.7	1.7
Cismon Marcasite 18	1.8	1.13E+04	2.66E+05	70	480	1.004171	-41.3	3.2
Cismon Marcasite 19	5.1	1.10E+04	2.61E+05	70	480	1.004171	-48.0	1.2
Cismon Marcasite 20	2.2	9.73E+03	2.29E+05	70	480	1.004171	-41.3	3.2
Cismon Marcasite 21	2.8	1.01E+04	2.40E+05	70	480	1.004171	-52.6	2.5
Cismon Marcasite 22	6.5	7.45E+03	1.78E+05	70	480	1.004171	-54.7	1.4
Cismon Marcasite 23	3.7	1.10E+04	2.62E+05	70	480	1.004171	-51.0	1.9
Cismon Marcasite 24	3.6	1.59E+04	3.78E+05	70	480	1.004171	-49.8	1.4
Cismon Marcasite 25	4.2	1.50E+04	3.54E+05	70	480	1.004171	-45.0	1.4
Cismon Marcasite 26	4.4	1.70E+04	4.01E+05	70	480	1.004171	-46.1	1.2
Cismon Marcasite 27	3.9	1.74E+04	4.13E+05	70	480	1.004171	-51.1	1.3
Cismon Marcasite 28	1.7	1.63E+04	3.88E+05	70	480	1.004171	-54.5	2.4
Cismon Marcasite 29	3.4	1.54E+04	3.65E+05	70	480	1.004171	-50.3	1.5
Cismon Marcasite 30	2.3	1.29E+04	3.04E+05	70	480	1.004171	-46.8	2.0
Cismon Marcasite 31	3.7	1.50E+04	3.56E+05	70	480	1.004171	-48.4	1.5
Cismon Marcasite 32	4.7	1.67E+04	3.96E+05	70	480	1.004171	-48.0	1.2
Cismon Marcasite 33	2.3	1.03E+04	2.44E+05	70	480	1.004171	-47.6	2.1
Cismon Marcasite 34	1.5	1.13E+04	2.69E+05	70	480	1.004171	-50.6	2.5
Cismon Marcasite 35	1.7	9.41E+03	2.21E+05	70	480	1.004171	-40.0	2.6
Cismon Marcasite 36	4.1	1.38E+04	3.27E+05	70	480	1.004171	-51.6	1.3
Cismon Marcasite 37	2.4	1.31E+04	3.10E+05	70	480	1.004171	-49.5	2.3
Cismon Marcasite 38	2.2	1.40E+04	3.33E+05	70	480	1.004171	-51.0	1.9
Cismon Marcasite 39	1.9	1.44E+04	3.43E+05	70	480	1.004171	-51.5	2.7
Cismon Marcasite 40	1.4	1.33E+04	3.17E+05	70	480	1.004171	-51.4	4.3

Cismon Marcasite 41	8.6	1.26E+04	2.99E+05	70	480	1.004171	-50.0	0.8
Cismon Marcasite 42	4.2	1.49E+04	3.54E+05	70	480	1.004171	-49.5	1.1
Cismon Marcasite 43	4.4	1.83E+04	4.35E+05	70	480	1.004171	-52.9	0.9
Cismon Marcasite 44	3.1	1.50E+04	3.57E+05	70	480	1.004171	-51.1	1.2
Cismon Marcasite 45	3.6	1.57E+04	3.74E+05	70	480	1.004171	-52.8	1.6
Cismon Marcasite 46	2.3	1.52E+04	3.61E+05	70	480	1.004171	-52.2	1.9
Cismon Marcasite 47	2.5	1.16E+04	2.76E+05	70	480	1.004171	-51.6	2.6
Cismon Marcasite 48	1.9	1.23E+04	2.92E+05	70	480	1.004171	-48.9	2.1
Cismon Marcasite 49	3.4	1.49E+04	3.54E+05	70	480	1.004171	-52.4	1.3
Cismon Marcasite 50	4.2	1.40E+04	3.34E+05	70	480	1.004171	-52.1	1.2
Cismon Marcasite 51	6.0	1.37E+04	3.25E+05	70	480	1.004171	-51.1	0.9
Cismon Marcasite 52	2.5	9.67E+03	2.31E+05	70	480	1.004171	-54.7	2.4
Cismon Marcasite 53	2.3	1.53E+04	3.62E+05	70	480	1.004171	-43.7	2.6
Cismon Marcasite 54	1.3	1.55E+04	3.68E+05	70	480	1.004171	-47.8	2.5
Cismon Marcasite 55	2.7	1.34E+04	3.15E+05	70	480	1.004171	-42.2	2.3
Cismon Marcasite 56	12.1	1.34E+04	3.20E+05	70	480	1.004171	-53.2	0.5
Cismon Marcasite 57	6.4	1.07E+04	2.56E+05	70	480	1.004171	-54.5	1.7
Cismon Marcasite 58	2.3	8.36E+03	1.98E+05	70	480	1.004171	-50.2	2.7
Cismon Marcasite 59	3.7	8.83E+03	2.10E+05	70	480	1.004171	-53.8	2.0
Cismon Marcasite 60	4.5	1.14E+04	2.73E+05	70	480	1.004171	-56.5	1.3
Cismon Marcasite 61	3.6	1.19E+04	2.87E+05	70	480	1.004171	-61.3	1.5
Cismon Marcasite 62	3.2	9.63E+03	2.28E+05	70	480	1.004171	-47.0	1.8
Cismon Marcasite 63	4.0	1.17E+04	2.76E+05	70	480	1.004171	-48.4	1.5
Cismon Marcasite 64	2.8	1.20E+04	2.85E+05	70	480	1.004171	-50.2	2.1
Cismon Marcasite 65	0.9	8.81E+03	2.10E+05	70	480	1.004171	-54.4	2.8
Cismon Marcasite 66	3.1	1.28E+04	3.03E+05	70	480	1.004171	-47.3	1.7
Cismon Marcasite 67	3.2	1.21E+04	2.87E+05	70	480	1.004171	-45.1	1.9
Cismon Marcasite 68	3.4	1.28E+04	3.04E+05	70	480	1.004171	-49.1	1.5
Cismon Marcasite 69	4.3	1.27E+04	3.01E+05	70	480	1.004171	-46.4	1.2
Cismon Marcasite 70	8.1	1.33E+04	3.13E+05	70	480	1.004171	-42.5	0.8
Cismon Marcasite 71	3.6	1.13E+04	2.68E+05	70	480	1.004171	-48.3	1.3
Cismon Marcasite 72	2.3	1.25E+04	2.94E+05	70	480	1.004171	-42.9	2.0
Cismon Marcasite 73	3.0	1.15E+04	2.71E+05	70	480	1.004171	-45.5	2.2
Cismon Marcasite 74	2.6	1.04E+04	2.43E+05	70	480	1.004171	-39.9	2.1
Cismon Marcasite 75	2.5	1.05E+04	2.48E+05	70	480	1.004171	-43.9	2.2
Cismon Marcasite 76	4.4	9.76E+03	2.31E+05	70	480	1.004171	-45.9	1.5

Cismon Pyrite 5	4.5	1.06E+04	2.50E+05	70	480	0.998614	-34.8	1.6
Cismon Pyrite 6	5.9	1.10E+04	2.62E+05	70	480	0.998614	-49.2	1.1
Cismon Pyrite 7	6.8	1.19E+04	2.82E+05	70	480	0.998614	-39.5	1.1
Cismon Pyrite 8	8.0	1.15E+04	2.75E+05	70	480	0.998614	-46.8	0.7
Cismon Marcasite 77	5.3	1.31E+04	3.12E+05	70	480	1.004171	-54.3	1.0
Cismon Pyrite 9	13.0	1.33E+04	3.16E+05	70	480	0.998614	-45.9	0.5
Cismon Pyrite 10	10.2	1.23E+04	2.92E+05	70	480	0.998614	-47.7	0.6
Cismon Pyrite 11	5.7	9.64E+03	2.25E+05	70	480	0.998614	-28.7	1.0
Cismon Pyrite 12	6.9	1.08E+04	2.54E+05	70	480	0.998614	-40.7	0.8
Cismon Pyrite 13	23.2	9.42E+03	2.24E+05	70	480	0.998614	-45.9	0.3
Cismon Pyrite 14	9.2	1.00E+04	2.39E+05	100	960	0.998359	-48.7	0.9
Cismon Pyrite 15	8.9	1.13E+04	2.68E+05	100	960	0.998359	-39.4	0.8
Cismon Pyrite 16	6.4	1.09E+04	2.56E+05	100	960	0.998359	-38.1	1.2
Cismon Pyrite 17	6.4	1.10E+04	2.64E+05	100	960	0.998359	-52.1	1.2
Cismon Pyrite 18	7.2	1.09E+04	2.57E+05	100	960	0.998359	-40.4	0.8
Cismon Pyrite 19	6.8	8.67E+03	2.04E+05	100	960	0.998359	-36.9	1.2
Cismon Pyrite 20	8.9	1.02E+04	2.40E+05	100	960	0.998359	-39.9	0.9
Cismon Pyrite 21	5.0	1.09E+04	2.58E+05	100	960	0.998359	-37.8	1.2
Cismon Pyrite 22	3.5	9.86E+03	2.32E+05	100	960	0.998359	-35.7	1.4
Cismon Pyrite 23	5.1	1.01E+04	2.37E+05	100	960	0.998359	-35.1	1.1
Cismon Pyrite 24	4.5	1.07E+04	2.53E+05	100	960	0.998359	-39.7	1.2
Cismon Pyrite 25	4.1	9.48E+03	2.23E+05	100	960	0.998359	-37.2	1.3
Cismon Pyrite 26	5.0	1.13E+04	2.66E+05	100	960	0.998359	-35.4	1.3
Cismon Pyrite 27	6.5	9.48E+03	2.26E+05	100	960	0.998359	-49.3	1.0
Cismon Pyrite 28	5.5	1.05E+04	2.51E+05	100	960	0.998359	-50.7	1.2
Cismon Pyrite 29	6.0	1.01E+04	2.38E+05	100	960	0.998359	-35.8	1.2
Cismon Pyrite 30	5.9	1.08E+04	2.57E+05	100	960	0.998359	-43.4	1.2
Cismon Pyrite 31	6.1	9.19E+03	2.16E+05	100	960	0.998359	-35.3	1.2
Cismon Pyrite 32	4.6	9.10E+03	2.14E+05	100	960	0.998359	-37.7	1.7
Cismon Pyrite 33	5.6	1.11E+04	2.63E+05	100	960	0.998359	-43.0	1.2
Cismon Pyrite 34	7.7	1.03E+04	2.45E+05	100	960	0.998359	-43.1	1.2
Cismon Pyrite 35	6.0	9.98E+03	2.36E+05	100	960	0.998359	-41.9	1.3
Cismon Pyrite 36	6.7	7.61E+03	1.82E+05	100	960	0.998359	-51.1	1.1
Cismon Pyrite 37	4.8	1.00E+04	2.37E+05	100	960	0.998359	-40.7	1.3
Cismon Pyrite 38	4.2	1.01E+04	2.38E+05	100	960	0.998359	-38.4	1.5
Cismon Pyrite 39	6.6	1.08E+04	2.58E+05	100	960	0.998359	-49.0	1.1

Cismon Pyrite 40	7.4	9.74E+03	2.31E+05	100	960	0.998359	-45.3	0.8
Cismon Pyrite 41	3.7	8.45E+03	2.01E+05	100	960	0.998359	-47.8	1.4
Cismon Pyrite 42	4.6	9.49E+03	2.24E+05	100	960	0.998359	-38.9	1.2
Cismon Pyrite 43	6.8	1.18E+04	2.79E+05	100	960	0.998359	-37.9	1.1
Cismon Pyrite 44	7.2	1.09E+04	2.57E+05	100	960	0.998359	-37.1	1.0
Cismon Pyrite 45	6.4	1.08E+04	2.56E+05	100	960	0.998359	-42.5	0.9
Cismon Pyrite 46	5.8	1.14E+04	2.70E+05	100	960	0.998359	-45.0	1.0
Cismon Pyrite 47	6.4	1.02E+04	2.39E+05	100	960	0.998359	-36.5	1.1
Cismon Pyrite 48	4.6	1.04E+04	2.45E+05	100	960	0.998359	-41.9	1.4
Cismon Pyrite 49	5.9	1.02E+04	2.42E+05	100	960	0.998359	-41.0	1.0
Cismon Pyrite 50	5.3	1.00E+04	2.37E+05	100	960	0.998359	-40.8	1.3
Cismon Marcasite 88	5.5	9.50E+03	2.28E+05	100	960	1.003913	-59.9	1.1
Cismon Marcasite 89	8.2	1.29E+04	3.07E+05	100	960	1.003913	-50.3	0.7
Cismon Marcasite 90	6.4	1.23E+04	2.94E+05	100	960	1.003913	-53.4	0.8
Cismon Marcasite 91	3.6	1.08E+04	2.54E+05	100	960	1.003913	-44.3	1.6
Cismon Marcasite 92	2.3	9.49E+03	2.26E+05	100	960	1.003913	-54.2	1.9
Cismon Marcasite 93	3.0	8.94E+03	2.15E+05	100	960	1.003913	-60.0	2.1
Cismon Marcasite 94	5.0	1.04E+04	2.49E+05	100	960	1.003913	-56.5	1.3
Cismon Marcasite 95	5.3	1.30E+04	3.11E+05	100	960	1.003913	-55.8	1.2
Cismon Pyrite 51	5.1	1.06E+04	2.51E+05	100	960	0.998359	-41.0	1.4
Cismon Marcasite 96	3.7	1.20E+04	2.84E+05	100	960	1.003913	-48.6	1.8
Cismon Marcasite 97	3.0	1.21E+04	2.86E+05	100	960	1.003913	-50.7	1.5
Cismon Marcasite 98	2.4	1.13E+04	2.69E+05	100	960	1.003913	-56.2	1.6
Cismon Marcasite 99	3.9	1.23E+04	2.91E+05	100	960	1.003913	-47.6	1.3
Cismon Marcasite 100	3.4	1.30E+04	3.08E+05	100	960	1.003913	-50.7	1.5
Cismon Marcasite 101	4.2	9.93E+03	2.36E+05	100	960	1.003913	-49.3	1.4
Cismon Marcasite 102	7.3	1.23E+04	2.94E+05	100	960	1.003913	-53.9	1.0
Cismon Marcasite 103	5.0	1.22E+04	2.90E+05	100	960	1.003913	-47.6	2.0
Cismon Marcasite 104	4.9	1.16E+04	2.76E+05	100	960	1.003913	-51.4	1.7
Cismon Marcasite 105	5.9	1.16E+04	2.76E+05	100	960	1.003913	-54.4	1.2
Cismon Marcasite 106	4.3	1.15E+04	2.70E+05	100	960	1.003913	-42.8	1.5
Cismon Marcasite 107	3.5	1.20E+04	2.87E+05	100	960	1.003913	-58.9	1.6
Cismon Marcasite 108	2.9	1.09E+04	2.60E+05	100	960	1.003913	-53.1	2.3
Cismon Marcasite 109	5.6	1.20E+04	2.84E+05	100	960	1.003913	-42.9	1.3
Cismon Marcasite 110	5.5	1.00E+04	2.39E+05	100	960	1.003913	-55.6	1.2
Cismon Marcasite 111	3.7	1.17E+04	2.78E+05	100	960	1.003913	-50.3	1.7

Cismon Marcasite 112	4.8	1.26E+04	3.00E+05	100	960	1.003913	-54.8	1.1
Cismon Marcasite 113	4.0	1.20E+04	2.82E+05	100	960	1.003913	-42.1	1.4
Cismon Marcasite 114	2.4	1.17E+04	2.79E+05	100	960	1.003913	-54.1	1.9
Cismon Marcasite 115	5.2	1.17E+04	2.78E+05	100	960	1.003913	-53.2	1.1
Cismon Marcasite 116	2.9	1.33E+04	3.12E+05	100	960	1.003913	-42.4	1.8
Cismon Marcasite 117	3.8	1.12E+04	2.67E+05	100	960	1.003913	-51.7	1.4
Cismon Marcasite 118	4.9	1.13E+04	2.68E+05	100	960	1.003913	-49.0	1.4
Cismon Marcasite 119	5.1	1.24E+04	2.95E+05	100	960	1.003913	-51.7	1.3
Cismon Marcasite 120	4.6	1.17E+04	2.79E+05	100	960	1.003913	-49.6	1.3
Cismon Marcasite 121	3.3	1.19E+04	2.86E+05	100	960	1.003913	-59.4	1.5
Cismon Marcasite 122	4.6	1.23E+04	2.89E+05	100	960	1.003913	-44.8	1.4
Cismon Marcasite 123	3.7	1.32E+04	3.10E+05	100	960	1.003913	-43.6	1.5
Cismon Marcasite 124	4.6	1.20E+04	2.83E+05	100	960	1.003913	-45.6	1.3
Cismon Marcasite 125	3.3	1.01E+04	2.40E+05	100	960	1.003913	-48.9	1.5
Cismon Marcasite 126	3.4	9.83E+03	2.32E+05	100	960	1.003913	-44.9	2.3
Cismon Marcasite 127	3.5	1.02E+04	2.43E+05	100	960	1.003913	-56.5	1.4
Cismon Marcasite 128	5.3	8.92E+03	2.13E+05	100	960	1.003913	-56.8	1.4
Cismon Marcasite 129	3.7	1.06E+04	2.50E+05	100	960	1.003913	-46.3	2.8
Cismon Marcasite 130	2.1	1.15E+04	2.72E+05	100	960	1.003913	-49.5	2.5
Cismon Marcasite 131	1.5	9.51E+03	2.26E+05	100	960	1.003913	-52.6	3.6
Cismon Marcasite 132	3.4	1.08E+04	2.55E+05	100	960	1.003913	-44.5	1.8
Cismon Marcasite 133	2.5	9.53E+03	2.28E+05	100	960	1.003913	-58.7	1.9
Cismon Marcasite 134	4.7	9.80E+03	2.33E+05	100	960	1.003913	-51.2	1.2
Cismon Marcasite 135	2.6	8.63E+03	2.04E+05	100	960	1.003913	-44.4	1.8
Cismon Marcasite 136	1.8	1.15E+04	2.70E+05	130	700	1.003913	-39.6	2.2
Cismon Marcasite 137	3.0	1.19E+04	2.82E+05	130	700	1.003913	-47.8	1.8
Cismon Marcasite 138	4.3	1.31E+04	3.09E+05	130	700	1.003913	-45.4	1.5
Cismon Marcasite 139	6.5	1.26E+04	2.99E+05	130	700	1.003913	-47.9	1.0
Cismon Marcasite 140	3.2	1.36E+04	3.20E+05	130	700	1.003913	-44.0	1.5
Cismon Pyrite 52	3.9	1.20E+04	2.87E+05	130	700	0.998359	-48.4	1.8
Cismon Marcasite 141	5.8	1.36E+04	3.18E+05	130	700	1.003913	-37.8	1.2
Cismon Marcasite 142	5.2	1.21E+04	2.85E+05	130	700	1.003913	-39.8	1.8
Cismon Marcasite 143	8.2	1.37E+04	3.22E+05	130	700	1.003913	-39.8	1.0
Cismon Marcasite 144	5.8	1.30E+04	3.08E+05	130	700	1.003913	-45.4	1.2
Cismon Marcasite 145	2.6	1.65E+04	3.87E+05	130	700	1.003913	-36.8	2.3
Cismon Marcasite 146	8.2	1.36E+04	3.22E+05	130	700	1.003913	-46.2	0.8

Cismon Marcasite 147	3.1	1.17E+04	2.78E+05	130	700	1.003913	-49.3	2.2
Cismon Marcasite 148	3.7	1.22E+04	2.88E+05	130	700	1.003913	-41.3	1.9
Cismon Marcasite 149	2.4	1.31E+04	3.10E+05	130	700	1.003913	-45.6	2.0
Cismon Marcasite 150	6.1	1.41E+04	3.31E+05	130	700	1.003913	-39.1	1.4
Cismon Marcasite 151	4.1	1.38E+04	3.25E+05	130	700	1.003913	-43.5	1.5
Cismon Marcasite 152	5.0	1.22E+04	2.87E+05	130	700	1.003913	-40.2	1.4
Cismon Marcasite 153	7.7	1.35E+04	3.21E+05	130	700	1.003913	-51.7	1.0
Cismon Marcasite 154	3.1	1.14E+04	2.70E+05	130	700	1.003913	-46.7	1.7
Cismon Marcasite 155	3.6	1.01E+04	2.36E+05	130	700	1.003913	-37.7	2.0
Cismon Marcasite 156	3.3	9.99E+03	2.36E+05	130	700	1.003913	-44.9	2.3
Cismon Marcasite 157	1.8	7.54E+03	1.78E+05	130	700	1.003913	-42.4	3.1
Cismon Marcasite 158	2.4	1.00E+04	2.37E+05	130	700	1.003913	-49.3	2.9
Cismon Pyrite 53	2.9	1.05E+04	2.50E+05	130	700	0.998359	-51.6	2.2
Cismon Pyrite 54	2.7	1.08E+04	2.56E+05	130	700	0.998359	-40.6	1.7
Cismon Marcasite 159	4.5	1.26E+04	2.99E+05	130	700	1.003913	-47.5	1.4
Cismon Marcasite 160	2.1	1.25E+04	2.95E+05	130	700	1.003913	-41.2	1.5
Cismon Marcasite 161	6.5	1.26E+04	3.00E+05	130	700	1.003913	-52.3	0.9
Cismon Marcasite 162	4.3	1.15E+04	2.72E+05	130	700	1.003913	-49.8	1.1
Cismon Marcasite 163	2.8	1.18E+04	2.78E+05	130	700	1.003913	-42.3	1.7
Cismon Marcasite 164	1.6	1.03E+04	2.43E+05	130	700	1.003913	-39.7	2.2
Cismon Marcasite 165	3.9	1.24E+04	2.92E+05	130	700	1.003913	-42.4	1.5
Cismon Marcasite 166	3.4	1.37E+04	3.23E+05	130	700	1.003913	-40.4	1.4
Cismon Marcasite 167	7.2	1.24E+04	2.93E+05	130	700	1.003913	-43.9	0.8
Cismon Marcasite 168	3.9	1.34E+04	3.14E+05	130	700	1.003913	-41.7	1.3
Cismon Marcasite 169	3.5	1.24E+04	2.92E+05	130	700	1.003913	-44.3	1.4
Cismon Marcasite 170	4.0	1.34E+04	3.17E+05	130	700	1.003913	-48.6	2.2
Cismon Marcasite 171	2.7	1.01E+04	2.40E+05	130	700	1.003913	-47.0	2.0
Cismon Pyrite 55	33.0	1.03E+04	2.45E+05	130	700	0.998359	-48.3	0.3
Cismon Pyrite 56	4.1	1.14E+04	2.70E+05	130	700	0.998359	-38.9	1.5
Cismon Pyrite 57	2.9	1.17E+04	2.73E+05	130	700	0.998359	-31.0	2.2
Cismon Pyrite 58	3.0	1.00E+04	2.36E+05	130	700	0.998359	-34.4	2.3
Cismon Pyrite 59	2.6	1.27E+04	2.98E+05	130	700	0.998359	-38.0	1.7
Cismon Pyrite 60	2.4	1.14E+04	2.67E+05	130	700	0.998359	-32.2	2.6
Cismon Pyrite 61	6.7	1.22E+04	2.89E+05	130	700	0.998359	-42.9	1.1
Cismon Pyrite 62	2.7	1.22E+04	2.90E+05	130	700	0.998359	-48.4	1.7
Cismon Pyrite 63	5.0	1.27E+04	2.97E+05	130	700	0.998359	-33.1	1.4

Cismon Pyrite 64	3.9	1.25E+04	2.96E+05	130	700	0.998359	-45.3	1.7
Cismon Pyrite 65	6.0	9.74E+03	2.30E+05	130	700	0.998359	-39.2	1.4
Cismon Pyrite 66	4.4	1.02E+04	2.39E+05	130	700	0.998359	-31.7	1.8
Cismon Pyrite 67	4.7	1.13E+04	2.68E+05	130	700	0.998359	-42.4	2.0
Cismon Pyrite 68	7.9	7.98E+03	1.91E+05	130	700	0.998359	-52.3	1.4
Cismon Pyrite 69	3.4	1.09E+04	2.61E+05	130	700	0.998359	-50.5	2.2
Cismon Pyrite 70	4.2	1.16E+04	2.73E+05	130	700	0.998359	-39.1	1.8
Cismon Pyrite 71	9.1	1.16E+04	2.73E+05	130	700	0.998359	-37.8	0.9
Cismon Pyrite 72	4.0	1.24E+04	2.93E+05	130	700	0.998359	-37.7	1.7
Cismon Pyrite 73	8.2	1.17E+04	2.75E+05	130	700	0.998359	-35.5	0.8
Cismon Pyrite 74	6.0	1.19E+04	2.82E+05	130	700	0.998359	-39.9	1.4
Cismon Pyrite 75	6.6	1.24E+04	2.92E+05	130	700	0.998359	-39.6	1.0
Cismon Pyrite 76	3.5	1.10E+04	2.60E+05	130	700	0.998359	-42.2	1.9
Cismon Pyrite 77	3.9	1.28E+04	3.04E+05	130	700	0.998359	-47.1	1.5
Cismon Pyrite 78	2.9	1.28E+04	3.03E+05	130	700	0.998359	-41.0	2.5
Cismon Pyrite 79	8.0	1.24E+04	2.94E+05	130	700	0.998359	-42.0	1.1
Cismon Pyrite 80	5.8	1.32E+04	3.13E+05	130	700	0.998359	-44.3	1.0
Cismon Pyrite 81	4.7	1.21E+04	2.88E+05	130	700	0.998359	-46.0	1.4
Cismon Pyrite 82	9.4	1.29E+04	3.09E+05	130	700	0.998359	-50.4	0.7
Cismon Pyrite 83	6.0	1.29E+04	3.04E+05	130	700	0.998359	-39.5	1.4
Cismon Pyrite 84	5.8	1.22E+04	2.89E+05	130	700	0.998359	-39.2	1.1
Cismon Pyrite 85	3.5	1.22E+04	2.88E+05	130	700	0.998359	-40.0	1.6
Cismon Pyrite 86	6.4	1.02E+04	2.42E+05	130	700	0.998359	-42.1	1.6
Cismon Pyrite 87	5.4	8.95E+03	2.13E+05	130	700	0.998359	-47.4	1.7
Cismon Pyrite 88	5.5	1.22E+04	2.88E+05	130	700	0.998359	-41.7	1.2
Cismon Pyrite 89	5.0	1.23E+04	2.91E+05	130	700	0.998359	-40.3	1.3
Cismon Pyrite 90	4.7	1.18E+04	2.78E+05	130	700	0.998359	-35.9	1.6
Cismon Pyrite 91	5.7	1.34E+04	3.17E+05	130	700	0.998359	-41.1	1.4
Cismon Pyrite 92	4.3	1.15E+04	2.71E+05	130	700	0.998359	-40.5	1.7
Cismon Pyrite 93	10.2	1.21E+04	2.87E+05	130	700	0.998359	-39.7	0.7
Cismon Pyrite 94	5.8	9.96E+03	2.38E+05	130	700	0.998359	-51.5	1.5
Cismon Pyrite 95	10.4	1.01E+04	2.38E+05	130	700	0.998359	-43.3	0.9
Cismon Pyrite 96	5.2	8.98E+03	2.14E+05	130	700	0.998359	-47.0	1.8
Cismon Pyrite 97	7.3	1.14E+04	2.70E+05	130	700	0.998359	-45.5	1.0
Cismon Pyrite 98	18.2	1.25E+04	2.97E+05	130	700	0.998359	-44.6	0.4
Cismon Pyrite 99	7.9	1.15E+04	2.74E+05	130	700	0.998359	-45.9	1.2

Cismon Pyrite 100	5.5	9.04E+03	2.16E+05	130	700	0.998359	-50.0	2.2
Cismon Pyrite 101	3.7	9.05E+03	2.15E+05	130	700	0.998359	-44.4	2.2
Cismon Pyrite 102	6.4	7.39E+03	1.75E+05	130	700	0.998359	-43.2	1.3
Cismon Pyrite 103	3.3	8.38E+03	1.98E+05	130	700	0.998359	-40.4	3.0
Cismon Pyrite 104	6.7	1.10E+04	2.62E+05	130	700	0.998359	-46.8	1.2
Cismon Pyrite 105	5.2	1.23E+04	2.91E+05	130	700	0.998359	-45.2	1.9
Cismon Pyrite 106	5.8	1.14E+04	2.72E+05	130	700	0.998359	-47.8	1.4
Cismon Pyrite 107	4.3	9.61E+03	2.26E+05	130	700	0.998359	-36.2	1.8
Cismon Pyrite 108	5.5	1.32E+04	3.13E+05	130	700	0.998359	-40.3	1.4
Cismon Pyrite 109	3.1	9.97E+03	2.38E+05	130	700	0.998359	-50.0	2.3
Cismon Pyrite 110	4.0	9.82E+03	2.32E+05	130	700	0.998359	-38.8	1.8
Cismon Pyrite 111	6.9	1.24E+04	2.93E+05	130	700	0.998359	-37.6	1.0
Cismon Pyrite 112	4.2	1.29E+04	3.07E+05	130	700	0.998359	-45.9	1.4
Cismon Pyrite 113	6.0	1.19E+04	2.79E+05	130	700	0.998359	-35.6	1.2
Wards Pyrite 17b	80.0	1.08E+04	2.45E+05	100	20	0.998359	-1.0	0.9
Wards Marcasite 26	23	1.60E+04	3.62E+05	20	30	0.997025	4.6	0.5
Wards Pyrite 18	17.6	1.80E+04	4.06E+05	20	30	1.002329	-1.0	0.7
Demerara Pyrite 1	2.4	1.31E+04	2.92E+05	20	60	1.002117	18.9	2.0
Demerara Marcasite 1	2	1.27E+04	2.98E+05	20	60	0.996982	-30.1	3.1
Demerara Pyrite 2	2	1.76E+04	4.11E+05	20	60	1.001933	-30.1	2.5
Demerara Pyrite 3	6.4	1.49E+04	3.48E+05	20	60	1.001933	-32.1	0.8
Demerara Pyrite 4	5.2	1.35E+04	3.15E+05	20	60	1.001749	-32.4	1.0
Demerara Marcasite 2	2.4	1.70E+04	3.98E+05	20	60	0.996869	-30.3	1.7
Demerara Marcasite 3	1.6	1.67E+04	3.89E+05	20	60	0.996832	-24.9	1.8
Demerara Marcasite 4	0.8	1.06E+04	2.49E+05	20	60	0.996832	-33.9	6.6
Wards Marcasite 26b	23	1.62E+04	3.67E+05	20	30	0.996424	4.6	0.6
Wards Pyrite 18b	17.6	1.84E+04	4.17E+05	20	30	0.999382	-1.0	0.4
Wards Marcasite 26c	23	1.87E+04	4.24E+05	20	30	0.995855	4.6	0.5
Wards Pyrite 18c	17.6	2.14E+04	4.86E+05	20	30	0.99928	-1.0	0.6
Demerara Pyrite 5	6	1.65E+04	3.88E+05	20	60	0.999211	-36.3	1.2
Demerara Pyrite 6	4.8	1.46E+04	3.41E+05	20	60	0.999152	-30.6	1.0
Demerara Pyrite 7	2.4	1.32E+04	2.96E+05	20	60	0.999092	8.8	1.6
Demerara Pyrite 8	0.8	8.56E+03	1.99E+05	20	60	0.999092	-23.1	4.1
Demerara Marcasite 5	2.4	1.71E+04	4.03E+05	20	60	0.9955	-31.0	1.9
Demerara Pyrite 9	2.4	1.67E+04	3.80E+05	20	60	0.998973	-6.8	2.1
Demerara Marcasite 6	2.4	1.60E+04	3.74E+05	20	60	0.995328	-24.6	2.0

Demerara Pyrite 10	2.8	1.48E+04	3.46E+05	20	60	0.998854	-29.7	1.3
Demerara Pyrite 11	1	1.51E+04	3.50E+05	20	60	0.998795	-23.1	2.6
Demerara Pyrite 12	1.6	1.69E+04	3.94E+05	20	60	0.998795	-29.3	2.1
Demerara Pyrite 13	4	1.36E+04	3.15E+05	20	60	0.998795	-21.1	1.3
Demerara Pyrite 14	7.2	1.60E+04	3.69E+05	20	60	0.998259	-18.4	0.5
Demerara Pyrite 15	3.2	1.51E+04	3.54E+05	20	60	0.9982	-29.4	1.6
Wards Marcasite 26d	23	1.85E+04	4.19E+05	20	30	0.994223	4.6	0.5
Wards Pyrite 18d	17.6	2.13E+04	4.83E+05	20	30	0.998145	-1.0	0.5
Wards Marcasite 26e	23	1.86E+04	4.22E+05	20	30	0.994282	4.6	0.5
Wards Pyrite 18e	17.6	2.11E+04	4.79E+05	20	30	0.998445	-1.0	0.4
Demerara Pyrite 16	2.4	1.47E+04	3.45E+05	20	60	0.998306	-29.5	1.6
Demerara Pyrite 17	2.4	1.64E+04	3.82E+05	20	60	0.998186	-26.6	1.4
Demerara Pyrite 18	3.2	1.61E+04	3.80E+05	20	60	0.998186	-36.6	1.5
Demerara Pyrite 19	0.8	1.42E+04	3.26E+05	20	60	0.998186	-10.2	4.8
Demerara Pyrite 20	4.4	1.46E+04	3.39E+05	20	60	0.998066	-25.0	0.8
Demerara Pyrite 21	6.4	1.62E+04	3.75E+05	20	60	0.997947	-19.2	0.7
Demerara Marcasite 7	1.6	1.63E+04	3.81E+05	20	60	0.993999	-22.6	2.2
Demerara Marcasite 8	2.4	1.43E+04	3.33E+05	20	60	0.993944	-22.4	1.8
Demerara Pyrite 22	1.6	1.35E+04	3.12E+05	20	60	0.997707	-17.4	2.4
Demerara Marcasite 9	2	1.65E+04	3.82E+05	20	60	0.993889	-15.3	1.6
Demerara Pyrite 23	1.2	1.54E+04	3.61E+05	20	60	0.997587	-33.1	2.8
Demerara Pyrite 24	2.4	1.15E+04	2.70E+05	20	60	0.997467	-32.6	2.0
Wards Marcasite 26f	23	1.77E+04	4.01E+05	20	30	0.993343	4.6	0.5
Wards Pyrite 18f	17.6	2.02E+04	4.60E+05	20	30	0.9964	-1.0	0.5
Wards Marcasite 26g	23	1.47E+04	3.33E+05	20	30	0.994393	4.6	0.7
Wards Pyrite 18g	17.6	1.65E+04	3.76E+05	20	30	0.997258	-1.0	0.6
Demerara Pyrite 25	1.2	1.53E+04	3.59E+05	20	60	0.997301	-33.9	2.2
Demerara Marcasite 10	1.6	1.41E+04	3.31E+05	20	60	0.994316	-26.0	2.3
Demerara Pyrite 26	4.8	1.14E+04	2.69E+05	20	60	0.997328	-34.2	1.0
Demerara Marcasite 11	6.4	1.18E+04	2.74E+05	20	60	0.994269	-20.5	1.1
Demerara Marcasite 12	2	1.26E+04	2.96E+05	20	60	0.994269	-30.5	2.2
Demerara Pyrite 27	2	1.40E+04	3.26E+05	20	60	0.997354	-23.7	1.9
Demerara Pyrite 28	5.6	1.18E+04	2.72E+05	20	60	0.99738	-18.1	1.0
Demerara Pyrite 29	4	1.30E+04	3.02E+05	20	60	0.997407	-23.6	1.2
Demerara Pyrite 30	0.48	1.12E+04	2.66E+05	20	60	0.997407	-38.6	8.4
Demerara Pyrite 31	0.64	1.10E+04	2.54E+05	20	60	0.997407	-18.3	6.9

Demerara Pyrite 32	0.48	8.41E+03	1.96E+05	20	60	0.997407	-26.1	8.7
Demerara Marcasite 13	2	1.25E+04	2.92E+05	20	60	0.994081	-24.8	1.9
Demerara Marcasite 14	2	1.73E+04	4.05E+05	20	60	0.994033	-29.2	2.0
Demerara Pyrite 33	4.4	1.32E+04	3.11E+05	20	60	0.997486	-36.3	0.9
Demerara Marcasite 15	2.4	1.40E+04	3.29E+05	20	60	0.993986	-30.3	1.7
Demerara Pyrite 34	4	6.05E+03	1.42E+05	20	60	0.997486	-29.3	2.4
Demerara Marcasite 16	2.4	1.48E+04	3.49E+05	20	60	0.993939	-31.0	1.7
Demerara Pyrite 35	5.6	1.20E+04	2.79E+05	20	60	0.997539	-22.7	0.8
Demerara Pyrite 36	2	1.33E+04	3.12E+05	20	60	0.997566	-34.7	2.0
Demerara Pyrite 37	1.2	1.38E+04	3.23E+05	20	60	0.997566	-29.9	3.1
Demerara Pyrite 38	6	1.19E+04	2.80E+05	20	60	0.997592	-33.3	0.8
Demerara Pyrite 39	8.8	1.21E+04	2.81E+05	20	60	0.997619	-23.7	0.9
Demerara Pyrite 40	9.2	1.19E+04	2.78E+05	20	60	0.997645	-28.5	0.7
Demerara Marcasite 17	2.4	1.31E+04	3.08E+05	20	60	0.993656	-31.9	1.9
Demerara Pyrite 41	4.4	1.17E+04	2.71E+05	20	60	0.997698	-25.4	1.2
Demerara Pyrite 42	1.2	1.25E+04	2.96E+05	20	60	0.997698	-37.4	3.7
Wards Marcasite 26h	23	1.37E+04	3.10E+05	20	30	0.993424	4.6	0.5
Wards Pyrite 18h	17.6	1.56E+04	3.54E+05	20	30	0.997802	-1.0	0.6
Demerara Pyrite 43	58.5	1.56E+04	3.61E+05	80	960	1.000064	-19.0	0.1
Wards Pyrite 19	28	1.58E+04	3.59E+05	80	60	1.000064	-1.0	0.6
Wards Marcasite 27	60	1.38E+04	3.11E+05	50	45	0.998931	4.6	0.3
Demerara Marcasite 18	46.5	1.45E+04	3.38E+05	50	90	0.997372	-27.6	0.4
Wards Marcasite 27b	60	1.60E+04	3.63E+05	50	45	0.995132	4.6	0.3
Wards Marcasite 26i	23	1.44E+04	3.28E+05	25	30	0.987262	4.6	0.4
Wards Pyrite 18i	17.6	1.56E+04	3.57E+05	25	30	0.993831	-1.0	0.8
Demerara Pyrite 44	19.5	1.16E+04	2.72E+05	25	90	0.993565	-26.6	0.4
Demerara Pyrite 45	3	1.23E+04	2.84E+05	25	90	0.993565	-13.2	1.0
Demerara Marcasite 19	17	1.25E+04	2.90E+05	25	90	0.986891	-9.7	0.3
Wards Marcasite 26j	23	1.30E+04	2.97E+05	25	30	0.986642	4.6	0.4
Wards Pyrite 18j	17.6	1.50E+04	3.42E+05	25	30	0.992685	-1.0	0.9

Chapter 4: Deconvolving microbial and environmental controls on marine sedimentary pyrite sulfur isotope ratios

R. N. Bryant[1], C. Jones[1], V. Pasquier[2], I. Halevy[2], D. A. Fike[1]

[1]Department of Earth & Planetary Sciences, Washington University in Saint Louis, USA.

[2]Department of Earth & Planetary Sciences, Weizmann Institute of Science, Israel.

Abstract

Reconstructions of past environmental conditions and biological activity are often based on stable isotope proxies whose interpretations are inherently non-unique. This is particularly true of the sulfur isotopic composition of sedimentary pyrite ($\delta^{34}S_{pyr}$), which is used to reconstruct ocean-atmosphere oxidation state and track the evolution of several microbial metabolic pathways. We present a novel microanalytical approach to deconvolve the multiple signals that influence $\delta^{34}S_{pyr}$, yielding both the unambiguous determination of biological fractionation and novel information about depositional conditions. We apply this approach to recent glacial-interglacial sediments, which feature >70‰ variations in $\delta^{34}S_{pyr}$ across these environmental transitions. Despite profound environmental change, the biological fractionation (ε_{mic}) remained essentially invariant throughout this interval and the observed range in $\delta^{34}S$ was instead driven by climate-induced variations in sedimentation rate.

4.1 Main Text

The sedimentary pyrite sulfur isotope record ($\delta^{34}S_{pyr}$) is a robust archive of past biogeochemical cycling, yet considerable uncertainty remains about how to interpret these signatures, which reflect a complex mixture of biological and environmental forcings and can be impacted by multiple stages of mineral precipitation. Previously, stratigraphic variations in $\delta^{34}S_{pyr}$ have been interpreted to reflect changes in the global biogeochemical sulfur cycle, such as changes in the sulfur isotope signature of marine sulfate ($\delta^{34}S_{SWsulfate}$) (Adams et al., 2010; Gill et al., 2011; Gomes et al., 2016), or the operation of specific microbial pathways (e.g., sulfate reduction, disproportionation, or sulfide oxidation) (Canfield and Teske, 1996; Fike et al., 2006; Parnell et al., 2010). However, recent work has focused on the potential impact that local environmental

conditions might have in modulating the $\delta^{34}S$ signature that is ultimately preserved in sedimentary pyrites (Aller et al., 2010; Claypool, 2004; Fike et al., 2015; Pasquier et al., 2017).

The importance of depositional conditions was highlighted recently with the identification of large-amplitude (>70‰) stratigraphic fluctuations in $\delta^{34}S_{pyr}$ correlating with ~100,000 year Pleistocene glacial-interglacial cycles in the PRGL1-4 core, Gulf of Lion, France (Pasquier et al., 2017) (Figure 4.1A).

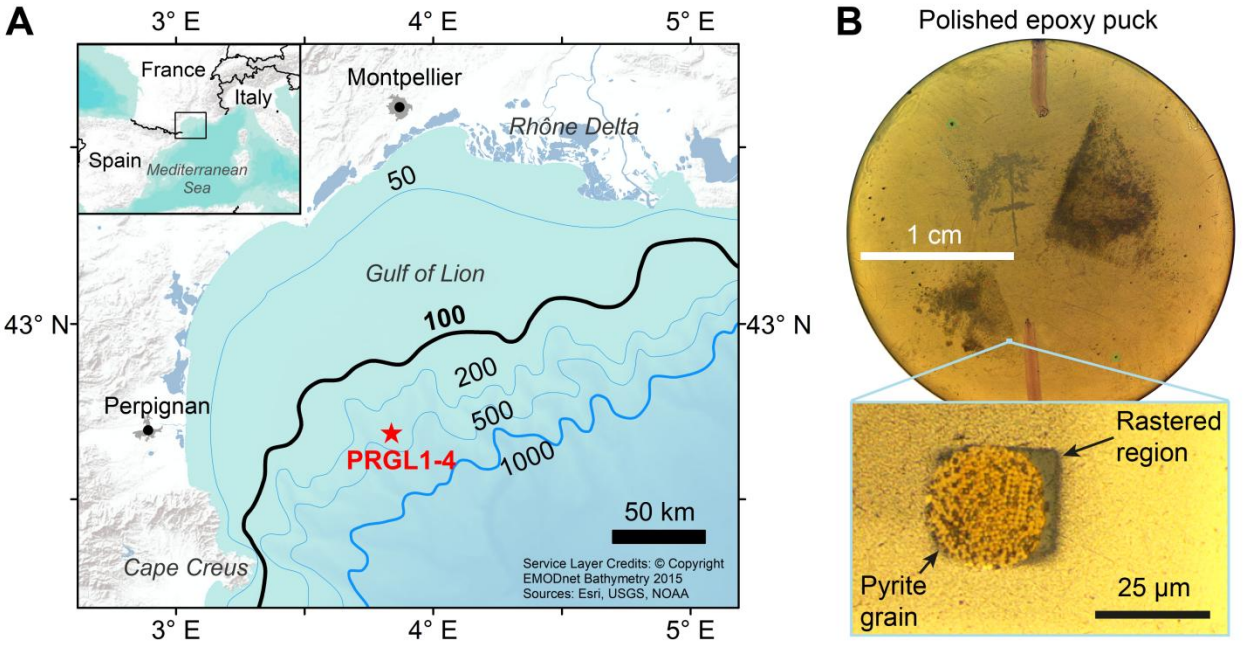

Figure 4.1. Study site map and example of mounted sedimentary pyrite. (A) Location of core PRGL1-4 (red star) in the Gulf of Lion, Northwest Mediterranean. The thick black line marks the approximate location of the coastline during the last glacial maximum. Inset shows the position of the Gulf of Lion in Southern Europe. (B) Photomicrograph of Gulf of Lion sediment pyrite extracts mounted in a 2.5-cm diameter epoxy puck and polished. Inset shows a close-up of an epoxy-mounted pyrite grain after rastering during SIMS scanning ion imaging.

Due to the long (13 million year) residence time of sulfate in the ocean (Berner, 2001), such rapid, large fluctuations in $\delta^{34}S_{pyr}$ could not reflect changes in $\delta^{34}S_{SWsulfate}$. Instead, glacial increases in $\delta^{34}S_{pyr}$ with respect to interglacials were hypothesized to have resulted from changes in either biological or environmental forcings. Potential biological drivers for increased $\delta^{34}S_{pyr}$

include increases in the cell-specific sulfate reduction rate (csSRR) or decreases in the presence of microbial disproportionation, causing a decrease in the fractionation (ε_{mic}) between marine sulfate and microbially produced sulfide (Bradley et al., 2016; Leavitt et al., 2013; Parnell et al., 2010; Sim et al., 2011b, 2011a). Alternatively, increased sedimentation could decrease pore water 'openness', the degree to which sulfate consumed by sulfate-reducing microbes in sediment pore waters is replenished by diffusion from the overlying water column (Claypool, 2004). In other words, the $\delta^{34}S_{pyr}$ signal could arise from two broad classes of explanations, relying on inherent changes to the microbial community structure or metabolic activity, or externally forced changes in ambient environmental parameters. The former could be driven by changing organic carbon and nutrient availability between glacial/interglacial environments; the latter, by changes in sedimentation associated with varying riverine flux of sediments driven by glacioeustatic sea level changes. In general, both types of information (biological and environmental) are of extreme interest to those trying to reconstruct past changes in Earth's surface environment. To complicate matters, increased sedimentation can drive changes in organic carbon and nutrients reaching the zones of sulfate reduction (Canfield, 1991; Toth and Lerman, 1977), where the resulting increases in net sulfate reduction would further decrease the diffusive communication between water column and sediment pore waters. Perhaps unsurprisingly then, it has not yet been possible to distinguish between these fundamentally different (microbiological vs. environmental) classes of explanations in driving the observed variation in the bulk sedimentary $\delta^{34}S_{pyr}$ record from the Gulf of Lion (Pasquier et al., 2017), or indeed other similar records from throughout Earth history (Jones and Fike, 2013; Parnell et al., 2010).

Here, we demonstrate a novel approach to deconvolve the multiple ecological and environmental components that contribute to the aggregate $\delta^{34}S_{pyr}$ signature. Specifically, we use secondary ion mass spectrometry (SIMS) scanning ion imaging (Bryant et al., 2019; Jones et al., 2018) to analyze the sulfur isotope composition of numerous individual pyrite grains (Figure 4.1B) separated from a single sediment sample (see supplementary materials). Optical microscopy is used to confirm the absence of multiple generations of pyrite within individual grains prior to SIMS isotopic analysis (Figure 4.1B). This method was applied to five samples that span the large-amplitude stratigraphic fluctuations in $\delta^{34}S_{pyr}$ observed across one cycle of glacial retreat and subsequent advance (147 to 65.3 ka) in the Gulf of Lion (Pasquier et al., 2017). As pyrites grow within the sediments, they continue to sample the evolving pore water hydrogen sulfide pool and reflect its evolving isotopic composition (Bryant et al., 2019; Fike et al., 2015; Shawar et al., 2018). A time series of pore water sulfide $\delta^{34}S$ through the sediment burial process (Figure 4.2A) is therefore expected to be recorded in the population of pyrites in a given sample (Figure 4.2B) (Bryant et al., 2019). In this case, the minimum $\delta^{34}S_{pyr}$ value in a sample would reflect ε_{mic}, and the overall spread of $\delta^{34}S_{pyr}$ to higher values would reflect the degree of closed-system evolution of pore water sulfide during pyrite formation. As such, this approach can yield novel biological and environmental information that can aid interpretation of bulk isotopic data.

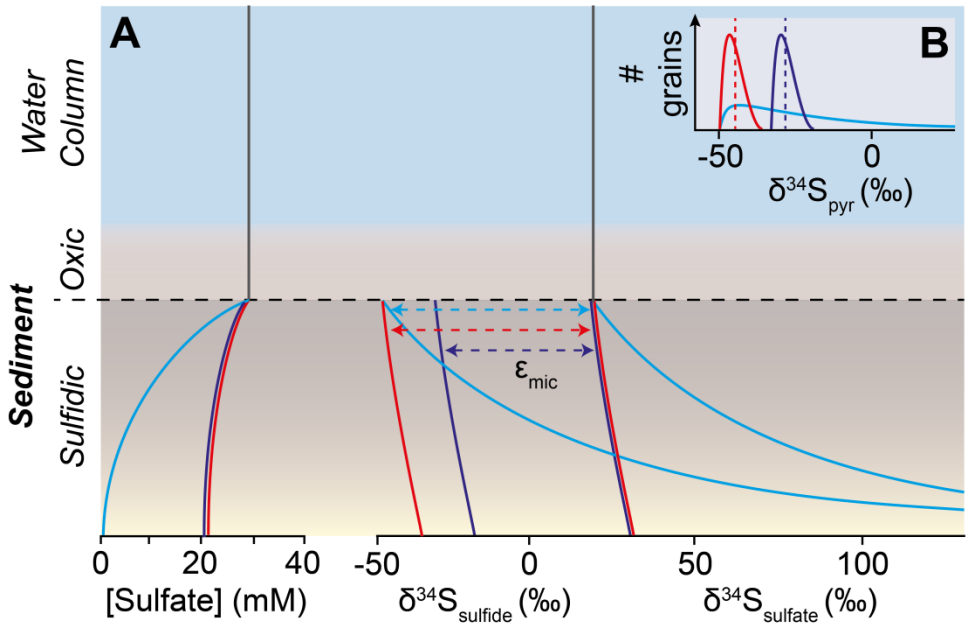

Figure 4.2. Schematic explanations for bulk $\delta^{34}S_{pyr}$ oscillations in PRGL1-4. (A) The evolution of sulfate concentration, and sulfide and sulfate $\delta^{34}S$ below the chemocline, and (B) corresponding $\delta^{34}S_{pyr}$ distributions (solid) and bulk values (dashed). Departure from the expected interglacial scenario, with large ε_{mic} and relatively open-system pore water evolution (red), may be due to *i*) no change in ε_{mic} and more closed-system pore water evolution (light blue), or *ii*) smaller ε_{mic} and relatively open-system pore water evolution (purple).

Ranges in grain-specific $\delta^{34}S_{pyr}$ data (Figure 4.3A and Table S4.1) overlap with corresponding bulk values in all cases. The minima of the five sampled intervals all fall between −55.0±1.1 and −45.7±1.4‰, whereas the overall and inter-quartile ranges are larger for samples with higher bulk values. Glacial pyrites display a weak negative correlation between apparent grain size and $\delta^{34}S_{pyr}$ values (n=76, p-value = 0.072; Figure S4.1), whereas there is no significant correlation for interglacial pyrites (n=39, p-value = 0.487; Figure S4.1). In general, the median values from the grain specific analyses track bulk values for the same samples. There is minimal offset between these in interglacial samples, but some discrepancy exists for the glacial samples (Figure 4.3A). This discrepancy may arise from the wide range of $\delta^{34}S_{pyr}$ values in individual grains for these samples (Figure 4.3, A and B), from the necessarily incomplete sampling of individual microanalyzed grains, and the challenges of this method for measuring grains smaller

than ~1 μm (Bryant et al., 2019), which based on the correlation between apparent grain size and $\delta^{34}S$ (Figure S4.1) are expected to be enriched in ^{34}S relative to the larger grains. For all samples, intra-grain isotopic heterogeneity typically did not exceed 2‰, and had no consistent directionality (Figure S4.2).

Assuming a constant water column $\delta^{34}S_{sulfate}$ value of 20.6‰ over the time interval studied (Böttcher et al., 1998), grain-specific $\delta^{34}S_{pyr}$ minima suggest that ε_{mic}, a function of csSRR (Bradley et al., 2016; Leavitt et al., 2013; Sim et al., 2011b, 2011a), was nearly invariant (<10‰ variation, while bulk values changed by ~47‰), and centered around values of ~70‰ between 147 and 65.3 ka (Figure 4.3A). This calculated ε_{mic} approaches the expected equilibrium fractionation between sulfate and hydrogen sulfide (Eldridge et al., 2016) and indicates that, despite the profound environmental changes across glacial-interglacial regimes, there was no detectable change in the activity of sulfate-reducing microbes. As such, the observed large temporal changes in bulk $\delta^{34}S_{pyr}$ in this time interval (~47‰) (Pasquier et al., 2017) were not driven by changes in biological activity and instead reflect other environmental changes. The large inter-grain $\delta^{34}S$ variability we observed in glacial pyrite populations (Figure 4.3, A and B) provides evidence that these environmental changes modulated the communication between sedimentary pore waters and the overlying water column (Bryant et al., 2019). Specifically, these results indicate decreased diffusive communication of sediment pore waters with the overlying water column in response to basin-scale marine regression during glacial times. The basinward movement of the coastline resulted in an increased sedimentation rate at the site (Pasquier et al., 2017), due in part to the greater export of terrigenous detrital material (Frigola et al., 2012). Rapid sedimentation would have more effectively isolated pore waters from ready communication with the water column, decreasing the diffusive flux of sulfate from water

column to pore waters relative to the net rate of sulfate reduction (Claypool, 2004). The result of such a scenario would be a strong enrichment in ^{34}S of pore water sulfate and sulfide with depth in the sediment column (Figure 4.2A) (Jorgensen, 1979), which under continued pyrite formation would have produced the tail of positive $\delta^{34}S_{pyr}$ values observed in glacial samples (Figure 4.3, A and B, and Figure S4.1).

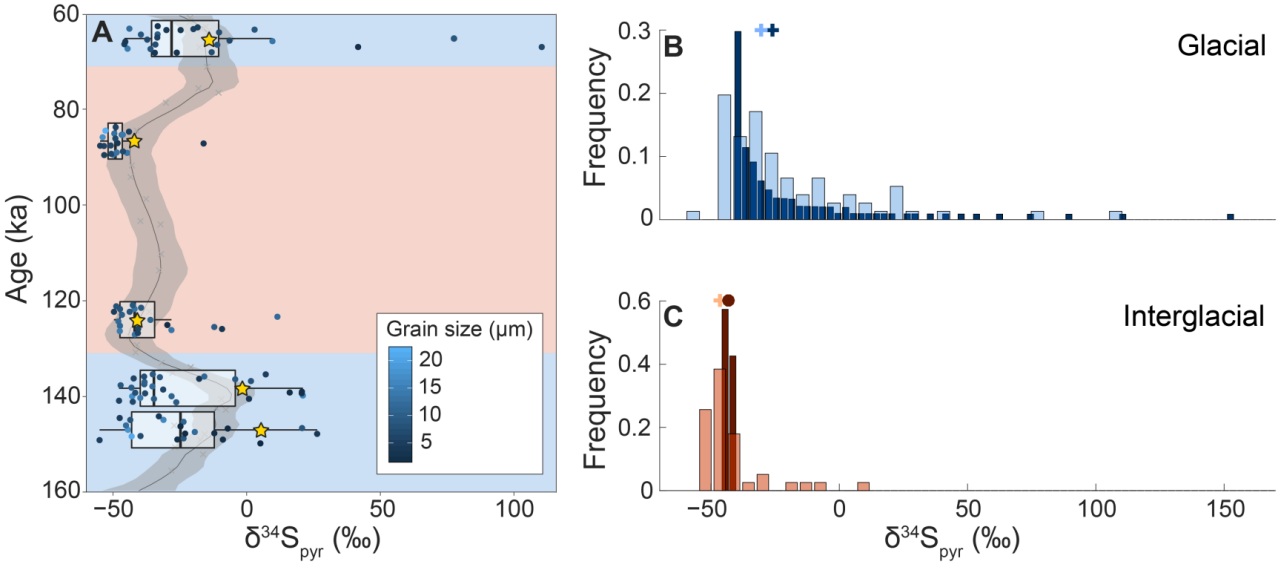

Figure 4.3. SIMS $\delta^{34}S_{pyr}$ data for samples from PRGL1-4. (A) Box and whisker plots of SIMS $\delta^{34}S_{pyr}$ values plotted against sample age. Individual data are colored by grain size and jittered for clarity. All bulk $\delta^{34}S_{pyr}$ data (Pasquier et al., 2017), and those corresponding to the samples used in this study, shown as gray × symbols and gold stars, respectively. The gray region is the 95% confidence interval of a smoothed loess function through all bulk data. (B) Histograms of the glacial SIMS and model (Halevy et al., n.d.) $\delta^{34}S_{pyr}$ values (light and dark blue, respectively). Measured and modeled median $\delta^{34}S_{pyr}$ values are shown as + symbols. (C) Histograms of the interglacial SIMS and model $\delta^{34}S_{pyr}$ values (light and dark red, respectively). The measured median and modeled average $\delta^{34}S_{pyr}$ value are shown as + symbol and a circle, respectively.

A biologically informed diagenetic model (Halevy et al., n.d.) run under depositional conditions (i.e., sedimentation rate; porosity; bottom water oxygen concentration; organic carbon and reactive iron mass fractions; Table S4.2) inferred to be present during the deposition of the different samples (Pasquier et al., 2017) produces pyrite histograms that agree with the corresponding $\delta^{34}S_{pyr}$ results presented here (Figure 4.3, B and C). The model demonstrates that

higher glacial sedimentation rates, independently constrained in core PRGL1-4 (Pasquier et al., 2017), are enough to drive the change observed in the $\delta^{34}S_{pyr}$ distributions. Thus, our interpretation of the results is consistent with the current understanding of the controls on isotopic fractionation during sulfate reduction (Bradley et al., 2016; Leavitt et al., 2013; Sim et al., 2011b, 2011a), controls of system openness on pore water sulfide isotopic evolution (Claypool, 2004; Fike et al., 2015), and the kinetics of authigenic pyrite formation (Rickard and Luther, 1997; Rickard, 1975). Importantly, application of the diagenetic model to a variety of ancient and modern environments suggests that the mechanisms governing glacial-interglacial variation in $\delta^{34}S_{pyr}$ values in the Gulf of Lion sediments explain much of the observed $\delta^{34}S_{pyr}$ range globally (Halevy et al., n.d.).

This grain-specific approach demonstrates that pyrite is a sensitive recorder of the early diagenetic evolution of pore water sulfide in marine sediments, as has recently been suggested (Bryant et al., 2019). That the magnitude of inter-grain isotopic variability in modern marine sedimentary pyrite populations can be so large (Figure 4.3, A and B) and the magnitude of intra-grain isotopic variability so small (Figure S4.2) is a testament to the nature of framboidal pyrite formation in such environments. It has long been suggested that the uniformity of microcrystal size and morphology in a framboid reflects an initial rapid burst of nucleation, followed by a short duration of diffusion-controlled growth (LaMer, 1952). For the first time, high-precision isotopic evidence unambiguously supports this hypothesis. The large inter-grain and minimal intra-grain isotopic variability observed in glacial samples requires that growth of framboids initiated over a range of depths, and occurred only for short durations for each grain. In each case, growth may have been terminated by local reactant diffusion limitation, exacerbated by decreasing local permeability associated with authigenesis. Although we observed limited intra-

grain $\delta^{34}S_{pyr}$ variability here (Figure S4.2), the approach used is also ideal for samples characterized by both inter- and intra-grain variability (Bryant et al., 2019), wherein the combination of both types of variability would reveal the full extent of closed-system pore water evolution and the relative growth durations of individual pyrites.

The potential applications of this approach are numerous. In sediments formed beneath oxic water columns with a high temporal resolution relative to the residence time of sulfate in the ocean, the grain-specific $\delta^{34}S_{pyr}$ minimum provides an estimate of ε_{mic}, and the range indicates the extent of closed-system pore water distillation. In the rock record, if coupled with $\delta^{34}S_{SWsulfate}$ data from barite, carbonate-associated sulfate, or evaporites (Canfield, 2001; Fike et al., 2015; Paytan, 2004), grain-specific $\delta^{34}S_{pyr}$ data could be used to reconstruct ancient ε_{mic} without the issues plaguing current approaches (Fike et al., 2015). This approach could also be used to test previous interpretations of $\delta^{34}S_{pyr}$ records (e.g., about pulses of global pyrite burial or evolving seawater sulfate reservoirs), especially when made in the absence of time-equivalent $\delta^{34}S_{SWsulfate}$ data (Gorjan et al., 2012; Jones and Fike, 2013; Parnell et al., 2010; Zhang et al., 2009). In sum, this approach enables time- and locale-specific metabolic and depositional information to be readily obtained from sedimentary samples, providing scope for reassessing interpretations of the extensive but previously inscrutable bulk $\delta^{34}S_{pyr}$ record.

Acknowledgments

We thank George Claypool, Jill Pasteris, the members of the Fike, Bradley, Catalano and Konecky Labs at Washington University in St. Louis, and the Halevy Lab at the Weizmann Institute of Science for their constant helpful discussions over the past several years. RNB was generously supported by a McDonnell Center for the Space Sciences Graduate Fellowship. This work was enabled by DOE/BER (#DE-SC0014613) and NSF/EAR (#1229370), and a Packard Fellowship to DAF. IH acknowledges a European Research Council Starting Grant (#337183). The drilling operation was conducted within the European project PROMESS 1 (contract EVR1-CT-2002-40024).

Supplementary Materials

Materials and Methods

Materials

Five modern (Pleistocene-Holocene age) sediment samples from core PRGL1-4 in the Gulf of Lion, NW Mediterranean basin (water depth of 298 meters) were used for this study. These samples span marine isotope stages 6 to 4 (i.e., one cycle of glacial retreat and subsequent glacial advance), and were chosen to reflect the large range in bulk $\delta^{34}S_{pyr}$ between the marine isotope stages reported previously (Pasquier et al., 2017). Sample names and ages, in 10^3 years before present (ka), are as follows: p119 (147 ka), p103 (138.3 ka), p90 (124 ka), p82 (86.7 ka), and p74 (65.3 ka).

Following Bryant et al. (2019), fragments of Washington University in St. Louis SIMS Lab's in-house pyrite were used as an internal sulfur isotope standard for SIMS measurements. The in-house pyrite is a single large (~2cm-diameter) hydrothermal euhedral pyrite crystal obtained from Ward's Science (Rochester, NY), sourced from the San Jose de Huanzala Mine, Peru. This material has a bulk $\delta^{34}S$ value of-1.0 ± 0.1‰ (1σ, n=3) and was determined to be isotopically homogeneous using a combination of EA-IR-MS and SIMS sulfur isotope ratio measurements of separate individual fragments of the crystal (Bryant et al., 2019).

Methods

Pyrite isolation

As the analytical procedure requires intact, non-oxidized pyrite framboids, we utilized a physical procedure (Bryant et al., 2019) to isolate these from the marine sediment samples. Carbonate minerals were removed from dried, powdered sediment samples by three sequential 10-minute

treatments with 6M hydrochloric acid. Insoluble residues were rinsed five times with deionized water and dried in an oven at 60°C for 24 hours. Then, 45 mL lithium polytungstate heavy liquid (LST; density of 2.85 g/cm^3) was added to 250 mg dried insoluble residue in a 50 mL falcon tube. Samples were thoroughly mixed with a vortex mixer and deflocculated using an ultrasonic cleaner (35 kHz) for 15 minutes. Mixtures were centrifuged at 3000 RPM for 38 minutes, and the heavy mineral separates were removed from the tubes using plastic micro-pipettes. The heavy extracts were rinsed 5 times with deionized water, transferred to 1.5 mL micro centrifuge tubes, and placed in an ultrasonic cleaner (35 kHz) for 5 minutes. After the suspensions were allowed to settle for 10 minutes, the supernatants were transferred to separate microtubes using plastic micro-pipettes. The material that had settled after 10 minutes was dried in a vacuum oven at 60°C for 12 hours.

Sample mounting

We again followed the procedure of Bryant et al. (2019) in order to prepare the samples for SIMS. Dried samples were transferred onto the surface of the base of a 1-inch round acrylic mould coated with isooctane. After adding samples and powdered internal pyrite standard (see above), the upper half of the mould was filled with epoxy (1-(2-aminoethyl) piperazine; 1,-8-diamino-p-menthane; and Araldite 506 epoxy resin), which was cured for 72 h at 60°C in an oven. The cured epoxy puck was subsequently polished with a 6 μm polishing pad, 3 μm diamond paste, and 1 μm diamond paste, exposing the pyrite standard and samples, and achieving a flat surface. Laser Raman microprobe (Bryant et al., 2018) and petrographic analysis (Figure S4.2, D) were used to confirm the presence of samples at the surface of the polished epoxy puck, and the size of each grain to be analyzed was measured using calibrated reflected

light microscope images. The epoxy puck surface was coated with ~50 nm thick Au to ensure conductivity for SIMS analysis.

SIMS sulfur isotope experiments

Pyrite grains were pre-sputtered by Cs^+ bombardment for 300 seconds with a 1 nA primary beam current at the desired raster size (15-25 μm). Sulfur isotopic ratio experiments were then performed by Cs^+ bombardment of the same raster squares, using an electron multiplier (EM) detector on a CAMECA IMS 7f-GEO (Fitchburg, WI, USA) at Washington University in St. Louis to collect counts of $^{32}S^-$ and $^{34}S^-$ for each pixel (grids of 128x128 pixels) for 120 planes (1 minute per plane; 30 seconds per ion). The SIMS stage was x-y calibrated to a stitched optical microscope image of the epoxy puck using digital video camera footage of the gold-coated sample surface in the analysis chamber. After calculating raw isotope ratios for each grain by taking the mean $^{34}S^-/^{32}S^-$ ion count ratio of a central area of the grain over the multiple analysis planes, various corrections were applied to data, including a dead time correction, an interpolation of $^{34}S^-$ counts to align in time with those on $^{32}S^-$, and a quasi-simultaneous arrival (QSA) effect correction. The ratio of the QSA coefficient (β) to the primary ion flux (J) was used to facilitate the QSA correction (Jones et al., 2017). β/J values were determined for each session, via data obtained from the internal standard grains, using the relationship

$$R_{\mathrm{exp}} = R_{\mathrm{cor}} + (\beta/J) \times {}^{34}\mathrm{S}_{\mathrm{exp}} \qquad \text{(S4.1)}$$

where R_{exp} and $^{34}S_{\mathrm{exp}}$ are dead time corrected $^{34}S/^{32}S$ ratio and ^{34}S count rate, respectively, and R_{cor} is the QSA corrected $^{34}S/^{32}S$ ratio. For most grains, this correction led to an increase in $\delta^{34}S$ of ~1‰. The instrumental mass fractionation was then corrected for by calculating the fractionation factor ($^{34}\alpha$) based on the mean raw (from SIMS) and expected (–1.0‰, from EA-

IR-MS) $\delta^{34}S_{pyrite}$ value of the population of internal pyrite standard fragments and dividing the average $^{34}S^{-}/^{32}S^{-}$ ratio of each sedimentary pyrite grain by the appropriate $^{34}\alpha$.

Supplementary Text

Explanation of isotope ratio notation

The S-isotopic composition of pyrite is expressed here in the standard delta notation (in units of per mil, ‰) relative to the Vienna Canyon Diablo Troilite (VCDT) reference standard for sulfur (Ding et al., 1999),

$$\delta^{34}S_{sample} = \left(\frac{R_{sample}}{R_{VCDT}} - 1\right) \times 1000 \qquad (4.2)$$

where *R* represents $^{34}S/^{32}S$ ratios.

Details of numerical model

The numerical model used to validate interpretations of results in this study is detailed in a companion paper (Halevy et al., n.d.). The depositional parameters used to simulate glacial and interglacial conditions at the sample site are summarized in Table S4.2. We note that the only differences between glacial and interglacial intervals were in the sedimentation rate and porosity, the latter of which varied by a relatively small fraction and barely affected the outcome of the model simulations. The main control on the difference between the bulk and microscale S isotope composition of pyrite in the studied sediments is the sedimentation rate, through its effect on the openness of the sedimentary system.

The sedimentation rate, porosity, organic carbon mass fraction, iron mass fraction and sediment dry density were constrained directly from core PRGL1-4. The sedimentation rate and organic mass fraction were taken from the study of Pasquier et al. (2017). The sedimentation

rates were averaged over the interglacial and glacial intervals separately. The organic carbon mass fraction shows variability, but no clear difference between glacial and interglacial intervals, with an average value of about 0.6 w% (Pasquier et al., 2017). This value is measured ~8 meters below the seafloor, and given typical organic matter decay rates (Middleburg, 1989), would be ~2 w% close to the sediment-water interface. The porosity and sediment wet density were taken from the PROMESS1 cruise report (Berné, 2004). The sediment dry density was obtained by dividing the wet density by the solid fraction (1 – porosity). We found dry density values between 2,602 and 2,652 kg m^{-3} with no clear difference between glacial and interglacial intervals, and chose to use the average value of 2,628 kg m^{-3}. The mass fraction of reactive iron was measured, and no systematic difference was observed between glacial and interglacial intervals, both of which showed an average value of ~1 w% reactive iron (Pasquier, n.d.).

The temperature at the seafloor, cell density parameters and dissolved O_2 concentrations (DO_2) were constrained in the study area from published work. Estimates of cell density parameters relevant for the study area were taken from a global quantification of microbial cell density in marine sediments (Kallmeyer et al., 2015). Temperature and DO_2 at the sediment-water interface were determined in the Gulf of Lion, but at a maximal depth of 162 m (Berné, 2004). At this depth, the temperature is between 13 and 14°C, and the DO_2 is between ~230 and ~270 μM. However, the water depth at the PRGL1-4 site is 298 m, and we used nearby depth profiles of temperature and DO_2 (Coppola et al., 2018, 2017) to extrapolate the sediment-water interface measurements to the study site. The temperature in the Gulf of Lion at a water depth of the PRGL1-4 site (~300 m) is ~13°C (Coppola et al., 2018, 2017), and it is expected to have been slightly colder during glacial intervals. At a temperature of 7-13°C, the variation in the equilibrium sulfate-sulfide S isotope fractionation is <2‰ (Eldridge et al., 2016), and we chose a

seafloor temperature of 10°C to represent both glacial and interglacial intervals. Dissolved O_2 concentrations in the Gulf of Lion at the water depth of the PRGL1-4 drilling site vary between ~180 and ~220 μM (Coppola et al., 2018, 2017), and we chose a value of 200 μM to represent both glacial and interglacial intervals.

The concentration and isotopic composition of seawater sulfate were taken to be the global average values (28 mM and 20.6‰ VCDT). Given the residence time of sulfate in the ocean, these values are expected to have characterized both glacial and interglacial intervals.

Supplementary Figures & Tables

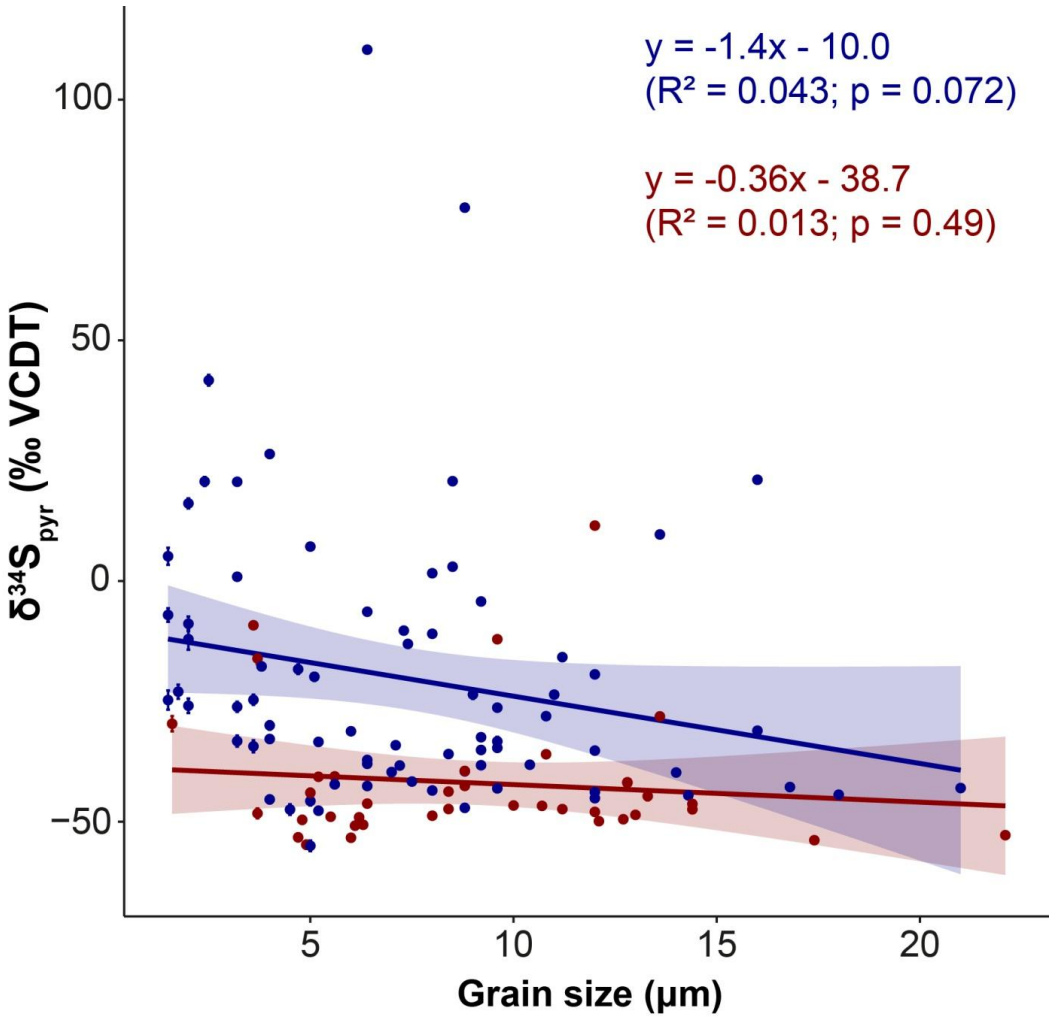

Figure S4.1. Grain specific $\delta^{34}S_{pyr}$ and grain size data for all glacial samples (in blue) and all interglacial samples (in red) from PRGL1-4; shaded regions are the 95% confidence intervals for the linear regressions shown, the formulas and goodness of fit information for which are shown in the upper right corner of the plot. Error bars (only visible for the smallest grains, as most error bars were smaller than the symbols used) are the standard error over SIMS analysis cycles.

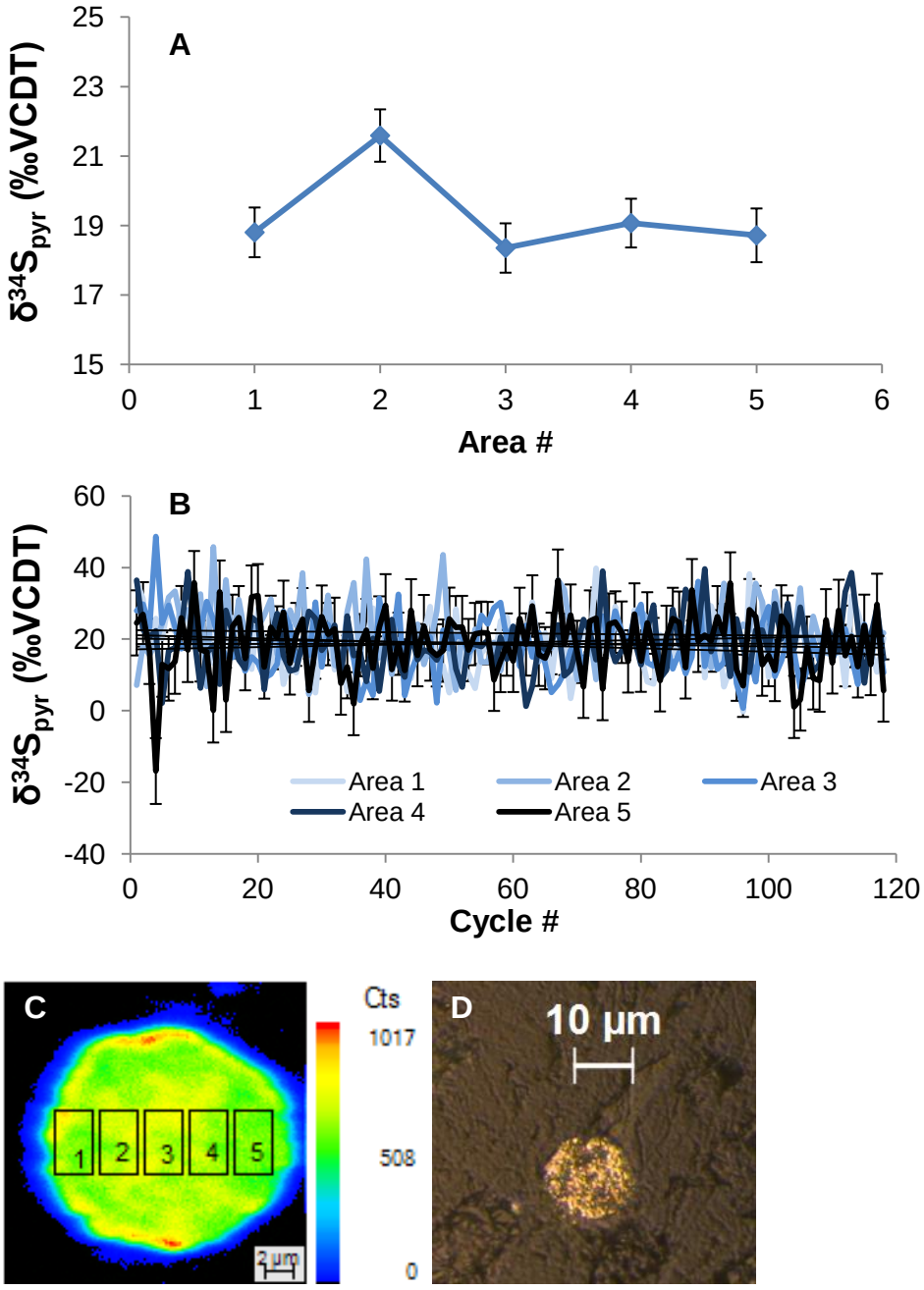

Figure S4.2. Internal variability in $\delta^{34}S$ within a pyrite grain with an enriched mean $\delta^{34}S_{pyr}$ value (p103_4; see Table S4.1), shown as transects along (A) the x-axis (horizontal), and (B) the z-axis (depth). The data correspond to regions 1 to 5 in the SIMS ^{32}S image (from cycle #1) in (C). A reflected light microscope image (taken through a 50x objective) of this polished grain, surrounded by epoxy, is shown in (D).

Table S4.1. Sulfur isotope data for samples from PRGL1-4. Listed grain sizes were measured using optical microscopy of polished grains prior to SIMS analyses, and therefore likely underestimate true grain size (Jones et al., 2018). Listed secondary ion counts (per time and area) are dead time-corrected but not QSA corrected. Listed $\delta^{34}S_{pyr}$ values are fully corrected (including for the instrumental mass fractionation, IMF), and reported relative to Vienna Canyon Diablo Troilite (VCDT). Listed standard errors refer to the standard error of $\delta^{34}S_{pyr}$ over the listed number of cycles.

Sample	Grain size (μm)	Counts ^{34}S/s/px	Counts ^{32}S/s/px	Raster size (μm)	Cycles	IMF ($^{34}\alpha$)	$\delta^{34}S_{pyr}$ (‰ VCDT)	Std. error (1σ, ‰)
p119_1	9	8.59E+03	2.00E+05	25	180	0.9975	-23.6	0.9
p119_2	16	1.03E+04	2.42E+05	25	180	0.9975	-31.1	0.4
p119_3	18	1.04E+04	2.46E+05	25	180	0.9975	-44.4	0.4
Wards_1	1 to 3	4.94E+03	1.12E+05	25	180	0.9975	-1.0	6.0
p119_4	4	1.97E+04	4.77E+05	15	93	0.9928	26.4	0.7
p119_5	2	1.55E+04	3.56E+05	15	120	0.9928	-8.9	1.5
p119_6	4	1.92E+04	4.55E+05	15	120	0.9928	-32.8	0.6
p119_7	2	1.93E+04	4.51E+05	15	108	0.9928	-25.9	1.5
p119_8	4.5	1.90E+04	4.52E+05	15	94	0.9928	-47.5	1.1
p119_9	1.75	2.04E+04	4.75E+05	15	120	0.9928	-23.0	1.5
p119_10	2	1.93E+04	4.42E+05	15	60	0.9928	-12.1	2.2
p119_11	1.5	1.05E+04	2.47E+05	15	120	0.9928	5.1	1.8
Wards_2	3.5	2.21E+04	5.03E+05	15	120	0.9928	-1.0	0.6
p119_12	11	1.24E+04	2.88E+05	15	180	0.9975	-23.6	0.2
p119_13	5	1.04E+04	2.50E+05	15	106	0.9962	-55.0	1.1
p119_14	12	1.20E+04	2.84E+05	15	180	0.9975	-45.1	0.3
p119_15	8	1.13E+04	2.69E+05	15	180	0.9975	-43.5	0.4
p119_16	1.5	1.11E+04	2.60E+05	15	120	0.9898	-24.7	2.0
p119_17	1.5	1.18E+04	2.72E+05	15	150	0.9898	-7.1	1.4
p119_18	8.5	1.38E+04	3.05E+05	15	180	0.9975	20.7	0.3
p119_19	12	1.52E+04	3.51E+05	15	144	0.9975	-19.4	0.2
p119_20	21	1.56E+04	3.68E+05	15	180	0.9975	-43.0	0.4
p119_21	7	1.37E+04	3.23E+05	15	180	0.9975	-39.7	0.6
Wards_3	7	1.23E+04	2.80E+05	15	75	0.9975	-1.0	0.7

Wards_4	1.5	9.33E+03	2.13E+05	15	18	0.9898	-1.0	2.3
Wards_5	5	1.46E+04	3.32E+05	15	75	0.9962	-1.0	0.6
Wards_6	40	1.97E+04	4.44E+05	20	120	1.0032	-1.0	0.2
Wards_7	18	1.56E+04	3.51E+05	20	120	1.0047	-1.0	0.2
Wards_8	1.5	1.49E+04	3.35E+05	20	120	1.0048	-1.0	1.3
p82_1	12.1	1.34E+04	3.17E+05	20	120	1.0048	-49.9	0.4
p82_2	3.7	1.15E+04	2.72E+05	20	120	1.0048	-48.3	1.0
p82_3	3.7	1.62E+04	3.70E+05	20	120	1.0048	-16.1	1.1
p82_4	10.7	1.36E+04	3.20E+05	20	120	1.0048	-46.7	0.4
p82_5	5	1.69E+04	3.98E+05	20	120	1.0048	-44.0	0.9
p82_6	6.3	1.28E+04	3.03E+05	20	120	1.0048	-50.6	0.6
p82_7	4.7	1.27E+04	3.03E+05	20	120	1.0048	-53.3	0.8
p82_8	14.4	1.39E+04	3.27E+05	20	120	1.0048	-46.3	0.3
p82_9	5.5	1.26E+04	2.97E+05	20	120	1.0048	-49.0	0.6
p82_10	13.3	1.55E+04	3.67E+05	20	120	1.0048	-44.7	0.8
p82_11	13	1.18E+04	2.80E+05	20	79	1.0048	-48.6	0.3
p82_12	12.7	1.35E+04	3.20E+05	20	120	1.0048	-49.5	0.3
p82_13	6.2	1.28E+04	3.04E+05	20	120	1.0048	-49.1	0.6
p82_14	6.1	1.41E+04	3.35E+05	20	120	1.0048	-50.8	0.6
p82_15	17.4	1.44E+04	3.42E+05	20	120	1.0047	-53.9	0.2
p82_16	22.1	1.39E+04	3.31E+05	20	120	1.0047	-52.8	0.2
p82_17	6.4	1.27E+04	2.99E+05	20	120	1.0048	-46.3	0.7
p82_18	6	1.19E+04	2.82E+05	20	120	1.0048	-53.3	0.7
p82_19	4.9	1.29E+04	3.06E+05	20	120	1.0048	-54.8	0.8
Wards_9	18	1.40E+04	3.16E+05	20	120	1.0050	-1.0	0.3
p74_1	8.5	1.35E+04	3.02E+05	20	120	1.0050	3.0	0.5
p74_2	5.1	1.45E+04	3.33E+05	20	120	1.0050	-19.9	0.8
p74_3	7.4	1.48E+04	3.38E+05	20	120	1.0050	-13.1	0.7
p74_4	4.7	7.93E+03	1.82E+05	20	120	1.0050	-18.3	1.0
p74_5	14.3	1.04E+04	2.46E+05	20	120	1.0050	-44.5	0.3
p74_6	12	1.05E+04	2.46E+05	20	120	1.0050	-43.9	0.4

p74_7	7.1	9.71E+03	2.26E+05	20	120	1.0050	-34.1	0.7
p74_8	7.3	1.02E+04	2.31E+05	20	120	1.0050	-10.3	0.4
p74_9	3.6	1.13E+04	2.63E+05	20	120	1.0050	-34.3	1.2
Wards_10	40	1.91E+04	4.30E+05	20	120	1.0014	-1.0	0.2
Wards_11	1.5	1.68E+04	3.79E+05	20	120	1.0007	-1.0	1.9
Wards_12	2	1.70E+04	3.86E+05	20	120	0.9948	-1.0	0.7
Wards_13	11	1.61E+04	3.65E+05	20	120	0.9979	-1.0	0.3
p90_1	8.4	1.72E+04	4.09E+05	20	120	0.9979	-47.4	0.4
p90_2	12.8	1.75E+04	4.12E+05	20	120	0.9979	-41.8	0.3
p90_3	5.2	1.83E+04	4.31E+05	20	120	0.9979	-40.7	0.5
p90_4	12	1.75E+04	3.91E+05	20	120	0.9979	11.5	0.4
p90_5	12.8	1.63E+04	3.86E+05	20	120	0.9979	-41.9	0.3
p90_6	10	1.46E+04	3.47E+05	20	120	0.9979	-46.6	0.4
p90_7	3.6	1.78E+04	4.06E+05	20	120	0.9979	-9.2	0.7
p90_8	8.8	1.41E+04	3.33E+05	20	120	0.9979	-42.6	0.5
p90_9	9.6	2.08E+04	4.75E+05	20	120	0.9979	-12.1	0.4
p90_10	10.8	2.13E+04	5.00E+05	20	120	0.9979	-36.0	0.3
p90_11	13.6	1.89E+04	4.40E+05	20	120	0.9979	-28.1	0.3
p90_12	1.6	1.37E+04	3.19E+05	20	120	0.9979	-29.7	1.6
p90_13	8.4	1.72E+04	4.07E+05	20	120	0.9979	-43.8	0.5
p90_14	8	1.73E+04	4.11E+05	20	120	0.9979	-48.8	0.3
p90_15	5.6	1.62E+04	3.83E+05	20	120	0.9979	-40.6	0.5
p90_16	12	1.79E+04	4.24E+05	20	120	0.9979	-48.0	0.3
p90_17	11.2	1.60E+04	3.80E+05	20	120	0.9979	-47.4	0.4
p90_18	14.4	1.61E+04	3.83E+05	20	120	0.9979	-47.4	0.2
p90_19	8.8	1.59E+04	3.74E+05	20	120	0.9979	-39.5	0.4
p90_20	4.8	1.35E+04	3.21E+05	20	120	0.9979	-49.6	0.8
Wards_14	20	2.09E+04	4.73E+05	20	120	0.9961	-1.0	0.2
Wards_15	20	1.87E+04	4.25E+05	20	120	0.9949	-1.0	0.2
Wards_16	2	1.33E+04	3.05E+05	20	120	0.9892	-1.0	0.8
p74_10	9.6	9.80E+03	2.32E+05	20	115	0.9915	-33.3	0.9

p74_11	3.2	1.19E+04	2.80E+05	20	120	0.9915	-33.3	1.2
p74_12	8	1.50E+04	3.46E+05	20	120	0.9915	-11.0	0.4
p74_13	6.4	1.36E+04	3.23E+05	20	120	0.9915	-37.2	0.6
p74_14	5	1.34E+04	3.20E+05	20	120	0.9915	-45.7	0.9
p74_15	8.4	1.41E+04	3.32E+05	20	120	0.9915	-36.0	0.5
p74_16	3.2	1.39E+04	3.25E+05	20	120	0.9915	-26.1	1.1
p74_17	4	1.50E+04	3.52E+05	20	120	0.9915	-30.0	0.9
p74_18	3.6	1.51E+04	3.53E+05	20	120	0.9915	-24.7	1.1
p74_19	8.8	1.34E+04	3.17E+05	20	120	0.9915	-39.5	0.4
p74_20	2.5	1.28E+04	2.80E+05	20	120	0.9915	41.7	1.1
p74_21	5.2	1.39E+04	3.27E+05	20	120	0.9915	-33.4	0.7
Wards_17	11	1.52E+04	3.46E+05	20	120	0.9915	-1.0	0.4
Wards_18	20	2.05E+04	4.66E+05	20	120	0.9931	-1.0	0.2
Wards_19	2	1.47E+04	3.36E+05	20	120	0.9878	-1.0	0.68
p74_22	6.4	2.00E+04	4.10E+05	20	120	0.9930	110.4	0.5
p74_23	4	1.81E+04	4.30E+05	20	120	0.9930	-45.4	0.8
p74_24	6.4	1.75E+04	4.02E+05	20	120	0.9930	-6.4	0.6
p74_25	13.6	1.97E+04	4.43E+05	20	120	0.9930	9.7	0.2
p74_26	8.8	1.87E+04	3.96E+05	20	120	0.9930	77.6	0.3
p103_1	3.8	1.84E+04	4.26E+05	20	120	0.9930	-17.8	0.8
p103_2	16.8	1.67E+04	3.97E+05	20	120	0.9930	-42.8	0.2
p103_3	11.2	1.73E+04	4.00E+05	20	120	0.9930	-15.8	0.3
p103_4	16	1.79E+04	3.99E+05	20	120	0.9930	21.0	0.2
p103_5	9.6	1.68E+04	3.97E+05	20	120	0.9930	-34.7	0.4
p103_6	9.6	1.73E+04	4.06E+05	20	120	0.9930	-26.3	0.4
p103_7	9.2	1.49E+04	3.40E+05	20	120	0.9930	-4.3	0.4
p103_8	14	1.53E+04	3.63E+05	20	120	0.9930	-39.8	0.3
p103_9	8.8	1.56E+04	3.72E+05	20	120	0.9930	-47.1	0.3
p103_10	9.2	1.38E+04	3.27E+05	20	120	0.9930	-38.3	0.4
p103_11	6.4	1.53E+04	3.64E+05	20	120	0.9930	-42.6	0.5
p103_12	5.6	1.40E+04	3.33E+05	20	120	0.9930	-42.3	0.6

p103_13	9.2	1.46E+04	3.44E+05	20	120	0.9930	-35.1	0.4
p103_14	6.4	1.51E+04	3.58E+05	20	120	0.9930	-38.0	0.6
p103_15	6	1.54E+04	3.63E+05	20	120	0.9930	-31.2	0.6
p103_16	8	1.90E+04	4.31E+05	20	120	0.9930	1.6	0.3
p103_17	5.2	1.39E+04	3.33E+05	20	120	0.9930	-47.7	0.7
Wards_20	11	1.82E+04	4.17E+05	20	120	0.9850	-1.0	0.4
p103_18	12	1.89E+04	4.48E+05	20	120	0.9850	-35.2	0.3
p103_19	10.4	1.80E+04	4.30E+05	20	120	0.9850	-38.2	0.3
p103_20	5	1.98E+04	4.51E+05	20	120	0.9850	7.1	0.3
p103_21	7.2	1.38E+04	3.29E+05	20	120	0.9850	-38.3	0.5
p103_22	9.2	1.84E+04	4.35E+05	20	120	0.9850	-32.5	0.4
p103_23	9.6	1.86E+04	4.46E+05	20	120	0.9850	-43.1	0.3
p103_24	10.8	1.92E+04	4.52E+05	20	120	0.9850	-28.1	0.3
p103_25	7.5	1.67E+04	3.99E+05	20	120	0.9850	-41.7	0.3
p103_26	3.2	1.65E+04	3.77E+05	20	120	0.9853	0.9	0.7
p103_27	3.2	1.92E+04	4.31E+05	20	120	0.9853	20.6	0.6
p103_28	2	2.31E+04	5.21E+05	20	120	0.9853	16.1	1.1
p103_29	2.4	2.13E+04	4.78E+05	20	120	0.9853	20.7	0.9
Wards_21	11	1.57E+04	3.61E+05	20	120	0.9853	-1.0	0.3

Table S4.2. Depositional parameters used in the diagenetic model (Halevy et al., n.d.) to simulate the local environmental conditions present at the sample site in glacial and interglacial intervals. See Supplementary Text for details. All gray-shaded parameters were constrained from core PRGL1-4, and only the dark gray-shaded parameters (sedimentation rate and porosity) differed between simulations of glacial and interglacial intervals.

Parameter	Interglacial value	Glacial value
Sedimentation rate (m y^{-1})	1.5×10^{-3}	0.2×10^{-3}
Porosity at the seafloor (unitless)	0.44	0.41
Mass fraction organic carbon at seafloor (w%)	2	2
Mass fraction reactive iron at seafloor (w%)	1	1
Sediment dry density (kg m^{-3})	2,628	2,628
Temperature at the seafloor (°C)	10	10
Cell density 1 m below seafloor (cell cm^{-3})	1×10^{8}	1×10^{8}
Cell density decay exponent (unitless)	–0.5	–0.5
Dissolved O_2 concentration at seafloor (μM)	200	200
Seawater sulfate concentration (mM)	28	28
Seawater sulfate $\delta^{34}S$ (‰ VCDT)	20.6	20.6

Chapter 5: Explaining the OAE-2 iron sulfide-organic sulfur isotope divergence at Demerara Rise

R. N. Bryant[1], C. Jones[1], M. R. Raven[2], J. D. Owens[3], and D. A. Fike[1]

[1]Department of Earth & Planetary Sciences, Washington University in Saint Louis, St. Louis, MO 63130, USA.

[2]Department of Earth Science, University of California, Santa Barbara, CA 93106, USA.

[3]Department of Earth, Ocean and Atmospheric Science, Florida State University, Tallahassee, FL 32306, USA.

Abstract

Bulk 'pyrite' S isotope ratios ($\delta^{34}S_{CRS}$) from Demerara Rise in the southern North Atlantic shift toward more negative values just before the onset of the Cenomanian-Turonian Ocean Anoxic Event (OAE-2). These observations have led to suggestions that global S cycling dynamics were perturbed by the environmental changes associated with OAE-2. Throughout the same interval, however, bulk organic S isotope ratios ($\delta^{34}S_{OS}$) are largely invariant. It is challenging to definitively explain the negative shift in $\delta^{34}S_{CRS}$, and why it diverges from $\delta^{34}S_{OS}$. Our understanding is further complicated by the fact that bulk $\delta^{34}S_{CRS}$ measurements can integrate over multiple phases and mineralogies (e.g., pyrite and marcasite, both FeS_2 polymorphs), and can reflect multiple environmental and ecological factors. In order to address the origin of these differences – and the environmental and/or ecological drivers that gave rise to them, here we investigate grain-specific S-isotopic composition of Fe sulfide minerals from pre- and syn-OAE-2 sedimentary rocks from Demerara Rise using secondary ion mass spectrometry (SIMS). Two texturally distinct Fe sulfide phases exist prior to OAE-2 (pyrite framboids and irregular pyrite aggregates), though Fe sulfides are dominated volumetrically by large cemented pyrite aggregates and marcasite during OAE-2. These different textural groups have distinct S-isotopic compositions that are largely consistent though the onset of OAE-2. As such, the secular change in $\delta^{34}S_{CRS}$ values likely reflects their changing volumetric proportions in each sample. All textural groups in every sample feature substantial intra-grain $\delta^{34}S$ variability, suggesting that they predominantly formed in an environment characterized by partial closed-system distillation (i.e., in sediment pore waters, or within sinking particles in the water column). We use grain-specific $\delta^{34}S$ distributions to rule out both increasing microbial fractionation and increasing system openness as mechanisms for the observed decrease in $\delta^{34}S_{CRS}$. We instead attribute the

negative shift in $\delta^{34}S_{CRS}$ to an increase in the kinetics of Fe sulfidization, which enhanced the ^{34}S-depleted signal sequestered in Fe sulfides.

5.1 Introduction

The Cenomanian-Turonian Boundary Ocean Anoxic Event (OAE-2) was an interval of apparent geographically extensive enhanced organic matter (OM) burial and CO_2 drawdown, marked by a transient positive C isotope excursion in the marine carbonate record (Jarvis et al., 2011). Enhanced primary productivity is thought to have depleted oceanic oxygen concentrations (Schlanger and Jenkyns, 1976), leading to enhanced preservation of OM (Barron, 1983), a sharp decline in carbonate precipitation, and the formation of remarkably OM-rich sediments. At Demerara Rise, a site in the proto-North Atlantic during the Cretaceous (ODP 1258; Erbacher et al., 2005; Figure 5.1), average pre-OAE-2 sediments contain 8% OM by weight, whereas average syn-OAE-2 sediments contain ~20% OM by weight (Raven et al., 2019).

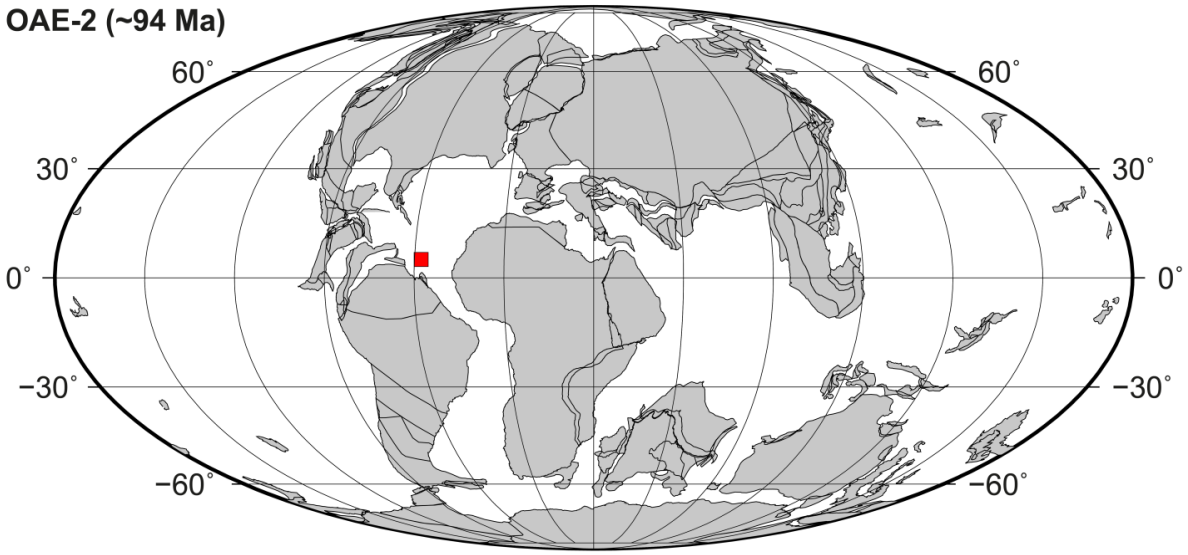

Figure 5.1. Paleogeographic map during OAE-2 (~94 Ma) showing the location of Demerara Rise (marked by the red square) in the proto-North Atlantic. Map generated using the ODSN Plate Tectonic Reconstruction Service (http://www.odsn.de/odsn/services/paleomap/paleomap.html).

Due to the intimate connection between the global C and S cycles (Berner, 2001, 1989; Canfield, 2004; Fike et al., 2015; Garrels and Lerman, 1981), many have used the S-isotopic composition of different operationally defined S-bearing phases to probe the response of the global S cycle to OAE-2. S-isotopic compositions are expressed here in the standard delta notation (in units of permil, ‰) relative to the Vienna Canyon Diablo Troilite (VCDT) reference standard for S (Ding et al., 1999),

$$\delta^{34}S_{sample} = \left(\frac{R_{sample}}{R_{VCDT}} - 1\right) \times 1000 \qquad (5.1)$$

where *R* represents $^{34}S/^{32}S$ ratios. S-isotopic compositions of chromium-reducible S ($\delta^{34}S_{CRS}$; Canfield 1986), which targets pyrite as well as its polymorph marcasite, in addition to elemental S and a host of monosulfide minerals, at several different sites become more ^{34}S-depleted toward the onset of OAE-2. Various factors have been suggested to have caused the decreasing $\delta^{34}S_{CRS}$, including declining ocean sulfate concentration (Adams et al., 2010), chemocline migration (Gomes et al., 2016), increasing contribution of intermediate valence S species to the buried CRS pool (Hetzel et al., 2009; Kolonic et al., 2002), and changes in Fe sulfide formation kinetics (Raven et al., 2019).

Recently, Raven et al. (2019) found that the S-isotopic composition of organic S ($\delta^{34}S_{OS}$) at Demerara Rise was largely invariant before, during, and after OAE-2 with values ~0‰. As a result, the S-isotopic offset between CRS and OS steadily increased leading up to OAE-2 (Figure 5.2). The divergence of these two S isotope records provides clear constraints on the environmental changes impacting them. Interpreting the OS pool as largely having formed through sulfurization of OM in the water column, Raven et al. (2019) suggested that the increasing offset between $\delta^{34}S_{CRS}$ and $\delta^{34}S_{OS}$ at Demerara Rise reflected an increase in the range

of depths Fe sulfides formed, from only in the water column before OAE-2 to forming in both the water column and sediment pore waters during OAE-2. Such a scenario would require either a decrease in the kinetics of Fe sulfidization or an increase in the supply of Fe, such that more Fe would be likely to reach the sediments before reacting with reduced S. Other observations further indicate that Fe cycling at Demerara Rise was perturbed by OAE-2. For example, the median abundance of Fe sulfides in the carbonate-free fraction of Demerara Rise sediments is slightly higher during OAE-2 than before OAE-2 (Raven et al., 2019; Figure S1).

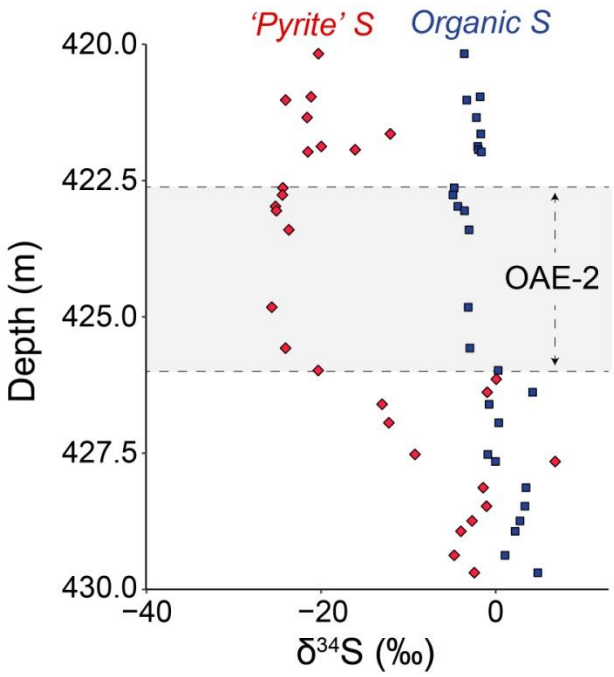

Figure 5.2. Bulk S-isotopic compositions of 'pyrite' (CRS) and organic S through OAE-2 at Demerara Rise, after Raven et al. (2019).

Although Raven et al. (2019) offer a self-consistent argument, definitively interpreting bulk $\delta^{34}S_{CRS}$ records is challenging, as bulk $\delta^{34}S_{CRS}$ values can reflect variable contributions by multiple generations of mineral growth (Cui et al., 2018) and in this case is further complicated by the presence of multiple mineralogies (e.g., pyrite and marcasite, both FeS_2 polymorphs; Bryant et al., 2019). In addition, $\delta^{34}S_{CRS}$ values can reflect multiple environmental (e.g., the

'openness' of the environment of mineral formation with respect to sulfate; Bryant et al., 2019; Fike et al., 2015) and ecological factors (e.g., the magnitude of the biological fractionation associated with microbial sulfate reduction, ε_{mic}; (Leavitt et al., 2013; Sim et al., 2011b, 2011a; Wing and Halevy, 2014). Any of these factors could have contributed to the observed decrease in $\delta^{34}S_{CRS}$ toward the onset of OAE-2 at Demerara Rise, and cannot be ruled out on the basis of $\delta^{34}S_{CRS}$ data alone. However, the lack of substantive change within the OS signal suggests that any perturbation likely impacted the timing or locus of Fe sulfide formation rather than inherently changing S cycling.

Pinpointing the driver(s) of the decrease in bulk $\delta^{34}S_{CRS}$ values toward the onset of OAE-2 at Demerara Rise will provide important information about changes to the regional biogeochemical cycles of C, S and Fe leading up to and during OAE-2. Here, we seek to do so using grain-specific S isotope analyses. A scanning ion imaging method of secondary ion mass spectrometry (SIMS) was recently developed for microcrystalline Fe sulfides and produces S isotope data that are a direct record of the isotopic composition of reduced S species in the fluids from which the Fe sulfides formed (Bryant et al., 2019). By applying this method in a comparative study of Fe sulfides from sediments deposited before and during OAE-2 at Demerara Rise, we will establish the various contributions to, and mechanisms responsible for, the observed secular change in bulk $\delta^{34}S_{CRS}$.

5.2 Methods and Materials

5.2.1 Samples

We obtained three powdered sediment samples from ODP Site 1258 (drilled at a modern water depth of 3192.2 meters, near the base of the western slope of Demerara Rise). The samples are highly OM-rich laminated black shales from core depths of 429.4, 426.6 and 422.8 meters (using the composite depths of Erbacher et al., 2005). For reference, the OAE-2 interval occurs between depths of ~426.0 and ~422.5 m (Raven et al., 2019). The black shales of Demerara Rise were previously interpreted to have been deposited at a rate of ~1 cm/kyr beneath a water column that was likely similar to a modern oxygen minimum zone before/after OAE-2 and stratified with euxinic (oxygen poor, sulfide rich) bottom waters during OAE-2 (Hetzel et al., 2009).

5.2.2 Extraction of iron sulfides

A shatter box was employed to powder the samples for no longer than 1 minute. Carbonate minerals were removed by three sequential 10-min treatments with 6M hydrochloric acid, before the insoluble residue was rinsed five times with deionized water and dried in an oven at 60°C for 24 h. The insoluble residues were then powdered by mortar and pestle. For each sample, a 0.25 g aliquot of insoluble residue powder was added to 45 mL of Lithium Polytungstate Heavy Liquid (LST) in a 50-mL centrifuge tube. The contents of these tubes were mixed for 1 min using a vortex mixer at the highest speed, then placed in an ultrasonic bath (35 kHz) for 15 min to de-flocculate the powders. Following Bryant et al. (2019), the tubes were spun in a centrifuge for 38 min at 3000 rpm to allow Fe sulfide grains of diameters ≥0.5 μm to settle out. After centrifugation, heavy fractions were removed from the tubes using a plastic micropipette, placed in new 50-mL centrifuge tubes, rinsed and spun down (5 min at 2000 rpm) five times in deionized water, and dried overnight at 60°C in a vacuum oven.

5.2.3 Imaging

For each sample, Fe sulfide grains were mounted in 1-inch rounds of epoxy, along with fragments of the in-house marcasite and pyrite S-isotopic standards, and polished to 1 μm, as in Bryant et al. (2019). Epoxy mounts were imaged using reflected light optical microscopy (2.5x objective for stitched image used for SIMS stage calibration, 50-80x for regions of interest). For the syn-OAE-2 sample (422.8 m), representative Fe sulfide aggregates were previously imaged by Scanning Electron Microscopy (SEM) in Bryant et al. (2019).

5.2.4 Laser Raman microprobe analysis

The identities of all Fe sulfide grains in regions of interest of the epoxy puck were confirmed using laser Raman microprobe analysis (1 mW laser power, 80x objective, 20 analyses of 1 s duration, as in Bryant et al. (2018)). All Fe sulfide grains present were either pyrite or marcasite, and thus were easily distinguishable based on the positions of the two dominant bands in Raman spectra obtained: marcasite has prominent bands at ~324 and ~387 Δcm^{-1}, whereas pyrite has prominent bands at ~343 and ~379 Δcm^{-1} (Bryant et al., 2018).

5.2.5 SIMS sulfur isotope analyses

We used fragments of hydrothermal pyrite and marcasite crystals, both previously demonstrated to be isotopically homogeneous (Bryant et al., 2019), as S-isotopic standards in SIMS experiments. Following Bryant et al. (2019), environmental Fe sulfide grains were pre-sputtered by Cs^+ bombardment for 300 s with a 1 nA beam current at raster sizes at least several microns larger than the exposed grains (20–80 μm). S isotopic ratio analyses were then performed in "scanning ion imaging mode" by Cs^+ bombardment (beam diameter of <1 μm, current of ~10 pA) of the same raster squares using an electron multiplier (EM) detector on a IMS 7f-GEO SIMS instrument (CAMECA, Fitchburg, WI, USA) at Washington University in Saint Louis (St Louis, MO, USA) to collect counts of $^{32}S^-$ and $^{34}S^-$ for each pixel (grids of 128×128 pixels) for

between 20 and 480 planes (1 min per plane). In post-processing, raw isotope ratios were calculated by taking the mean $^{34}S^{-}/^{32}S^{-}$ ion count ratio of a central area of each grain integrated over all analysis planes. Various corrections were applied to the data, including a dead-time correction, an interpolation of $^{34}S^{-}$ counts to align in time with those on $^{32}S^{-}$, and a quasi-simultaneous arrival (QSA) effect correction (Bryant et al., 2019; Jones et al., 2017). Finally, instrumental mass fractionation was then corrected for by calculating the mineral-specific fractionation factor ($^{34}\alpha$) based on the mean raw (from SIMS) and known $\delta^{34}S$ value of the population of internal hydrothermal pyrite or marcasite standards and dividing the average $^{34}S^{-}/^{32}S^{-}$ ratio of each environmental Fe sulfide grain by the appropriate value of $^{34}\alpha$.

5.3 Results

5.3.1 Iron sulfide minerals and textures

Optical microscopy and laser Raman microprobe analyses suggested that all samples contained exclusively Fe sulfide minerals, which can be grouped as follows: (i) pyrite framboids (~1-30 μm spheroidal to sub-spheroidal clusters of equidimensional and equimorphic pyrite microcrystals; Ohfuji and Rickard, 2005; Figure 5.3A-C), (ii) irregular pyrite aggregates (microscopic non-spheroidal clusters of pyrite microcrystals; Figure 5.3D-H), (iii) cemented pyrite aggregates (angular pyrite aggregates in which microcrystals are challenging to discern due to pyritic cementation; Figure 5.3I), and (iv) marcasite (as aggregates of intergrown euhedral microcrystals, or as fully cemented aggregates; Figure 5.3J, K).

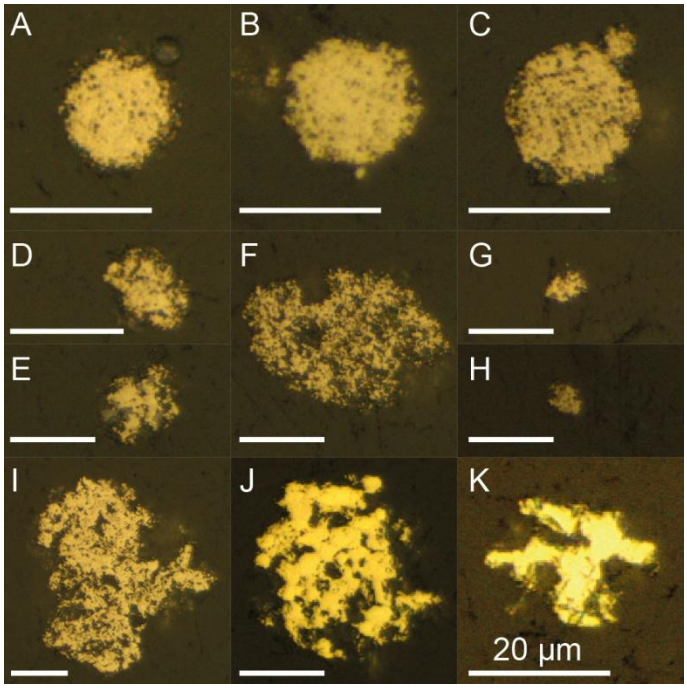

Figure 5.3. Reflected light optical microscope images (all scale bars are 20 µm) of different Fe sulfide minerals and textures from Demerara Rise samples. (A-C) infilled pyrite framboids from depths of 429.4 (pre-OAE-2), 426.6 (pre-OAE-2) and 422.8 meters (syn-OAE-2); (D-H) irregular pyrite aggregates from depths of 429.4, 426.6 and 422.8 meters; (I) cemented pyrite aggregate from a depth of 422.8 meters, and (J-K) marcasite from a depth of 422.8 meters.

By assuming that every Fe sulfide grain imaged is roughly spherical and non-porous, and cut directly through its equator, we roughly estimated the relative proportions of the different Fe sulfide groups in each sample – these are summarized in Table 5.1, and in Figure 5.4A. Average pyrite framboid sizes are large (~10 µm) prior to OAE-2 and very small (~4 µm) during OAE-2 (Table 5.1).

Table 5.1. Framboid sizes, and relative abundances of different Fe sulfide minerals and textures in the three samples from Demerara Rise, as inferred from optical microscopy and laser Raman microprobe analysis. The samples from depths of 429.4 and 426.6 m are pre-OAE-2 and the sample from a depth of 422.8 m is syn-OAE-2.

Sample depth (m)	Mean framboid size (μm)	Vol. % pyrite framboids	Vol. % irregular pyrite	Vol. % cemented pyrite aggregate	Vol. % marcasite
422.8	4.2 ± 3.4 (1σ)	3.5	0.1	63.0	33.3
426.6	10.3 ± 4.2 (1σ)	16.5	83.5	0	0
429.4	9.6 ± 3.3 (1σ)	32.5	67.5	0	0

Based on our limited number of samples, the proportion of FeS_2 in a sample present as pyrite framboids appears to decline leading into OAE-2, whereas the proportion as irregular pyrite aggregates is very high before OAE-2 and is very low during OAE-2. Marcasite and large cemented pyrite aggregates are volumetrically dominant during OAE-2.

5.3.2 SIMS sulfur isotope analyses

Inter-grain $\delta^{34}S$ variability

Grain-specific $\delta^{34}S$ values obtained using SIMS scanning ion imaging (Table S5.1) reflect the integrated value for the exposed cross-sectional areas of polished grains (Bryant et al., 2019; Jones et al., 2018); although these multiple-image-plane analyses integrate depth somewhat, the $\delta^{34}S$ values reported in this section may not always be representative of the integrated value of the entire grain. Regardless, in all samples pyrite framboids and irregular pyrite aggregates appear to be the most ^{34}S-depleted and ^{34}S-enriched textural groups, respectively (Figure 5.4A). Unlike the bulk $\delta^{34}S_{CRS}$ data of Raven et al. (2019), neither group's isotopic composition shows strong stratigraphic variability, each differing by less than 8‰ between the three samples. In the

deepest sample (429.4 m; pre-OAE-2), pyrite framboids have a minimum $\delta^{34}S$ value of –36.1 ± 0.8‰ (1 standard error; Figure 5.4A, B), an average $\delta^{34}S$ value of –21.5 ± 8.9‰ (1σ; n=18; Figure 5.4A, B), and a maximum $\delta^{34}S$ value of +0.4 ± 0.8‰ (1 standard error; Figure 5.4A, B). Irregular pyrite aggregates have a minimum $\delta^{34}S$ value of –18.3 ± 0.8‰ (1 standard error; Figure 5.4A), an average $\delta^{34}S$ value of –4.9 ± 10.5‰ (1σ; n=6; Figure 5.4A), and a maximum $\delta^{34}S$ value of +11.3 ± 0.9‰ (1 standard error; Figure 5.4A). In the sample immediately below OAE-2 (426.6 m), pyrite framboids have a minimum $\delta^{34}S$ value of –36.2 ± 1.1‰ (1 standard error; Figure 5.4A, B), an average $\delta^{34}S$ value of –26.0 ± 5.6‰ (1σ; n=8; Figure 5.4A, B), and a maximum $\delta^{34}S$ value of –18.9 ± 0.6‰ (1 standard error; Figure 5.4A, B). Irregular pyrite aggregates have a minimum $\delta^{34}S$ value of –16.0 ± 1.7‰ (1 standard error; Figure 5.4A), an average $\delta^{34}S$ value of –12.8 ± 2.6‰ (1σ; n=4; Figure 5.4A), and a maximum $\delta^{34}S$ value of –9.8 ± 0.4‰ (1 standard error; Figure 5.4A). In the sample within OAE-2 (422.8 m), pyrite framboids have a minimum $\delta^{34}S$ value of –37.4 ± 3.7‰ (1 standard error; Figure 5.4A, B), an average $\delta^{34}S$ value of –28.3 ± 6.0‰ (1σ; n=35; Figure 5.4A, B) and a maximum $\delta^{34}S$ value of –13.2 ± 1.0‰ (1 standard error; Figure 5.4A, B). Irregular pyrite aggregates have a minimum $\delta^{34}S$ value of –18.4 ± 0.5‰ (1 standard error; Figure 5.4A), an average $\delta^{34}S$ value of –11.8 ± 6.0‰ (1σ; n=3; Figure 5.4A), and a maximum $\delta^{34}S$ value of –6.8 ± 2.1‰ (1 standard error; Figure 5.4A). In the same sample, marcasites have a minimum $\delta^{34}S$ value of –33.9 ± 6.6‰ (1 standard error; Figure 5.4A), an average $\delta^{34}S$ value of –23.9 ± 11.8‰ (1σ; n=20; Figure 5.4A), and a maximum $\delta^{34}S$ value of +18.9 ± 2.0‰ (1 standard error; Figure 5.4A). Finally, a single large (~60 μm) cemented pyrite aggregate has a $\delta^{34}S$ value of –19.0 ± 0.1‰ (1 standard error; Figure 5.4A).

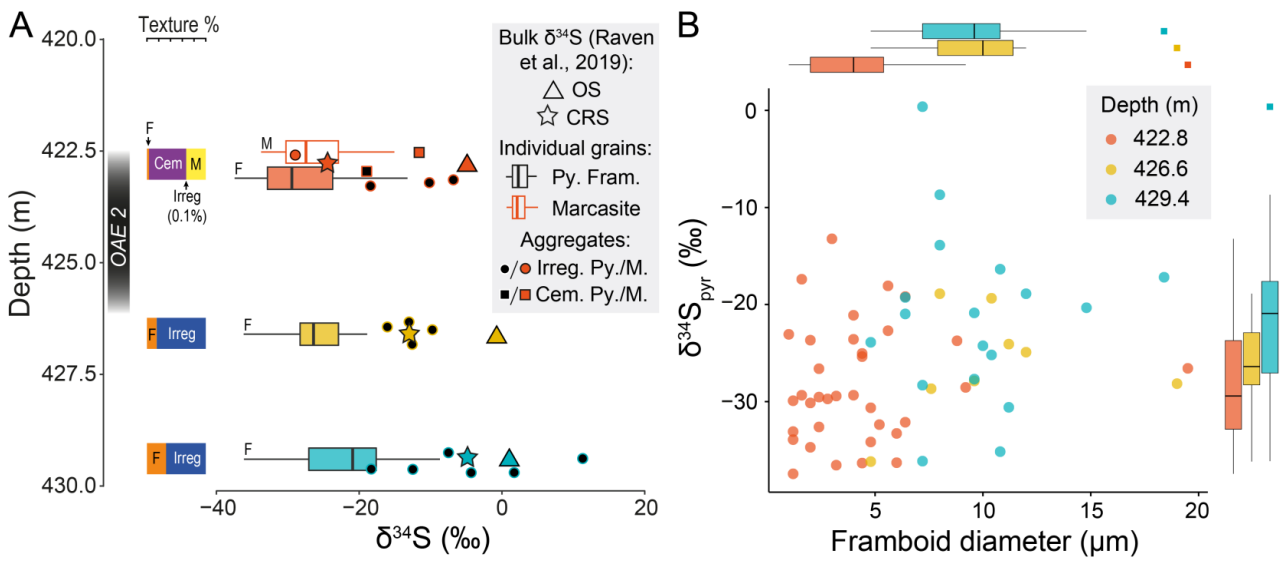

Figure 5.4. Records of Fe sulfide texture/mineralogy and S-isotope change through OAE-2 at Demerara Rise. (A) Proportions of different Fe sulfide minerals/textures (F=pyrite framboid, Irreg=irregular pyrite aggregate, Cem=cemented pyrite aggregate, M=marcasite); black outline box and whisker plots (F) are for pyrite framboid SIMS $\delta^{34}S$, orange outline box and whisker plot (M) is for individual marcasite grain SIMS $\delta^{34}S$; jittered black circles are irregular pyrite aggregate SIMS $\delta^{34}S$ values, the black square is the SIMS $\delta^{34}S$ value of a cemented pyrite aggregate, the orange circle is the SIMS $\delta^{34}S$ value of an irregular marcasite aggregate, and the orange square is the SIMS $\delta^{34}S$ value of a cemented marcasite aggregate; black-outlined stars and triangles are the bulk $\delta^{34}S_{CRS}$ and $\delta^{34}S_{OS}$ values, respectively, for the samples used in this study, from Raven et al. (2019). (B) Cross plot of pyrite framboid SIMS $\delta^{34}S$ values vs. their diameters, with marginal box and whisker plots, where squares are outliers.

Assuming that that all grains imaged by optical microscope but not measured by SIMS have the same average $\delta^{34}S$ value as the grains of similar texture measured by SIMS, a volume-adjusted SIMS $\delta^{34}S$ value can be estimated for the Fe sulfides imaged from each sample. Volume-adjusted $\delta^{34}S$ values are –10.5, –14.7, and –21.8‰ for the samples from depths of 429.4, 426.6, and 422.8 meters, respectively (Table 5.2). These values are reasonably close to the previously reported bulk $\delta^{34}S_{CRS}$ values (–4.7, –13.0, and –24.4‰; Table 5.2; Raven et al., 2019), suggesting that our subset of physically extracted Fe sulfides analyzed by SIMS are broadly representative of bulk Fe sulfides in the samples.

Table 5.2. Volume-adjusted Fe sulfide-$\delta^{34}S$ values (this study) compared with bulk CRS- and OS-$\delta^{34}S$ values from Raven et al. (2019). The samples from depths of 429.4 and 426.6 m are pre-OAE-2 and the sample from a depth of 422.8 m is syn-OAE-2.

Sample depth (m)	Volume-adjusted Fe sulfide $\delta^{34}S$ (‰)	Bulk $\delta^{34}S_{CRS}$ (‰)	Bulk $\delta^{34}S_{OS}$ (‰)
422.8	–21.8	–24.4	–4.9
426.6	–14.7	–13.0	–0.7
429.4	–10.5	–4.7	1.1

Intra-grain $\delta^{34}S$ variability

In order to understand the system(s) in which the different Fe sulfide textures formed, it can be useful to probe intra-grain $\delta^{34}S$ variability (Bryant et al., 2019; Cui et al., 2018). Using our $^{32}S^-$ and $^{34}S^-$ ion images of Fe sulfides from Demerara Rise, we now investigate intra-grain isotopic variability across multiple ~1-5 µm diameter regions within individual Fe sulfides representing all Fe sulfide textures identified in these samples. In some cases, there may be indiscernible variability that occurs on scales smaller than the size of the primary beam (~0.5 µm) or with a magnitude smaller than the precision of individual measurements. To ensure that the apparent intra-grain variability is larger than that which would be expected based on the precision of the method, we always compare the standard deviation of intra-grain measurements to the average standard error over cycles associated with individual intra-grain measurements (Bryant et al., 2019). Where variation in $\delta^{34}S$ can be discerned within individual grains, we test for spatial autocorrelation using global Moran's I. We also test for linear correlation between the distance of the center of regions of interest from the nearest grain edge and their $\delta^{34}S$ values (see explanation of both tests in Supplement).

Pyrite framboids

For all three samples, pyrite framboids feature discernible intra-grain $\delta^{34}S$ variability (Figure 5), the clearest cases of which form spatial trends similar to those seen in cm-scale pyrite structures, for example core-rim ^{34}S-enrichments in Archean-age pyrite nodules (Fischer et al., 2014), exoskeleton-appendage ^{34}S-enrichments in Ordovician-age pyritized trilobites (Briggs et al., 1991), and centripetal ^{34}S-enrichments in Ediacaran pyritized *Conotubus* fossils (Schiffbauer et al., 2014), but never previously observed in framboids. Although some grains show intra-grain variation in $^{32}S^-$ ion counts, there is only a significant (albeit weak) trend between counts and $\delta^{34}S$ for one grain (Figure 5.5F; Figure S5.2F; *p*-value = 0.048) – this trend appears to be largely driven by one anomalously high-count region close to the right edge of the grain. There is a positive correlation between mean $\delta^{34}S$ value of a framboid and the standard deviation of intra-grain $\delta^{34}S$ measurements in the x-y plane (Figure S5.3, Appendix). In the deepest sample (429.4 m), pyrite framboids are mostly infilled (i.e., individual microcrystals are only clearly visible toward the edges of framboids; Figure 5.5A, B) and feature moderate intra-grain variation in $\delta^{34}S$ (average $1\sigma = \pm 4.5‰$, compared to an average intra-grain standard error of $\pm 2.1‰$, 1σ, n=43). A large framboid (Figure 5.5A) features clear core-rim radial enrichments in ^{34}S (Table S5.2). A smaller framboid (Figure 5.5B) has a relatively ^{34}S-enriched infilled central region and a relatively ^{34}S-depleted, non-infilled outer region (Table S5.2). In the sample from immediately below OAE-2 (426.6 m), framboids are again mostly infilled (Figure 5.5C, D) and feature moderate intra-grain variation in $\delta^{34}S$ (average $1\sigma = \pm 5.6‰$, compared to an average intra-grain standard error of $\pm 2.5‰$, 1σ, n=34). A smaller framboid (Figure 5.5C) displays no clear spatial trend in intra-grain $\delta^{34}S$ values (Table S5.2), whereas a larger framboid (Figure 5.5D) features clear core-rim radial enrichments in ^{34}S (Table S5.2). In the sample from within OAE-2 (422.8

m), a small, partially infilled framboid (Figure 5.5E) has negligible intra-grain variation in $\delta^{34}S$ in the x-y plane ($1\sigma = \pm 3.0‰$, compared to an average intra-grain standard error of ±3.4‰, 1σ, n=10; Table S5.2). In contrast, a larger infilled framboid (Figure 5.5F) has clear core-rim radial enrichments in ^{34}S ($1\sigma = \pm 4.4‰$, compared to an average intra-grain standard error of ±1.5‰, 1σ, n=30; Table S5.2). Generally, where substantial isotopic variability can be discerned, it takes the form of radial enrichments in ^{34}S that are visible in cross sections (e.g., Figure 5.5A, D, and F). These patterns are representative for the populations of framboids in all the samples studied.

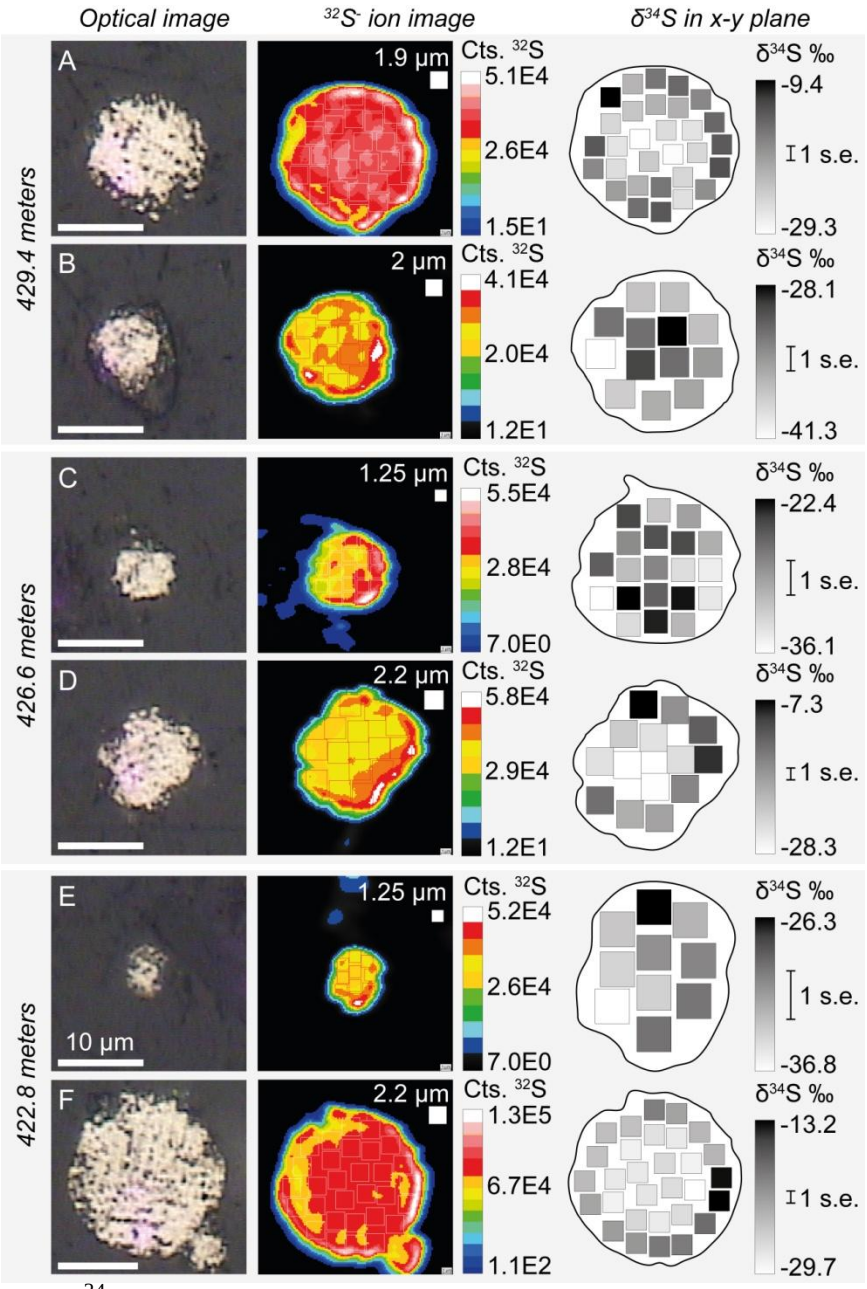

Figure 5.5. Internal $\delta^{34}S$ variability in framboids from (A, B) the deepest pre-OAE-2 sample, (C, D) the sample just before OAE-2, and (E, F) the syn-OAE-2 sample. From left-right, panels display: optical microscope images, where scale bars are all 10 μm; $^{32}S^-$ ion images, accumulated over 60-90 cycles, with inset showing the size of sub-sampled regions; and $\delta^{34}S$ values of the sub-sampled regions, where the error bar indicates the average of the standard errors for the different sub-sampled regions.

Irregular pyrite aggregates

As with the pyrite framboids, irregular pyrite aggregates from all three samples feature discernible intra-grain $\delta^{34}S$ variability. In some cases, this variability again takes the form of core-rim ^{34}S enrichments, but other patterns include positive spatial autocorrelation without radial trends. Although some grains show intra-grain variation in $^{32}S^-$ ion counts, there is only a significant trend between counts and $\delta^{34}S$ for one grain (Figure 5.6F; Figure S5.4F; *p*-value = 0.0089) – this trend appears to be largely driven by two anomalously high-count regions sampled close to a rough grain edge. There is no correlation between mean $\delta^{34}S$ value of an irregular aggregate and the standard deviation of intra-grain $\delta^{34}S$ measurements in the x-y plane (Figure S5.3). In the deepest pre-OAE-2 sample (429.4 m), irregular pyrite aggregates (Figure 5.6A-C) again feature substantial intra-grain variation in $\delta^{34}S$ (average $1\sigma = \pm 6.8‰$, compared to an average intra-grain standard error of ±2.4‰, 1σ, n=47). One of these aggregates (Figure 5.6A) displays positive spatial autocorrelation (Table S5.2), two of these aggregates (Figure 5.6A, C) feature relatively ^{34}S-depleted cores and relatively ^{34}S-enriched edges, (Table S5.2), whereas one (Figure 5.6B) displays no clear spatial isotopic trend (Table S5.2). In the sample from just before OAE-2 (426.6 m), irregular pyrite aggregates (Figure 5.6D-F) feature substantial intra-grain variation in $\delta^{34}S$ (average $1\sigma = \pm 5.5‰$, compared to an average intra-grain standard error of ±2.1‰, 1σ, n=61). One larger aggregate (Figure 5.6D) shows no clear spatial isotopic trend in the x-y plane (Table S5.2), whereas another large aggregate (Figure 5.6E) shows very clear positive spatial autocorrelation without any radial trend (Table S5.2). The $\delta^{34}S$ values in a smaller aggregate (Figure 5.6F) are again positively spatially autocorrelated when viewed in the x-y plane, but are also higher toward the grain edges (Table S5.2). Finally, in the sample from within OAE-2 (422.8 m), an irregular pyrite aggregate (Figure 5.6G) features some intra-grain

variation in $\delta^{34}S$ ($1\sigma = \pm 4.4‰$, compared to an average intra-grain standard error of $\pm 2.3‰$, 1σ, n=11). Viewed in the x-y plane, the aggregate is clearly more ^{34}S-enriched towards its edges (Table S5.2). Generally, where substantial isotopic variability can be discerned, it takes the form of radial (Figure 5.6A, C, F, and G) or lateral/linear (Figure 5.6E) enrichments in ^{34}S. These patterns are representative for the populations of irregular aggregates in all the samples studied.

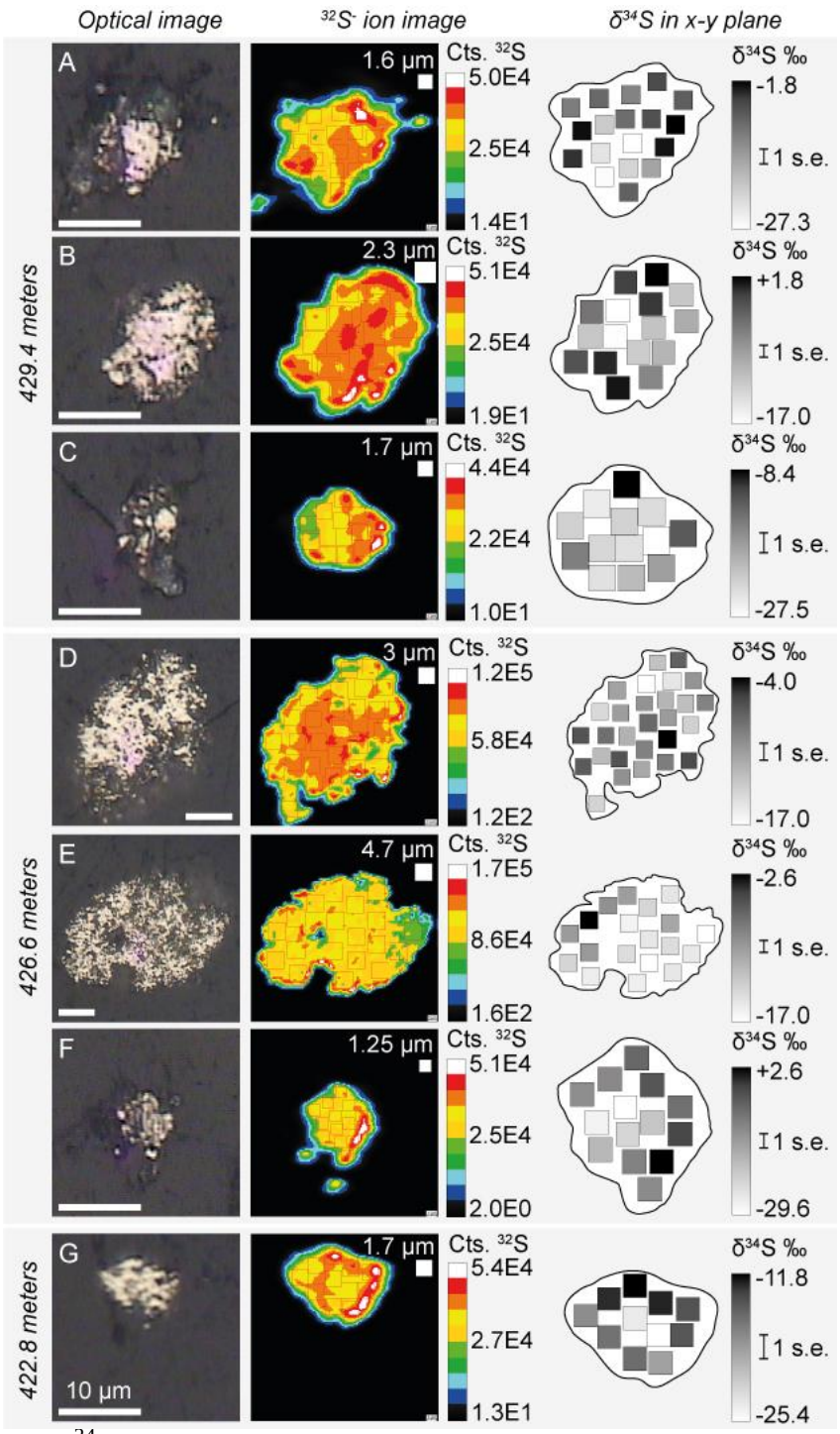

Figure 5.6. Internal $\delta^{34}S$ variability in irregular pyrite aggregates from (A, B, C) the deepest pre-OAE-2 sample, (D, E, F) the sample just before OAE-2, and (G) the syn-OAE-2 sample. From left-right, panels display: optical microscope images, where scale bars are all 10 µm; $^{32}S^{-}$ ion images, accumulated over 60-90 cycles, with inset showing the size of sub-sampled regions; and $\delta^{34}S$ values of the sub-sampled regions, where the error bar indicates the average of the standard errors for the different sub-sampled regions.

Cemented pyrite aggregate

In the sample from within OAE-2, the single cemented pyrite aggregate (Figure 5.7A) has a large amount of intra-grain $\delta^{34}S$ variability when viewed in the x-y plane ($1\sigma = \pm 7.2‰$, compared to an average intra-grain standard error of ±0.9‰, 1σ, n=26). Although there is intra-grain variation in $^{32}S^-$ ion counts, there is no trend between counts and $\delta^{34}S$ (Figure S5.5). The aggregate features positive spatial autocorrelation and radial ^{34}S-enrichment (Table S5.2) and is more ^{34}S-enriched toward its top edge (Figure 5.7A; Figure S5.6A).

Marcasite

In the sample from within OAE-2 (the only marcasite-bearing sample; Table 5.1), the cemented marcasite aggregate (perhaps a single anhedral crystal; Figure 5.7B) has a large amount of intra-grain $\delta^{34}S$ variability when viewed in the x-y plane ($1\sigma = \pm 19.1‰$, compared to an average intra-grain standard error of ±2.0‰, 1σ, n=16), whereas the irregular marcasite aggregate (Figure 5.7C) has a lesser but still easily resolved degree of intra-grain $\delta^{34}S$ variability ($1\sigma = \pm 7.4‰$, compared to an average intra-grain standard error of ±2.2‰, 1σ, n=18). Although both grains show intra-grain variation in $^{32}S^-$ ion counts, there is no trend between counts and $\delta^{34}S$ (Figure S5.5B-C). The more ^{34}S-enriched areas are farther from the center of the cemented marcasite aggregate (Figure 5.7B; Figure S5.6B), but closer to a central linear region of the irregular marcasite aggregate, parallel to the top/bottom edges (Figure 5.7C; Figure S5.6C). Neither grain displays autocorrelation or a simple radial trend (Table S5.2).

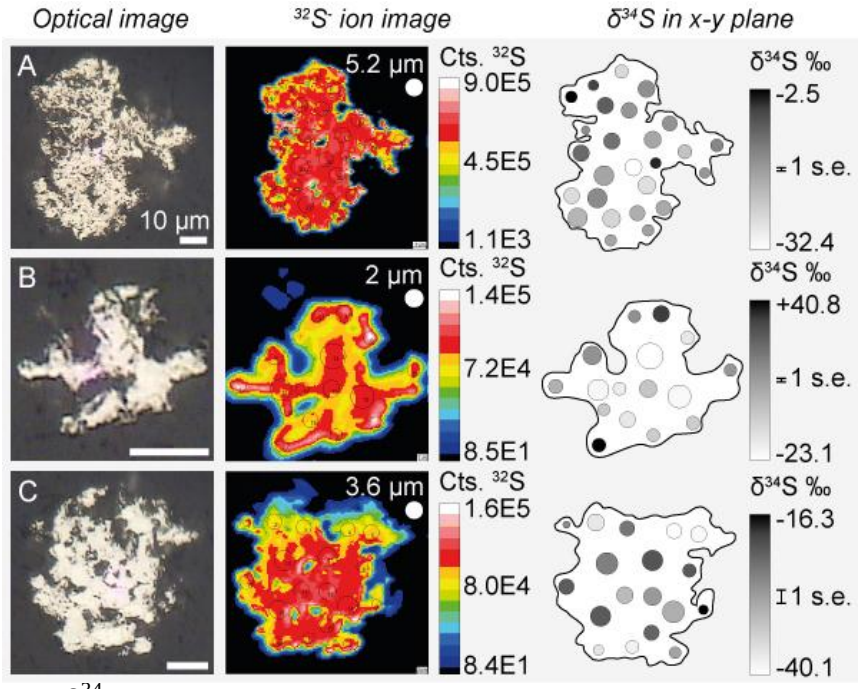

Figure 5.7. Internal $\delta^{34}S$ variability in (A) a cemented pyrite aggregate, (B) a cemented marcasite aggregate, and (C) a non-cemented marcasite aggregate, from the syn- OAE-2 sample. From left-right, panels display: optical microscope images, where scale bars are all 10 µm; $^{32}S^{-}$ ion images, accumulated over 90-480 cycles, with inset showing the size of sub-sampled regions; and $\delta^{34}S$ values of sub-sampled regions, where the error bar indicates the average of the standard errors for the different sub-sampled regions.

5.4 Discussion

There are several different Fe sulfide minerals and textures present in the sediments of Demerara Rise, the relative proportions of which change noticeably after the onset of OAE-2 (Table 5.1; Figure 5.4A). Grain-specific analyses reveal that each textural group carries a distinct average S isotopic signature (Figure 5.4A), and thus any change in the proportions of these groups inevitably will result in a change to the bulk $\delta^{34}S_{CRS}$ value. In particular, the near-disappearance of ^{34}S-enriched irregular pyrite aggregates and the appearance of a large ^{34}S-depleted cemented pyrite aggregate, in addition to a non-cemented marcasite aggregate, correspond with the stark decrease in bulk $\delta^{34}S_{CRS}$ values during OAE-2 at Demerara Rise. All mineral phases and textural groups feature resolvable intra-grain variability (Figures 5.5-5.7). The non-random spatial

distribution of the intra-grain variability in the majority of grains (Table S5.2) suggests that they formed in fluids whose isotopic compositions were evolving. This information is summarized in Figure 5.8. Below we seek to address why more ^{34}S-depleted S appears to have been incorporated into Fe sulfides during OAE-2 – in doing so, we integrate our results with the bulk δ^{34}S records of pyrite and organic S (Hetzel et al., 2009; Raven et al., 2019).

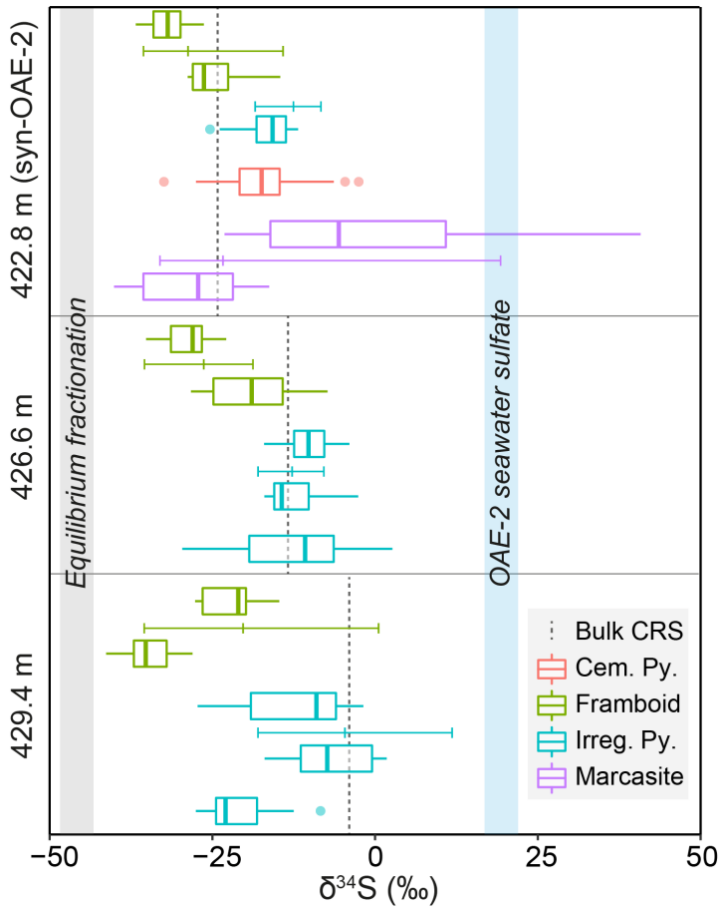

Figure 5.8. Box/whisker plots (with outliers) of intra-grain δ^{34}S observed in the x-y plane within the different Fe sulfide mineral grains in Figures 5.5-5.7. The ranges record the range of pore water sulfide δ^{34}S present during the growth of each grain. Estimates for ocean sulfate δ^{34}S (blue bar) and equilibrium offset at 20°C (gray bar) are from Paytan (2004) and Eldridge et al. (2016), respectively. Thin colored lines show the range and mean of inter-grain δ^{34}S values for each textural group.

5.4.1 The origin of the divergence between bulk CRS and OS $\delta^{34}S$ values

A major unknown is whether the Fe sulfides that constitute the CRS fraction of Demerara Rise sediments formed in the water column or in the sediments. Water column Fe sulfide formation has never been observed under oxic conditions, despite predictions of microbial sulfate reduction in sinking particles (Bianchi et al., 2018). In contrast, pyrite framboids are known to form in modern euxinic water columns (Suits and Wilkin, 1998; Wilkin et al., 1996), though it is not clear whether this is a water-column process or if it involves microenvironments in sinking organic particles. Measurements of dissolved sulfide in modern euxinic systems with initial sulfate concentrations similar to that of the mid-Cretaceous ocean display only very small isotopic enrichments with depth in the water column (Gomes and Johnston, 2017). If all Fe sulfide grains were to form by the abiotic sulfidization of sinking Fe particles, one might not therefore expect any inter- or intra-grain isotopic variability. Alternatively, if sinking particles housed both Fe and OM, sulfate reduction in microenvironments and reaction of progressively ^{34}S-enriched sulfide with Fe could produce a population of Fe sulfide grains featuring intra- and/or inter-grain isotopic variability (Louca and Crowe, 2017). Problematically, the exact same pattern could be expected for Fe sulfide grains formed in sediment pore waters, due to the progressive consumption and isotopic enrichment of residual sulfate. Fe sulfide populations from all three samples studied feature substantial inter- (Figure 5.4) and intra-grain (Figures 5.5-5.8; Table S5.2) isotopic variability, the latter of which likely contributed to the former (Figure S5.3). Therefore Fe sulfides likely formed (and were later in some cases progressively infilled from core-rim – see Figure 5.5B for an example of incomplete infilling) either in sinking particles hosting active sulfate reduction, or in sediment pore waters. Because both these scenarios involve sulfate reduction in a (variably) diffusively-limited (‘closed’) environment, and in-situ

reaction with Fe^{3+}-bearing minerals (likely transiently protected by adsorbed OM if reaching the sediment prior to sulfidization), we can use this system as context for ascribing mechanisms to the decrease in $\delta^{34}S_{CRS}$ toward the onset of OAE-2.

As long as the magnitude of isotopic fractionation during microbial sulfate reduction (ε_{mic}) is relatively constant, the first Fe sulfide material to form in a partially closed system is expected to be the most ^{34}S-depleted, whereas the last-formed material should be the most ^{34}S-enriched due to the effects of Rayleigh distillation during sulfate reduction (Bryant et al., 2019; Jorgensen, 1979). In such a system, the primary controls on bulk $\delta^{34}S_{CRS}$ values are (i) the magnitude of ε_{mic}, (ii) the openness of the system with respect to the diffusion of water column sulfate (Claypool, 2004), (iii) the availability of Fe to react with the reduced S species to form Fe sulfides, and (iv) the kinetics of Fe sulfidization, most likely driven by Fe reactivity (Bryant et al., 2019; Fike et al., 2015; Shawar et al., 2018). Additional factors of unknown importance for $\delta^{34}S_{CRS}$ are ambient pH and E_h, as these may affect the saturation state of different sulfide minerals in the system, and the operation of different Fe sulfide formation pathways (Benning et al., 2000; Murowchick and Barnes, 1986; Poulton, 2003; Rickard, 1975; Wan et al., 2017). The primary control on ε_{mic} is the cell-specific rate of sulfate reduction (csSRR) (Leavitt et al., 2013; Sim et al., 2011a, 2011b), which is thought to relate to the availability of electron donors (Wing and Halevy, 2014). High e^--donor availability would increase csSRR and decrease ε_{mic}, resulting in bulk Fe sulfides that are less isotopically offset from seawater sulfate, and thus relatively more ^{34}S-enriched. In a more closed system, the rate of sulfate reduction is high relative to the rate of diffusion of sulfate from the water column – this ensures that the isotopic composition of remaining aqueous sulfate and product sulfide become more ^{34}S-enriched, resulting in a greater intra-sample range of preserved Fe sulfide $\delta^{34}S$ values. Greater Fe availability (i.e., higher

abundance) will ensure a more representative range of isotopic compositions of aqueous sulfide is recorded in the range of isotopic compositions of Fe sulfide material (inter- and/or intra-grain). Lower Fe availability might cause Fe to be exhausted while the concentration of sulfate in the system is still high, resulting in less ^{34}S-enriched sulfide being sequestered and leading to more ^{34}S-depleted bulk Fe sulfides (Fike et al., 2015). However, lower Fe sulfidization kinetics might lessen the rate of Fe sulfide formation relative to the rate of sulfate reduction, resulting in less ^{34}S-depleted sulfide being sequestered, leading to more ^{34}S-enriched bulk Fe sulfides (Bryant et al., 2019; Shawar et al., 2018). To summarize, the decreasing trend in bulk Fe sulfide δ^{34}S values at Demerara Rise must have resulted from either, (i) increasing ε_{mic}, (ii) increasing system openness, (iii) decreasing Fe availability, (iv) increasing Fe sulfidization kinetics, or a combination of two or more of these factors. We will use a combination of inter- and intra-grain δ^{34}S values to test the relative contributions of these factors to the previously observed changes in bulk Fe sulfide δ^{34}S values (Hetzel et al., 2009; Raven et al., 2019).

Inter- (Figure 5.4) and intra-grain data (Figures 5.5-5.8) show that all samples have minimum grain-specific δ^{34}S values of close to −40‰. Assuming that seawater sulfate had a consistent δ^{34}S value of ~+19‰ (Paytan, 2004), this implies that ε_{mic} was close to the equilibrium fractionation between sulfate and sulfide (~66‰ at the estimated temperature for bottom waters over Demerara Rise during the mid-Cretaceous climate maximum, ~20°C; Eldridge et al., 2016; Friedrich et al., 2012, 2008) both before and during OAE-2 in whatever environment the Fe sulfide grains formed (sinking particles or pore waters). Therefore, using our grain-specific data we can rule out increasing ε_{mic} as the mechanism responsible for the declining bulk Fe sulfide δ^{34}S values prior to OAE-2.

If increasing system openness were responsible for the declining bulk Fe sulfide $\delta^{34}S$ values, this would be exhibited as a narrowing range of inter- and intra-grain $\delta^{34}S$ values toward OAE-2 (Bryant et al., 2019; Fike et al., 2015; Jorgensen, 1979). We observe no such trend within the pyrites. In fact, the addition of marcasite to the Fe sulfide pool during OAE-2 served to increase the range of preserved $\delta^{34}S$ values to include strongly positive values (Figures 5.4A, 5.8). In addition, non-random intra-grain $\delta^{34}S$ heterogeneities (e.g., radial and bidirectional ^{34}S-enrichments, and positive spatial autocorrelation; Figures 5.5-5.7; Table S5.2 and Figure S5.6) suggest that most Fe sulfides in all three samples formed under at least partially closed-system conditions where sulfate was being consumed by microbial sulfate reduction faster than it could be replenished by diffusion of sulfate from the water column. Therefore, our grain-specific data enable us to rule out increasing system openness as the mechanism responsible for the declining bulk Fe sulfide $\delta^{34}S$ values prior to OAE-2.

If decreasing Fe availability were responsible for the declining bulk $\delta^{34}S_{CRS}$ values, this should be exhibited as a narrowing in the range of inter- and intra-grain $\delta^{34}S$ values toward OAE-2 (Fike et al., 2015). No such trend was observed. In addition, the median abundance of Fe sulfides in the carbonate-free fraction of sediments was actually higher for syn-OAE-2 sediments than for pre-OAE-2 sediments (Raven et al., 2019; Figure S5.1). These observations suggest that the abundance of Fe was not the major factor limiting CRS $\delta^{34}S$ values, and changes in this parameter were not responsible for the declining bulk Fe sulfide $\delta^{34}S$ values prior to OAE-2.

A final possible explanation for the declining bulk Fe sulfide $\delta^{34}S$ values relates to the kinetics of Fe sulfidization. If increasing kinetics (i.e., the average rate of Fe sulfide formation relative to the average rate of sulfate reduction) drove the observed trend, this would result in a higher proportion of Fe sulfide material featuring more ^{34}S-depleted compositions during OAE-

2, without necessarily requiring a change in the range of compositions recorded relative to the pre-OAE-2 samples. Inter- (Figure 5.4) and intra-grain (Figures 5.5-5.8) observations confirm that the syn-OAE-2 sample indeed features the largest proportion of ^{34}S-depleted material, while maintaining a large intra-sample range. Additionally, inter- and intra-grain δ^{34}S distributions for all minerals and textures in the syn-OAE-2 sample are negatively skewed (Figures 5.4, 5.8). The near-total absence of the most ^{34}S-enriched textural group (irregular pyrite aggregates; Figures 5.4, 5.8) from the syn-OAE-2 sample suggests that this increase in the kinetics of Fe sulfide formation may have resulted in physical differences in the Fe sulfides that formed, when compared with those formed prior to OAE-2. The presence of more overgrown/irregular Fe sulfide textures prior to OAE-2 (Table 5.1; Figure 5.5), likely indicates that Fe sulfide surfaces were in contact with dissolved reactants for longer durations (Bryant et al., 2019; Wilkin et al., 1996). The occurrence of marcasite suggests that the pH in the system was also lower during OAE-2 than before (Murowchick and Barnes, 1986; Schieber, 2007). Given the overlap between the isotopic compositions of pyrite and marcasite in the sample (Figure 5.4), they likely formed in similar conditions, perhaps concurrently. However, the larger inter- and intra-grain δ^{34}S ranges for marcasite (Figure 5.8; Figure S5.6) suggest that conditions conducive to marcasite formation (i.e., low pH) persisted for longer than those more conducive to pyrite formation. The elevated OM contents of the syn-OAE-2 sediments might have contributed to the unusually low pH inferred for this site and measured at others (e.g., off Angola; Siesser, 1978), by intensifying proton liberating metabolic activity such as fermentation (Vandewiele et al., 2009), methanogenesis (Arndt et al., 2006; Soetaert et al., 2007), and organic acid production.

5.4.2 Why did Fe sulfidization kinetics increase during OAE-2?

Fe isotope data has been used to suggest that the dominant source of Fe to Demerara Rise was hydrothermal (mostly likely from the Caribbean Large Igneous Province, CLIP; Du Vivier et al., 2014), before, during and after OAE-2 (Owens et al., 2012). This does not rule out a change in the mineralogy or physical characteristics of the Fe source. For example, an increase in the surface area to volume ratio of hydrothermal Fe oxyhydroxides could have occurred. This would almost certainly have enhanced Fe sulfide formation in the euxinic water column. Alternatively, if hydrothermal Fe was in part delivered as pyrite nanoparticles, as has been observed in the modern ocean (Yücel et al., 2011), this could have increased the kinetics of Fe sulfide formation at Demerara Rise by lowering the supersaturation limit in micro-niches (Harmandas et al., 1998), whether in sinking particles or sediment pore waters. The latter explanation is perhaps more likely if the dominant source of Fe was the CLIP, given that oxidized Fe could not readily travel the long distances (>1000 km) necessary to reach Demerara Rise in a euxinic water column, unless protected by prior adsorption of OM species (Meyers, 2007; Yücel et al., 2011).

Another possible explanation for the inferred increase in the kinetics of Fe sulfidization at Demerara Rise during OAE-2 relates to the low pH inferred for the site due to the presence of marcasite. The rate of Fe dissolution during the reaction of Fe oxyhydroxides with dissolved sulfide has been shown experimentally to be a function of pH, for example peaking at a pH of 5.5 for ferrihydrite in a seawater solution (Poulton, 2003). This low pH value is not common in marine sediment pore waters, but is notable for being close to the pH below which marcasite is expected to form preferentially over pyrite, ~5 (Murowchick and Barnes, 1986). The increase in the kinetics of Fe sulfidization during OAE-2 inferred from the SIMS isotopic data in this study

is therefore consistent with the observation of marcasite in syn-OAE-2 sediments, both in this study and others (Schieber, 2011; Siesser, 1978).

5.4.3 Implications for framboid size distributions as a redox proxy

A high-profile and oft-employed redox proxy uses framboid size distributions to infer paleo-redox conditions (Wilkin et al., 1996). This proxy is largely empirical in nature, but is based upon the idea that there is a limited size a water column-grown framboid can reach before it settles out, whereas a framboid forming in sediment pore waters is not subject to the same limitation – therefore, smaller framboid sizes are more indicative of water column pyrite formation, and hence euxinia. Problematically, the controls on the size of framboids forming in sediment pore waters are not well understood, though a recent study posits a simple balance of diffusion and pyrite precipitation as the control on size (Rickard, 2019a). In addition, there is substantial overlap between the mean diameters of framboids formed in modern euxinic water columns and in sediments underlying oxic water columns (Rickard, 2019b). As such, false positives and negatives are possible with this proxy.

Prior work suggests that local euxinia may have existed before, during and after OAE-2 in the water column overlying Demerara Rise (Friedrich et al., 2009; Hetzel et al., 2009; Owens et al., 2016; Raven et al., 2019). Based on the framboid size redox proxy (Wilkin et al., 1996), average framboid sizes are therefore expected to be ~5 ± 1.7 μm (1σ) for all three samples. However, they are estimated to be 4.2 ± 3.4 μm (1σ, n=35), 10.3 ± 4.2 μm (1σ, n=8), and 9.6 ± 3.3 μm (1σ, n=18) for the samples from 422.8 (syn-OAE-2), 426.6 (pre-OAE-2), and 429.4 meters' depth (pre-OAE-2), respectively. The only sample to closely correspond to the expectation for euxinic conditions is the sample from during OAE-2, although the spread is still larger than expected. This enhanced range of apparent diameters might be a function of our

measurement of 2D slices through framboids (spheres), a practice that inherently results in size distributions with a smaller mean and a larger spread than the true grain size distribution (Jones et al., 2018). Taken at face value, this proxy suggests minimal or infrequent euxinia prior to the onset of OAE-2. The lack of agreement between the framboid size redox proxy and other redox indicators warrants further investigation.

5.5 Conclusions

We have characterized and conducted grain-specific S isotopic analyses on a diverse array of Fe sulfide minerals and textures from three samples prior to and during OAE-2 from Demerara Rise, using a recently honed SIMS imaging approach (Bryant et al., 2019). The different Fe sulfide minerals/textures have distinct and relatively constant isotopic compositions, the relative proportions of these differ between the samples, and these differences in abundance appear sufficient to explain the previously reported variations in bulk $\delta^{34}S_{CRS}$ values for the samples (Raven et al., 2019). All the textures we analyzed feature substantial intra-grain $\delta^{34}S$ variability and therefore likely formed in a diffusively limited system, either in sinking particles or in sediment pore waters. Variations in ε_{mic}, open-system behavior, and overall Fe flux can be ruled out for driving the decrease in $\delta^{34}S_{CRS}$. Instead, the negative shift in bulk $\delta^{34}S_{CRS}$ values likely reflects an increase in the kinetics of Fe sulfidization leading into and during OAE-2, resulting in more of the early ^{34}S-depleted sulfide produced during sulfate reduction being incorporated into Fe sulfides. The cause of this change requires further elucidation. Finally, it should be noted that although other indicators, including high ratios of reactive to total Fe (Hetzel et al., 2009; Owens et al., 2016), elevated Fe/Al and Co/Al ratios (Hetzel et al., 2009), and a relative scarcity of benthic foraminifera (Friedrich et al., 2009), point to euxinic conditions in the water column

above Demerara Rise before and during OAE-2, a common pyrite framboid size redox proxy suggests minimal euxinia prior to OAE-2.

Acknowledgements

The authors thank Itay Halevy, Jeff Catalano, Jill Pasteris and the members of the Fike, Bradley and Catalano Labs at Washington University, whose enthusiastic discussions yielded improvements to this work. RNB acknowledges support from the McDonnell Center for the Space Sciences at Washington University in St. Louis. We also acknowledge funding to DAF from DOE/BER (#DE-SC0014613) and from the donors of the American Chemical Society Petroleum Research Fund (#57548-ND2) for partial support of this research.

Supplement

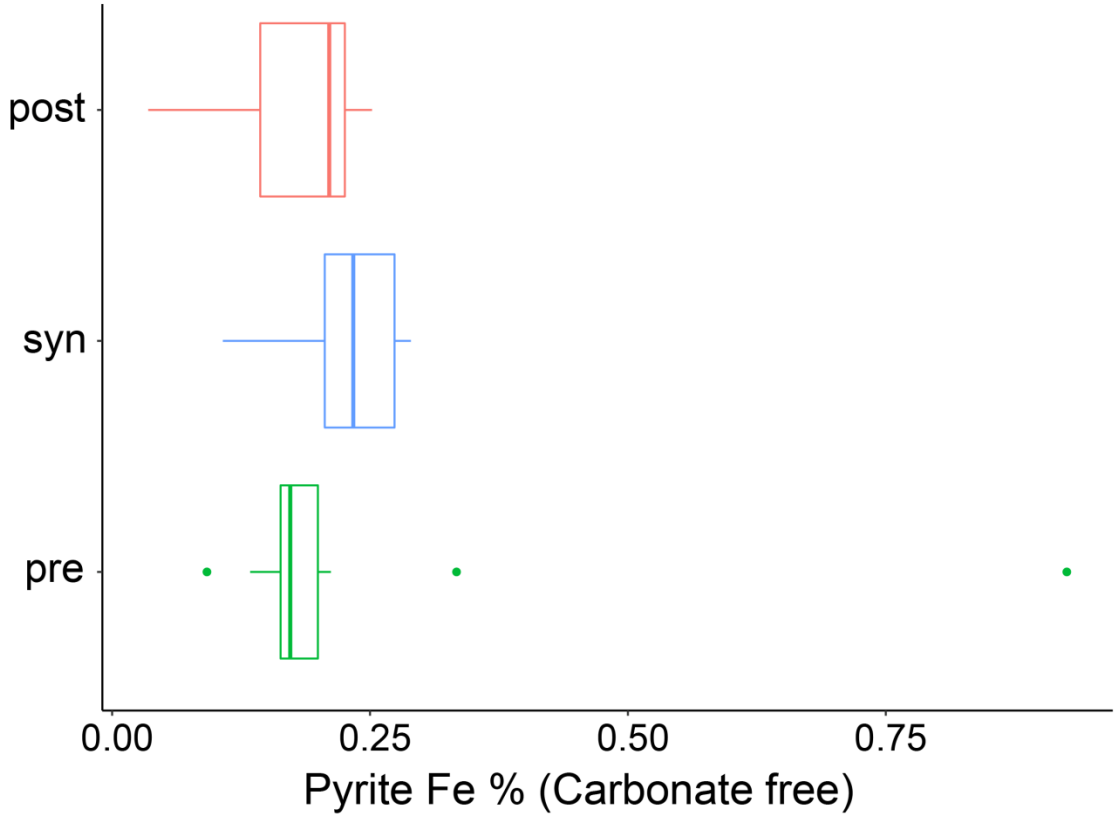

Figure S5.1. Box and whisker plots with outliers of carbonate free ‘pyrite’ Fe abundance in pre-, syn-, and post-OAE-2 sediments from the Demerara Rise, after (Raven et al., 2019).

Table S5.1: Sulfur isotope data for individual iron sulfide grains from the Demerara Rise, labeled by the relevant core depth in meters and the mineral I.D., and in-house isotope standards, labeled with 'Wards' and the mineral I.D. Listed grain sizes were measured using optical microscopy of polished grains prior to SIMS analyses, and therefore likely underestimate true grain size. Listed secondary ion counts (per time and area) are dead time-corrected but not QSA corrected. Listed $\delta^{34}S$ values are fully corrected (including for the instrumental mass fractionation, IMF), and reported relative to Vienna Canyon Diablo Troilite (VCDT). Listed standard errors refer to the standard error of $\delta^{34}S$ over the listed number of cycles. Data are reported in chronological order.

Sample	Grain size (µm)	Counts ^{34}S/s/px	Counts ^{32}S/s/px	Raster size (µm)	Cycles	IMF ($^{34}\alpha$)	$\delta^{34}S$ (‰ VCDT)	Std. error (1σ, ‰)
Wards Marcasite 1	23	1.60E+04	3.62E+05	20	30	0.99692	4.6	0.5
Wards Pyrite 1	17.6	1.80E+04	4.06E+05	20	30	1.00233	-1.0	0.7
422.8 Pyrite 1	2.4	1.31E+04	2.92E+05	20	60	1.00212	18.9	2.0
422.8 Marcasite 1	2	1.27E+04	2.98E+05	20	60	0.99688	-30.0	3.1
422.8 Pyrite 2	2	1.76E+04	4.11E+05	20	60	1.00193	-30.1	2.5
422.8 Pyrite 3	6.4	1.49E+04	3.48E+05	20	60	1.00193	-32.1	0.8
422.8 Pyrite 4	5.2	1.35E+04	3.15E+05	20	60	1.00175	-32.4	1.0
422.8 Marcasite 2	2.4	1.70E+04	3.98E+05	20	60	0.99680	-30.2	1.7
422.8 Marcasite 3	1.6	1.67E+04	3.89E+05	20	60	0.99677	-24.8	1.8
422.8 Marcasite 4	0.8	1.06E+04	2.49E+05	20	60	0.99677	-33.9	6.6
426.6 Pyrite 1	9.6	1.36E+04	3.16E+05	20	60	1.00120	-27.9	0.6
426.6 Pyrite 2	8	1.45E+04	3.35E+05	20	60	1.00102	-18.9	0.6
426.6 Pyrite 3	7.6	1.39E+04	3.23E+05	20	60	1.00083	-28.7	0.7
426.6 Pyrite 4	7.2	1.35E+04	3.10E+05	20	60	1.00065	-12.6	0.9
426.6 Pyrite 5	0.8	1.09E+04	2.49E+05	20	60	1.00065	-14.0	4.8
426.6 Pyrite 6	0.8	9.51E+03	2.18E+05	20	60	1.00065	-13.2	6.6
426.6 Pyrite 7	4.8	1.26E+04	2.95E+05	20	60	1.00047	-36.2	1.1
429.4 Pyrite 1	12.8	1.39E+04	3.19E+05	20	60	1.00028	-12.5	0.5
429.4 Pyrite 2	12	1.48E+04	3.41E+05	20	60	1.00010	-18.9	0.6
429.4 Pyrite 3	9.6	1.41E+04	3.26E+05	20	60	0.99992	-20.9	0.7
429.4 Pyrite 4	16	1.58E+04	3.60E+05	20	60	0.99973	-4.3	0.3
429.4 Pyrite 5	14.8	1.56E+04	3.61E+05	20	60	0.99955	-20.3	0.4
Wards Marcasite 2	23	1.62E+04	3.67E+05	20	30	0.99647	4.6	0.6

Wards Pyrite 2	17.6	1.84E+04	4.17E+05	20	30	0.99938	-1.0	0.4
Wards Marcasite 3	23	1.87E+04	4.24E+05	20	30	0.99575	4.6	0.5
Wards Pyrite 3	17.6	2.14E+04	4.86E+05	20	30	0.99928	-1.0	0.6
422.8 Pyrite 5	6	1.65E+04	3.88E+05	20	60	0.99921	-36.3	1.2
422.8 Pyrite 6	4.8	1.46E+04	3.41E+05	20	60	0.99915	-30.6	1.0
422.8 Pyrite 7	2.4	1.32E+04	2.96E+05	20	60	0.99909	8.8	1.6
422.8 Pyrite 8	0.8	8.56E+03	1.99E+05	20	60	0.99909	-23.1	4.1
422.8 Marcasite 5	2.4	1.71E+04	4.03E+05	20	60	0.99543	-31.0	1.9
422.8 Pyrite 9	2.4	1.67E+04	3.80E+05	20	60	0.99897	-6.8	2.1
422.8 Marcasite 6	2.4	1.60E+04	3.74E+05	20	60	0.99528	-24.6	2.0
422.8 Pyrite 10	2.8	1.48E+04	3.46E+05	20	60	0.99885	-29.7	1.3
422.8 Pyrite 11	1	1.51E+04	3.50E+05	20	60	0.99879	-23.1	2.6
422.8 Pyrite 12	1.6	1.69E+04	3.94E+05	20	60	0.99879	-29.3	2.1
422.8 Pyrite 13	4	1.36E+04	3.15E+05	20	60	0.99879	-21.1	1.3
426.6 Pyrite 8	11.2	1.61E+04	3.74E+05	20	60	0.99874	-24.1	0.5
426.6 Pyrite 9	12	1.61E+04	3.75E+05	20	60	0.99868	-24.9	0.5
426.6 Pyrite 10	10.4	1.62E+04	3.75E+05	20	60	0.99862	-19.4	0.4
429.4 Pyrite 6	10	1.65E+04	3.83E+05	20	60	0.99856	-24.2	0.5
429.4 Pyrite 7	9.6	1.57E+04	3.67E+05	20	60	0.99850	-27.5	0.5
429.4 Pyrite 8	8	1.57E+04	3.58E+05	20	60	0.99844	-8.7	0.8
429.4 Pyrite 9	10.8	1.65E+04	3.81E+05	20	60	0.99838	-16.4	0.4
429.4 Pyrite 10	7.2	1.67E+04	3.89E+05	20	60	0.99832	-28.3	0.7
429.4 Pyrite 11	8	1.63E+04	3.69E+05	20	60	0.99832	1.7	0.6
422.8 Pyrite 14	7.2	1.60E+04	3.69E+05	20	60	0.99826	-18.4	0.5
422.8 Pyrite 15	3.2	1.51E+04	3.54E+05	20	60	0.99820	-29.4	1.6
Wards Marcasite 4	23	1.85E+04	4.19E+05	20	30	0.99429	4.6	0.5
Wards Pyrite 4	17.6	2.13E+04	4.83E+05	20	30	0.99815	-1.0	0.5
Wards Marcasite 5	23	1.86E+04	4.22E+05	20	30	0.99435	4.6	0.5
Wards Pyrite 5	17.6	2.11E+04	4.79E+05	20	30	0.99844	-1.0	0.4
422.8 Pyrite 16	2.4	1.47E+04	3.45E+05	20	60	0.99831	-29.5	1.6
422.8 Pyrite 17	2.4	1.64E+04	3.82E+05	20	60	0.99819	-26.6	1.4

422.8 Pyrite 18	3.2	1.61E+04	3.80E+05	20	60	0.99819	-36.6	1.5
422.8 Pyrite 19	0.8	1.42E+04	3.26E+05	20	60	0.99819	-10.2	4.8
422.8 Pyrite 20	4.4	1.46E+04	3.39E+05	20	60	0.99807	-25.0	0.8
422.8 Pyrite 21	6.4	1.62E+04	3.75E+05	20	60	0.99795	-19.2	0.7
422.8 Marcasite 7	1.6	1.63E+04	3.81E+05	20	60	0.99407	-22.7	2.2
422.8 Marcasite 8	2.4	1.43E+04	3.33E+05	20	60	0.99401	-22.5	1.8
422.8 Pyrite 22	1.6	1.35E+04	3.12E+05	20	60	0.99771	-17.4	2.4
422.8 Marcasite 9	2	1.65E+04	3.82E+05	20	60	0.99396	-15.3	1.6
422.8 Pyrite 23	1.2	1.54E+04	3.61E+05	20	60	0.99759	-33.1	2.8
422.8 Pyrite 24	2.4	1.15E+04	2.70E+05	20	60	0.99747	-32.6	2.0
429.4 Pyrite 12	10.4	1.57E+04	3.67E+05	20	60	0.99735	-25.2	0.6
429.4 Pyrite 13	4.8	1.56E+04	3.64E+05	20	60	0.99723	-23.9	1.0
429.4 Pyrite 14	6.4	1.55E+04	3.58E+05	20	60	0.99711	-19.3	0.7
429.4 Pyrite 15	11.2	1.56E+04	3.65E+05	20	60	0.99699	-30.6	0.4
429.4 Pyrite 16	18.4	1.75E+04	4.03E+05	20	60	0.99687	-17.2	0.5
429.4 Pyrite 17	12	1.58E+04	3.62E+05	20	60	0.99675	-7.5	0.4
429.4 Pyrite 18	8	1.56E+04	3.59E+05	20	60	0.99663	-13.9	0.8
429.4 Pyrite 19	7.2	1.47E+04	3.48E+05	20	60	0.99651	-36.1	0.8
429.4 Pyrite 20	6.4	1.51E+04	3.49E+05	20	60	0.99651	-21.0	0.8
429.4 Pyrite 21	4	1.74E+04	3.92E+05	20	60	0.99651	11.3	0.9
Wards Marcasite 6	23	1.77E+04	4.01E+05	20	30	0.99340	4.6	0.5
Wards Pyrite 6	17.6	2.02E+04	4.60E+05	20	30	0.99640	-1.0	0.5
Wards Marcasite 7	23	1.47E+04	3.33E+05	20	30	0.99442	4.6	0.7
Wards Pyrite 7	17.6	1.65E+04	3.76E+05	20	30	0.99726	-1.0	0.6
422.8 Pyrite 25	1.2	1.53E+04	3.59E+05	20	60	0.99730	-33.9	2.2
422.8 Marcasite 10	1.6	1.41E+04	3.31E+05	20	60	0.99435	-26.1	2.3
422.8 Pyrite 26	4.8	1.14E+04	2.69E+05	20	60	0.99733	-34.2	1.0
422.8 Marcasite 11	6.4	1.18E+04	2.74E+05	20	60	0.99430	-20.5	1.1
422.8 Marcasite 12	2	1.26E+04	2.96E+05	20	60	0.99430	-30.5	2.2
422.8 Pyrite 27	2	1.40E+04	3.26E+05	20	60	0.99735	-23.7	1.9
422.8 Pyrite 28	5.6	1.18E+04	2.72E+05	20	60	0.99738	-18.1	1.0

422.8 Pyrite 29	4	1.30E+04	3.02E+05	20	60	0.99741	-23.6	1.2
422.8 Marcasite 13	2	1.25E+04	2.92E+05	20	60	0.99411	-24.8	1.9
422.8 Marcasite 14	2	1.73E+04	4.05E+05	20	60	0.99406	-29.3	2.0
422.8 Pyrite 30	4.4	1.32E+04	3.11E+05	20	60	0.99749	-36.3	0.9
422.8 Marcasite 15	2.4	1.40E+04	3.29E+05	20	60	0.99401	-30.4	1.7
422.8 Pyrite 31	4	6.05E+03	1.42E+05	20	60	0.99749	-29.3	2.4
422.8 Marcasite 16	2.4	1.48E+04	3.49E+05	20	60	0.99397	-31.0	1.7
422.8 Pyrite 32	5.6	1.20E+04	2.79E+05	20	60	0.99754	-22.7	0.8
422.8 Pyrite 33	2	1.33E+04	3.12E+05	20	60	0.99757	-34.7	2.0
422.8 Pyrite 34	1.2	1.38E+04	3.23E+05	20	60	0.99757	-29.9	3.1
422.8 Pyrite 35	6	1.19E+04	2.80E+05	20	60	0.99759	-33.3	0.8
422.8 Pyrite 36	8.8	1.21E+04	2.81E+05	20	60	0.99762	-23.7	0.9
422.8 Pyrite 37	9.2	1.19E+04	2.78E+05	20	60	0.99764	-28.5	0.7
422.8 Marcasite 17	2.4	1.31E+04	3.08E+05	20	60	0.99368	-31.9	1.9
422.8 Pyrite 38	4.4	1.17E+04	2.71E+05	20	60	0.99770	-25.4	1.2
422.8 Pyrite 39	1.2	1.25E+04	2.96E+05	20	60	0.99770	-37.4	3.7
429.4 Pyrite 22	10.8	1.17E+04	2.74E+05	20	60	0.99772	-35.2	0.5
429.4 Pyrite 23	8	1.24E+04	2.86E+05	20	60	0.99775	-18.3	0.8
429.4 Pyrite 24	7.2	1.16E+04	2.62E+05	20	60	0.99778	0.4	0.8
Wards Marcasite 8	23	1.37E+04	3.10E+05	20	30	0.99345	4.6	0.5
Wards Pyrite 8	17.6	1.56E+04	3.54E+05	20	30	0.99780	-1.0	0.6
Wards Pyrite 9	28	1.23E+04	2.78E+05	80	60	1.00355	-1.0	7.9
422.8 Pyrite 40	58.5	1.56E+04	3.61E+05	80	960	1.00006	-19.0	0.1
Wards Pyrite 10	28	1.58E+04	3.59E+05	80	60	1.00006	-1.0	0.6
Wards Marcasite 9	60	1.38E+04	3.11E+05	50	45	0.99882	4.6	0.3
Wards Pyrite 11	28	1.87E+04	4.25E+05	50	45	0.99796	-1.0	0.3
422.8 Marcasite 18	46.5	1.45E+04	3.38E+05	50	180	0.99726	-27.5	0.4
426.6 Pyrite 11	37.5	1.41E+04	3.23E+05	50	180	0.99720	-13.0	0.3
Wards Marcasite 10	60	1.60E+04	3.63E+05	50	45	0.99502	4.6	0.3
Wards Pyrite 12	28	1.81E+04	4.11E+05	50	45	0.99705	-1.0	0.3
Wards Marcasite 11	23	1.53E+04	3.48E+05	35	45	0.99164	4.6	0.5

Wards Pyrite 13	17.6	1.68E+04	3.82E+05	35	45	0.99810	-1.0	0.7
426.6 Pyrite 12	23.5	1.14E+04	2.63E+05	35	90	0.99650	-9.8	0.4
Wards Pyrite 14	28	1.72E+04	3.92E+05	35	45	0.99514	-1.0	0.2
Wards Marcasite 12	23	1.45E+04	3.31E+05	35	45	0.98980	4.6	0.3
Wards Pyrite 15	17.6	1.61E+04	3.68E+05	35	45	0.99505	-1.0	0.6
Wards Marcasite 13	23	1.44E+04	3.28E+05	25	30	0.98730	4.6	0.4
Wards Pyrite 16	17.6	1.56E+04	3.57E+05	25	30	0.99383	-1.0	0.8
422.8 Pyrite 41	19.5	1.16E+04	2.72E+05	25	90	0.99356	-26.6	0.4
422.8 Pyrite 42	3	1.23E+04	2.84E+05	25	90	0.99356	-13.2	1.0
422.8 Marcasite 19	17	1.25E+04	2.90E+05	25	90	0.98692	-9.8	0.3
426.6 Pyrite 13	19	1.17E+04	2.74E+05	25	90	0.99295	-28.2	0.4
426.6 Pyrite 14	1.5	1.13E+04	2.62E+05	25	90	0.99295	-16.0	1.7
Wards Marcasite 14	23	1.30E+04	2.97E+05	25	30	0.98667	4.6	0.4
Wards Pyrite 17	17.6	1.50E+04	3.42E+05	25	30	0.99268	-1.0	0.9

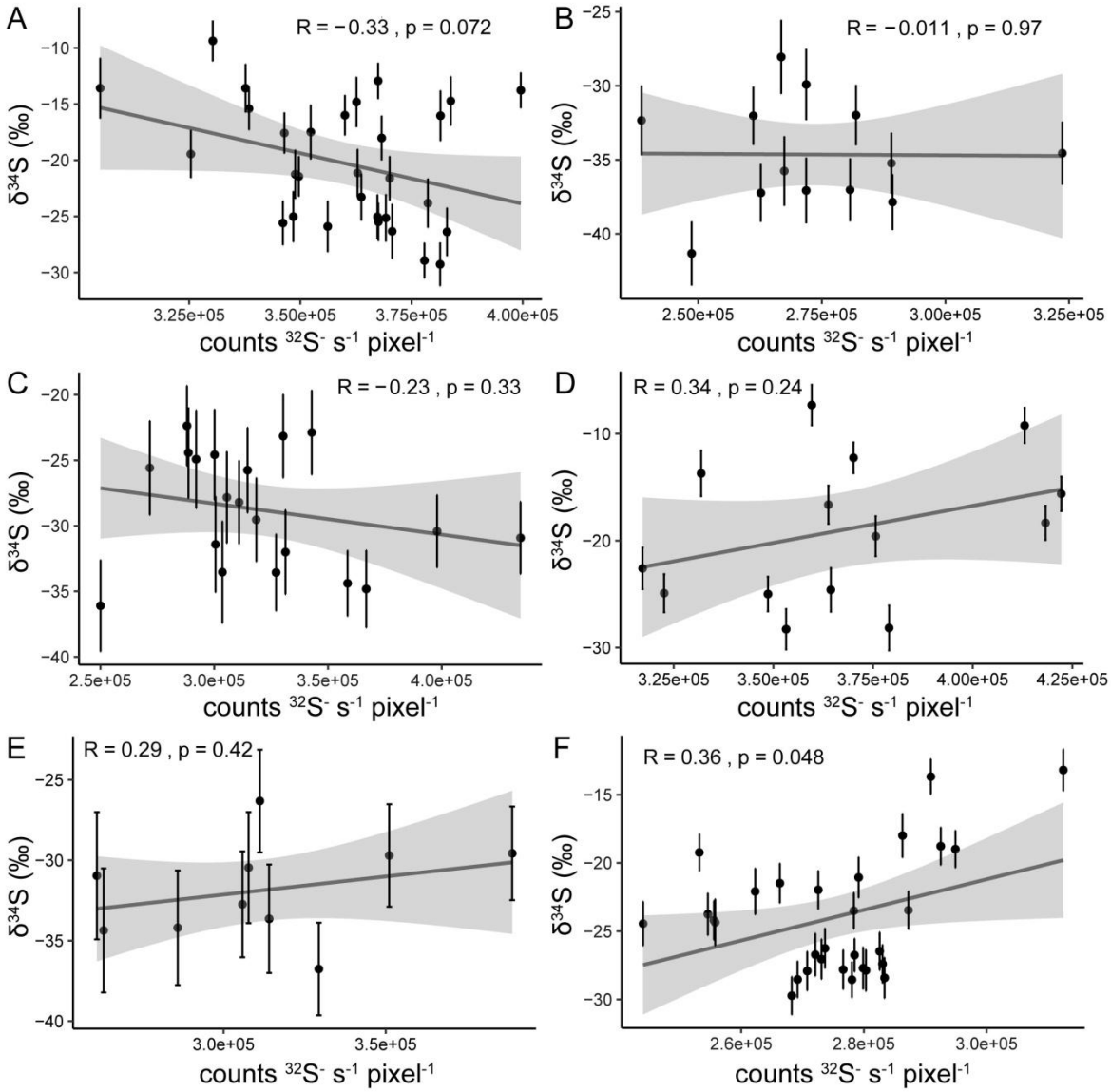

Figure S5.2. Intra-grain $\delta^{34}S$ vs. time- and area-normalized $^{32}S^-$ counts in multiple regions of interest in framboids from (A, B) the deepest pre-OAE-2 sample, (C, D) the sample just before OAE-2, and (E, F) the syn-OAE-2 sample. Parts A-F correspond to parts A-F in Figure 5.5 (main text). Error bars represent the standard error over cycles. The gray lines are linear regressions, where the gray shaded regions are 95% confidence intervals. Listed p-values are Pearson correlation coefficients.

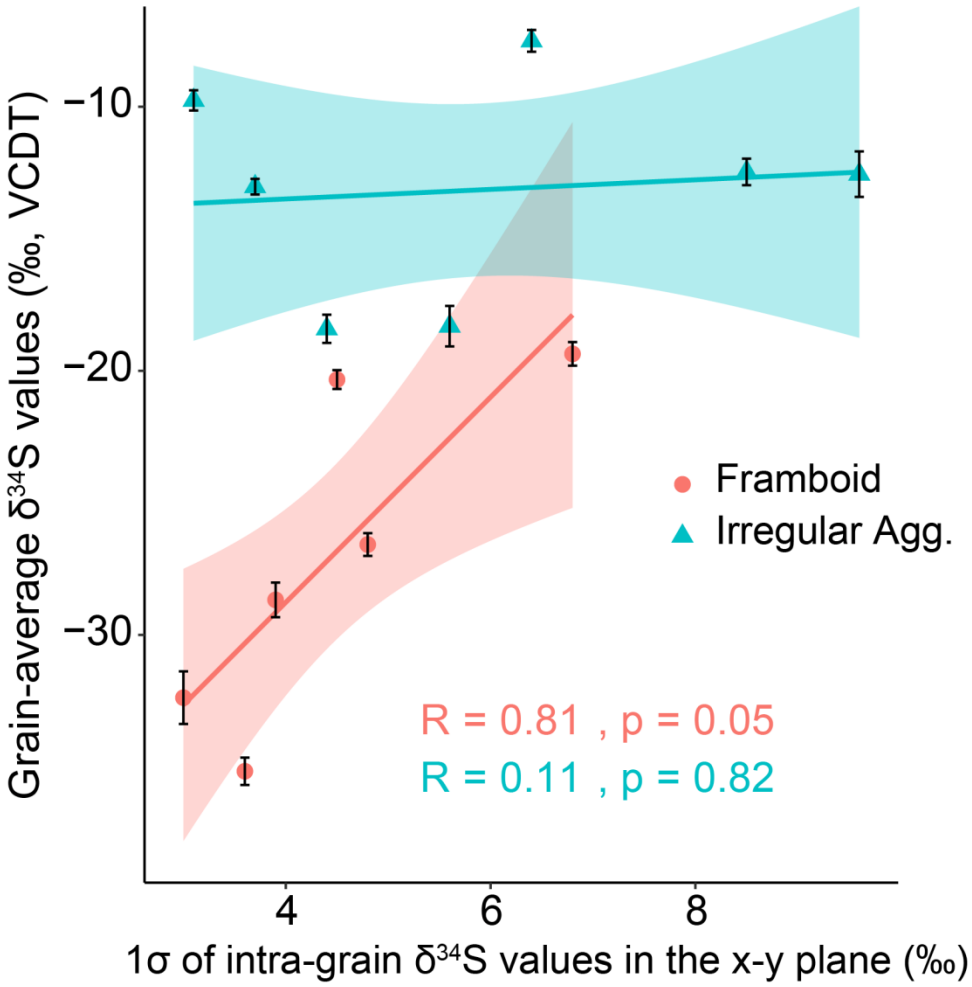

Figure S5.3. Standard deviations of intra-grain $\delta^{34}S$ values for multiple regions within pyrite grains (from all three samples) vs. the average $\delta^{34}S$ values for the corresponding grains. Blue data correspond to irregular pyrite aggregates and red data correspond to pyrite framboids. Error bars represent the standard error over cycles. The thick lines are linear regressions, where the shaded regions are 95% confidence intervals. Listed p-values are Pearson correlation coefficients.

Table S5.2. Measures of intra-grain spatial $\delta^{34}S$ variability in the grains seen in Figures 5.5-5.7 (main text). For the global Moran's I test, if the observed statistic is positive and over 1 SD greater than the expected statistic under the null hypothesis of no spatial autocorrelation (a function of *n*), intra-grain $\delta^{34}S$ values are positively spatially autocorrelated. The *p*-value indicates the significance of the autocorrelation. For the radial linear test, a negative R value indicates enrichment in ^{34}S toward the edges of a grain. The *p*-value indicates the significance of this linear correlation. For both tests, *p*-values < 0.1 are highlighted in bold.

	Global Moran's I test				Radial linear test	
Figure	**Observed**	**Expected**	**SD (1σ)**	***p*-value**	**R value**	***p*-value**
5A	-0.0017	-0.034	0.027	0.22	-0.74	**3.7E-06**
5B	-0.089	-0.083	0.043	0.9	0.79	**0.0013**
5C	-0.074	-0.053	0.034	0.52	0.29	0.21
5D	-0.03	-0.077	0.046	0.31	-0.7	**0.0054**
5E	-0.077	-0.11	0.051	0.5	-0.2	0.57
5F	0.034	-0.034	0.026	**0.0083**	-0.7	**1.7E-05**
6A	0.0097	-0.059	0.037	**0.064**	-0.42	**0.085**
6B	-0.045	-0.067	0.041	0.60	-0.32	0.22
6C	-0.12	-0.083	0.042	0.38	-0.47	**0.099**
6D	-0.0091	-0.037	0.027	0.31	0.044	0.82
6E	0.078	-0.056	0.036	**0.00016**	-0.27	0.27
6F	0.021	-0.077	0.043	**0.024**	-0.56	**0.038**
6G	-0.088	-0.1	0.05	0.81	-0.88	**0.00036**
7A	0.014	-0.04	0.031	**0.083**	-0.34	**0.087**
7B	-0.052	-0.067	0.04	0.72	-0.42	0.11
7C	-0.068	-0.059	0.04	0.81	0.011	0.97

Global Moran's I: In order to test for autocorrelation of intra-grain $\delta^{34}S$ values (i.e., whether closer regions have more/less similar values than more distant regions), we used global Moran's I (Moran, 1950). We assigned each intra-grain region of interest x- and y-coordinates using the top left corner of each ion image as the origin, and the center of each region of interest as the datum. We then generated a matrix of inverse distance weights by doing the following. We generated a distance matrix, took the inverse of the matrix values, and replaced the diagonal entries with zero. This produces a matrix where each off-diagonal entry [*i*, *j*] in the matrix is equal to 1/(distance between point *i* and point *j*). We then used the Moran.I function in the "ape" package in R (Paradis et al., 2004) weighted by our inverse distance matrix to calculate global Moran's I. *Radial linear correlation*: To test for radial $\delta^{34}S$ patterns, we measured the distance between the center of each region of interest and the nearest grain edge (as inferred from the accumulated $^{32}S^-$ ion image). We then calculated R and *p*-values (Pearson's correlation) for the linear regression between distance and $\delta^{34}S$. Note that where autocorrelation exists, this can cause underestimation of *p*-values.

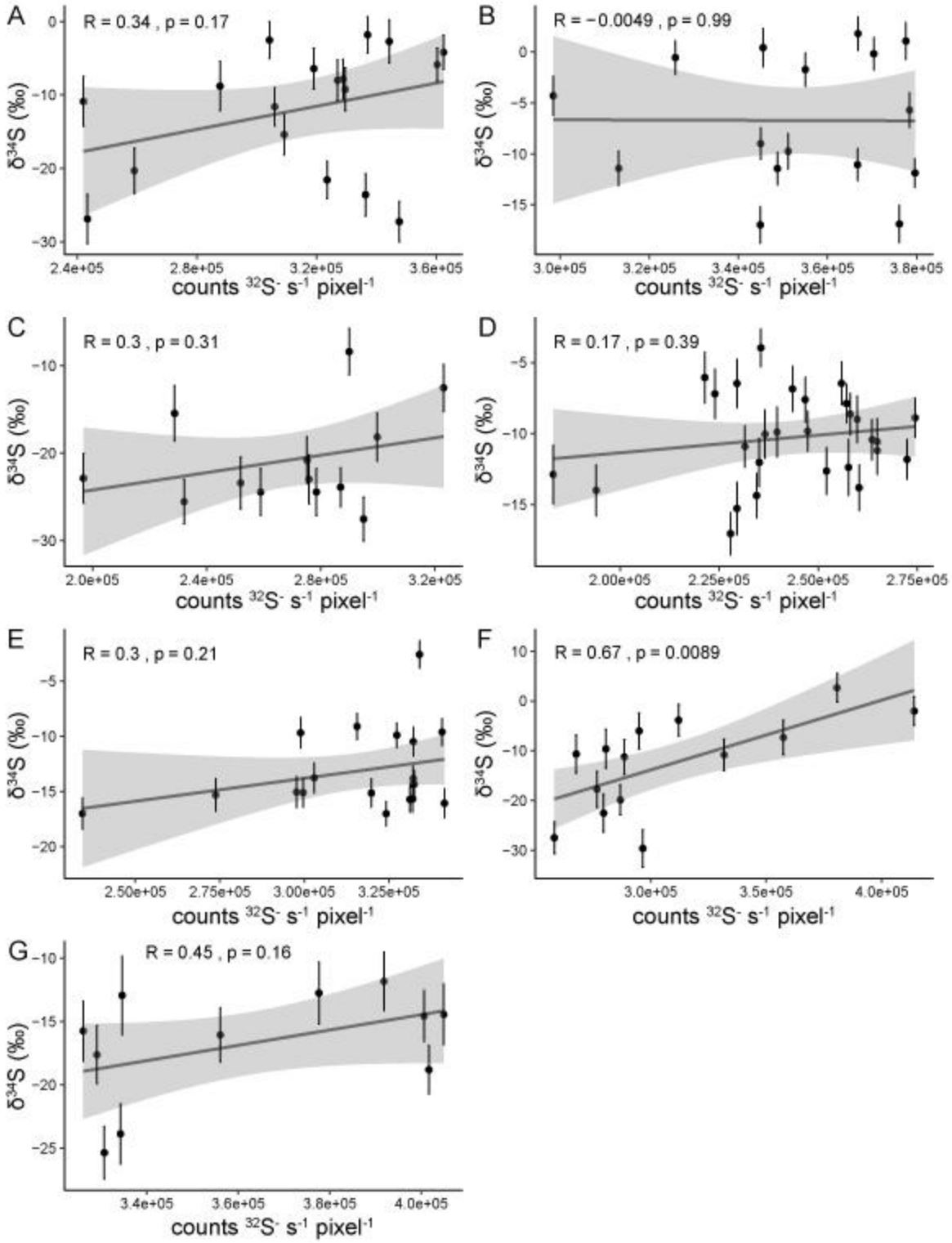

Figure S5.4. Intra-grain $\delta^{34}S$ vs. time- and area-normalized $^{32}S^-$ counts in multiple regions of interest in irregular pyrite aggregates from (A, B, C) the deepest pre-OAE-2 sample, (D, E, F) the sample just before OAE-2, and (G) the syn-OAE-2 sample. Parts A-G correspond to parts A-G in Figure 5.6 (main text). Error bars represent the standard error over cycles. The gray lines are linear regressions, where the gray shaded regions are 95% confidence intervals. Listed p-values are Pearson correlation coefficients.

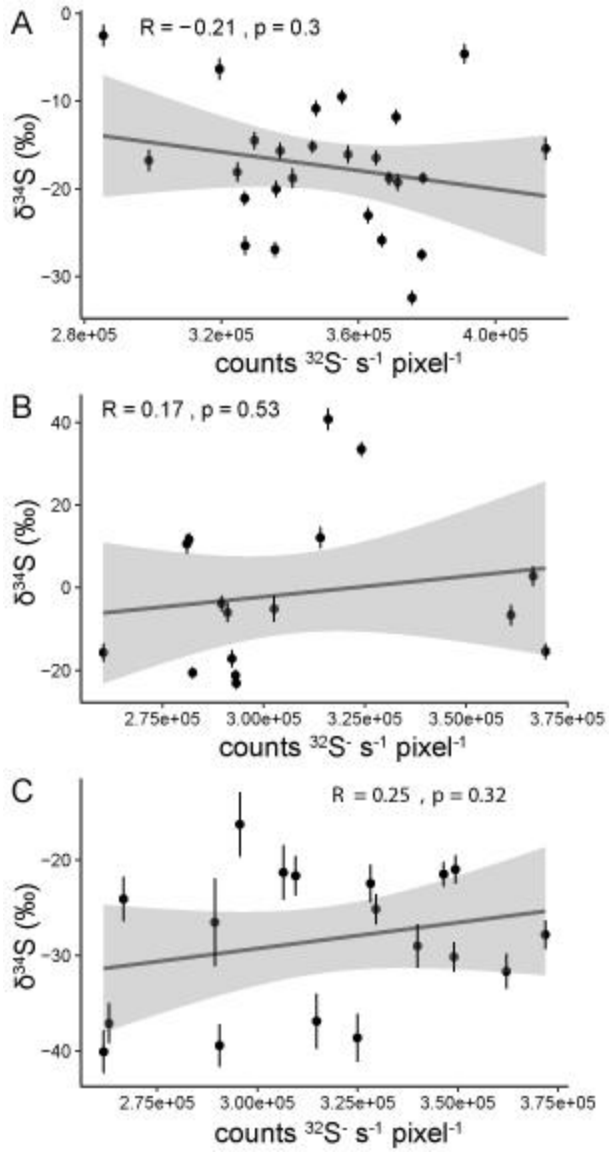

Figure S5.5. Intra-grain $\delta^{34}S$ vs. time- and area-normalized $^{32}S^-$ counts in multiple regions of interest in (A) a cemented pyrite aggregate, (B) a cemented marcasite aggregate, and (C) a non-cemented marcasite aggregate, from the syn-OAE-2 sample. Parts A-C correspond to parts A-C in Figure 5.7 (main text). Error bars represent the standard error over cycles. The gray lines are linear regressions, where the gray shaded regions are 95% confidence intervals. Listed p-values are Pearson correlation coefficients.

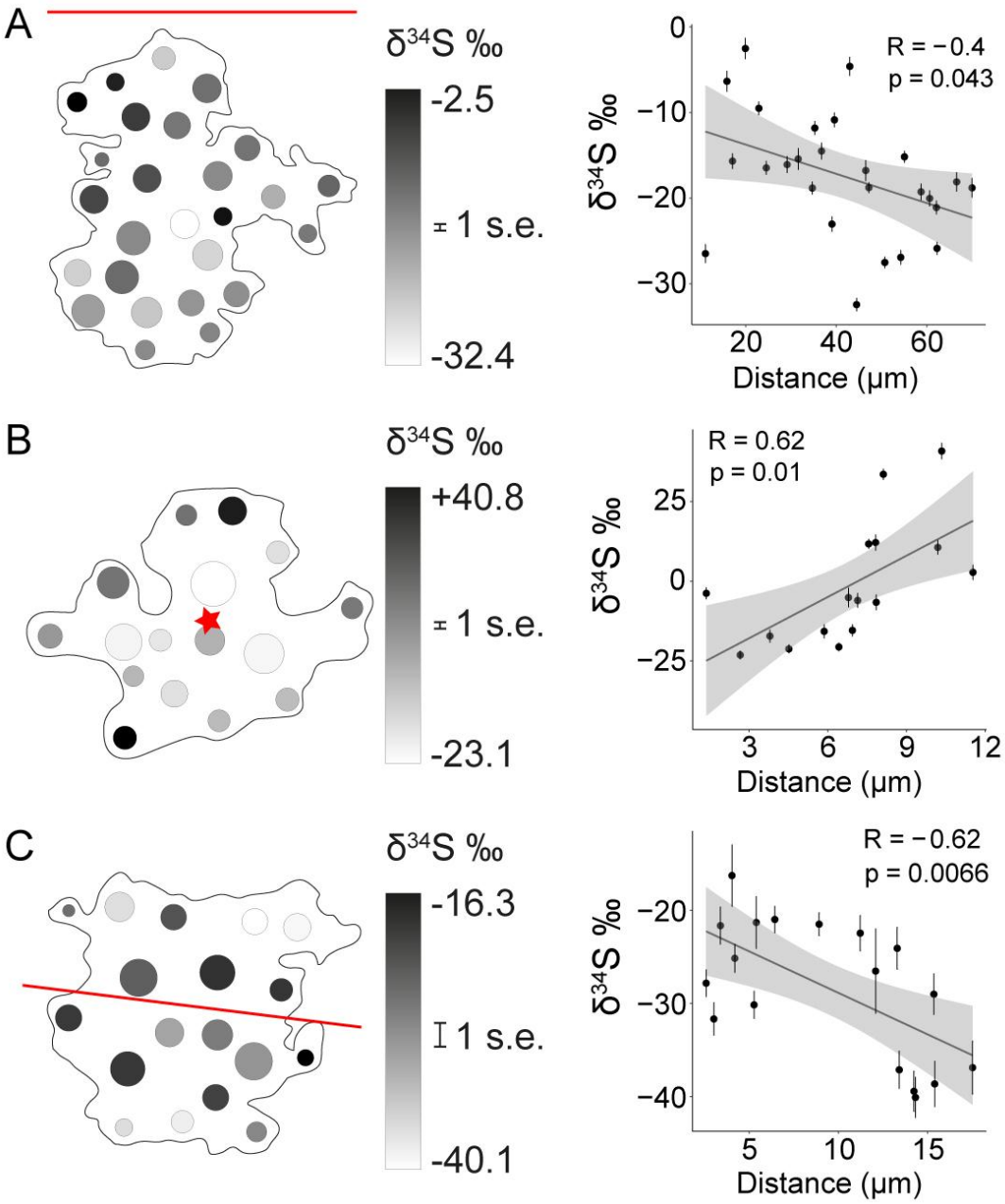

Figure S5.6. Internal $\delta^{34}S$ variability over the x-y plane for (A) a cemented pyrite aggregate, (B) a cemented marcasite aggregate, and (C) a non-cemented marcasite aggregate, from the syn-OAE-2 sample. Parts A-C correspond to parts A-C in Figure 5.7 (main text) and Figure S5.5. The left panels show $\delta^{34}S$ values of the sub-sampled regions, where the error bar indicates the average standard error over cycles, and the red line or star is the reference point for spatial pattern analysis. The right panels display $\delta^{34}S$ values of the sub-sampled circular regions vs. the distance of the circle center from the red reference point (i.e., star or line). Error bars represent the standard error over cycles. The gray lines are linear regressions, where the gray shaded regions are 95% confidence intervals. Listed p-values are Pearson correlation coefficients.

Chapter 6: Conclusions and future directions

6.1 Conclusions

In Chapter 2, faced with a need to be able to confirm the mineral identity of individual iron sulfide grains (particularly, pyrite) prior to grain-specific geochemical analyses, we determined the magnitude of several effects on the Raman spectrum of pyrite. Firstly, we identified a heating effect that can cause sufficient downshift in Raman bands to encompass and also explain most of the band position variability in previously reported Raman spectra for pyrite. The magnitude of this effect is most easily minimized through the use of low (sub-mW) laser powers. Secondly, we confirmed the expectation that the band intensity ratios in Raman spectra for pyrite vary due to changes in unit cell orientation with respect to the laser's plane of polarization. In sum, experimental set-up (laser wavelength and power, objective N.A.) and physical nature of the sample (grain size, morphology, and orientation) determine the position, relative intensity, and relative area of Raman bands for key iron sulfide minerals.

In Chapter 3, we detailed novel procedures for reconstructing local paleo-environmental conditions associated with iron sulfide mineral formation. These procedures included the physical isolation, mounting, and sulfur isotopic analysis of pyrite and marcasite grains from marine sediments and sedimentary rocks. All procedures were tested extensively on isotopically homogeneous marcasite and pyrite of hydrothermal origin, pyrites from modern sediments in Santa Barbara basin, and marcasites and pyrites from two mid-Cretaceous black shales. The overall procedure was found to produce statistically robust $\delta^{34}S$ data that is representative of bulk iron sulfide $\delta^{34}S$ ratios. Importantly, this procedure is the first to allow precise and accurate determination of intra-grain $\delta^{34}S$ variability at the micro-scale within iron sulfide grains. Additionally, we concluded that measured inter-grain $\delta^{34}S$ variability was a direct record of the

$\delta^{34}S$ values of aqueous reduced sulfur in the fluid(s) from which the iron sulfides precipitated, to the degree that iron was still available. Thus, this technique allows local environmental conditions associated with iron sulfide formation to be reconstructed.

In Chapter 4, we employed the analytical procedures detailed in Chapters 2 and 3 to investigate the mechanism(s) responsible for large magnitude $\delta^{34}S_{pyr}$ oscillations associated with glacial-interglacial environmental changes in Gulf of Lion sediments. By generating statistically robust populations of individual microscale pyrite analyses from samples spanning two glacial-interglacial transitions, we were able to both determine the true magnitude of microbial fractionation (ε_{mic}), which is a direct measure of microbial activity in marine sediments, and reconstruct the details of local depositional environments and how they modulated exchange fluxes between the sediments and overlying water column. These capabilities are entirely unique to this novel method. We found that while minimum grain-specific $\delta^{34}S_{pyr}$ values were similar for all samples, the inter-grain range of $\delta^{34}S_{pyr}$ values was larger for samples with larger bulk $\delta^{34}S_{pyr}$ values. In addition, all grains featured no discernible intra-grain $\delta^{34}S_{pyr}$ variability. From these observations, we interpreted that while ε_{mic} (and thus microbial activity) did not change in response to glacial-interglacial cycles, the diffusive exchange of sulfate between the water column and sediment pore waters was severely limited in glacial intervals, leading to rapid ^{34}S-enrichment of the aqueous sulfur pool during microbial sulfate reduction, which was recorded as large inter-grain $\delta^{34}S_{pyr}$ ranges. An independently constrained diagenetic model suggests that this glacial data is consistent with the high sedimentation rates inferred for glacial intervals in the Gulf of Lion. The minimal intra-grain $\delta^{34}S_{pyr}$ variability we observed likely indicates that the growth of individual pyrite grains in the same sample initiated at different times and continued only for very short durations in each

case. As a result, this method provides a new way to tell time (i.e., the order in which pyrites formed), opening new avenues of research.

Finally, in Chapter 5, we again applied the micro-analytical tools discussed in Chapters 2 and 3 to investigate the cause of a marked decline in bulk iron sulfide $\delta^{34}S$ values leading up to and throughout the Cenomanian-Turonian Ocean Anoxic Event (OAE-2). We found that samples from before and during OAE-2 featured several distinct iron sulfide minerals (i.e., pyrite and marcasite) and textures (e.g., framboids vs. irregular aggregates). The different iron sulfide minerals/textures were found to be isotopically distinct and the relative proportions of these differed between the samples. These differences are largely consistent with the previously reported bulk iron sulfide $\delta^{34}S$ values for the samples. All the textures we analyzed featured substantial intra-grain $\delta^{34}S$ variability and we interpreted this to mean that they likely formed in a system characterized by low diffusive exchange with the water column, either in sinking particles or in sediment pore waters. The negative shift in bulk iron sulfide $\delta^{34}S$ values likely reflects an increase in the kinetics of Fe sulfidization toward the onset of OAE-2, leading to more of the early ^{34}S-depleted sulfide produced during sulfate reduction being incorporated into iron sulfides.

6.2 Future directions

Although the conclusions of this dissertation suggest that many past studies utilizing Δ_{pyr} may have interpreted the results incorrectly, this realization opens many doors for future research activities. For example, the apparent sensitivity of Δ_{pyr} to local depositional parameters such as sedimentation rate suggests that it could readily be used as a proxy for past local changes in sedimentation rate, which may be linked to environmental changes on larger, possibly global spatial scales, such as glaciations and/or tectonic upheaval. If previous observations of Δ_{pyr} can

be categorized in the context of the sedimentary facies they are associated with, there is certainly scope for extracting meaningful supra-local environmental information from the rock record.

Perhaps one of the most exciting outcomes of this work is the identification of grain-specific $\delta^{34}S_{pyr}$ minima (coupled with coeval $\delta^{34}S_{CAS}$ data) as a proxy for ε_{mic} in the ancient rock record. Our understanding of the controls on ε_{mic} has improved greatly in the last decade, and can be summarized as the following: (1) if sulfate is abundant, ε_{mic} is sensitive to electron donor availability, and (2) if sulfate is not abundant, ε_{mic} is sensitive to sulfate availability (Bradley et al., 2016). Broadly speaking, estimates of ε_{mic} could be used as a proxy for either past sulfate or electron donor availability, depending on the time- and locale-specific abundance of sulfate in the environment. ε_{mic} could be possibly be used to estimate marine sulfate concentration prior to the Paleoproterozoic Great Oxygenation Event (GOE). Additionally, ε_{mic} could be used to investigate the timing and magnitude of major transitions in oceanic redox, most notably the Paleoproterozoic GOE. The main challenge for anyone wishing to carry out this work will undoubtedly be finding rocks that carry a pristine signal of early diagenetic sulfur cycling, despite their extreme age and likely sub-greenschist facies (or higher) metamorphic grade. Framboidal pyrite (the least ambiguous early diagenetic iron sulfide phase) is rare in such rocks and is known to recrystallize during greenschist facies regional metamorphism (Powell, 2003), possibly leading to sulfur isotope homogenization on scales from micrometers to kilometres. As long as the original population of pyrite in the sedimentary protoliths of these metamorphic rocks featured some inter-grain $\delta^{34}S$ variability, homogenization would lead to inaccurate estimates of ε_{mic}. Despite the many challenges, some rock sequences have recently emerged as promising candidates for this research, as demonstrated by apparent sample-to-sample and intra-sample iron sulfide-$\delta^{34}S$ variability obtained via grain-specific isotopic analyses. These include micrometer-

sized pyrites in the 2.7 Gyr-old Tumbiana Fm. in Western Australia (Marin-Carbonne et al., 2018) and disseminated micrometer-sized and framboidal pyrites in the 2.45 to 2.22 Gyr-old Turee Creek Group, also in Western Australia (Philippot et al., 2018).

The relationship between sedimentation rate and Δ_{pyr} could also be of use to the study of fossil preservation processes. Rapid burial resulting in sulfate limitation has been suggested as a possible mechanism for the preservation of soft-bodied fossils that would normally be degraded (Gaines et al., 2012), the most famous examples of which are found in the Cambrian-aged Burgess Shale Fauna (Conway Morris, 1986). The primary evidence for this claim was the observation of uniformly lower Δ_{pyr} values in fossil-bearing strata compared to those in non fossil-bearing strata in the Cambrian-aged Chengjiang Biota. Our findings support the suggestion that soft-bodied 'Burgess Shale-type' fossil preservation occurred in sediments that were deposited rapidly, leading to closed-system early marine diagenesis. This hypothesis could be tested more rigorously with the addition of further SIMS $\delta^{34}S_{pyr}$ data, for sections that have not been too heavily metamorphosed. SIMS approaches have already been used to investigate the related 'Beecher's Trilobite-type' fossil preservation pathway, and found that pyritization of Ediacaran soft-bodied fossils occurred in closed-system early diagenetic conditions (Schiffbauer et al., 2014), similar to those invoked for the Burgess Shale-type preservation.

Finally, the observation that modern glacial sedimentary pyrites feature no intra-grain $\delta^{34}S$ variability on the micro-scale, and yet show large inter-grain $\delta^{34}S$ variability, would seem to imply that they grow over short durations. However, there is still scope for intra-microcrystal $\delta^{34}S$ variability. Although there is currently no suitable method to test this, atom probe tomography (APT) has recently shown great promise for spatially resolved isotope ratio analysis

at the nano-scale (Valley et al., 2014). With further methodological development, this analytical approach could be used to detect nano-scale $\delta^{34}S$ variability within iron sulfide microcrystals.

References

Adams, D.D., Hurtgen, M.T., Sageman, B.B., 2010. Volcanic triggering of a biogeochemical cascade during Oceanic Anoxic Event 2. Nat. Geosci. 3, 201–204. doi:10.1038/ngeo743

Aller, R.C., Heilbrun, C., Panzeca, C., Zhu, Z., Baltzer, F., 2004. Coupling between sedimentary dynamics, early diagenetic processes, and biogeochemical cycling in the Amazon-Guianas mobile mud belt: Coastal French Guiana, in: Marine Geology. pp. 331–360. doi:10.1016/j.margeo.2004.04.027

Aller, R.C., Madrid, V., Chistoserdov, A., Aller, J.Y., Heilbrun, C., 2010. Unsteady diagenetic processes and sulfur biogeochemistry in tropical deltaic muds: Implications for oceanic isotope cycles and the sedimentary record. Geochim. Cosmochim. Acta 74, 4671–4692. doi:10.1016/j.gca.2010.05.008

Arndt, S., Brumsack, H.J., Wirtz, K.W., 2006. Cretaceous black shales as active bioreactors: A biogeochemical model for the deep biosphere encountered during ODP Leg 207 (Demerara Rise). Geochim. Cosmochim. Acta 70, 408–425. doi:10.1016/j.gca.2005.09.010

Barron, E.J., 1983. A warm, equable Cretaceous: The nature of the problem. Earth Sci. Rev. 19, 305–338. doi:10.1016/0012-8252(83)90001-6

Bassil, A., Puech, P., Tubery, L., Bacsa, W., Flahaut, E., 2006. Controlled laser heating of carbon nanotubes. Appl. Phys. Lett. 88. doi:10.1063/1.2199467

Bayliss, P., 1977. Crystal structure refinement of a weakly anisotropic pyrite. Am. Mineral. 62, 1168–1172.

Bellanca, A., Claps, M., Erba, E., Masetti, D., Neri, R., Premoli Silva, I., Venezia, F., 1996. Orbitally induced limestone/marlstone rhythms in the albian-cenomanian cismon section (Venetian region, northern Italy): Sedimentology, calcareous and siliceous plankton distribution, elemental and isotope geochemistry. Palaeogeogr. Palaeoclimatol. Palaeoecol. 126, 227–260. doi:10.1016/S0031-0182(96)00041-7

Benning, L.G., Wilkin, R.T., Barnes, H.L., 2000. Reaction pathways in the Fe-S system below 100°C. Chem. Geol. 167, 25–51. doi:10.1016/S0009-2541(99)00198-9

Berelson, W.M., Morine, L., Sessions, A.L., Rollins, N., Fleming, J.C., Schwalbach, J., 2018. Santa Barbara Basin Flood Layers: Impact on Sediment Diagenesis. SEPM Spec. Publ. No. 110. doi:10.2110/sepmsp.110.11

Berner, R.A., 2006. GEOCARBSULF: A combined model for Phanerozoic atmospheric O2 and CO2. Geochim. Cosmochim. Acta 70, 5653–5664. doi:10.1016/j.gca.2005.11.032

Berner, R.A., 2001. Modeling atmospheric O2 over Phanerozoic time. Geochim. Cosmochim. Acta 65, 685–694. doi:10.1016/S0016-7037(00)00572-X

Berner, R.A., 1989. Biogeochemical cycles of carbon and sulfur and their effect on atmospheric oxygen over phanerozoic time. Glob. Planet. Change 1, 97–122. doi:10.1016/0921-8181(89)90018-0

Berner, R.A., 1982. Burial of organic carbon and pyrite sulfur in the modern ocean: Its geochemical and environmental significance. Am. J. Sci. 282, 451–473. doi:10.2475/ajs.282.4.451

Bhandari, K.P., Roland, P.J., Kinner, T., Cao, Y., Choi, H., Jeong, S., Ellingson, R.J., 2015. Analysis and characterization of iron pyrite nanocrystals and nanocrystalline thin films derived from bromide anion synthesis. J. Mater. Chem. A 3, 6853–6861. doi:10.1039/C4TA06320A

Bianchi, D., Weber, T.S., Kiko, R., Deutsch, C., 2018. Global niche of marine anaerobic metabolisms expanded by particle microenvironments. Nat. Geosci. 11, 263–268. doi:10.1038/s41561-018-0081-0

Borjigin, T., Yin, L., Bian, L., Yuan, X., Zhou, C., Meng, F., Xie, X., Bao, F., 2014. Nano-Scale Spheroids and Fossils from the Ediacaran Doushantuo Formation in China. Open 5, 1–9.

Böttcher, M.E., Brumsack, H.-J., de Lange, G.J., 1998. Sulfate reduction and related stable isotope (^{34}S, ^{18}O) variations in interstitial waters from the eastern Mediterranean. Proc. Ocean Drill. Program, Sci. Results 160, 365–373. doi:papers3://publication/uuid/E5C1ECBC-54C3-4F55-BF0F-D1EF9ACADBB5

Bradley, A.S., Leavitt, W.D., Schmidt, M., Knoll, A.H., Girguis, P.R., Johnston, D.T., 2016. Patterns of sulfur isotope fractionation during microbial sulfate reduction. Geobiology 14, 91–101. doi:10.1111/gbi.12149

Briggs, D.E.G., Bottrell, S.H., Raiswell, R., 1991. Pyritization of soft-bodied fossils: Beecher's Trilobite Bed, Upper Ordovician, New York State. Geology 19, 1221–1224. doi:10.1130/0091-7613(1991)019<1221:POSBFB>2.3.CO;2

Brook, E.J., Buizert, C., 2018. Antarctic and global climate history viewed from ice cores. Nature. doi:10.1038/s41586-018-0172-5

Bryant, R.N., Jones, C., Raven, M.R., Gomes, M.L., Berelson, W.M., Bradley, A.S., Fike, D.A., 2019. Sulfur isotope analysis of microcrystalline iron sulfides using secondary ion mass spectrometry imaging: Extracting local paleo-environmental information from modern and ancient sediments. Rapid Commun. Mass Spectrom. 33, 491–502. doi:10.1002/rcm.8375

Bryant, R.N., Pasteris, J.D., Fike, D.A., 2018. Variability in the Raman Spectrum of Unpolished Growth and Fracture Surfaces of Pyrite Due to Laser Heating and Crystal Orientation. Appl. Spectrosc. 72, 37–47. doi:10.1177/0003702817736516

Calizo, I., Balandin, A.A., Bao, W., Miao, F., Lau, C.N., N., L.C., 2007. Temperature Dependence of the Raman Spectra of Graphene and Graphene Multilayers. Nano Lett. 7, 2645. doi:10.1021/nl071033g

Canfield, D.E., 2005. THE EARLY HISTORY OF ATMOSPHERIC OXYGEN: Homage to Robert M. Garrels. Annu. Rev. Earth Planet. Sci. 33, 1–36. doi:10.1146/annurev.earth.33.092203.122711

Canfield, D.E., 2004. The evolution of the Earth surface sulfur reservoir. Am. J. Sci. 304, 839–861. doi:10.2475/ajs.304.10.839

Canfield, D.E., 2001. Biogeochemistry of Sulfur Isotopes. Rev. Mineral. Geochemistry 43, 607–636. doi:10.2138/gsrmg.43.1.607

Canfield, D.E., 1991. Sulfate reduction in deep-sea sediments. Am. J. Sci. 291, 177–188. doi:10.2475/ajs.291.2.177

Canfield, D.E., Farquhar, J., 2009. Animal evolution, bioturbation, and the sulfate concentration

of the oceans. Proc. Natl. Acad. Sci. 106, 8123–8127. doi:10.1073/pnas.0902037106

Canfield, D.E., Raiswell, R., Westrich, J.T., Reaves, C.M., Berner, R.A., 1986. The use of chromium reduction in the analysis of reduced inorganic sulfur in sediments and shales. Chem. Geol. 54, 149–155. doi:10.1016/0009-2541(86)90078-1

Canfield, D.E., Teske, A., 1996. Late proterozoic rise in atmospheric oxygen concentration inferred from phylogenetic and sulphur-isotope studies. Nature 382, 127–132. doi:10.1038/382127a0

Cavalazzi, B., Barbieri, R., Cady, S.L.S., George, A.D., Gennaro, S., Westall, F., Lui, A., Canteri, R., Rossi, A.P., Ori, G.G., Taj-Eddine, K., 2012. Iron-framboids in the hydrocarbon-related Middle Devonian Hollard Mound of the Anti-Atlas mountain range in Morocco: Evidence of potential microbial biosignatures. Sediment. Geol. 263–264, 183–193. doi:10.1016/j.sedgeo.2011.09.007

Chambers, L.A. LA, Trudinger, P.A., Smith, J.W., Burns, M.S., 1975. Fractionation of sulfur isotopes by continuous cultures of Desulfovibrio desulfuricans. Can. J. … 21, 1602–7. doi:10.1139/m75-234

Chio, C.H., Sharma, S.K., Lucey, P.G., Muenow, D.W., 2003. Effects of particle size and laser-induced heating on the Raman spectra of alpha quartz grains. Appl. Spectrosc. 57, 774–783. doi:10.1366/000370203322102852

Ci, L., Zhou, Z., Song, L., Yan, X., Liu, D., Yuan, H., 2003. Temperature dependence of resonant Raman scattering in double-wall carbon nanotubes. Appl. Phys. 82.

Claypool, G.E., 2004. Ventilation of marine sediments indicated by depth profiles of pore water sulfate and δ34S. Geochemical Soc. Spec. Publ. 9, 59–65. doi:10.1016/S1873-9881(04)80007-5

Clough, R., Evans, P., Catterick, T., Evans, E.H., 2006. δ34S measurements of sulfur by multicollector inductively coupled plasma mass spectrometry. Anal. Chem. 78, 6126–6132. doi:10.1021/ac060875h

Conway Morris, S., 1986. The community structure of the Middle Cambrian phyllopod bed (Burgess Shale). Palaeontology 29, 423–467.

Coppola, L., Legendre, L., Lefevre, D., Prieur, L., Taillandier, V., Diamond Riquier, E., 2018. Seasonal and inter-annual variations of dissolved oxygen in the northwestern Mediterranean Sea (DYFAMED site). Prog. Oceanogr. 162, 187–201. doi:10.1016/j.pocean.2018.03.001

Coppola, L., Prieur, L., Taupier-Letage, I., Estournel, C., Testor, P., Lefevre, D., Belamari, S., LeReste, S., Taillandier, V., 2017. Observation of oxygen ventilation into deep waters through targeted deployment of multiple Argo-O 2 floats in the north-western Mediterranean Sea in 2013. J. Geophys. Res. Ocean. 122, 6325–6341. doi:10.1002/2016JC012594

Craddock, P.R., Rouxel, O.J., Ball, L.A., Bach, W., 2008. Sulfur isotope measurement of sulfate and sulfide by high-resolution MC-ICP-MS. Chem. Geol. 253, 102–113. doi:10.1016/j.chemgeo.2008.04.017

Cui, H., Brussel, V.U., Kitajima, K., Fournelle, J., Ishida, A., 2018. Questioning the Biogenicity of Neoproterozoic Superheavy Pyrite by SIMS. Am. Mineral. 103, 1362–1400.

doi:10.2138/am-2018-6489

Danise, S., Cavalazzi, B., Dominici, S., Westall, F., Monechi, S., Guioli, S., 2012. Evidence of microbial activity from a shallow water whale fall (Voghera, northern Italy). Palaeogeogr. Palaeoclimatol. Palaeoecol. 317–318, 13–26. doi:10.1016/j.palaeo.2011.12.001

Dash, S., Singh, A., Ajikumar, P.K., Subramanian, H., Rajalakshmi, M., Tyagi, A.K., Arora, A.K., Narasimhan, S. V., Raj, B., 2002. Synthesis and characterization of nanocrystalline thoria obtained from thermally decomposed thorium carbonate. J. Nucl. Mater. 303, 156–168. doi:10.1016/S0022-3115(02)00816-4

Ding, T., Bai, R., Li, Y., Wan, D., Zou, X., Zhang, Q., 1999. Determination of the absolute32S/34S ratio of IAEA-S-1 reference material and V-CDT sulfur isotope standard. Sci. China Ser. D Earth Sci. 42, 45–51. doi:10.1007/BF02878497

Downs, R., Hall-Wallace, M., 2003. The American Mineralogist crystal structure database. Am. Mineral.

Downs, R.T., 2006. The RRUFF Project: an integrated study of the chemistry, crystallography, Raman and infrared spectroscopy of minerals. Progr. Abstr. 19th Gen. Meet. Int. Mineral. Assoc. Kobe, Japan 117.

Drake, H., Åström, M.E., Tullborg, E.L., Whitehouse, M., Fallick, A.E., 2013. Variability of sulphur isotope ratios in pyrite and dissolved sulphate in granitoid fractures down to 1km depth - Evidence for widespread activity of sulphur reducing bacteria. Geochim. Cosmochim. Acta 102, 143–161. doi:10.1016/j.gca.2012.10.036

Drake, H., Whitehouse, M.J., Heim, C., Reiners, P.W., Tillberg, M., Hogmalm, K.J., Dopson, M., Broman, C., Åström, M.E., 2018. Unprecedented34S-enrichment of pyrite formed following microbial sulfate reduction in fractured crystalline rocks. Geobiology 16, 556–574. doi:10.1111/gbi.12297

Du Vivier, A.D.C., Selby, D., Sageman, B.B., Jarvis, I., Gröcke, D.R., Voigt, S., 2014. Marine 187Os/188Os isotope stratigraphy reveals the interaction of volcanism and ocean circulation during Oceanic Anoxic Event 2. Earth Planet. Sci. Lett. 389, 23–33. doi:10.1016/j.epsl.2013.12.024

Eldridge, D.L., Guo, W., Farquhar, J., 2016. Theoretical estimates of equilibrium sulfur isotope effects in aqueous sulfur systems: Highlighting the role of isomers in the sulfite and sulfoxylate systems. Geochim. Cosmochim. Acta 195, 171–200. doi:10.1016/j.gca.2016.09.021

Erbacher, J., Friedrich, O., Wilson, P.A., Birch, H., Mutterlose, J., 2005. Stable organic carbon isotope stratigraphy across Oceanic Anoxic Event 2 of Demerara Rise, western tropical Atlantic. Geochemistry, Geophys. Geosystems 6. doi:10.1029/2004GC000850

Everall, N.J., Lumsdon, J., Christopher, D.J., 1991. The effect of laser-induced heating upon the vibrational raman spectra of graphites and carbon fibres. Carbon N. Y. 29, 133–137. doi:10.1016/0008-6223(91)90064-P

Fike, D.A., Bradley, A.S., Rose, C. V., 2015. Rethinking the Ancient Sulfur Cycle. Annu. Rev. Earth Planet. Sci. 43, 593–622. doi:10.1146/annurev-earth-060313-054802

Fike, D.A., Grotzinger, J.P., Pratt, L.M., Summons, R.E., 2006. Oxidation of the Ediacaran

ocean. Nature 444, 744–747. doi:10.1038/nature05345

Fischer, W.W., Fike, D.A., Johnson, J.E., Raub, T.D., Guan, Y., Kirschvink, J.L., Eiler, J.M., 2014. SQUID-SIMS is a useful approach to uncover primary signals in the Archean sulfur cycle. Proc. Natl. Acad. Sci. 111, 5468–5473. doi:10.1073/pnas.1322577111

Fleischer, P., 1972. Mineralogy and sedimentation history, Santa Barbara Basin, California. J. Sediment. Res. 42, 49–58. doi:10.1306/74D72487-2B21-11D7-8648000102C1865D

Flinter, B.H., 1959. The magnetic separation of some alluvial minerals in Malaya. Am. Mineral. 44, 738–751.

Fossing, H., Jørgensen, B.B., 1989. Measurement of bacterial sulfate reduction in sediments: Evaluation of a single-step chromium reduction method. Biogeochemistry 8, 205–222. doi:10.1007/BF00002889

Friedrich, O., Erbacher, J., Moriya, K., Wilson, P.A., Kuhnert, H., 2008. Warm saline intermediate waters in the Cretaceous tropical Atlantic Ocean. Nat. Geosci. 1, 453–457. doi:10.1038/ngeo217

Friedrich, O., Erbacher, J., Wilson, P.A., Moriya, K., Mutterlose, J., 2009. Paleoenvironmental changes across the Mid Cenomanian Event in the tropical Atlantic Ocean (Demerara Rise, ODP Leg 207) inferred from benthic foraminiferal assemblages. Mar. Micropaleontol. 71, 28–40. doi:10.1016/j.marmicro.2009.01.002

Friedrich, O., Norris, R.D., Erbacher, J., 2012. Evolution of middle to late Cretaceous oceans-A 55 m.y. Record of Earth's temperature and carbon cycle. Geology 40, 107–110. doi:10.1130/G32701.1

Frigola, J., Canals, M., Cacho, I., Moreno, A., Sierro, F.J., Flores, J.A., Berné, S., Jouet, G., Dennielou, B., Herrera, G., Pasqual, C., Grimalt, J.O., Galavazi, M., Schneider, R., 2012. A 500 kyr record of global sea-level oscillations in the Gulf of Lion, Mediterranean Sea: New insights into MIS 3 sea-level variability. Clim. Past 8, 1067–1077. doi:10.5194/cp-8-1067-2012

Fu, J., Hu, Z., Li, J., Yang, L., Zhang, W., Liu, Y., Li, Q., Zong, K., Hu, S., 2017. Accurate determination of sulfur isotopes (: δ33S and δ34S) in sulfides and elemental sulfur by femtosecond laser ablation MC-ICP-MS with non-matrix matched calibration. J. Anal. At. Spectrom. 32. doi:10.1039/c7ja00282c

Gaines, R.R., Hammarlund, E.U., Hou, X., Qi, C., Gabbott, S.E., Zhao, Y., Peng, J., Canfield, D.E., 2012. Mechanism for Burgess Shale-type preservation. Proc. Natl. Acad. Sci. 109, 5180–5184. doi:10.1073/pnas.1111784109

Gambacorta, G., Bersezio, R., Weissert, H., Erba, E., 2016. Onset and demise of Cretaceous oceanic anoxic events: The coupling of surface and bottom oceanic processes in two pelagic basins of the western Tethys. Paleoceanography 31, 732–757. doi:10.1002/2015PA002922

Gao, J., Fike, D., Aller, R., 2013. Enriched Pyrite delta34S Signals in Modern Tropical Deltaic Muds. AGU Fall Meet. Abstr.

Garrels, R.M., Lerman, A., 1981. Phanerozoic cycles of sedimentary carbon and sulfur. Proc. Natl. Acad. Sci. U. S. A. 78, 4652–4656. doi:10.1073/pnas.78.8.4652

Giesemann, A., Jäger, H.J., Norman, A.L., Krouse, H.R., Brand, W.A., 1994. On-Line Sulfur-

Isotope Determination Using an Elemental Analyzer Coupled to a Mass Spectrometer. Anal. Chem. 66, 2816–2819. doi:10.1021/ac00090a005

Gill, B.C., Lyons, T.W., Young, S.A., Kump, L.R., Knoll, A.H., Saltzman, M.R., 2011. Geochemical evidence for widespread euxinia in the Later Cambrian ocean. Nature 469, 80–83. doi:10.1038/nature09700

Goldhaber, M., Kaplan, I., 1982. Controls and consequences of sulfate reduction rates in recent marine sediments. Acid Sulfate Weather. 119, 42–55.

Gomes, M.L., Fike, D.A., Bergmann, K.D., Jones, C., Knoll, A.H., 2018. Environmental insights from high-resolution (SIMS) sulfur isotope analyses of sulfides in Proterozoic microbialites with diverse mat textures. Geobiology 16, 17–34. doi:10.1111/gbi.12265

Gomes, M.L., Hurtgen, M.T., Sageman, B.B., 2016. Biogeochemical sulfur cycling during Cretaceous oceanic anoxic events: A comparison of OAE1a and OAE2. Paleoceanography 31, 233–251. doi:10.1002/2015PA002869

Gomes, M.L., Johnston, D.T., 2017. Oxygen and sulfur isotopes in sulfate in modern euxinic systems with implications for evaluating the extent of euxinia in ancient oceans. Geochim. Cosmochim. Acta 205, 331–359. doi:10.1016/j.gca.2017.02.020

Gorjan, P., Kaiho, K., Fike, D.A., Xu, C., 2012. Carbon- and sulfur-isotope geochemistry of the Hirnantian (Late Ordovician) Wangjiawan (Riverside) section, South China: Global correlation and environmental event interpretation. Palaeogeogr. Palaeoclimatol. Palaeoecol. 337–338, 14–22. doi:10.1016/j.palaeo.2012.03.021

Grassineau, N. V., 2006. High-precision EA-IRMS analysis of S and C isotopes in geological materials. Appl. Geochemistry. doi:10.1016/j.apgeochem.2006.02.015

Grassineau, N. V., Mattey, D.P., 1998. Measurement of sulphur isotopic compositions of sulphide minerals using new continuous He-flow EA-MS technology, in: Goldschmidt Conference. pp. 537–538.

Grassineau, N. V., Mattey, D.P., Lowry, D., 2001. Sulfur isotope analysis of sulfide and sulfate minerals by continuous flow-isotope ratio mass spectrometry. Anal. Chem. 73, 220–225. doi:10.1021/ac000550f

Greenwood, J.P., Mojzsis, S.J., Coath, C.D., 2000. Sulfur isotopic compositions of individual sulfides in Martiian meteorites ALH840001 and Nakhla: Implications for crust-regolith exchanges on Mars. Earth Planet. Sci. Lett. 184, 23–35. doi:10.1016/S0012-821X(00)00301-0

Habicht, K.S., Gade, M., Thamdrup, B., Berg, P., Canfield, D.E., 2002. Calibration of sulfate levels in the archean ocean. Science 298, 2372–4. doi:10.1126/science.1078265

Halevy, I., Fike, D.A., Bryant, R.N., Pasquier, V., Sela-Adler, M., Wenk, C.B., Turchyn, A. V., Wing, B.A., Claypool, G.E., n.d. Sedimentary parameters control the sulfur isotope composition of pyrite. Science This issue.

Harmandas, N.G., Navarro Fernandez, E., Koutsoukos, P.G., 1998. Crystal Growth of Pyrite in Aqueous Solutions. Inhibition by Organophosphorus Compounds. Langmuir 14, 1250–1255. doi:10.1021/la970354c

Harrison, A., Thode, H., 1958. Mechanism of the bacterial reduction of sulphate from isotope

fractionation studies. Trans. Faraday Soc. 54, 84–92.

Hart, T., Aggarwal, R., Lax, B., 1970. Temperature Dependence of Raman Scattering in Silicon. Phys. Rev. B 1, 638–642. doi:10.1103/PhysRevB.1.638

Hetzel, A., Böttcher, M.E., Wortmann, U.G., Brumsack, H.J., 2009. Paleo-redox conditions during OAE 2 reflected in Demerara Rise sediment geochemistry (ODP Leg 207). Palaeogeogr. Palaeoclimatol. Palaeoecol. 273, 302–328. doi:10.1016/j.palaeo.2008.11.005

Hoehler, T.M., Jørgensen, B.B., 2013. Microbial life under extreme. Nat. Rev. Microbiol. 11, 83–94. doi:10.1038/nrmicro2939

Huang, F., Yue, K., Tan, P., Zhang, S., Shi, Z., 1998. Temperature dependence of the Raman spectra of carbon nanotubes. J. Appl. Phys. 84. doi:http://dx.doi.org/10.1063/1.368585

Imai, H., Kawasaki, M., Yamaguchi, M., Takahashi, M., 1985. Mineralization and paragenesis of the Huanzala mine, central Peru. Econ. Geol. 80, 461–478. doi:10.2113/gsecongeo.80.2.461

Ivor Roberts, F., 1982. Trace element chemistry of pyrite: A useful guide to the occurrence of sulfide base metal mineralization. J. Geochemical Explor. 17, 49–62. doi:10.1016/0375-6742(82)90019-X

Jarvis, I., Lignum, J.S., Gröcke, D.R., Jenkyns, H.C., Pearce, M.A., 2011. Black shale deposition, atmospheric CO 2 drawdown, and cooling during the Cenomanian-Turonian Oceanic Anoxic Event. Paleoceanography 26, n/a-n/a. doi:10.1029/2010PA002081

Johnston, D.T., Farquhar, J., Canfield, D.E., 2007. Sulfur isotope insights into microbial sulfate reduction: When microbes meet models. Geochim. Cosmochim. Acta 71, 3929–3947. doi:10.1016/j.gca.2007.05.008

Jones, C., Fike, D.A., Meyer, K.M., 2018. SIMS Methodology for Isotopic Ratio Measurement of Micro-Grains in Thin Sections: True Grain Size Estimation and Deconvolution of Inter-Grain Size Gradients and Intra-Grain Radial Gradients. Geostand. Geoanalytical Res. doi:10.1111/ggr.12247

Jones, C., Fike, D.A., Peres, P., 2017. Investigation of the quasi-simultaneous arrival (QSA) effect on a CAMECA IMS 7f-GEO. Rapid Commun. Mass Spectrom. 31, 623–630. doi:10.1002/rcm.7828

Jones, D.S., Fike, D.A., 2013. Dynamic sulfur and carbon cycling through the end-Ordovician extinction revealed by paired sulfate-pyrite δ34S. Earth Planet. Sci. Lett. 363, 144–155. doi:10.1016/j.epsl.2012.12.015

Jorgensen, B.B., 1979. A theoretical model of the stable sulfur isotope distribution in marine sediments. Geochim. Cosmochim. Acta 43, 363–374. doi:10.1016/0016-7037(79)90201-1

Jørgensen, B.B., Marshall, I.P.G., 2015. Slow Microbial Life in the Seabed. Ann. Rev. Mar. Sci. 8, 311–332. doi:10.1146/annurev-marine-010814-015535

Kallmeyer, J., Pockalny, R., Adhikari, R.R., Smith, D.C., D'Hondt, S., 2015. Global distribution of microbial abundance and biomass in subseafloor. Proc. Natl. Acad. Sci. 109, 16213–16216. doi:10.1073/pnas.95.12.6578

Kamber, B.S., Whitehouse, M.J., 2007. Micro-scale sulphur isotope evidence for sulphur cycling in the late Archean shallow ocean. Geobiology 5, 5–17. doi:10.1111/j.1472-4669.2006.00091.x

Kaplan, I.R., Rittenberg, S.C., 1964. Microbiological Fractionation of Sulphur Isotopes. J. Gen. Microbiol. 34, 195–212. doi:10.1099/00221287-34-2-195

Kehrl, L., Conway, H., Holschuh, N., Campbell, S., Kurbatov, A. V., Spaulding, N.E., 2018. Evaluating the Duration and Continuity of Potential Climate Records From the Allan Hills Blue Ice Area, East Antarctica. Geophys. Res. Lett. 45, 4096–4104. doi:10.1029/2018GL077511

Kleppe, A., Jephcoat, A., 2004. High-pressure Raman spectroscopic studies of FeS2 pyrite. Mineral. Mag. 68, 433–441. doi:10.1180/0026461046830196

Kolonic, S., Sinninghe Damsté, J.S., Böttcher, M.E., Kuypers, M.M.M., Kuhnt, W., Beckmann, B., Scheeder, G., Wagner, T., 2002. Geochemical characterization of Cenomanian/Turonian black shales from the Tarfaya Basin (SW Morocco). J. Pet. Geol. 25, 325–350. doi:10.1111/j.1747-5457.2002.tb00012.x

Kozdon, R., Kita, N.T., Huberty, J.M., Fournelle, J.H., Johnson, C.A., Valley, J.W., 2010. In situ sulfur isotope analysis of sulfide minerals by SIMS: Precision and accuracy, with application to thermometry of ~3.5Ga Pilbara cherts. Chem. Geol. 275, 243–253. doi:10.1016/j.chemgeo.2010.05.015

LaFlamme, C., Martin, L., Jeon, H., Reddy, S.M., Selvaraja, V., Caruso, S., Bui, T.H., Roberts, M.P., Voute, F., Hagemann, S., Wacey, D., Littman, S., Wing, B., Fiorentini, M., Kilburn, M.R., 2016. In situ multiple sulfur isotope analysis by SIMS of pyrite, chalcopyrite, pyrrhotite, and pentlandite to refine magmatic ore genetic models. Chem. Geol. 444, 1–15. doi:10.1016/j.chemgeo.2016.09.032

Lafuente, B., Downs, R.T., Yang, H., Stone, N., 2016. The power of databases: The RRUFF project, in: Armbruster, T., Danisi, R.M. (Eds.), Highlights in Mineralogical Crystallography. W. De Gruyter Berlin, Germany, pp. 1–29. doi:10.1515/9783110417104-003

LaMer, V.K., 1952. Nucleation in Phase Transitions. Ind. Eng. Chem. 44, 1270–1277. doi:10.1021/ie50510a027

Large, R.R., Halpin, J.A., Danyushevsky, L. V., Maslennikov, V. V., Bull, S.W., Long, J.A., Gregory, D.D., Lounejeva, E., Lyons, T.W., Sack, P.J., McGoldrick, P.J., Calver, C.R., 2014. Trace element content of sedimentary pyrite as a new proxy for deep-time ocean-atmosphere evolution. Earth Planet. Sci. Lett. 389, 209–220. doi:10.1016/j.epsl.2013.12.020

Large, R.R., Maslennikov, V. V., Robert, F., Danyushevsky, L. V., Chang, Z., 2007. Multistage sedimentary and metamorphic origin of pyrite and gold in the Giant Sukhoi log deposit, Lena Gold Province, Russia. Econ. Geol. 102, 1233–1267. doi:10.2113/gsecongeo.102.7.1233

Lau, M.C.Y., Kieft, T.L., Kuloyo, O., Linage-Alvarez, B., Van Heerden, E., Lindsay, M.R., Magnabosco, C., Wang, W., Wiggins, J.B., Guo, L., Perlman, D.H., Kyin, S., Shwe, H.H., Harris, R.L., Oh, Y., Yi, M.J., Purtschert, R., Slater, G.F., Ono, S., Wei, S., Li, L., Lollar, B.S., Onstott, T.C., Karl, D.M., 2016. An oligotrophic deep-subsurface community dependent on syntrophy is dominated by sulfur-driven autotrophic denitrifiers. Proc. Natl. Acad. Sci. E7927–E7936. doi:10.1073/pnas.1612244113

Leavitt, W.D., Halevy, I., Bradley, A.S., Johnston, D.T., 2013. Influence of sulfate reduction

rates on the Phanerozoic sulfur isotope record. Proc. Natl. Acad. Sci. 110, 11244–11249. doi:10.1073/pnas.1218874110

Lentfer, C.J., Cotter, M.M., Boyd, W.E., 2003. Particle settling times for gravity sedimentation and centrifugation: A practical guide for Palynologists. J. Archaeol. Sci. 30, 149–168. doi:10.1006/jasc.2001.0786

Li, C., Sessions, A.L., Valentine, D.L., Thiagarajan, N., 2011. Organic Geochemistry D / H variation in terrestrial lipids from Santa Barbara Basin over the past 1400 years : A preliminary assessment of paleoclimatic relevance. Org. Geochem. 42, 15–24. doi:10.1016/j.orggeochem.2010.09.011

Li, H.D., Yue, K.T., Lian, Z.L., Zhan, Y., Zhou, L.X., Zhang, S.L., Shi, Z.J., Gu, Z.N., Liu, B.B., Yang, R.S., Yang, H.B., Zou, G.T., Zhang, Y., Iijima, S., 2000. Temperature dependence of the Raman spectra of single-wall carbon nanotubes. Appl. Phys. Lett. 76, 2053–2055. doi:10.1063/1.126252

Libowitzky, E., 1994. Anisotropic pyrite: A polishing effect. Phys. Chem. Miner. 21, 97–103. doi:10.1007/BF00205220

Loh, E., 1973. Optical vibrations in sheet silicates. J. Phys. C Solid State Phys. 6, 1091–1104. doi:10.1088/0022-3719/6/6/022

Louca, S., Crowe, S.A., 2017. Microscale reservoir effects on microbial sulfur isotope fractionation. Geochim. Cosmochim. Acta 203, 117–139. doi:10.1016/j.gca.2017.01.007

Loveday, J., 1973. Methods for analysis of irrigated soils. Commonw. Bur. Soils B2 - Commonw. Bur. Soils.

Lyons, T.W., Reinhard, C.T., Planavsky, N.J., 2014. The rise of oxygen in Earth's early ocean and atmosphere. Nature. doi:10.1038/nature13068

Mann, M.E., Bradley, R.S., Hughes, M.K., 1999. Northern hemisphere temperatures during the past millennium: Inferences, uncertainties, and limitations. Geophys. Res. Lett. 26, 759–762. doi:10.1029/1999GL900070

Mao, B., Dong, Q., Exstrom, C.L., Huang, J., 2014. Surface thermal stability of iron pyrite nanocrystals: Role of capping ligands. Thin Solid Films 562, 361–366. doi:10.1016/j.tsf.2014.04.033

Marin-Carbonne, J., Remusat, L., Sforna, M.C., Thomazo, C., Cartigny, P., Philippot, P., 2018. Sulfur isotope's signal of nanopyrites enclosed in 2.7 Ga stromatolitic organic remains reveal microbial sulfate reduction. Geobiology 16, 121–138. doi:10.1111/gbi.12275

Mason, P.R.D., Košler, J., de Hoog, J.C.M., Sylvester, P.J., Meffan-Main, S., 2006. In situ determination of sulfur isotopes in sulfur-rich materials by laser ablation multiple-collector inductively coupled plasma mass spectrometry (LA-MC-ICP-MS). J. Anal. At. Spectrom. 21, 177–186. doi:10.1039/B510883G

Mernagh, T.P., Trudu, A.G., 1993. A laser raman microprobe study of some geologically important sulfide minerals. Chem. Geol. 103, 113–127.

Meyer, N.R., Zerkle, A.L., Fike, D.A., 2017. Sulphur cycling in a Neoarchaean microbial mat. Geobiology 15, 353–365. doi:10.1111/gbi.12227

Meyers, S.R., 2007. Production and preservation of organic matter: The significance of iron.

Paleoceanography 22, PA4211. doi:10.1029/2006PA001332

Middleburg, J., 1989. A simple rate model for organic matter decomposition in marine sediments.pdf. Geochim. Cosmochim. Acta 53, 1577–1581.

Moran, P.A.P., 1950. Notes on continuous stochastic phenomena. Biometrika 37, 17–23. doi:10.1093/biomet/37.1-2.17

Morrison, J., Fourel, F., Churchman, D., 2000. Isotopic sulphur analysis by CF-IRMS.

Murowchick, J.B., Barnes, H.L., 1987. Effects of temperature and degree of supersaturation on pyrite morphology. Am. Mineral. 72, 24–1250.

Murowchick, J.B., Barnes, H.L., 1986. Marcasite precipitation from hydrothermal solutions. Geochim. Cosmochim. Acta 50, 2615–2629. doi:10.1016/0016-7037(86)90214-0

Nasdala, L., Beyssac, O., William Schopf, J., Bleisteiner, B., 2012. Application of Raman-based images in the Earth sciences. Springer, Berlin, Heidelberg, pp. 145–187. doi:10.1007/978-3-642-28252-2_5

Nasdala, L., Smith, D., Kaindl, R., Zeimann, M.A., 2004. Raman spectroscopy: Analytical perspectives in mineralogy research. EMU Notes Mineral. 6, 1–63. doi:10.1180/EMU-notes.6.7

Nemanich, R.J., Solin, S.A., Martin, R.M., 1981. Light scattering study of boron nitride microcrystals. Phys. Rev. B 23, 6348–6356.

Newhouse, W.H., 1936. Opaque oxides and sulphides in common igneous rocks. Bull. Geol. Soc. Am. 47, 1–52. doi:10.1130/GSAB-47-1

Ohfuji, H., Rickard, D., 2005. Experimental syntheses of framboids - A review. Earth-Science Rev. 71, 147–170. doi:10.1016/j.earscirev.2005.02.001

Osswald, S., Mochalin, V.N., Havel, M., Yushin, G., Gogotsi, Y., 2009. Phonon confinement effects in the Raman spectrum of nanodiamond. Phys. Rev. B - Condens. Matter Mater. Phys. 80, 075419(9). doi:10.1103/PhysRevB.80.075419

Owens, J.D., Lyons, T.W., Li, X., MacLeod, K.G., Gordon, G., Kuypers, M.M.M., Anbar, A., Kuhnt, W., Severmann, S., 2012. Iron isotope and trace metal records of iron cycling in the proto-North Atlantic during the Cenomanian-Turonian oceanic anoxic event (OAE-2). Paleoceanography 27, n/a-n/a. doi:10.1029/2012PA002328

Owens, J.D., Reinhard, C.T., Rohrssen, M., Love, G.D., Lyons, T.W., 2016. Empirical links between trace metal cycling and marine microbial ecology during a large perturbation to Earth's carbon cycle. Earth Planet. Sci. Lett. 449, 407–417. doi:10.1016/j.epsl.2016.05.046

Pačevski, A., Libowitzky, E., Živković, P., Dimitrijević, R., Cvetković, L., 2008. Copper-bearing pyrite from the Čoka Marin polymetallic deposit, Serbia: Mineral inclusions or true solid-solution? Can. Mineral. 46, 249–261. doi:10.3749/canmin.46.1.249

Papineau, D., Mojzsis, S.J., Coath, C.D., Karhu, J.A., McKeegan, K.D., 2005. Multiple sulfur isotopes of sulfides from sediments in the aftermath of Paleoproterozoic glaciations. Geochim. Cosmochim. Acta 69, 5033–5060. doi:10.1016/j.gca.2005.07.005

Paradis, E., Claude, J., Strimmer, K., 2004. APE: Analyses of Phylogenetics and Evolution in R language. Bioinformatics 20, 289–290. doi:10.1093/bioinformatics/btg412

Paris, G., Sessions, A.L., Subhas, A. V., Adkins, J.F., 2013. MC-ICP-MS measurement of δ34S and Δ33S in small amounts of dissolved sulfate. Chem. Geol. 345, 50–61. doi:10.1016/j.chemgeo.2013.02.022

Parnell, J., Boyce, A.J., Mark, D., Bowden, S., Spinks, S., 2010. Early oxygenation of the terrestrial environment during the Mesoproterozoic. Nature 468, 290–293. doi:10.1038/nature09538

Pasquier, V., n.d. Unpublished results.

Pasquier, V., Sansjofre, P., Rabineau, M., Revillon, S., Houghton, J., Fike, D.A., 2017. Pyrite sulfur isotopes reveal glacial−interglacial environmental changes. Proc. Natl. Acad. Sci. 114, 5941–5945. doi:10.1073/pnas.1618245114

Paytan, A., 2004. Seawater Sulfur Isotope Fluctuations in the Cretaceous. Science 304, 1663–1665. doi:10.1126/science.1095258

Philippot, P., Ávila, J.N., Killingsworth, B.A., Tessalina, S., Baton, F., Caquineau, T., Muller, E., Pecoits, E., Cartigny, P., Lalonde, S. V., Ireland, T.R., Thomazo, C., Van Kranendonk, M.J., Busigny, V., 2018. Globally asynchronous sulphur isotope signals require re-definition of the Great Oxidation Event. Nat. Commun. 9, 2245. doi:10.1038/s41467-018-04621-x

Poulton, S.W., 2003. Sulfide oxidation and iron dissolution kinetics during the reaction of dissolved sulfide with ferrihydrite. Chem. Geol. 202, 79–94. doi:10.1016/S0009-2541(03)00237-7

Powell, W., 2003. Greenschist-facies metamorphism of the Burgess Shale and its implications for models of fossil formation and preservation. Can. J. Earth Sci. 40, 13–25. doi:10.1139/e02-103

Prabhu, R.R., Khadar, M.A., 2008. Study of optical phonon modes of CdS nanoparticles using Raman spectroscopy. Bull. Mater. Sci. 31, 511–515.

Proske, U., Wood, R., Fallon, S., Stevenson, J., 2015. Use of heavy liquid density separation to remove pyrite from sediment samples for radiocarbon dating. Quat. Geochronol. 25, 66–71. doi:10.1016/j.quageo.2014.10.002

Raiswell, R., Plant, J., 1980. The incorporation of trace elements into pyrite during diagenesis of black shales, Yorkshire, England. Econ. Geol. 75, 684–699. doi:10.2113/gsecongeo.75.5.684

Rajalakshmi, M., Arora, A.K., 1999. Optical properties of selenium nanoparticles dispersed in polymer. Solid State Commun. 110, 75–80. doi:10.1016/S0038-1098(99)00055-1

Rajalakshmi, M., Arora, A.K., Bendre, B.S., Mahamuni, S., 2000. Optical phonon confinement in zinc oxide nanoparticles. J. Appl. Phys. 87, 2445–2448. doi:10.1063/1.372199

Rajalakshmi, M., Arora, A.K., Dash, S., Tyagi, A.K., 2003. Raman scattering investigations of nanocrystalline thorium oxide. J. Nanosci. Nanotechnol. 3, 420–422. doi:10.1166/jnn.2003.167

Raravikar, N., Keblinski, P., Rao, A., Dresselhaus, M., Schadler, L., Ajayan, P., 2002. Temperature dependence of radial breathing mode Raman frequency of single-walled carbon nanotubes. Phys. Rev. B 66, 1–9. doi:10.1103/PhysRevB.66.235424

Raven, M.R., Fike, D.A., Bradley, A.S., Gomes, M.L., Owens, J.D., Webb, S.L.A., 2019. Paired organic matter and pyrite δ34S records reveal mechanisms of carbon, sulfur, and iron cycle disruption during Ocean Anoxic Event 2. Earth Planet. Sci. Lett. 512, 27–38. doi:10.31223/OSF.IO/K97BW

Richter, H., Wang, Z.P., 1981. The one phonon Raman spectrum in microcrystalline silicon. Solid State Commun. 21, 625–629.

Riciputi, L.R., Paterson, B.A., Ripperdan, R.L., 1998. Measurement of light stable isotope ratios by SIMS: Int. J. Mass Spectrom. 178, 81–112. doi:10.1016/S1387-3806(98)14088-5

Rickard, D., 2019a. How long does it take a pyrite framboid to form? Earth Planet. Sci. Lett. 513, 64–68. doi:10.1016/j.epsl.2019.02.019

Rickard, D., 2019b. Sedimentary pyrite framboid size-frequency distributions: A meta-analysis. Palaeogeogr. Palaeoclimatol. Palaeoecol. doi:10.1016/j.palaeo.2019.03.010

Rickard, D., 2012. Sulfidic Sediments and Sedimentary Rocks, Developments in Sedimentology. Elsevier B.V. doi:10.1016/B978-0-444-52989-3.00017-9

Rickard, D., Luther, G.W., 1997. Kinetics of pyrite formation by the H2S oxidation of iron(II) monosulfide in aqueous solutions between 25 and 125 degrees C: The mechanism. Geochim. Cosmochim. Acta 61, 135–147. doi:doi:10.1016/S0016-7037(96)00321-3

Rickard, D.T., 1975. Kinetics and mechanism of pyrite formation at low temperatures. Am. J. Sci. 275, 636–652. doi:10.2475/ajs.275.6.636

Rolo, A., Vieira, L., Gomes, M., Ribeiro, J., Belsley, M.., dos Santos, M.., 1998. Growth and characterisation of cadmium sulphide nanocrystals embedded in silicon dioxide films. Thin Solid Films 312, 348–353. doi:10.1016/S0040-6090(97)00233-2

S Berné, 2004. PROMESS1 Summary cruise Report: past global changes investigated by drilling Mediterranean continental margins. Unpublished cruise report, Research Institute for Exploration of the Sea (IFREMER), Brest, France.

Schieber, J., 2011. Marcasite in Black Shales--a Mineral Proxy for Oxygenated Bottom Waters and Intermittent Oxidation of Carbonaceous Muds. J. Sediment. Res. 81, 447–458. doi:10.2110/jsr.2011.41

Schieber, J., 2007. Oxidation of detrital pyrite as a cause for Marcasite Formation in marine lag deposits from the Devonian of the eastern US. Deep. Res. Part II Top. Stud. Oceanogr. 54, 1312–1326. doi:10.1016/j.dsr2.2007.04.005

Schiffbauer, J.D., Xiao, S., Cai, Y., Wallace, A.F., Hua, H., Hunter, J., Xu, H., Peng, Y., Kaufman, A.J., 2014. A unifying model for Neoproterozoic-Palaeozoic exceptional fossil preservation through pyritization and carbonaceous compression. Nat. Commun. 5, 5754. doi:10.1038/ncomms6754

Schlanger, S.O., Jenkyns, H.C., 1976. Cretaceous oceanic anoxic events: causes and consequences. Geol. en Mijnbouw/Netherlands J. Geosci. 55, 179–184. doi:10.3233/BME-151338

Schneider, C.A., Rasband, W.S., Eliceiri, K.W., 2012. NIH Image to ImageJ: 25 years of image analysis. Nat. Methods. doi:10.1038/nmeth.2089

Shawar, L., Halevy, I., Said-Ahmad, W., Feinstein, S., Boyko, V., Kamyshny, A., Amrani, A.,

2018. Dynamics of pyrite formation and organic matter sulfurization in organic-rich carbonate sediments. Geochim. Cosmochim. Acta 241, 219–239. doi:10.1016/j.gca.2018.08.048

Siesser, W.G., 1978. Petrography and geochemistry of pyrite and marcasite in DSDP Leg 40 sediments. Initial Reports Deep Sea Drill. Proj. 38–41, 767–775.

Sim, M.S., Bosak, T., Ono, S., 2011a. Large sulfur isotope fractionation does not require disproportionation. Science 333, 74–77. doi:10.1126/science.1205103

Sim, M.S., Ono, S., Donovan, K., Templer, S.P., Bosak, T., 2011b. Effect of electron donors on the fractionation of sulfur isotopes by a marine Desulfovibrio sp. Geochim. Cosmochim. Acta 75, 4244–4259. doi:10.1016/j.gca.2011.05.021

Soetaert, K., Hofmann, A.F., Middelburg, J.J., Meysman, F.J.R., Greenwood, J., 2007. Reprint of "The effect of biogeochemical processes on pH." Mar. Chem. 106, 380–401. doi:10.1016/j.marchem.2007.06.008

Sourisseau, C., Cavagnat, R., Fouassier, M., 1991. The vibrational properties and valence force fields of FeS2, RuS2 pyrites and FeS2 marcasite. J. Phys. Chem. Solids 52, 537–544. doi:10.1016/0022-3697(91)90188-6

Studley, S.A., Ripley, E.M., Elswick, E.R., Dorais, M.J., Fong, J., Finkelstein, D., Pratt, L.M., 2002. Analysis of sulfides in whole rock matrices by elemental analyzer- continuous flow isotope ratio mass spectrometry. Chem. Geol. 192, 141–148. doi:10.1016/S0009-2541(02)00162-6

Suits, N.S., Wilkin, R.T., 1998. Pyrite formation in the water column and sediments of a meromictic lake. Geology 26, 1099–1102. doi:10.1130/0091-7613(1998)026<1099:PFITWC>2.3.CO;2

Sunagawa, I., 1957. Variations in crystal habit of pyrite. Geol. Surv. Japan 175, 1–41.

Tan, P., Deng, Y., Zhao, Q., Cheng, W., 1999. The intrinsic temperature effect of the Raman spectra of graphite. Appl. Phys. Lett. 74, 1818. doi:10.1063/1.123096

Thode, H.G., Monster, J., Dunford, H.B., 1961. Sulphur isotope geochemistry. Geochim. Cosmochim. Acta 25, 159–174. doi:10.1016/0016-7037(61)90074-6

Thornton, S.E., 1986. Origin of mass flow sedimentary structures in hemipelagic basin deposits: Santa Barbara Basin, California Borderland. Geo-Marine Lett. 6, 15–19. doi:10.1007/BF02311691

Tlili, A., Smith, D., Beny, J., 1989. A Raman microprobe study of natural micas. Mineral. Mag. 53, Part 2, 165–179.

Toth, D.J., Lerman, A., 1977. Organic matter reactivity and sedimentation rates in the ocean. Am. J. Sci. 277, 465–485. doi:10.2475/ajs.277.4.465

Tsu, R., Hernandez, J.G., 1982. Temperature dependence of silicon Raman lines. Appl. Phys. Lett. 41, 1016–1018. doi:10.1063/1.93394

Vallentyne, J.R., 1963. Isolation of pyrite spherules from recent sediments. Limnol. Oceanogr. 8, 16–30. doi:10.4319/lo.1963.8.1.0016

Valley, J.W., Cavosie, A.J., Ushikubo, T., Reinhard, D.A., Lawrence, D.F., Larson, D.J., Clifton,

P.H., Kelly, T.F., Wilde, S.A., Moser, D.E., Spicuzza, M.J., 2014. Hadean age for a post-magma-ocean zircon confirmed by atom-probe tomography. Nat. Geosci. 7, 219–223. doi:10.1038/ngeo2075

Valley, J.W., Kita, N.T., 2009. In-situ oxygen isotope geochemistry by Ion Microprobe. Mineral. Assoc. Canada Short Course 41, 19–63.

Vandewiele, S., Cowie, G., Soetaert, K., Middelburg, J.J., 2009. Amino acid biogeochemistry and organic matter degradation state across the Pakistan margin oxygen minimum zone. Deep. Res. Part II Top. Stud. Oceanogr. 56, 376–392. doi:10.1016/j.dsr2.2008.05.035

Vasilevskiy, M.I., Rolo, a G., Gomes, M.J.M., Vikhrova, O. V, Ricolleau, C., 2001. Impact of disorder on optical phonons confined in CdS nano-crystallites embedded in a SiO2 matrix. J. Physics-Condensed Matter 13, 3491–3509. doi:10.1088/0953-8984/13/14/320

Viera, G., Huet, S., Boufendi, L., Bertran, E., 2001. Crystal size and temperature measurements in nanostructured silicon using Raman spectroscopy. J. Appl. Phys. 90, 4175. doi:10.1063/1.1398601

Vogt, H., Chattopadhyay, T., Stolz, H.J., 1983. Complete first-order Raman spectra of the pyrite structure compounds FeS2, MnS2 AND SiP2. J. Phys. Chem. Solids 44, 869–873. doi:10.1016/0022-3697(83)90124-5

Volkov, I.I., Fomina, L.S., 1974. Influence of organic material and processes of sulfide formation on distribution of some trace elements in deep-water sediments of Black Sea, in: The Black Sea - Geology, Chemistry and Biology. pp. 456–476.

Wan, M., Schröder, C., Peiffer, S., 2017. Fe(III):S(-II) concentration ratio controls the pathway and the kinetics of pyrite formation during sulfidation of ferric hydroxides. Geochim. Cosmochim. Acta 217, 334–348. doi:10.1016/j.gca.2017.08.036

Wang, R.P., Zhou, G.W., Liu, Y.L., Pan, S.H., Zhang, H.Z., Yu, D.P., Zhang, Z., 2000. Raman spectral study of silicon nanowires: High-order scattering and phonon confinement effects. Phys. Rev. B 61, 16827–16832. doi:10.1103/PhysRevB.61.16827

Wei, Z.H., Qiu, Y.C., Chen, H.N., Yan, K.Y., Zhu, Z.L., Kuang, Q., Yang, S.H., 2014. Magnetic-field-assisted aerosol pyrolysis synthesis of iron pyrite sponge-like nanochain networks as cost-efficient counter electrodes in dye-sensitized solar cells. J. Mater. Chem. A 2, 5508–5515. doi:10.1039/c4ta00199k

Wenk, C.B., Wing, B.A., Halevy, I., 2017. Electron carriers in microbial sulfate reduction inferred from experimental and environmental sulfur isotope fractionations. ISME J. doi:10.1038/ismej.2017.185

White, S.S.N., 2009. Laser Raman spectroscopy as a technique for identification of seafloor hydrothermal and cold seep minerals. Chem. Geol. 259, 240–252. doi:10.1016/j.chemgeo.2008.11.008

Whitehouse, M.J., Kamber, B.S., Fedo, C.M., Lepland, A., 2005. Integrated Pb- and S-isotope investigation of sulphide minerals from the early Archaean of southwest Greenland. Chem. Geol. 222, 112–131. doi:10.1016/j.chemgeo.2005.06.004

Wilkin, R.T., Barnes, H.L., Brantley, S.L., 1996. The size distribution of framboidal pyrite in modern sediments: An indicator of redox conditions. Geochim. Cosmochim. Acta 60,

3897–3912. doi:10.1016/0016-7037(96)00209-8

Wing, B.A., Halevy, I., 2014. Intracellular metabolite levels shape sulfur isotope fractionation during microbial sulfate respiration. Proc. Natl. Acad. Sci. U. S. A. 111, 18116–25. doi:10.1073/pnas.1407502111

Xu, J., Xue, H., Yang, X., Wei, H., Li, W., Li, Z., Zhang, W., Lee, C.S., 2014. Synthesis of honeycomb-like Mesoporous pyrite FeS2 Microspheres as efficient counter electrode in quantum dots sensitized solar cells. Small 10, 4754–4759. doi:10.1002/smll.201401102

Yu, D., Sun, X., Lee, C., Bello, I., Lee, S., 1998. Synthesis of Boron Nitride Nanotubes by Means of Excimer Laser Ablation at High Temperature. Appl. Phys. Lett. 72, 1966.

Yücel, M., Gartman, A., Chan, C.S., Luther, G.W., 2011. Hydrothermal vents as a kinetically stable source of iron-sulphide-bearing nanoparticles to the ocean. Nat. Geosci. 4, 367–371. doi:10.1038/ngeo1148

Zhang, T., Shen, Y., Zhan, R., Shen, S., Chen, X., 2009. Large perturbations of the carbon and sulfur cycle associated with the Late Ordovician mass extinction in South China. Geology 37, 299–302. doi:10.1130/G25477A.1

Zhu, K.R., Zhang, M.S., Chen, Q., Yin, Z., 2005. Size and phonon-confinement effects on low-frequency Raman mode of anatase TiO2 nanocrystal. Phys. Lett. Sect. A Gen. At. Solid State Phys. 340, 220–227. doi:10.1016/j.physleta.2005.04.008

Zhu, Z.Y., Jiang, S.Y., Ciobanu, C.L., Yang, T., Cook, N.J., 2017. Sulfur isotope fractionation in pyrite during laser ablation: Implications for laser ablation multiple collector inductively coupled plasma mass spectrometry mapping. Chem. Geol. 450, 223–234. doi:10.1016/j.chemgeo.2016.12.037

Zouboulis, E., Grimsditch, M., 1991. Raman scattering in diamond up to 1900K. Phys. Rev. B 43, 3–6.